NATIONAL TRANSPORTATION SAFETY BOARD

Office of Research and Engineering
Washington, D.C. 20594

October 10, 2002

Aircraft Performance

Group Chairman's Aircraft Performance Study
by John O'Callaghan

TABLE OF CONTENTS

NATIONAL TRANSPORTATION SAFETY BOARD

Office of Research and Engineering
Washington, D.C. 20594

October 10, 2002

Aircraft Performance

Group Chairman's Aircraft Performance Study
by John O'Callaghan

A. ACCIDENT

Location:	Belle Harbor, New York
Date:	November 12, 2001
Time:	09:17 AM Eastern Standard Time (EST)
Flight:	American Airlines Flight 587
Aircraft:	Airbus A300B4-605R, Registration N14053
NTSB#:	DCA02MA001

B. GROUP

Chairman: John O'Callaghan
National Resource Specialist - Aircraft Performance
National Transportation Safety Board (NTSB)
490 L'Enfant Plaza E, SW
Washington, DC 20594

Members: Dominique Buisson
Department Manager - Aerodynamic and Handling
Engineering Directorate
Airbus Industrie
1 Rond Point Maurice Bellonte
31707 Blagnac Cedex, France

Captain Jerry Mumfrey
F100/A300 Technical Pilot, Flight Operations Technical
American Airlines
4601 Highway 360
Fort Worth, Texas 76155

Steven O'Neal
Flight Test Engineer
Federal Aviation Administration (FAA)
Seattle Aircraft Certification Office, ANM-160S
1601 Lind Avenue, S.W.
Renton, Washington 98055-4056

Yann Torres
Investigator – Engineering Department
Bereau Enquetes - Accidents (BEA)
Bâtiment 153 - Aéroport du Bourget
93352 Le Bourget Cedex, France

Jim Willson
Manager of Flight Safety
Allied Pilots Association (APA)
O'Connell Building - 14600 Trinity Blvd., Suite 500
Fort Worth, Texas 76155-2512

C. SUMMARY

On November 12, 2001, at approximately 9:17 AM Eastern Daylight Time (EDT), American Airlines flight 587 (AAL587), an Airbus Industrie A300-600, was destroyed when it crashed into a residential area of Belle Harbor, New York, shortly after takeoff from runway 31L at John F. Kennedy International Airport (JFK), Jamaica, New York. Before impact, the vertical stabilizer, rudder, and left and right engines departed the airplane. The 2 pilots, 7 flight attendants, 251 passengers, and 5 persons on the ground were killed. Visual meteorological conditions prevailed and an instrument flight rules flight plan had been filed for the flight destined for Santo Domingo, Dominican Republic. The scheduled passenger flight was conducted under 14 *Code of Federal Regulations* (CFR) Part 121.

The purpose of the Aircraft Performance Group (ACPG) is to determine and analyze the motion of the aircraft and the physical forces that produce that motion. In particular, the Group attempts to define the aircraft position and orientation throughout the flight, and determine its response to control inputs, system failures, external disturbances, or other factors that could affect its trajectory. For this investigation, the ACPG is also responsible for determining the loads (forces and moments) that the aircraft motion produces on the vertical stabilizer.

The data the ACPG uses to determine the aircraft motion and resulting loads includes but is not limited to the following:

- Wreckage location and condition.
- Ground scars / markings and damage to ground structures.
- Air Route Surveillance Radar (ARSR) & Airport Surveillance Radar (ASR) data.

- Digital Flight Data Recorder (DFDR) data.
- Cockpit Voice Recorder (CVR) information.
- Weather information.
- Output from computer programs and simulations that calculate aircraft performance and structural loads.
- Ground and flight tests.

This aircraft performance study describes the results of using the data listed above in defining, as far as possible, the motion of American Airlines flight 587, and the resulting structural loads on the vertical stabilizer. The study introduces the aircraft motion data collected during the investigation, describes the methods used to extract additional aircraft motion information from DFDR, radar, CVR, and weather data, and presents the results of these calculations. The difficulties of working with low sample rate data and flight control surface position data that has been filtered prior to being recorded on the DFDR are also described. Finally, the study presents the results of simulations performed by Airbus to determine the expected motion of the aircraft given the control surface positions recorded by the DFDR, and the results of Airbus and NTSB calculations of the structural loads on the vertical stabilizer throughout the accident sequence.

D. DETAILS OF THE INVESTIGATION

I. Wreckage Location and Condition, Ground Scars and Markings, and Damage to Surface Structures

The wreckage of flight 587 was confined to an area of approximately 500 ft by 300 ft. The location of the main impact crater was measured with a hand-held Global Positioning System (GPS) receiver as N 40° 34' 37.59" Latitude, W 73° 51' 01.31" Longitude (approximately at the corner of Beach 131st St. and Newport Ave.). The impact crater was about 150 ft. in diameter. The tail section of the airplane (horizontal stabilizer and vertical stabilizer fuselage attach points) was located outside of the crater, approximately 100 ft. to the East, across Beach 131st St. Two houses were destroyed by the impact of the airplane, and two other houses were subsequently destroyed by the post-crash fire. In addition, 4 houses were lightly damaged by fire.

The left engine was found about 680 ft. North of the main impact crater, lightly damaging a building at a gas station. The right engine was found about 850 ft. Northeast of the main impact crater, damaging a boat parked in a driveway.

The vertical stabilizer and rudder were found floating in Jamaica Bay, approximately 0.7 NM (4250 ft.) from the main impact site. The locations of the vertical stabilizer and rudder, left and right engines, and main impact crater are shown in Figure 1a, along with the flight path of the airplane as recorded by the JFK ASR-9 radar (see Section D-II for more information on radar data). The large distances between the locations of the main impact site and the engines and vertical tail and rudder indicate that the latter departed the airplane prior to the main impact.

The positions of various items of interest at the main impact site were measured using a hand-held GPS receiver. These items included the main impact crater, the right and left engines, the tail section of the airplane, and various ground structures near the impact site that were not impacted by the airplane.

The height of various ground structures near the main impact site that were not struck by the airplane were measured in order to determine a lower limit for possible airplane flight path angles before impact. The locations of these structures and other elements of the accident debris field are plotted as distances North and East of the main impact crater in Figure 1b. The latitude and longitude coordinates and height of the surveyed objects is tabulated in Table 1. Table 1 also indicates the angle from the horizontal from the top of the surveyed structure to the impact crater (column labeled “angle” in Table 1). This angle is the minimum flight path angle the airplane would need to clear the structure on its way to the impact crater, if it were passing directly over the structure.

Note that because the structures surrounding the impact crater are only 30 to 40 ft. high, and are all further than 40 ft. from the impact crater, the largest angle shown in Table 1 is 25 degrees (down). However, this is only a lower limit, and given the confined area of the wreckage, it is likely that the flight path angle at impact was much steeper than 25 degrees.

II. Radar Data

Description of Radar Sites That Tracked AAL587

In general, two types of radar are used to provide position and track information, both for aircraft cruising at high altitudes between airport terminal airspaces, and those operating at low altitude and speeds within terminal airspaces.

Air Route Surveillance Radars (ARSRs) are long range (250 NM) radars used to track aircraft cruising between terminal airspaces. ARSR antennas rotate at 5 to 6 RPM, resulting in a radar return every 10 to 12 seconds. A block of airspace may be covered by more than one ARSR antenna, in which case the data from these antennas are fed to an FAA central computer where the returns are sorted and the data converted to latitude, longitude, and altitude information. The converted data is displayed to the FAA Air Route Traffic Control Center (ARTCC) controller, and recorded electronically in National Track Analysis Program (NTAP) text format. While an aircraft may be detected by several ARSRs, the ARTCC controller will only see one radar return on his display for that aircraft, and only one set of position data will be recorded in NTAP format for that aircraft. The raw data generated by each ARSR is not recorded in the NTAP file; rather, the position information computed by sorting through the returns from all the ARSRs sending data is recorded. The New York ARTCC (ZNY) recorded two secondary radar returns from AAL587 (see below).

FAA Airport Surveillance Radars (ASRs) are short range (60 NM) radars used to provide air traffic control services in terminal areas. ASR antennas rotate at about 13 RPM, resulting in a radar return about every 4.6 seconds. The FAA records the data received by

each site in Continuous Data Recording (CDR) text format. The FAA ASR-9 radars at the following stations received returns from AAL587: Kennedy (JFK), Newark (EWR), White Plains (HPN), and Islip (ISP).

Primary and Secondary Radar Returns

A radar detects the position of an object by broadcasting an electronic signal that is reflected by the object and returned to the radar antenna. These reflected signals are called *primary returns.* Knowing the speed of the radar signal and the time interval between when the signal was broadcast and when it was returned, the distance, or range, from the radar antenna to the reflecting object can be determined. Knowing the direction the radar antenna was pointing when the signal was broadcast, the direction (or bearing, or azimuth) from the radar to the object can be determined. Range and azimuth from the radar to the object define the object's position. In general, primary returns are not used to measure the altitude of sensed objects, though some ARSRs do have height estimation capability. ASRs do not have height estimation capabilities.

The strength or quality of the return signal from the object depends on many factors, including the range to the object, the object's size and shape, and atmospheric conditions. In addition, any object in the path of the radar beam can potentially return a signal, and a reflected signal contains no information about the identity of the object that reflected it. These difficulties make distinguishing individual aircraft from each other and other objects (e.g., flocks of birds) based on primary returns alone unreliable and uncertain.

To improve the consistency and reliability of radar returns, aircraft are equipped with transponders that sense beacon interrogator signals broadcast from radar sites, and in turn broadcast a response signal. Thus, even if the radar site is unable to sense a weak reflected signal (primary return), it will sense the response signal broadcast by the transponder and be able to determine the aircraft position. The response signal can also contain additional information, such as the identifying "beacon code" for the aircraft, and the aircraft's pressure altitude (also called "Mode C" altitude). The beacon code identifier for AAL587 was 2650. The beacon code identifier for Japan Airlines flight 47 (JAL47), which preceded AAL587 off of runway 31L from JFK, was 1710. Transponder signals received by the radar site are called *secondary returns*.

Recorded Radar Data

Each FAA ARTCC records the radar data used by that Center and displayed to its controllers. The New York ARTCC tracked AAL587 very briefly; only two long range ARSR secondary returns were recorded into an NTAP file. The parameters of interest in this file are:

- Universal Coordinated Time (UTC) of the radar return, in hours, minutes, and seconds.
- Transponder beacon code associated with the return (secondary returns only).
- Transponder reported altitude in hundreds of feet associated with the return (secondary returns only). The transponder reports pressure altitude, but the FAA computers adjust

this altitude for the current altimeter setting for the area in which the airplane is flying. This adjusted altitude is recorded in the NTAP file.
- Latitude and Longitude of the radar return as calculated by the ARTCC.

The ZNY secondary returns are presented in Table 11. No primary returns near the end of AAL587's flight were recorded by ZNY.

The data recorded by the JFK, EWR, HPN, and ISP ASR-9 radars in CDR format includes the following parameters:

- UTC time of the radar return, in hours, minutes, and seconds.
- Transponder beacon code (secondary returns only).
- Transponder reported altitude in hundreds of feet (secondary returns only). The transponder reports pressure altitude. The altitude recorded in the CDR includes both pressure altitude (based on a sea level pressure of 29.92 "Hg), and pressure altitude adjusted for altimeter setting (30.44 "Hg at the time of the accident). The adjusted altitude is presented in Tables 2-11 (see below). The resolution of the altitude data is ±50 ft.
- Slant Range from the radar antenna to the return, in NM. The accuracy of this data is ±1/16 NM or about ±380 ft.
- Azimuth relative to Magnetic North from the radar antenna to the return, in Azimuth Change Pulses (ACPs). ACP values range from 0 to 4096, where 0 = 0° magnetic and 4096 = 360° magnetic. Thus, the azimuth to the target in degrees would be:

  (Azimuth in degrees) = (360/4096) x (Azimuth in ACPs) = (0.08789) x (Azimuth in ACPs)

  The accuracy of this data is ±2 ACP or ±0.176 degrees. All the ASR-9 sites discussed in this Study use a magnetic variation of 13° W to compute magnetic azimuth.

Presentation of the Radar Data

The data listed above for ZNY and all the ASR-9 radars discussed in this Study are presented in Tables 2-11. All the secondary returns recorded for AAL587 are presented in the tables, but only those primary returns near the time and location of the end of the accident flight are presented. Secondary returns for JAL47 recorded by the JFK ASR-9 are presented in Table 4, through 09:16:19 EST (the approximate time of the accident).

In addition to the data recorded in FAA NTAP and CDR files, Tables 2-11 present several parameters derived using the recorded radar data and Cockpit Voice Recorder (CVR), ATC voice recordings, and radar site location information. These parameters include the local ATC time, the latitude and longitude of the radar returns, and the East and North coordinates of the returns relative to the impact site. Section D-III presents the relationship between the recorded radar time, the local ATC time reference used throughout this study, and the CVR and Digital Flight Data Recorder (DFDR) times. Range and azimuth data is converted into latitude and longitude and East and North coordinates using the WGS84 ellipsoid model of the Earth.

The radar data is presented graphically in Figures 2-8:

Figure 2 shows the location of the ASR-9 radar sites that tracked AAL587.

Figure 3a shows the primary and secondary radar returns from the ASR-9s plotted in East-North coordinates relative to the impact site.

Figure 3b is identical to Figure 3a, but with the plot gridlines replaced with a map background.

Figure 4a shows the secondary radar returns recorded by the JFK ASR-9 for both AAL587 and JAL47, as well as the primary returns recorded by the JFK ASR-9 near the time and location of the accident. The secondary returns in this Figure are labeled with the time of the return in local ATC time, and the Mode C reported altitude (corrected for altimeter setting). The primary returns are labeled with the time of the return only, in italic font.

Figure 4b is identical to Figure 4a, but with the plot gridlines replaced with a map background.

The top plot of Figure 5 shows the AAL587 Mode C altitude returns, corrected for altimeter setting, from ZNY and the four ASR-9 radars as a function of time. The bottom plot shows the Mode C altitude (corrected for altimeter setting) for AAL587 and JAL47 recorded by the JFK ASR-9 as a function of time.

Figure 6a shows the East and North positions of the secondary returns from AAL587 and JAL47 recorded by the JFK ASR-9 as a function of time. The primary returns recorded by the JFK ASR-9 near the time and location of the accident are also shown.

Figure 6b shows the horizontal and vertical separation between JAL47 and AAL587 as a function of time. The Figure indicates that the two aircraft were never closer than about 4.3 nautical miles horizontally and 3,800 feet vertically.

Figure 7 shows the altitude data used to correlate the radar and DFDR clocks, as described in Section D-III.

Finally, Figure 8 shows a plan view of the flight path of AAL587 during the last minute of flight, with the locations of the occurrence of CVR comments and sounds indicated.

III. Digital Flight Data Recorder (DFDR) and Cockpit Voice Recorder (CVR) Data

DFDR and CVR Data Description

The aircraft cockpit voice recorder (CVR) and digital flight data recorder (DFDR) were recovered from the accident wreckage and sent to Washington, DC for readout.

Descriptions of the DFDR and CVR and the recorder readout processes can be found in the Factual Reports of the Flight Data Recorder and Cockpit Voice Recorder Groups, respectively. The DFDR readout results in tabulated and plotted values of the recorded flight parameters versus time. The CVR readout results in a transcript of the CVR events, a partial list of which is shown in Table 12. Selected CVR events listed in Table 12 are also presented along with other information in various Figures throughout this study.

Coordination of ATC, Radar, DFDR, and CVR Times

The ASR-9 radars, the DFDR, and the CVR record their information with respect to time, but these recorded times are not synchronized. To use these data sources together, their times must be synchronized to a single reference time. This reference time is the local ATC EST time introduced in Section D-II and used throughout this study.

Time on the DFDR is measured in terms of the Subframe Reference Number (SRN), with one SRN equivalent to one second of time. The ATC EST time is related to the DFDR SRN by aligning the times of transmissions from the aircraft to ATC as recorded on the ATC transcript with microphone keying events recorded by the DFDR. The last communication from AAL587 occurred at about 09:15:41, and corresponds to the microphone keying event at SRN 832.77[1], and so the following relationship is established:

09:15:41 (EST) Local ATC Time = 832.77 DFDR SRN [1]

GMT Time is also recorded on the DFDR. Comparing the SRNs corresponding to the recorded GMT and using Equation [1] indicates that the GMT recorded by the DFDR is about 0.77 seconds ahead of the Local ATC Time (DFDR Time = ATC Time + 0.77 sec).

Because the JFK ASR-9 was the closest radar to and recorded the most returns from the accident flight, this site was chosen for correlating radar time to the DFDR and CVR and for information regarding the aircraft's position throughout the flight. The synchronization of the JFK ASR-9 time with the other ASR clocks or with ZNY has not been checked rigorously. However, in Figure 5, the good match of the Mode C altitudes from the various ASR-9 sites suggests that their clocks are relatively well synchronized.

The relationship between the UTC time recorded by the JFK ASR-9 radar and the DFDR time is established by comparing the altitude recorded by the DFDR with the (unadjusted) Mode C altitude recorded by the JFK ASR-9. Both altitudes are based on the static pressure sensed at the airplane's static pressure ports, and on a sea level pressure of 29.92 "Hg (i.e., both altitudes are pressure altitude). By adjusting the DFDR times so that the DFDR altitude falls within the ±50 ft. uncertainty band of the JFK Mode C altitude during the climb, the offset between DFDR time and JFK time can be determined.

This process is illustrated in Figure 7, and gives the result

[1] This keying event is not the last one recorded on the DFDR. The last keying event occurs at SRN 850.38, but there is no communication with ATC associated with this event.

14:15:00 (UTC) JFK ASR-9 Radar Time = 791.43 DFDR SRN [2]

Using Equations [1] and [2] gives

14:15:41.34 (UTC) JFK ASR-9 Time = 09:15:41 (EST) Local ATC Time [3]

So the radar clock is ahead of the ATC clock by 0.34 seconds.

The relationship between the times of events recorded on the CVR and the ATC reference time is established by first establishing the conversion from CVR to DFDR time, and then using the DFDR to ATC time conversion described by Equation [1].

The mapping of CVR event times to DFDR Subframe Reference Numbers is accomplished by comparing the times of events recorded on both the DFDR and CVR. In general, these common events include the start and end of radio transmissions (both recorders detect microphone keying activity), the activation of warning systems in the cockpit (a discrete changes state on the DFDR, and an aural alarm is heard on the CVR), and the end of both DFDR and CVR recordings upon impact. In this accident, however, the DFDR stopped recording in the air, about 13.6 seconds before impact, while the CVR continued recording until impact. While there are sounds similar to ECAM warning chimes recorded on the CVR, the first of these occurs almost simultaneously with the end of the DFDR recording, and no ECAM warning discretes change state on the DFDR. Consequently, only the microphone keying discretes could be used to correlate the CVR and DFDR times[2].

The time alignment of these common DFDR and CVR events is complicated by two factors:

- The DFDR Microphone Keying discretes are only sampled once every second, and so the times of these events have an uncertainty of -1 to +0 seconds.

- The CVR tape does not record a time parameter, and so the timing of CVR events must be determined at the time the tape is replayed. If the tape is not replayed at the same speed at which it was recorded, the CVR times established during the process will be in error. Furthermore, the speed of the CVR tape during recording can vary, so the appropriate playback speed may depend on the portion of tape being read.

The correct playback speed of the CVR tape can be approximated by adjusting it so that, upon playback, the AC electrical noise signal that bleeds into the CVR system and is recorded on the CVR produces a signal whose frequency matches that of the AC generator that produced the noise. The frequency of this generator is assumed to be exactly 400 Hz. If the CVR tape is played too quickly, the AC noise signal frequency will be greater than 400 Hz, and if it is played too slowly, the frequency will be less than 400 Hz. The actual AC generator on the airplane may not have been operating at exactly 400 Hz,

[2] Twelve microphone keying events throughout the 31 minute CVR recording were used in this study to define the relationship between the CVR times and DFDR Subframe Reference Numbers.

and the tape speed itself can vary during recording, so this method only gives a first approximation of the timing of CVR events.

The approximate CVR times of the common CVR/DFDR events, together with the precise DFDR SRNs defining the intervals in which those events occur on the DFDR, provide a series of constraints that help define the relationship between CVR times and DFDR SRNs. Any mathematical mapping between CVR time and DFDR SRN that satisfies these constraints may be used to define the time alignment between the two recorders. In practice, the preferred mapping is a straight line. If no single line will satisfy all the constraints, multiple lines are used. For the AAL587 CVR, three lines were required to satisfy the constraints imposed by microphone keying events. The results indicate that the portion of the CVR that recorded the end of the flight was played back at a speed about 1.6% faster than the recording speed, while at the beginning of the tape, the playback was only about 0.2% fast.

Once the mapping from CVR time to DFDR SRN is established, the times of all CVR events (even those that do not have corresponding events on the DFDR) can be converted to their equivalent DFDR SRN. Equation [1] can then be used to convert from DFDR SRN to the ATC EST reference time.

In Table 12, the time of CVR events is expressed in the reference ATC time.

IV. Performance Calculations based on DFDR Data

Overview

The DFDR records many, but not all, performance parameters of interest. Many additional parameters can be derived from the DFDR parameters; however, the DFDR parameters themselves can suffer from inherent measurement errors[3] and must be corrected before being used in these calculations.

This section describes the corrections applied to the DFDR data, and the calculations used to derive additional performance parameters from the corrected data. The airplane weight and center of gravity (CG) used in these calculations are 350,000 lb. and 29% Mean Aerodynamic Chord (MAC), respectively[4]. The vertical CG position used is 0.7 meters below the Fuselage Reference Line, and the lateral CG used is on the airplane's centerline. These are the nominal vertical and lateral CG positions assumed in the Airbus A300-600 Engineering Simulator. Further details on the calculations and the associated equations used in this Study are given in Appendix A.

The DFDR corrections discussed in this Study attempt to remove the following errors:

[3] "Measurement error" in this context means the difference between the actual true value of the quantity being measured and the measured or recorded value. It does not necessarily imply defects or malfunctions in the measurement and recording equipment itself.

[4] These values were obtained from the Operations Group.

- Altitude error associated with non-standard day conditions (pressure altitude to actual altitude estimate)
- Accelerometer location and bias errors
- Error in recorded rudder surface position due to filtering of rudder data by the System Data Acquisition Concentrator (SDAC) computer

Potential errors that are not accounted for in these calculations include recording latencies in the DFDR data, in which the time associated with a recorded value does not correspond exactly to the time the value was sampled, but has been delayed slightly by processing times in the airplane's systems. The delays are on the order of a fraction of a second, and their effects are still being investigated by the ACPG.

The performance parameters derived from the corrected DFDR data include:

- True airspeed
- Mach number
- Dynamic pressure and static temperature
- True altitude estimate and integrated altitude
- Rate of climb/descent
- Flight path angle
- Sideslip angle
- Wind speed and direction
- Angular rates and accelerations
- Load factors in cockpit
- Cockpit control forces
- Actual rudder position estimate based on recorded filtered position

The results of these corrections and derivations are presented in Figures 8-23. The "a" Figures present the results for the last 50 seconds of the flight; the "b" Figures show the last 12 seconds of the DFDR data in more detail. In what follows, a reference to a Figure number refers to both the "a" and "b" Figures, unless the "a" or "b" is explicit in the reference. Thus, for example, "Figure 10" refers to both Figures 10a and 10b, but "Figure 10a" refers only to that Figure.

Mach Number, Dynamic Pressure, Static Temperature, and True Airspeed Calculations

True airspeed equals the Mach number multiplied by the speed of sound; the speed of sound is a function of the static temperature, and the static temperature can be derived from total temperature and Mach number. Mach number can be found from calibrated airspeed and static pressure. Total temperature and calibrated airspeed are recorded directly by the DFDR, and the static pressure can be determined from the DFDR pressure altitude and known reference pressure of 29.92" Hg. Once static temperature and pressure are known, the static density can be calculated, and then dynamic pressure can be calculated using density and true airspeed[5].

[5] For more detail on these calculations and those that follow, see Appendix A.

Figures 10 and 11 show the results of these calculations. In Figure 10, the recorded calibrated airspeed points are shown, together with the cubic spline interpolation[6] through these points that serves as the basis for other airspeed calculations. The "Inertial True Airspeed" shown is the result of integrating the accelerometers to obtain an inertial speed that matches the groundspeed recorded on the DFDR, and then factoring in the wind to obtain airspeed (see Equation [8] and Figure 24b). The wind estimate used in this calculation is the same as that used in the sideslip angle estimate, and is described below.

The "Integrated Groundspeed" in the bottom of Figure 10 is the result of integrating the accelerometers (see "*Accelerometer Data Corrections and Integration*" below). The winds are added to this groundspeed in order to obtain the "Inertial True Airspeed."

The static temperature calculation is shown in Figure 23.

Pressure-Based True Altitude Calculation

The altitude recorded by the DFDR is pressure altitude; i.e., it is the altitude in the standard atmosphere corresponding to the static pressure sensed at the airplane's static port. The altitude in the actual atmosphere corresponding to the local static pressure generally does not equal the pressure altitude, and it is insufficient to simply adjust the pressure altitude for the local sea level pressure because, in general, the lapse rate of pressure with altitude does not match the lapse rate in the standard atmosphere.

To estimate the actual altitude of AAL587, the recorded pressure altitude is adjusted to account for the 30.44 "Hg altimeter setting. This places the airplane at the correct field elevation (12 ft., for JFK runway 31L). During the takeoff and climb, the change in altitude corresponding to a change in static pressure is calculated by solving the hydrostatic equation continuously. The hydrostatic equation describes the pressure increment across a differential element of air required to balance the weight of the element (see Appendix A). With static pressure and the static temperature values from the speed calculations, the density and weight of the air elements can be calculated throughout the flight.

The results of this calculation are shown in Figure 9 as the line labeled "True altitude based on pressure data." The line labeled "Integrated altitude" is the altitude that results from integrating the DFDR load factor data twice to derive aircraft position (described further below). It is a better estimate of the actual path of the airplane since it does not suffer from the static pressure sensing errors inherent in the DFDR altitude data; the difference between the "Accelerometer Integration" and "Corrected for Actual Atmosphere" lines indicate that the effects of these sensing errors can be significant, especially at the end of the flight, where the sideslip angle is large and the angular rates are high and the local pressure over the static pressure ports is disturbed. Since the airplane transponder that reports Mode C altitude also senses pressure from these ports, it is not surprising that the

[6] Throughout this Study, Akima cubic splines are used to interpolate data values between sampled DFDR data points.

Mode C data follows the DFDR pressure data trend and is erroneously high at the end of the flight.

The differences between the altitudes based on pressure and integrated accelerometer data are further illustrated in Figures 11 and 12, in the plots of rate of climb and flight path angle. Both these calculations are based on the first time derivative of the altitude data; one readily observes that the accelerometer-based data is smooth, whereas the pressure-based data contains unrealistic oscillations associated with the effects of interpolating between the sampled pressure altitude points.

The integrated altitude data is in very good agreement with the DFDR recorded radio altitude, as determined by the airplane's radar altimeter, though at the end of the DFDR data the integrated altitude is about 40 ft. lower than the radio altitude.

The radar sites tracking AAL587 stopped receiving transponder returns from the airplane shortly after the end of DFDR data. Consequently, there is no recorded DFDR or radar information about the altitude of the airplane during its final descent to the impact site. However, estimates of the airplane's altitude at four points during the descent was made based on images from a toll booth video camera that captured a portion of the accident flight. These estimates are detailed in the Video Study report performed in the NTSB Vehicle Recorders Division. The resulting altitudes are plotted in Figure 9a as red stars. The time and altitude of the "flash" from the airplane recorded on the video tape corresponds to the second point plotted in Figure 9a.

Accelerometer Data Corrections and Integration

An accurate estimate of the flight path of the airplane during relatively short intervals (about 30 to 60 seconds) can be obtained by integrating accelerometer data. However, the accelerometers are in general not located coincident with the center of gravity (CG) of the airplane, and so before integrating the load factors at the CG must be calculated from the accelerometer data and the rotational velocity and acceleration of the airplane described by the time history of the yaw, pitch and roll angles. Furthermore, accelerometers generally contain small offsets, or "biases," that produce large errors in speed and position if not removed prior to integration. The values of the biases can be determined by trial and error, selecting them so that the aircraft position that results from integrating the accelerations agrees with known positions determined from another source (see Appendix A).

In this study, accelerometer biases were chosen so that the integrated position and altitude during level flight between DFDR SRN = 820 seconds and DFDR SRN = 853 seconds (09:15:28.23 to 09:16:01.23) agree well with the North and East positions calculated by integrating DFDR track angle and ground speed, and with both the radio altitude recorded during the period and the calculated true pressure-based altitude. The values of the biases (in g's) are as follows:

Longitudinal Load Factor Bias (Δn_x) = 0.00410
Lateral Load Factor Bias (Δn_y) = 0.00900
Vertical Load Factor Bias (Δn_z) = -0.02350

The corrected load factor value is obtained by adding the bias to the recorded value. Note that the vertical load factor (n_z) is equal and opposite to the normal load factor recorded on the DFDR (nlf), because the z axis of the airplane points down (see Figure 24a), but the nlf recorded by the DFDR is positive upwards. The magnitude of the accelerometer biases is illustrated graphically in Figure 15. The Figure shows the DFDR load factors together with the "Corrected" load factors, which have been adjusted to reflect values at the CG and shifted by the bias values.

The altitude resulting from the accelerometer integration is plotted in Figure 9; the initial altitude for the integration has been set equal to the initial "True altitude based on pressure data." This altitude is the proper target for the accelerometer integration (prior to the large rudder movements) because, unlike the radio altitude, it is not affected by the terrain below the aircraft.

Sideslip Angle and Wind Calculations

The sideslip angle (β) is the angle that the velocity vector of the airplane makes with the airplane's plane of symmetry (see Figure 24a). This angle is as fundamental to the airplane's lateral-directional performance and handling qualities as the angle of attack is to the longitudinal performance and handling qualities. The sideslip angle is essentially the angle of attack seen by the vertical tail[7], and as such it drives the side force coefficient of the vertical tail. Since the side force, and load, exerted by the vertical tail are directly proportional to the product of the side force coefficient, the dynamic pressure, and the vertical tail area, the sideslip angle can be an important contributor to the load on the vertical tail. Consequently, the value of the sideslip angle throughout the accident sequence is of significant interest.

Unfortunately, the A300-600, like most transport category aircraft, does not have β sensors, and so β must be calculated from other parameters. An estimate of β can be made if the side force (Y) characteristics of the airplane are known and if the side force generated during the flight can be calculated. The most significant contributors to the side force are β and rudder deflection (δr):

$$C_Y = \frac{Y}{\frac{1}{2}\rho V^2 S} = \frac{\partial C_Y}{\partial \beta}\beta + \frac{\partial C_Y}{\partial \delta r}\delta r + \{\textit{smaller terms}\} \qquad [4]$$

Where C_Y is the sideforce coefficient, ρ is the air density, V is true airspeed, and S is the wing reference area (2,800 ft^2). Ignoring the smaller terms, [4] can be solved for an estimate of β:

[7] β at the tail can be different than β at the CG because of sidewash and yaw rate effects, but the tail β depends primarily on the β at the CG.

$$\beta \cong \frac{C_Y - \left(\frac{\partial C_Y}{\partial \delta r}\right)\delta r}{\frac{\partial C_Y}{\partial \beta}} \qquad [5]$$

The derivatives $\partial C_Y / \partial \beta$ and $\partial C_Y / \partial \delta r$ are aerodynamic characteristics of the airplane that are known from wind tunnel and flight tests.

The side force Y can be calculated using

$$Y = W n_y \qquad [6]$$

Where n_y is the lateral load factor, corrected for the accelerometer bias calculated above.

Equation [4] will only hold true when the $\partial C_Y / \partial \beta$ and $\partial C_Y / \partial \delta r$ terms used reflect the real characteristics of the airplane, i.e., when the airplane is intact. Furthermore, during very dynamic conditions, the "smaller terms" in Equation [4] (such as sideforce due to yaw rate) can become important. After the tail separates from AAL587, the $\partial C_Y / \partial \beta$ term is reduced drastically and the $\partial C_Y / \partial \delta r$ term goes to zero by definition, and so the values used prior to that point are no longer valid. In addition, because of the very dynamic conditions prior to the tail separating, there is some risk in ignoring the "smaller terms" in Equation [4]. For these reasons, an additional method of calculating β is warranted.

From Figure 24a, we see that

$$\beta = \sin^{-1}\left(\frac{v}{V}\right) \qquad [7]$$

where V is total airspeed, and v is the component of V along the y body axis. The airspeed and its components in the body axes can be computed if the components of both the groundspeed and wind speed are known. Airspeed, groundspeed, and wind are related as follows:

$$\vec{V} = \vec{V}_G - \vec{V}_W \qquad [8]$$

where $\vec{V}$ is the airspeed vector, $\vec{V}_G$ is the groundspeed vector and $\vec{V}_W$ is the wind vector (see Figure 24b). The components of $\vec{V}_G$ in body axes result from the integration of the accelerometer data described above. The components of $\vec{V}_W$ can be calculated by transforming the components of the wind in Earth axes into body axis using the recorded Euler angles (yaw, pitch and roll).

The wind speed $\vec{V}_W$ is, in general, unknown; the wind estimates obtained from meteorological observations, and even the wind speed and direction data recorded by the

DFDR, are not precise or accurate enough to be used in a calculation of β. Instead, $\vec{V}_W$ must be computed using Equation [8], which requires the components of the airspeed $\vec{V}$ in body axes, and consequently, as indicated by Figure 24a, the values of angle of attack (α) and β. α is recorded on the DFDR, but β is of course unknown and the object of this series of calculations. However, until the final moments of the flight, the airplane can be assumed to be flying in a normal, coordinated manner[8], such that $\beta \approx 0$. Assuming zero β, the wind up until the final maneuver can be calculated. It is reasonable to assume that during the final few seconds, the wind speed and direction did not vary much, and that the values of these parameters throughout the maneuver were essentially equal to their values at the start of the maneuver. It is likely that AAL587 encountered wake turbulence just prior to the final maneuver (see below and Appendix B), and that this turbulence produced local changes in α and β on the airplane. Nonetheless, the velocity of the surrounding airmass in which AAL587 was flying (the bulk wind) probably remained stable over the 12 seconds or so of interest, and so a good estimate of the β that would be produced by the yawing motion of the airplane can be obtained. Increments to α and β produced by the turbulence would modify this "baseline" β over local parts of the airplane. To evaluate these second-order effects, simulation can be used, as described in Section D-V.

The results of the β calculations using Equations [5] and [7] are compared in Figure 13, and are in generally good agreement. Because of the limitations of the "side force buildup" method underlying Equation [5], the "inertial" β resulting from Equation [7] is probably more accurate. This is the value of β used in the NTSB load calculations discussed in Section VI. The wind speed and direction based on Equation [8] and used in the inertial β calculation are plotted in Figure 23.

Figure 13 also shows an "inertial sideslip at vertical tail." This β is computed by modifying the β at the CG to account for the angular motion of the airplane, which induces incremental velocities and angles at points away from the CG (see Section A-IV of Appendix A). The calculation accounts for the yaw rate of the airplane, but does not include sidewash effects. For a more sophisticated computation of the β at the tail that includes sidewash, see the loads calculations in Section D-VI.

Angular Rates and Accelerations and Load Factors in the Cockpit

The angular rates about the airplane body axes are calculated from the time derivative of the Euler angles as follows:

$$\begin{Bmatrix} P \\ Q \\ R \end{Bmatrix} = \begin{bmatrix} -\sin\theta & 0 & 1 \\ \sin\phi\cos\theta & \cos\phi & 0 \\ \cos\phi\cos\theta & -\sin\phi & 0 \end{bmatrix} \begin{Bmatrix} \dot{\psi} \\ \dot{\theta} \\ \dot{\phi} \end{Bmatrix} \qquad [9]$$

[8] The values of pitch, roll, and yaw, and vertical, longitudinal, and lateral load factors recorded by the DFDR are consistent with coordinated flight except during the two disturbances that occur in the final minute before the loss of DFDR data.

where P, Q, and R are the body axis roll, pitch, and yaw rates, respectively, and ψ, θ, and ϕ are the yaw, pitch, and roll angles, respectively. The angular accelerations are equal to the time derivatives of the angular rates. The results of the angular rate and acceleration calculations are shown in Figures 17 and 18, and indicate that the rates and accelerations obtained depend on the manner in which the values of the Euler angles in between the sampled data points are estimated. The blue curves in Figures 17 and 18 correspond to a cubic spline interpolation in between the data points, whereas the black lines correspond to a “minimum slope” interpolation that also uses cubic polynomials but in which the slope at each point is forced to be the smaller of the slopes of straight lines joining the point in question to the preceding and following points. Both interpolation methods go through every sampled data point. The Euler angles are sampled at 1 sample / second (1 Hz), and so no information about the rates and accelerations that has a frequency content higher than 0.5 Hz is contained in the data. Consequently, frequency content above 0.5 Hz that appears in the calculations in Figures 17 and 18 are simply artifacts of the interpolation method, and are estimates of what the real values may be, not measurements thereof. Since the cubic spline interpolation method gives smoother results with less high frequency content, the results of this method are used for other calculations requiring the angular rates or accelerations, such as the accelerometer integration calculations mentioned above, and the calculation of the load factors in the cockpit, described below.

As described in detail in Appendix A, the load factors at a point P away from the CG are given by

$$\vec{n}_P = \frac{\vec{a}_P - \vec{g}}{g} = \frac{\vec{a}_{CG} + \Delta\vec{a} - \vec{g}}{g} = \vec{n}_{CG} + \frac{\Delta\vec{a}}{g} \qquad [10]$$

where $\Delta\vec{a}$ is given by the second term in brackets in the following equation:

$$\vec{a}_P = \begin{Bmatrix} \dot{u} + wQ - vR \\ \dot{v} + uR - wP \\ \dot{w} + vP - uQ \end{Bmatrix} + \begin{Bmatrix} Q(yP - xQ) + R(zP - xR) + (z\dot{Q} - y\dot{R}) \\ R(zQ - yR) + P(xQ - yP) + (x\dot{R} - z\dot{P}) \\ P(xR - zP) + Q(yR - zQ) + (y\dot{P} - x\dot{Q}) \end{Bmatrix} = \vec{a}_{CG} + \Delta\vec{a} \qquad [11]$$

where {u, v, w} are the components of inertial speed in the body axes (determined from the accelerometer integration), {P, Q, R} are the components of the angular velocity in body axes (given by Equation [9]), and {x, y, z} are the coordinates of the point P in body axes.

Equations [10] and [11] indicate that the load factors at point P depend not only on the load factors at the CG (the first term in [10]), but also on the angular rates and accelerations (contained in the second term in [10]). Consequently, the uncertainty in the values of angular rates and accelerations arising from the limited sample rate of the Euler angles and choice of interpolation method carries into the calculation of load factors in the cockpit.

Figure 16 illustrates the range of load factor values that can result from three different methods of interpolating and curve fitting the Euler angles:

Method A: These are the results obtained from the cubic spline interpolation of the DFDR Euler angle data (the blue line in Figures 17 and 18). By definition, the interpolation is forced to pass through every point recorded on the DFDR.

Method B: A cubic spline curve fit of the second derivatives of the interpolated Euler angles from Method A are integrated twice to re-construct the angles. The re-constructed angles are used in the load factor calculation. The curve fits do not necessarily pass through every value of the second derivatives of the interpolations, but rather tend to "smooth" variations in these derivatives. Consequently, the peaks of load factor value resulting from using this method are lower than those resulting from Method A.

Method C: Cubic spline curve fits of the original DFDR Euler angle data are used in the load factor calculations. Unlike the interpolations, the curve fits do not necessarily pass through every value of the recorded angles, but again, tend to "smooth" variations in these angles. (Nonetheless, the match is very close; see Figure 16b).

Also shown on the load factor plots is the lateral load factor computed by the Airbus A300-600 engineering simulator when driven to try to match the event (the Airbus simulation is discussed further in Section D-V). Note that the lateral load factor computed by the simulator tends to have lower peaks than those resulting from Methods A, B, and C.

A measure of the confidence that can be placed in each of the methods is how well the Euler angles from which the load factors are computed match the original DFDR data. This is shown for each of the methods and for the Airbus engineering simulator results in Figure 16b.

All the interpolation / curve fit methods match the DFDR Euler angle data better than the Airbus simulation. Of these methods, Method C gives the lowest peak lateral load factor values at the cockpit, and still matches the Euler angle data very well (the match of pitch angle is not great in places, but pitch has a minor effect on lateral load factor). Also, Method C matches the Airbus simulation best, which is noteworthy because the simulation is computing a physically realizable load factor, the consequence of control surface movements, etc. (as opposed to the purely mathematical calculation based on the recorded Euler angles, with its range of solutions).

Because Method C matches the original Euler angle data well and also comes closest to the physically realizable load factors computed by the simulation, it is considered the best estimate of the actual load factors in the cockpit. The Method C load factors were therefore selected as the targets for driving the NASA Vertical Motion Simulator (VMS) during the representation of the accident in that device (see Section D-VII). It should always be kept in mind, however, that the cockpit load factor calculations are very dependent on the Euler angle data, that these angles are not sampled frequently enough to provide frequency content greater than 0.5 Hz., and that consequently there is considerable uncertainty in the calculations, as illustrated by the difference in the curves in Figure 16a.

Cockpit Control Forces

The DFDR does not record cockpit control forces, but it does record control positions (see Figures 19 and 20). The control forces can be estimated from the recorded positions and from the characteristics of the A300-600 flight control system.

The force required to move a cockpit control is the sum of the control breakout force (the force required to move the control out of its centering detent), friction forces, feel forces (spring-like forces designed into the system to provide the proper control "feel," or force feedback), and inertia and damping forces (forces proportional to the acceleration and velocity, respectively, of the control). Information regarding the breakout, friction, and feel forces were obtained from Airbus and used along with DFDR data to estimate the pedal, wheel, and column forces exerted during the flight. Inertial and damping forces are ignored in these calculations. The results of the calculations are shown in Figure 21.

Actual Rudder Position Estimate Based On Recorded Filtered Rudder Position

The position of the rudder surface throughout the flight is of critical importance in this accident. The motion of the airplane that results in a buildup of the sideslip angle is driven primarily by the rudder. After the sideslip angle, the rudder position itself is the most influential contributor to loads on the vertical stabilizer. To determine if the motion of the airplane can be explained in terms of the movements of the control surfaces alone, or whether external influences (such as winds) are also required, the position of the control surfaces must be known precisely.

While control surface positions, including the rudder position, are recorded on the DFDR, precise knowledge of the actual positions of the surfaces at all times during the accident is hampered by two factors: first, the sample rate of the control surface positions is not as high as it should be in order to capture rapid movements of the surfaces; and second, the information from the surface position sensors is passed through a first order lag filter before being recorded on the DFDR, which removes frequency content from the data and distorts the original signal, so that the surface positions recorded are not those that were actually detected by the sensors.

The digital nature of the DFDR data requires estimating the values of recorded parameters in between data points by interpolation or other methods (see, for example, the interpolation of the control wheel and column data in Figure 19). To capture a signal adequately, so that estimates of the signal values in between sample points are accurate, the sample rate must be matched to the frequency content of the data. Data that is relatively static, i.e., that changes slowly (has a low frequency content), can be sampled less often than data that changes rapidly (has a high frequency content). A sample rate that is too low risks missing peaks in dynamic signals, or abrupt but important changes in signals such as square waves or sawtooth waves.

All the cockpit controls and flight control surfaces on the accident airplane are sampled at 2 samples / second, except for the ailerons, which are sampled once a second. As shown in

Figures 19 and 20, 2 samples / sec is insufficient to define completely and accurately the rapid control wheel, column, and pedal inputs during the final seconds of DFDR data.

Sample rate limitations also affect the recorded control surface positions (elevator, ailerons, and rudder). In addition, the surface data (but not the cockpit controls) are filtered before being recorded on the DFDR. The filter removes high frequency content from the surface position signals (the filtered signals are used to present clean, noise-free control surface position information to the crew on the ECAM flight control page). During dynamic conditions, the values of the filtered signals can differ significantly from the values of the original signals, so that the filtered signals can not be used directly for any type of analysis, beyond concluding whether or not the original signals where static or dynamic. To obtain additional useful information, the original signal must be reconstructed from the filtered DFDR data points. However, it must be borne in mind that there can be numerous "reconstructed" signals that, when filtered, will match the DFDR data, and that no points in the reconstructed signal are actual measurements of the original signal: the entire reconstructed signal is only an estimate of the original signal.

To reconstruct the original signal, the mathematical definition of the filter must be known. Tests of the A300-600 SDAC computer that filters the control surface data[9] confirmed that the filter is a first-order lag with a time constant of 0.434 seconds[10] and a gain of 1.0. Mathematically, in the Laplace Transform domain the effect of the filter is expressed as

$$\delta_F = F(s)\delta \qquad [12]$$

where δ_F is the filtered signal, δ is the original signal, s is the Laplace variable, and F(s) is the filter transfer function, given by

$$F(s) = \left[\frac{1}{1+(T_c)s} \right] \qquad [13]$$

where T_c is the time constant of the filter (0.434 seconds).

The effect of a first-order lag filter on a step input is illustrated in Figure 25. Note that the *shape* of the original signal is distorted, and that the time constant of the filter is a measure of the slope of the line with which the filtered signal initially follows the step input (the filter's responsiveness). The filter does not simply *delay* the original signal by the time constant[11], and so, despite the name of the filter, it is inappropriate to think that the filtered signal simply *lags* behind the original signal by the time constant, and that therefore the original signal can be reconstructed by shifting the filtered signal times.

Solving [12] for δ and using the definition of F(s) in [13] gives

---

[9] See the DFDR Group Chairman's Factual Report.

[10] The filter is implemented in the SDAC computer digitally. The analog equivalent to this digital implementation is a first-order lag as described in Equation [13].

[11] The response of a first order lag filter to a ramp input will, after a brief period, be a ramp that lags the original signal by the time constant T_c. However, this behavior applies only to this special case.

$$\delta = F^{-1}(s)\delta_F = \left[\frac{1+(T_c)s}{1}\right]\delta_F \qquad [14]$$

Solving [14] with digital data results in a considerable amount of noise, or erratic jumps, in the resulting values of δ. This noise can be reduced by interpolating the filtered signal δ_F to a high sample rate (20 samples / second or higher) before solving [14], and then by curve-fitting the resulting δ. This is the process used to obtain the de-filtered rudder position estimate shown in Figure 20.

To confirm that the reconstructed signal is indeed a solution for the original signal, it is filtered using Equations [12] and [13], and the results compared with the recorded DFDR data. Figure 20 shows that when the reconstructed rudder position is filtered, the result matches the DFDR rudder data, and so the reconstructed rudder is a valid candidate for the actual rudder position. As noted above, however, there can be more than one original signal that, when filtered, matches the DFDR data, and so the rudder solution shown in Figure 20 is not unique. In fact, Airbus used the signal reconstruction process described above, along with the recorded pedal data and the (normal) constraints imposed by the rudder control system, to generate an initial estimate of "actual" rudder signal that differs in places from the reconstructed rudder shown in Figure 20, but that still matches the DFDR rudder data when filtered. Airbus used this initial rudder to drive their simulation of the accident, and through trial and error, refine the rudder estimate so that it not only matches DFDR rudder when filtered, but also is consistent with the DFDR pedal data and results in aircraft motion that matches (approximately) the DFDR Euler angles. The Airbus simulations are described in more detail in Section D-V. A comparison of the Airbus rudder and the reconstructed rudder from Figure 20 is shown in Figure 29. Note that towards the end of the DFDR data, both rudder position calculations exceed the normal limits expected from the Rudder Travel Limiter Unit (RTLU). The RTLU limits shown in Figure 29 were calculated by the System Group Chairman and account for the rate at which the RTLU motor can reduce the available rudder travel. The Systems Group is investigating the reasons why the rudder exceeded the expected RTLU limits, and is looking at the performance of the yaw control system, including the pedal inputs, yaw damper, and the RTLU itself.

V. Airbus Simulation of Final Seconds of Flight

Airbus engineers computed the response of the A300-600 to thrust levels and flight control inputs based on the DFDR recordings in order to compare the expected behavior of the airplane, as predicted by the simulator, with the actual behavior recorded by the DFDR. Such a comparison can help discern whether external forces or moments (such as from an atmospheric disturbance) are required to produce the motion of the airplane, or whether the motion can be accounted for completely by the forces and moments produced by the engine thrust and control surface positions. Since the flight control surface positions are filtered before being recorded by the DFDR, the simulation can not be driven with this data directly. Instead, Airbus engineers used the de-filtering process described in Section D-IV

and knowledge of the behavior of the airplane flight control system to estimate the actual surface positions. The validity of these estimates can be ascertained by filtering the estimated surface positions and comparing the result with the surface position data recorded on the DFDR. The rudder estimate can also be checked for consistency with the pedal positions and the expected behavior of the yaw damper.

This section provides a brief description of simulators in general, and then describes the implementation and results of Airbus simulation of the AAL587 accident in particular.

Simulation Overview

The simulations described in this Study are special applications of the Airbus A300-600 engineering simulator. The ways these special cases work are best understood in terms of how they differ from a “standard” simulation, in which a human pilot seated at the controls of a simulator cab (a mockup of an actual aircraft cockpit) makes control inputs as he would in a real airplane, and the simulation calculates the appropriate response in the control forces, airplane motion, instrument displays, and visual scene.

Figure 26 is a flow chart describing the logic and data flow in a standard simulation. The boxes with bold lines and non-italicized text represent simulation models, that is, units of computer code and data that describe the behavior of a part of the airplane or its systems mathematically. The boxes with non-bold lines and italicized text represent physical quantities or values computed by the simulation models. The arrows indicate which simulator models compute the various physical quantities, and how these quantities are in turn used as inputs by other models.

Starting with the box labeled “Human Pilot,” we see that by manipulating the simulator cab controls the pilot can generate inputs to the column, wheel, throttles, speedbrake handle, flaps, gear, and other cockpit controls duplicated in the cab. He can also provide inputs to the Flight Management Computer and Autopilot. In the case of desktop engineering simulations, which run on the computer without a cab, these “pilot” inputs are accomplished by computer code. For both desktop and cab-based simulations, the pilot inputs are eventually processed by the simulator flight controls model that calculates the appropriate response of the airplane control surfaces, and by the propulsion model that computes the response of the airplane’s engines. The aerodynamic model then uses the surface positions along with the motion state of the airplane (airspeed, altitude, etc.) to calculate aerodynamic forces and moments on the airplane. The propulsion model computes the thrust forces and moments. These forces and moments are used along with quantities calculated by the mass properties model in the solution of the equations of motion that determine the motion states, both angular and linear. Angular states are the airplane’s yaw, pitch and roll angles, and their time derivatives (angular rates and accelerations). Linear states are the components of the three dimensional position of the airplane in space and their time derivatives (velocities and accelerations). These states are also used as inputs in the various mathematical models that compute the quantities that eventually affect the forces and moments.

In the case of cab-based simulations, information about the airplane motion states and from the propulsion model are used to drive the visual displays and cockpit instruments in the cab. For simulator cabs on a motion base (such as the NASA VMS), the motion information can be used to maneuver the base in an attempt to duplicate, within limits, the acceleration cues felt by the pilots.

AAL587 Desktop Simulation

Airbus' desktop simulation of the AAL587 event differs from the "standard" simulation just described in that the position of the elevators, horizontal stabilizer, and rudder are driven directly with data prepared a priori, as opposed to calculating them within the simulator flight controls model based on cockpit control positions. In addition, the simulator propulsion model is used to calculate engine thrust from the engine N1 data recorded on the DFDR, as opposed to calculating thrust from throttle position.

Because the control surface positions recorded on the DFDR are filtered, they can not be used to drive the simulation directly. Instead, estimates of the actual surface positions, that result in the recorded positions when filtered, must be generated first (see Section D-IV). The control surface positions used in the simulation are shown in Figures 27-29, together with a comparison of the filtered positions with the DFDR data. The filtered elevator data matches the DFDR elevator data extremely well, except for a constant 1.8° nose-up shift relative to the DFDR data. Since while in trimmed flight the elevators are normally at neutral, this shift is probably the result of an offset in the elevator sensor; with neutral elevators, the simulator can trim the airplane with very nearly the same horizontal stabilizer position as recorded on the DFDR (see Figure 27), which would not be the case if the elevators on the airplane were truly deflected 1.8° nose-down. The CG used in the simulations is 28% MAC, which differs slightly from the 29% MAC CG location estimated at takeoff. Airbus estimates that the effect of this difference on the simulation results is negligible.

The filtered aileron position data match shown in Figure 28 is good, but not as good as the elevator match. The simulator control wheel also seems to lag the recorded control wheel, and does not achieve the same peaks as the recorded wheel. The only roll spoiler information recorded on the DFDR are discretes indicating whether a given spoiler panel is deflected or not; there is no indication of the actual spoiler panel position. Spoilers have a strong effect on roll, so it is unfortunate that there is no better spoiler data to compare to the simulator spoiler deflections. Nonetheless, the reasonably good match of the aileron data indicates that the simulator is probably using similar roll control inputs as were used on the accident flight.

Figure 29 shows the rudder angle used by the simulator. The filtered rudder matches the DFDR data very well. Note that the simulator rudder matches the "NTSB inverse filter calculation" rudder generally well, but does have some significant differences, such as the peaks at times 09:15:53.4, 09:15:57.2, and 09:15:58.5. Since both solutions, when filtered, match the DFDR data, there is no way to tell, based on the recorded rudder data alone, which is the better estimate of the actual rudder. However, the Airbus rudder is more square and better respects the limits of the RTLU (at least until 09:15:57), so assuming

that the pedal inputs were square (as opposed to the smooth, cubic-spline-based interpolation shown in Figure 20), the Airbus rudder is probably a better estimate of the actual rudder than the NTSB inverse-filter based rudder.

Simulation Results

Figure 30 shows that the simulator matches the DFDR airspeed very well. The simulator match of the DFDR pressure altitude is not good, but this is expected since the DFDR altitude probably contains pressure port related errors attributable to large sideslip angles. The simulator pressure altitude matches the true altitude estimate based on the accelerometer integrations (described in Section D-IV) almost perfectly, after the simulator altitude is shifted upwards to start at the same initial true altitude. This result increases confidence in the accuracy of both the true altitude calculation, and the simulator fidelity.

Figure 31 shows the simulator match of the DFDR Euler angles. The match of pitch and roll is very good, and the heading match is initially good, but the simulator then starts to lead the DFDR data. Nonetheless, the period and magnitude of the simulator heading oscillations is generally consistent with those recorded on the DFDR.

Figure 32 shows the simulator angle of attack and sideslip data. The α recorded on the DFDR is the vane α, which is affected by local flow induced by the angular rates of the airplane and therefore can differ from the α at the CG (see Section A-IV of Appendix A). Furthermore, the α data is filtered before being recorded on the DFDR. Figure 32 compares the α at the CG computed in the simulator, the simulator-based filtered vane α, the DFDR recorded vane α, and the inertial α computed from the accelerometer integrations. The simulator and DFDR vane α data agree well. The simulator CG α and the inertial CG α also agree well, except in the period from 09:15:51 – 09:15:53, where the simulator α is almost 2° lower than the inertial α. This disagreement can be attributed to the external winds used in the simulation and shown in Figure 34. These external winds are required to match the DFDR vane α data and the normal load factor drop at time 09:15:52.

The match of β to the NTSB-calculated inertial β is similar to the match of heading angle; initially the simulator agrees well with the β calculation, but the simulator then starts to lead the calculated data, though the period and amplitude of the sideslip oscillations are generally consistent. At time 09:15:58.5, the simulator and the calculated β diverge rapidly; this is evidence that the vertical tail probably departed the airplane at this time (the simulator does not account for the loss of the tail, and indicates that had the tail stayed on, the sideslip angle would have started to decrease in concert with the dynamics of the airplane). Time 09:15:58.5 also coincides with the “loud bang” noise heard on the DFDR, and with a +0.2 g increment in lateral load factor. Both events are consistent with the tail failing and departing the airplane: the noise can be associated with the rupture of the structure, and the lateral load factor increment can be associated with the sudden loss of side force to the left.

Figure 33 shows the simulator match of the DFDR load factor data. The excellent match of normal load factor is probably due to the erratic z-axis wind shown in Figure 34, which

appears tailored to force this result. The longitudinal load factor match is also very good, and the simulator lateral load factor starts to deviate from the DFDR data in the same areas as the heading and sideslip angle deviate from the DFDR heading and inertial sideslip calculations.

The simulator match of the accident event shown in Figures 27-34 is good, but not perfect. Factors that can cause the simulator to calculate motion that differs from that measured in flight include:

1. Errors in the flight sensors or other measuring/recording equipment.
2. Inaccuracies in the simulator aerodynamic and/or other mathematical models.
3. Improper simulator initialization or matching technique.
4. External forces or moments not modeled in the simulator.

The external winds needed to obtain the match of vane angle of attack and normal load factor indicate that the air surrounding the airplane is not quiet, which makes the atmosphere hard to model and a very precise match of the DFDR data hard to obtain. The disturbance in the atmosphere is likely due to a second encounter with the wake from the JAL 747 that preceded the accident airplane out of JFK (see Appendix B for information about work performed by the NASA Langley Research Center to model the wake from the 747).

While a better match of the DFDR data could probably be obtained by trial-and-error with external winds or other effects attributable to a wake encounter, the match in hand does provide important information about the accident sequence. The simulator results indicate that the motion of the airplane, and most importantly, the buildup of the sideslip angle, is consistent with and principally the result of the movements of the airplane's control surfaces, especially the rudder.

VI. Loads on the Vertical Stabilizer

The vertical stabilizer and rudder were found floating in Jamaica Bay, approximately 0.7 NM (4250 ft.) from the main impact site, indicating that they separated from the airplane during flight. Consequently, the loads (forces and moments) acting on the vertical stabilizer that caused this separation are of interest.

The loads on the vertical tail are a function of the flight condition of the airplane, and consist of both aerodynamic loads, produced by the pressure distribution over the tail, and inertial loads, produced by the acceleration of the mass of the tail itself. The loads presented in this study account for both aerodynamic and inertial loads, though the inertial loads are so small compared to the aerodynamic loads that in practice they could be ignored.

Factors that affect the aerodynamic and inertial loads include:

- Dynamic pressure and Mach number (which depend on airspeed and altitude)
- Sideslip angle and angle of attack at the CG
- Rudder deflection
- Aerodynamic sidewash from the fuselage which changes the β at the tail
- Yaw and roll rates, and rate of change of sideslip
- Structural elasticity, which changes the shape of the tail and consequently the aerodynamic loads acting on it
- Load factors at the center of mass of the tail (which in turn depend on the load factors at the CG and the angular rates and accelerations – see Equation [11])

Using data and methods provided by Airbus that describe the effects of these parameters on the vertical tail loads, the NTSB and Airbus calculated the shear, bending, and torsion loads on the vertical tail during the final seconds of DFDR data.

At a given altitude and airspeed, the factors that have the greatest effect on the loads are the sideslip angle and rudder deflection. The values of these parameters used by Airbus and the NTSB are shown in Figure 35. The rudder used in both the NTSB and Airbus calculations is the same rudder used in the Airbus simulation of the event, shown in Figure 29. The sideslip angle used in the NTSB calculation is the inertial β angle at the CG shown in Figures 13 and 32. The β at the tail resulting from the NTSB inertial β and aerodynamic sidewash and angular rate effects is also shown in Figure 35.

Figure 35 shows three sideslip calculations used by Airbus. These β calculations also correspond to three different load calculations performed by Airbus:

Airbus "Simulation:" This is the β calculated by the Airbus loads program, which solves the equations of motion of the airplane and simultaneously determines the loads on the structures. This simulation is different from the Airbus simulation discussed above, which is produced by the Airbus handling qualities group. For the "Airbus Simulation" loads shown in Figures 36-37, all of the flight condition data needed to calculate loads are taken from the loads simulator.

Airbus "Bypass:" This is the β calculated by the handling qualities simulator, and corresponds to the simulation described above and in Figures 27-34. For the "Airbus Bypass" loads shown in Figures 36-37, all of the flight condition data needed to calculate loads are taken from the handling qualities simulator.

Airbus "ny integration:" This is the inertial β calculated by Airbus based on an integration of the accelerometers, in a manner similar to that used to derive the NTSB inertial β. The NTSB and Airbus inertial β calculations are not identical, and this may be due to the fact that the Airbus calculation does not modify the DFDR accelerometer data to account for biases, as described in Section D-IV. For the "Airbus ny integration" loads shown in Figures 36-37, all of the flight condition data needed to calculate loads are derived from the DFDR data alone.

The results of the NTSB and Airbus loads calculations are shown in Figures 36 and 37. Figure 36 shows the shear and torsion loads in the vertical tail axis system (which is rotated about the y axis relative to the body axis system). Figure 37 shows the bending moment at the tail root chord in the fin axis system. Also shown in the Figures are the limit and ultimate shear, torsion, and bending static gust loads for the fin. The NTSB and all three Airbus calculations show that at the sound of the loud bang (the assumed separation point of the tail), the bending loads were extremely high, well above the ultimate load which the structure is certified to carry[12]. The performance of the structure under the loads shown in Figures 36 and 37 is being investigated by the Structures Group.

VII. NASA Vertical Motion Simulator (VMS) Activity

Overview

The information recorded on the DFDR and CVR can be used together with a motion-base simulator to recreate, within limits, the "experience" of the accident from the point of view of the flight crew. The Human Performance Group is particularly interested in such a representation, as it may provide insights about the environment surrounding the crew and the situation presented to them.

The representation of the accident in a simulator for human performance evaluation purposes requires that simulator recreation be as accurate and as "real" as can be. This means that every element of the simulator environment – the sights, sounds, control motions, and feelings of motion – should duplicate the actual accident scenario as much as possible. Of particular interest to the Human Performance Group are the sensations experienced by the flight crew as a result of the motion of the airplane and the associated load factors in the cockpit.

Traditional motion-based flight crew training simulators are mounted on hexapod motion systems, which can produce mild accelerations and load factors that enhance the experience of certain flight regimes such as takeoffs, landings, flight in turbulence, turn entries and entries into climbs and descents. However, because of their limited range of travel, these motion systems can not generate large or sustained load factors. In addition, the legs of the motion base are used to generate all the motions of the cab, so if they are being used to generate motion in one axis (pitch, for example), the range of motion in other axes (such as roll or lateral motion) will be reduced.

The NASA Vertical Motion Simulator (VMS) is a motion based simulator designed specifically to develop larger and more sustained load factors independently in all axes (forward/aft, up/down, left/right, and yaw, pitch, and roll). While the VMS also has its limits,

[12]The ultimate load is the maximum load which the structure is required to carry by the certification regulations; consequently, the rupture load (the load at which the structure actually fails) must be above the ultimate load. In testing during the development of the aircraft, the tail demonstrated load carrying ability above the ultimate load. The significance of these tests, and their bearing on the expected rupture load of the tail, is being investigated by the Structures Group.

it is much more capable than a hexapod based simulator, and is a better tool for recreating the load factor environment of flight 587.

The human performance testing performed in the VMS is described in the Human Performance Group Chairman's Factual Report. The Aircraft Performance Group Chairman assisted the Human Performance Group in the VMS effort by providing the data with which to drive the VMS motion, visual displays, instruments, and cockpit controls.

Data from the takeoff roll to the end of the DFDR data were used to drive the VMS. The portion of the data for the last 50 seconds of flight is the same as is plotted in Figures 9-23.

VMS Pedal Data

Two sets of pedal position data were used to backdrive the VMS pedal: a set based on the DFDR data, that duplicated the actual pedal movements during the flight; and a second set that represented the pedal movements that would have been required to command rudder deflections corresponding to the actual pedal movements, but with a rudder-ratio changer control system design. In the rudder-ratio changer design, full pedal deflection is required to obtain maximum available rudder, even though the available rudder is reduced with airspeed. This differs from the design of the A300-600 (and other aircraft) with a rudder limiter design, which limits the pedal travel available as the range of rudder travel is reduced, such that the amount of rudder obtained for a given pedal deflection is always the same.

The pedal position corresponding to a rudder ratio changer type design was calculated from the actual pedal data as follows:

$$\delta_{P\_RR} = \frac{\delta_{R\_CMD}}{(\delta_R / \delta_P)_{RR}} \cong \frac{(30/21)\delta_{P\_FDR}}{(\delta_{R\_MAX}/21)} = \frac{(30)\delta_{P\_FDR}}{\delta_{R\_MAX}} \qquad [15]$$

Where δ_{P_RR} is the rudder ratio changer pedal position, δ_{P_FDR} is the DFDR pedal position, δ_{R_CMD} is the A300-600 rudder command associated with the DFDR pedal position, $(\delta_R / \delta_P)_{RR}$ is the ratio of rudder to pedal for the ratio changer system (that varies as the allowable rudder range is reduced), (30/21) is the approximate ratio of rudder to pedal on the A300-600 (that does not vary with airspeed), and δ_{R_MAX} is the maximum available rudder at a given airspeed. The maximum pedal deflection is 21°. A comparison of δ_{P_RR} and δ_{P_FDR} is shown in Figure 38.

VMS Load Factor Data and Limitations

The cockpit load factors corresponding to "Method C" in Figure 16a served as the "targets" which the VMS motion system tried to duplicate. Because the VMS does have travel limits, these targets were not matched perfectly at every point in the flight; sustained load factors different from those of level flight or steady climbs, descents, or sideslips, for example, can

not be matched for long in any simulator. A comparison of the target load factors during the flight and the load factors the VMS was actually able to provide is shown in Figure 39.

The sample rate limitations discussed in Section D-IV that prevent a precise calculation of angular rates and accelerations and load factors away from the CG must be kept in mind when evaluating the load factors felt in the VMS. The target load factors, because they depend on the angular rates and accelerations, which in turn depend on the first and second derivatives of Euler angle data sampled only once per second, lose meaningful frequency content above 0.5 Hz that results from the angular motions of the airplane. The target load factors do contain meaningful frequency content above 0.5 Hz resulting from the load factor measurements near the CG; lateral and longitudinal load factors are sampled at 4 Hz, and vertical load factor is sampled at 8 Hz, so the cutoff frequencies for these signals are 2 Hz and 4 Hz, respectively. However, the load factors in the cockpit result from a combination of the load factors at the CG and the angular rates and accelerations, so if pilots can respond to acceleration signals with frequency content above 0.5 Hz, then the target accelerations presented in the VMS may only represent a part of the acceleration cues that are potentially meaningful to pilots.

E. CONCLUSIONS

The debris field, radar, DFDR, CVR, simulator, and loads program data presented in this Study are consistent with the following sequence of events concerning the motion of American Airlines Flight 587:

The airplane started its takeoff roll from runway 31L at 09:13:51, lifting off about 38 seconds later, about one minute and 40 seconds behind JAL47, a 747-400. AAL587 climbed to about 500 feet and entered a climbing left turn to a heading of 220° (magnetic). At 09:15:35, the airplane was climbing through 1,700 ft., wings approximately level on a heading of 220°. About one second later, ATC cleared AAL587 direct WAVEY intersection, and almost simultaneously, there was about a 0.3 g drop in normal load factor, a 0.04 g drop in longitudinal load factor, and a -0.07 g shift (left acceleration) in lateral load factor. Over the next five seconds, from 09:15:36 to 09:15:41, the control column moved from approximately neutral to 2° nose up, to 2° nose down, and back to neutral. During approximately the same period, the control wheel moved in a series of seven left and right movements, with peaks at 18° right, 30° left, 37° right, 34° left, 5° left, 21° left, and 23° right, before settling to between 5° and 6° left (see Figure 19a). The pedals moved from about 0.6° left (which could be an offset in the DFDR data) to about 0.6° right, then to 0.9° left, before settling back to between 0.6° and 0.7° left. Between 09:15:35 and 09:15:41, the rudder (which can be moved by the yaw damper as well as the pedals) moved about 2° left, then about 0.6° right, and then back to neutral. The rudder then oscillated twice between 0° and 1° left before settling in at about 0.5° left until 09:15:51. These rudder movements are within the authority of the yaw damper.

The pitch angle during the load factor excursions and cockpit control movements increased from 9° to 11.5° and then returned to about 10° before increasing again to 11°. The bank angle moved from 2° left wing down at 09:15:35 to wings level at 09:15:36, and then to 17° left wing down at 09:15:43, before ramping to 25° at 09:15:51.5. At about 09:15:44 the First Officer acknowledged the instruction to turn direct WAVEY, and the Captain commented about encountering wake turbulence, which the First Officer acknowledged. Work performed by the NASA Langley Research Center indicates that the atmospheric conditions of the day and the flight paths of JAL47 and AAL587 were conducive to AAL587 crossing the wake of JAL47 (see Appendix B).

At 09:15:51, the longitudinal, lateral, and normal load factors showed the beginnings of excursions similar to those that occurred at 09:15:36. By 09:52:52, the longitudinal load factor dropped from 0.20 g's to 0.14 g's; the lateral load factor shifted about –0.05 g's; and the normal load factor dropped from about 1.0 to 0.6 g's. In that same second, from 09:15:51 to 09:15:52, the control wheel and pedals started to move. The wheel moved from 6° left at 09:15:51.1 to 64° right at 09:15:51.5; the pedals moved from 0.3° left at 09:15:51.3 to 9° right at 09:15:51.9.

Over the course of the next 6.5 seconds, from 09:15:52 to 09:15:58.5, the pedals moved from 9° right to 9° left, back to 9° right at 09:15:54, where they increased to 11° right at 09:15:56 before moving to 13° left and then finally back to 7° right, where at 09:15:58.5, the performance data indicates the tail likely came off, coincident with the "loud bang" noise on the CVR (see Figure 20b). The pedals then moved briefly to 4° right before moving to 21° right for the remainder of the DFDR data.

The movements of the control wheel during this time parallel those of the pedal, and are mostly "coordinated" with them (in the sense that the wheel and pedals move left and right in tandem, not in the sense that the wheel and pedal movements would result in coordinated, zero-sideslip turns). The DFDR recorded data points at full left wheel deflection at 09:15:53.5 and 09:15:56.5, and at wheel deflections greater than 60° right at 09:15:51.5 and 09:15:55.5 (see Figure 19b). The only wheel movement not paralleled by the pedals occurs between 09:15:53.5 and 09:15:56, when the pedals moved to 9° right and then increased to 11° right, but the wheel shows a right to left movement between 09:15:53.5 and 09:15:54.5, and a left to right movement between 09:15:54.5 and 09:15:55.5 (in fact, after 09:15:55.5, the pedal movements appear to lag the wheel movements by about 0.5 seconds, whereas between 09:15:51 and 09:15:53.5, the lag appears to be only about 0.2 seconds). Airbus simulations, and the reconstructions of the rudder position from the filtered DFDR data, show aileron and rudder movements in directions consistent with the recorded movements of the wheel and pedals. The reconstructed rudder exceeds the expected rudder travel limits near the end of the DFDR data. The Systems Group is investigating the relationships between the cockpit control movements and the control surface positions, and the consistency of these relationships with the expected behavior of the control systems, including the effects of the yaw damper and the RTLU.

The movement of the control column between 09:15:52 and 09:16:01 is oscillatory, with four nose-down and four nose-up peaks. The nose-up peaks are between 2.5° and 4°, and the nose-down peaks are between 4° and 7.5°.

Airbus simulations indicate that the aircraft motion recorded by the DFDR is consistent with the control surface movements recorded on the DFDR. External winds are needed during the 10 seconds prior to the tail failure to match angle of attack and normal load factor well, and the simulator heading, after matching the DFDR data well initially, starts to lead the DFDR heading, but the gross movements of the airplane can be accounted for by the forces and moments generated by the deflection of the control surfaces.

The movements of the control surfaces described above and in Figures 19 and 20 created an oscillation in heading and sideslip angle that grew over time. As shown in Figures 13 and 32, at 09:15:53.2 β was -5°; at 09:15:55 β returned to 0°; at 09:15:57 β grew to -7°, and at 09:15:58.5, the tail failed with β at +10°. After the tail failure, β continued to grow and at the end of the DFDR data it had reached 31°.

The bending loads on the vertical tail that resulted from the combination of sideslip angle and rudder deflection during the flight are shown in Figure 37. At 09:15:53.2, with β = -5° and rudder = 11° left, the bending limit loads were exceeded slightly. At 09:15:56.8, with β = -7° and rudder = 10.2° left, the bending ultimate loads were almost reached. Finally, at the tail separation at 09:15:58.5, with β = 10° and rudder = 11.5° right, the bending loads were extremely high, and well above the ultimate load which the structure is certified to carry. The Structures Group is investigating the performance of the structure under the combination of loads developed during the flight.

_____

John O'Callaghan
National Resource Specialist - Aircraft Performance
Office of Research and Engineering

TABLES

Item	Item #	lat deg	lat min	lat sec	lon deg	lon min	lon sec	height ft	angle deg	comments
lft eng	1	40	34	44.16	73	50	59.82	0	0	441 B 129th St., Rockaway, Queens, NY
rgt eng	2	40	34	43.02	73	50	52.98	0	0	414 B 128th St., Rockaway, Queens, NY
surface in tree	3	40	34	39.84	73	51	0.9	32	-8	
house	4	40	34	39.84	73	51	0.66	33	-8	
house	5	40	34	39.3	73	51	0.6	36	-11	
house	6	40	34	38.64	73	51	2.1	32	-15	
pole	7	40	34	37.8	73	51	2.4	40	-25	
pole	8	40	34	38.64	73	51	0.6	33	-15	
house	9	40	34	38.04	73	51	0	30	-15	+ 7 ft. for peak
tree	10	40	34	37.8	73	51	2.52	41	-23	crater corner point
house	11	40	34	36.72	73	51	1.26	34	-21	
tree	12	40	34	36.84	73	51	1.56	34	-23	crater corner point
tree	13	40	34	36.66	73	51	1.92	33	-17	
tree	14	40	34	37.74	73	50	59.64	35	-15	crater corner point
house	15	40	34	37.38	73	51	0.42	30	-23	same height as 9
corner	16	40	34	37.98	73	51	1.5	0	0	crater corner point
tail section	17	40	34	37.32	73	51	2.88	0	0	
crater	18	40	34	37.59	73	51	1.305	0	0	average of crater corners
vertical	19	40	35	19.03	73	51	4.22	0	0	
rudder	20	40	35	13.18	73	51	2.47	0	0	

Table 1. Wreckage and surface structure items surveyed at accident site.

Radar Time HH:MM:SS UTC	ATC Time HH:MM:SS EST	Range NM	Azimuth ACPs	Mode C Altitude feet	Latitude	Longitude	Distance East of Impact, NM	Distance North of Impact, NM
14:14:34.90	09:14:34.56	1.09	3106	0	N 40° 38' 11.02"	W 73° 47' 23.79"	2.76	3.56
14:14:39.52	09:14:39.18	1.27	3173	300	N 40° 38' 16.91"	W 73° 47' 39.00"	2.57	3.65
14:14:44.26	09:14:43.92	1.44	3225	500	N 40° 38' 23.06"	W 73° 47' 52.58"	2.39	3.76
14:14:49.00	09:14:48.66	1.63	3259	700	N 40° 38' 28.23"	W 73° 48' 07.21"	2.21	3.84
14:14:53.41	09:14:53.07	1.83	3274	900	N 40° 38' 31.46"	W 73° 48' 22.57"	2.01	3.90
14:14:58.23	09:14:57.89	2.02	3268	1100	N 40° 38' 31.28"	W 73° 48' 37.46"	1.83	3.89
14:15:02.77	09:15:02.43	2.23	3252	1200	N 40° 38' 28.93"	W 73° 48' 54.17"	1.61	3.85
14:15:07.38	09:15:07.04	2.44	3226	1300	N 40° 38' 23.72"	W 73° 49' 10.87"	1.40	3.77
14:15:12.01	09:15:11.67	2.66	3191	1300	N 40° 38' 15.29"	W 73° 49' 28.06"	1.18	3.63
14:15:16.50	09:15:16.16	2.84	3151	1400	N 40° 38' 04.40"	W 73° 49' 41.14"	1.02	3.44
14:15:21.00	09:15:20.66	3.02	3105	1400	N 40° 37' 50.62"	W 73° 49' 52.92"	0.87	3.22
14:15:25.55	09:15:25.21	3.20	3060	1500	N 40° 37' 35.79"	W 73° 50' 03.18"	0.74	2.97
14:15:30.26	09:15:29.92	3.39	3016	1600	N 40° 37' 19.86"	W 73° 50' 12.68"	0.62	2.70
14:15:34.65	09:15:34.31	3.59	2975	1700	N 40° 37' 03.45"	W 73° 50' 21.62"	0.50	2.43
14:15:39.16	09:15:38.82	3.81	2937	1800	N 40° 36' 46.39"	W 73° 50' 30.80"	0.39	2.15
14:15:43.90	09:15:43.56	4.06	2903	2100	N 40° 36' 28.79"	W 73° 50' 41.05"	0.26	1.85
14:15:48.51	09:15:48.17	4.28	2870	2300	N 40° 36' 11.37"	W 73° 50' 47.89"	0.17	1.56
14:15:53.13	09:15:52.79	4.52	2836	2500	N 40° 35' 52.14"	W 73° 50' 54.11"	0.09	1.24
14:15:57.55	09:15:57.21	4.73	2801	2700	N 40° 35' 32.81"	W 73° 50' 56.20"	0.06	0.92
14:16:02.16	09:16:01.82	4.97	2768	3300	N 40° 35' 12.69"	W 73° 50' 58.56"	0.03	0.58

Table 2. JFK ASR9 secondary returns for AAL 587 (beacon code 2650).

Radar Time HH:MM:SS UTC	ATC Time HH:MM:SS EST	Range NM	Azimuth ACPs	Latitude	Longitude	Distance East of Impact, NM	Distance North of Impact, NM
14:16:02.28	09:16:01.94	4.91	2781	N 40° 35' 18.47"	W 73° 51' 01.51"	0.00	0.68
14:16:06.69	09:16:06.35	5.13	2758	N 40° 35' 01.86"	W 73° 51' 05.95"	-0.06	0.40
14:16:06.90	09:16:06.56	4.94	2775	N 40° 35' 15.22"	W 73° 51' 01.11"	0.00	0.63
14:16:06.90	09:16:06.56	5.13	2746	N 40° 34' 57.59"	W 73° 51' 01.05"	0.00	0.33
14:16:07.45	09:16:07.11	5.13	2746	N 40° 34' 57.59"	W 73° 51' 01.05"	0.00	0.33
14:16:11.40	09:16:11.06	5.34	2729	N 40° 34' 43.03"	W 73° 51' 06.00"	-0.06	0.09
14:16:11.40	09:16:11.06	5.19	2727	N 40° 34' 48.50"	W 73° 50' 56.53"	0.06	0.18
14:16:11.40	09:16:11.06	5.06	2760	N 40° 35' 05.30"	W 73° 51' 02.56"	-0.02	0.46
14:16:11.40	09:16:11.06	4.91	2779	N 40° 35' 17.76"	W 73° 51' 00.77"	0.01	0.67
14:16:11.85	09:16:11.51	5.34	2729	N 40° 34' 43.03"	W 73° 51' 06.00"	-0.06	0.09
14:16:16.02	09:16:15.68	5.25	2720	N 40° 34' 43.58"	W 73° 50' 56.90"	0.06	0.10
14:16:16.02	09:16:15.68	5.38	2721	N 40° 34' 38.51"	W 73° 51' 04.71"	-0.04	0.02

Table 3. JFK ASR9 primary returns in vicinity of impact site.

Radar Time HH:MM:SS UTC	ATC Time HH:MM:SS EST	Range NM	Azimuth ACPs	Mode C Altitude feet	Latitude	Longitude	Distance East of Impact, NM	Distance North of Impact, NM
14:12:57.99	09:12:57.65	1.41	3213	0	N 40° 38' 21.49"	W 73° 47' 50.32"	2.42	3.73
14:13:02.81	09:13:02.47	1.61	3264	200	N 40° 38' 28.91"	W 73° 48' 05.80"	2.23	3.85
14:13:07.43	09:13:07.09	1.81	3300	400	N 40° 38' 35.69"	W 73° 48' 20.74"	2.04	3.97
14:13:11.96	09:13:11.62	2.03	3322	600	N 40° 38' 41.36"	W 73° 48' 37.12"	1.83	4.06
14:13:16.59	09:13:16.25	2.27	3331	700	N 40° 38' 45.45"	W 73° 48' 55.37"	1.60	4.13
14:13:21.29	09:13:20.95	2.52	3326	900	N 40° 38' 46.83"	W 73° 49' 14.95"	1.35	4.15
14:13:25.82	09:13:25.48	2.75	3312	1100	N 40° 38' 45.55"	W 73° 49' 33.42"	1.11	4.13
14:13:30.45	09:13:30.11	2.98	3289	1300	N 40° 38' 41.22"	W 73° 49' 52.26"	0.88	4.06
14:13:35.06	09:13:34.72	3.19	3260	1500	N 40° 38' 34.06"	W 73° 50' 09.50"	0.66	3.94
14:13:39.56	09:13:39.22	3.39	3228	1700	N 40° 38' 24.83"	W 73° 50' 25.56"	0.45	3.79
14:13:44.07	09:13:43.73	3.56	3191	1800	N 40° 38' 12.86"	W 73° 50' 38.63"	0.29	3.59
14:13:48.69	09:13:48.35	3.72	3151	2000	N 40° 37' 58.82"	W 73° 50' 49.69"	0.15	3.35
14:13:53.42	09:13:53.08	3.86	3111	2200	N 40° 37' 43.91"	W 73° 50' 57.94"	0.04	3.10
14:13:57.84	09:13:57.50	4.02	3072	2300	N 40° 37' 28.21"	W 73° 51' 06.59"	-0.07	2.84
14:14:02.54	09:14:02.20	4.16	3034	2500	N 40° 37' 12.33"	W 73° 51' 12.31"	-0.14	2.58
14:14:07.08	09:14:06.74	4.33	2999	2600	N 40° 36' 56.25"	W 73° 51' 19.48"	-0.23	2.31
14:14:11.70	09:14:11.36	4.50	2967	2800	N 40° 36' 40.57"	W 73° 51' 25.76"	-0.31	2.05
14:14:16.20	09:14:15.86	4.70	2939	3000	N 40° 36' 25.01"	W 73° 51' 33.86"	-0.41	1.79
14:14:20.83	09:14:20.49	4.91	2913	3300	N 40° 36' 09.32"	W 73° 51' 41.89"	-0.52	1.53
14:14:25.45	09:14:25.11	5.11	2887	3500	N 40° 35' 53.21"	W 73° 51' 48.22"	-0.60	1.26
14:14:29.96	09:14:29.62	5.28	2860	3700	N 40° 35' 37.05"	W 73° 51' 51.02"	-0.63	0.99
14:14:34.58	09:14:34.24	5.45	2831	3800	N 40° 35' 19.58"	W 73° 51' 52.03"	-0.64	0.70
14:14:39.19	09:14:38.85	5.59	2800	3800	N 40° 35' 01.92"	W 73° 51' 49.09"	-0.61	0.41
14:14:43.59	09:14:43.25	5.73	2768	3900	N 40° 34' 43.74"	W 73° 51' 44.17"	-0.54	0.10
14:14:48.45	09:14:48.11	5.84	2734	4000	N 40° 34' 25.91"	W 73° 51' 35.03"	-0.43	-0.19
14:14:52.83	09:14:52.49	5.91	2697	4100	N 40° 34' 08.81"	W 73° 51' 20.64"	-0.25	-0.48
14:14:57.37	09:14:57.03	5.95	2662	4200	N 40° 33' 54.29"	W 73° 51' 04.30"	-0.04	-0.72
14:15:01.98	09:15:01.64	5.97	2625	4300	N 40° 33' 40.68"	W 73° 50' 44.74"	0.21	-0.95
14:15:06.48	09:15:06.14	5.95	2586	4400	N 40° 33' 29.27"	W 73° 50' 21.15"	0.51	-1.14
14:15:11.10	09:15:10.76	5.92	2549	4500	N 40° 33' 20.08"	W 73° 49' 57.62"	0.81	-1.29
14:15:15.85	09:15:15.51	5.84	2511	4600	N 40° 33' 14.41"	W 73° 49' 31.10"	1.15	-1.39
14:15:20.35	09:15:20.01	5.73	2473	4700	N 40° 33' 11.72"	W 73° 49' 03.55"	1.50	-1.43
14:15:24.76	09:15:24.42	5.61	2435	4900	N 40° 33' 11.11"	W 73° 48' 35.96"	1.85	-1.44
14:15:29.53	09:15:29.19	5.47	2396	5000	N 40° 33' 12.76"	W 73° 48' 07.86"	2.20	-1.41
14:15:34.12	09:15:33.78	5.31	2356	5100	N 40° 33' 16.90"	W 73° 47' 39.58"	2.56	-1.34
14:15:38.50	09:15:38.16	5.19	2313	5300	N 40° 33' 20.02"	W 73° 47' 11.18"	2.92	-1.29
14:15:43.33	09:15:42.99	5.08	2268	5500	N 40° 33' 23.96"	W 73° 46' 42.65"	3.29	-1.23
14:15:47.85	09:15:47.51	5.00	2220	5700	N 40° 33' 27.57"	W 73° 46' 13.49"	3.66	-1.16
14:15:52.26	09:15:51.92	4.95	2172	5900	N 40° 33' 31.00"	W 73° 45' 45.18"	4.02	-1.11
14:15:56.81	09:15:56.47	4.92	2122	6200	N 40° 33' 35.10"	W 73° 45' 16.31"	4.38	-1.04
14:16:01.41	09:16:01.07	4.94	2071	6400	N 40° 33' 37.74"	W 73° 44' 46.80"	4.76	-0.99
14:16:05.92	09:16:05.58	4.97	2021	6700	N 40° 33' 41.65"	W 73° 44' 17.99"	5.12	-0.93
14:16:10.53	09:16:10.19	5.05	1972	6900	N 40° 33' 44.02"	W 73° 43' 48.66"	5.50	-0.89
14:16:15.05	09:16:14.71	5.14	1923	7200	N 40° 33' 47.83"	W 73° 43' 19.03"	5.87	-0.82
14:16:19.57	09:16:19.23	5.27	1877	7400	N 40° 33' 50.45"	W 73° 42' 49.39"	6.25	-0.78

Table 4. JFK ASR9 secondary returns for JAL 47 (beacon code 1710), through 09:16:19 EST.

Radar Time HH:MM:SS UTC	ATC Time HH:MM:SS EST	Range NM	Azimuth ACPs	Mode C Altitude feet	Latitude	Longitude	Distance East of Impact, NM	Distance North of Impact, NM
14:14:48.57	09:14:48.23	17.63	1244	700	N 40° 38' 24.50"	W 73° 48' 07.63"	2.20	3.78
14:14:53.16	09:14:52.82	17.42	1243	900	N 40° 38' 27.54"	W 73° 48' 23.85"	2.00	3.83
14:14:57.71	09:14:57.37	17.22	1245	1100	N 40° 38' 25.75"	W 73° 48' 40.00"	1.79	3.80
14:15:02.52	09:15:02.18	17.02	1244	1200	N 40° 38' 28.70"	W 73° 48' 55.44"	1.60	3.85
14:15:07.14	09:15:06.80	16.81	1250	1300	N 40° 38' 20.93"	W 73° 49' 13.34"	1.37	3.72
14:15:11.67	09:15:11.33	16.63	1257	1300	N 40° 38' 11.63"	W 73° 49' 29.24"	1.17	3.57
14:15:16.38	09:15:16.04	16.47	1264	1400	N 40° 38' 02.41"	W 73° 49' 43.69"	0.98	3.41
14:15:21.01	09:15:20.67	16.36	1275	1400	N 40° 37' 46.99"	W 73° 49' 55.60"	0.83	3.15
14:15:25.55	09:15:25.21	16.27	1285	1500	N 40° 37' 33.09"	W 73° 50' 05.94"	0.70	2.92
14:15:30.36	09:15:30.02	16.19	1296	1600	N 40° 37' 17.82"	W 73° 50' 16.14"	0.57	2.67
14:15:34.98	09:15:34.64	16.13	1309	1700	N 40° 36' 59.61"	W 73° 50' 25.93"	0.45	2.37
14:15:39.60	09:15:39.26	16.08	1321	1800	N 40° 36' 42.93"	W 73° 50' 34.97"	0.33	2.09
14:15:44.22	09:15:43.88	16.03	1334	2100	N 40° 36' 25.00"	W 73° 50' 44.91"	0.21	1.79
14:15:48.85	09:15:48.51	16.02	1347	2300	N 40° 36' 06.64"	W 73° 50' 52.26"	0.11	1.48
14:15:53.46	09:15:53.12	16.05	1360	2600	N 40° 35' 47.73"	W 73° 50' 57.09"	0.05	1.17
14:15:58.12	09:15:57.78	16.11	1373	2700	N 40° 35' 28.29"	W 73° 51' 00.12"	0.02	0.84
14:16:02.73	09:16:02.39	16.19	1387	3700	N 40° 35' 07.12"	W 73° 51' 03.18"	-0.02	0.49

Table 5. EWR ASR9 secondary returns for AAL 587 (beacon code 2650).

Radar Time HH:MM:SS UTC	ATC Time HH:MM:SS EST	Range NM	Azimuth ACPs	Latitude	Longitude	Distance East of Impact, NM	Distance North of Impact, NM
14:16:02.73	09:16:02.39	16.19	1384	N 40° 35' 11.16"	W 73° 51' 00.54"	0.01	0.56
14:16:02.73	09:16:02.39	16.56	1392	N 40° 34' 52.45"	W 73° 50' 38.23"	0.29	0.25
14:16:07.12	09:16:06.78	16.19	1379	N 40° 35' 18.22"	W 73° 50' 57.41"	0.05	0.68
14:16:07.46	09:16:07.12	16.59	1373	N 40° 35' 19.34"	W 73° 50' 23.78"	0.48	0.70
14:16:07.46	09:16:07.12	16.34	1395	N 40° 34' 52.62"	W 73° 50' 56.55"	0.06	0.25
14:16:07.90	09:16:07.56	16.34	1395	N 40° 34' 52.62"	W 73° 50' 56.55"	0.06	0.25
14:16:11.97	09:16:11.63	16.22	1378	N 40° 35' 19.07"	W 73° 50' 54.55"	0.09	0.69
14:16:11.97	09:16:11.63	16.38	1389	N 40° 35' 00.34"	W 73° 50' 49.61"	0.15	0.38

Table 6. EWR ASR9 primary returns in vicinity of impact site.

Radar Time HH:MM:SS UTC	ATC Time HH:MM:SS EST	Range NM	Azimuth ACPs	Mode C Altitude feet	Latitude	Longitude	Distance East of Impact, NM	Distance North of Impact, NM
14:14:45.48	09:14:45.14	26.20	2291	600	N 40° 38' 25.67"	W 73° 47' 55.45"	2.36	3.80
14:14:50.19	09:14:49.85	26.16	2297	800	N 40° 38' 30.20"	W 73° 47' 55.45"	2.13	3.87
14:14:54.62	09:14:54.28	26.14	2304	1000	N 40° 38' 34.07"	W 73° 47' 55.45"	1.85	3.94
14:14:59.23	09:14:58.89	26.19	2305	1100	N 40° 38' 31.51"	W 73° 47' 55.45"	1.80	3.90
14:15:03.84	09:15:03.50	26.28	2312	1200	N 40° 38' 29.08"	W 73° 47' 55.45"	1.51	3.86
14:15:08.38	09:15:08.04	26.41	2317	1300	N 40° 38' 23.59"	W 73° 47' 55.45"	1.29	3.76
14:15:13.08	09:15:12.74	26.59	2320	1300	N 40° 38' 14.33"	W 73° 47' 55.45"	1.14	3.61
14:15:17.82	09:15:17.48	26.83	2324	1400	N 40° 38' 02.07"	W 73° 47' 55.45"	0.93	3.41
14:15:22.32	09:15:21.98	27.09	2327	1400	N 40° 37' 48.23"	W 73° 47' 55.45"	0.76	3.18
14:15:27.18	09:15:26.84	27.38	2329	1500	N 40° 37' 32.18"	W 73° 47' 55.45"	0.62	2.91
14:15:31.56	09:15:31.22	27.66	2329	1600	N 40° 37' 15.72"	W 73° 47' 55.45"	0.56	2.63
14:15:36.10	09:15:35.76	27.97	2331	1700	N 40° 36' 58.54"	W 73° 47' 55.45"	0.41	2.35
14:15:40.92	09:15:40.58	28.27	2332	1900	N 40° 36' 41.46"	W 73° 47' 55.45"	0.31	2.06
14:15:45.45	09:15:45.11	28.58	2333	2100	N 40° 36' 23.81"	W 73° 47' 55.45"	0.20	1.77
14:15:50.16	09:15:49.82	28.91	2334	2400	N 40° 36' 05.01"	W 73° 47' 55.45"	0.09	1.46
14:15:54.78	09:15:54.44	29.23	2334	2600	N 40° 35' 46.25"	W 73° 47' 55.45"	0.03	1.14
14:15:59.33	09:15:58.99	29.56	2332	2700	N 40° 35' 25.76"	W 73° 47' 55.45"	0.05	0.80
14:16:03.93	09:16:03.59	29.89	2330	2700	N 40° 35' 05.25"	W 73° 47' 55.45"	0.07	0.46

Table 7. HPN ASR9 secondary returns for AAL 587 (beacon code 2650).

Radar Time HH:MM:SS UTC	ATC Time HH:MM:SS EST	Range NM	Azimuth ACPs	Latitude	Longitude	Distance East of Impact, NM	Distance North of Impact, NM
14:16:03.93	09:16:03.59	29.72	2330	N 40° 35' 15.07"	W 73° 50' 53.35"	0.10	0.62
14:16:08.55	09:16:08.21	30.13	2330	N 40° 34' 50.96"	W 73° 50' 59.90"	0.02	0.22
14:16:08.56	09:16:08.22	30.00	2326	N 40° 34' 56.40"	W 73° 50' 43.62"	0.22	0.31
14:16:08.56	09:16:08.22	29.72	2332	N 40° 35' 16.19"	W 73° 51' 00.38"	0.01	0.64
14:16:09.21	09:16:08.87	30.13	2330	N 40° 34' 50.96"	W 73° 50' 59.90"	0.02	0.22
14:16:13.05	09:16:12.71	30.31	2330	N 40° 34' 40.38"	W 73° 51' 02.77"	-0.02	0.05
14:16:13.05	09:16:12.71	29.94	2331	N 40° 35' 02.69"	W 73° 51' 00.40"	0.01	0.42
14:16:13.05	09:16:12.71	29.72	2339	N 40° 35' 20.23"	W 73° 51' 24.95"	-0.30	0.71
14:16:13.05	09:16:12.71	30.09	2331	N 40° 34' 53.88"	W 73° 51' 02.82"	-0.02	0.27
14:16:13.51	09:16:13.17	30.31	2330	N 40° 34' 40.38"	W 73° 51' 02.77"	-0.02	0.05

Table 8. HPN ASR9 primary returns in vicinity of impact site.

Radar Time HH:MM:SS UTC	ATC Time HH:MM:SS EST	Range NM	Azimuth ACPs	Mode C Altitude feet	Latitude	Longitude	Distance East of Impact, NM	Distance North of Impact, NM
14:14:49.33	09:14:48.99	33.77	3028	-400	N 40° 38' 27.12"	W 73° 48' 11.08"	2.16	3.82
14:14:53.95	09:14:53.61	33.94	3032	900	N 40° 38' 36.04"	W 73° 48' 28.66"	1.94	3.97
14:14:58.57	09:14:58.23	34.13	3032	1100	N 40° 38' 32.72"	W 73° 48' 42.97"	1.76	3.92
14:15:02.98	09:15:02.64	34.34	3032	1200	N 40° 38' 29.04"	W 73° 48' 58.79"	1.55	3.86
14:15:07.80	09:15:07.46	34.58	3032	1300	N 40° 38' 24.83"	W 73° 49' 16.87"	1.33	3.79
14:15:12.43	09:15:12.09	34.81	3031	1300	N 40° 38' 17.73"	W 73° 49' 32.97"	1.12	3.67
14:15:17.16	09:15:16.82	35.05	3028	1400	N 40° 38' 04.25"	W 73° 49' 47.28"	0.94	3.44
14:15:21.67	09:15:21.33	35.25	3025	1400	N 40° 37' 51.38"	W 73° 49' 58.49"	0.80	3.23
14:15:26.28	09:15:25.94	35.45	3021	1500	N 40° 37' 35.31"	W 73° 50' 08.26"	0.67	2.96
14:15:30.91	09:15:30.57	35.66	3017	1600	N 40° 37' 18.94"	W 73° 50' 18.62"	0.54	2.69
14:15:35.52	09:15:35.18	35.86	3013	1700	N 40° 37' 02.64"	W 73° 50' 28.07"	0.42	2.42
14:15:40.05	09:15:39.71	36.06	3008	1900	N 40° 36' 43.10"	W 73° 50' 35.91"	0.32	2.09
14:15:44.76	09:15:44.42	36.28	3004	2100	N 40° 36' 26.16"	W 73° 50' 46.47"	0.19	1.81
14:15:49.38	09:15:49.04	36.47	3000	2400	N 40° 36' 09.72"	W 73° 50' 54.61"	0.09	1.53
14:15:54.04	09:15:53.70	36.63	2994	2600	N 40° 35' 47.47"	W 73° 50' 57.31"	0.05	1.16
14:15:58.65	09:15:58.31	36.78	2989	2800	N 40° 35' 28.49"	W 73° 51' 00.55"	0.01	0.85
14:16:03.27	09:16:02.93	36.92	2984	3700	N 40° 35' 09.69"	W 73° 51' 02.68"	-0.02	0.53

Table 9. ISP ASR9 secondary returns for AAL 587 (beacon code 2650).

Radar Time HH:MM:SS UTC	ATC Time HH:MM:SS EST	Range NM	Azimuth ACPs	Latitude	Longitude	Distance East of Impact, NM	Distance North of Impact, NM
14:16:07.89	09:16:07.55	36.84	2981	N 40° 35' 01.81"	W 73° 50' 52.42"	0.11	0.40
14:16:12.51	09:16:12.17	37.00	2975	N 40° 34' 39.30"	W 73° 50' 54.20"	0.09	0.03
14:16:17.13	09:16:16.79	36.69	2977	N 40° 34' 52.55"	W 73° 50' 34.88"	0.34	0.25
14:16:17.13	09:16:16.79	36.81	2983	N 40° 35' 08.78"	W 73° 50' 53.46"	0.10	0.52

Table 10. ISP ASR9 primary returns in vicinity of impact site.

Radar Time HH:MM:SS UTC	ATC Time HH:MM:SS EST	Mode C Altitude feet	Latitude	Longitude	Distance East of Impact, NM	Distance North of Impact, NM
14:15:05	09:15:05	1300	N 40° 38' 15.00"	W 73° 49' 06.00"	1.46	3.62
14:15:54	09:15:54	2700	N 40° 35' 58.00"	W 73° 51' 18.00"	-0.21	1.34

Table 11. ZNY secondary returns for AAL 587 (beacon code 2650).

ATC Time	CVR Transcript Text
09:14:38.46	[HOT-2] heading select.
09:14:41.87	[HOT-1] clear left.
09:14:42.55	[TWR] American five eight seven heavy, turn left. fly the bridge climb. contact New York departure. good morning.
09:14:48.33	[RDO-1] American five eighty seven heavy, so long.
09:14:51.38	[HOT-1] gear's up.
09:14:52.45	[HOT-2] check speed, level change.
09:14:54.84	[HOT-2] flaps up.
09:14:56.52	[HOT-2] climb power.
09:14:57.14	[CAM] [sound of click]
09:15:00.02	[RDO-1] ah New York, American five eighty seven heavy, thirteen hundred feet, we're climbing to five thousand.
09:15:04.67	[DEP] American five eight seven heavy, New York departure. radar contact. climb maintain one three thousand.
09:15:10.18	[RDO-1] one three thousand feet, American five eighty seven heavy.
09:15:14.64	[HOT-2] one three I see, slats retract.
09:15:16.46	[HOT-1] slats.
09:15:17.21	[CAM] [sound of several clicks]
09:15:28.47	[HOT-1] clean machine.
09:15:29.34	[HOT-2] [sound similar to yawn] thank you.
09:15:36.43	[DEP] American five eighty seven heavy, turn left, proceed direct WAVEY.
09:15:37.25	[HOT-1] [sound of brief squeak and a rattle]
09:15:41.00	[RDO-1] uh, we'll turn direct WAVEY, American five eighty seven heavy.
09:15:44.35	[HOT-2] left turn direct WAVEY...
09:15:44.67	[HOT-1] little wake turbulence, huh?
09:15:45.60	[HOT-2] ...yeah.
09:15:47.31	[HOT-2] [sound similar to five sets of stabilizer trim switch clicks]
09:15:48.20	[HOT-2] two fifty thank you.
09:15:51.80	[CAM] [sound of a thump]
09:15:52.30	[CAM] [sound of click]
09:15:52.92	[CAM] [sound of two thumps]
09:15:54.19	[HOT-2] max power. [spoken in strained voice]
09:15:54.96	[HOT-1] you all right?
09:15:55.34	[HOT-2] yea, I'm fine.
09:15:56.29	[HOT-1] hang onto it. hang onto it.
09:15:56.60	[CAM] [sound of snap]
09:15:57.45	[HOT-2] let's go for power please.
09:15:57.69	[CAM] [sound of loud thump]
09:15:58.51	[CAM] [sound of loud bang]
09:16:00.00	[HOT-2] [sound similar to human grunt]
09:16:00.18	[CAM] [roaring noise starts and increases in amplitude]
09:16:00.97	[CAM] [sound similar to single ECAM chime]
09:16:00.98	[HOT-2] holy #
09:16:01.98	[CAM] [sound similar to single ECAM chime]
09:16:04.44	[CAM] [sound similar to stall warning repetitive chime for 1.9 sec]
09:16:06.20	"FLASH" ON TOLL BOOTH VIDEO
09:16:06.23	[CAM] [roaring noise decreases and ends]
09:16:07.45	[HOT-2] what the hell are we into *. we're stuck in it.
09:16:07.46	[CAM] [sound similar to continuous repetitive chimes for one second]
09:16:09.58	[CAM] [sound similar to continuous repetitive chimes for three seconds]

Table 12. Last 1.5 minutes of CVR transcript.

FIGURES

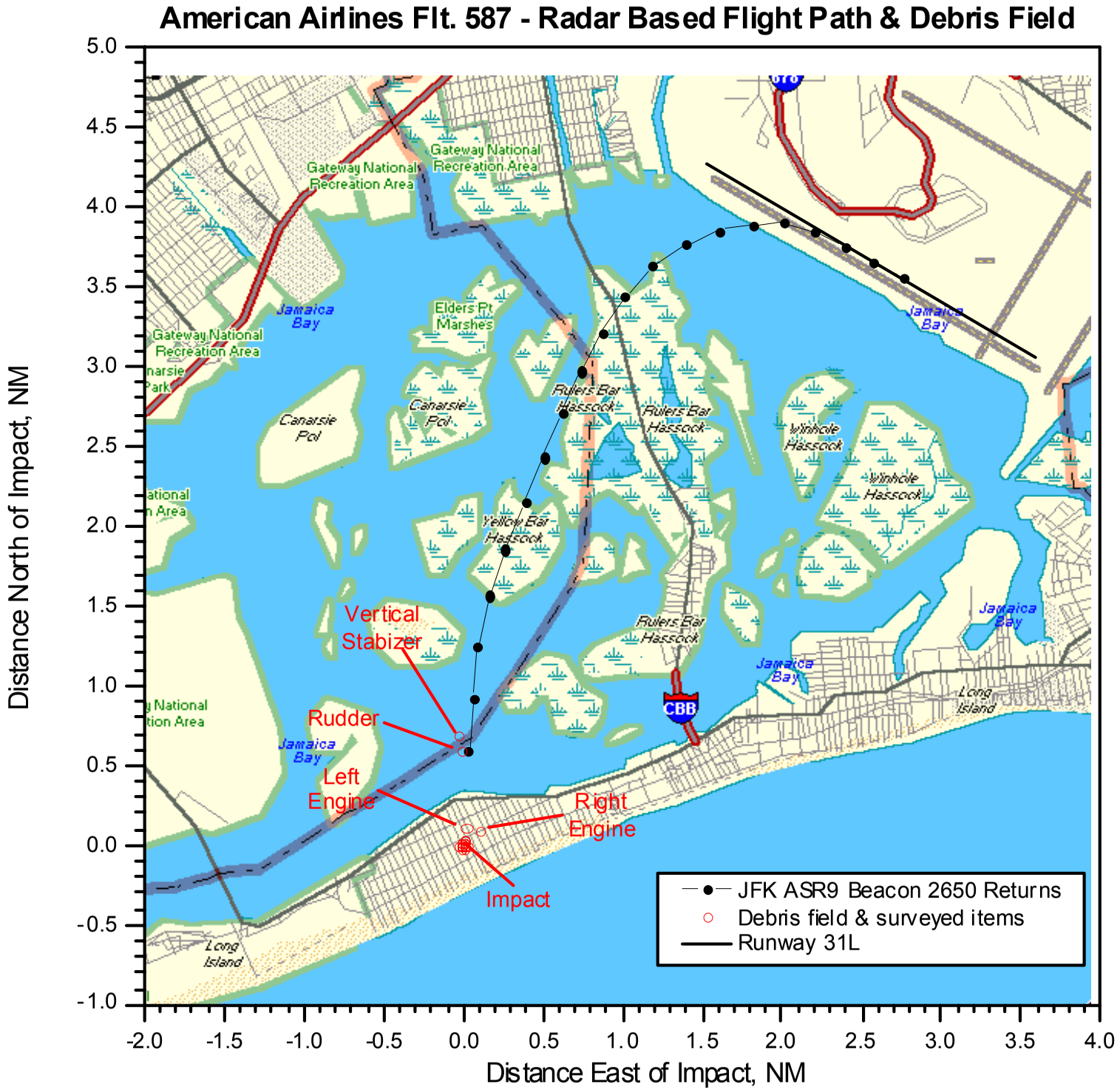
American Airlines Flt. 587 - Radar Based Flight Path & Debris Field
Distance North of Impact, NM
Distance East of Impact, NM
5.0
4.5
4.0
3.5
3.0
2.5
2.0
1.5
1.0
0.5
0.0
-0.5
-1.0
-2.0
-1.5
-1.0
-0.5
0.0
0.5
1.0
1.5
2.0
2.5
3.0
3.5
4.0
Vertical Stabizer
Rudder
Left Engine
Right Engine
Impact
JFK ASR9 Beacon 2650 Returns
Debris field & surveyed items
Runway 31L
Gateway National Recreation Area
Jamaica Bay
Elders Pt Marshes
Canarsie Pol
Rulers Bar Hassock
Yellow Bar Hassock
Wilshole Hassock
Long Island
CBB

Figure 1a.

Accident Site Debris Field as Mapped with Garmin GPS

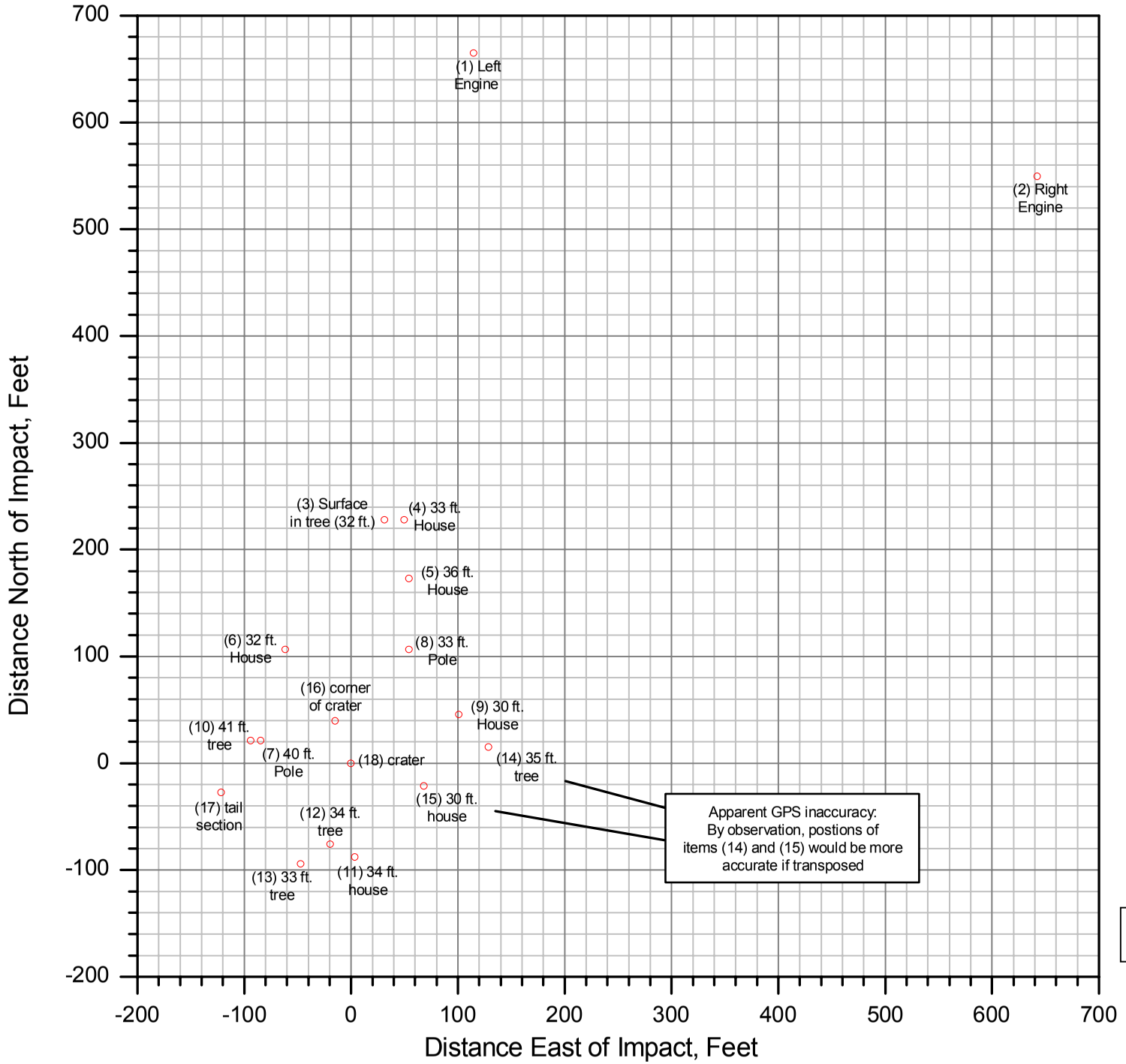

Figure 1b.

Airport Surveillance Radars (ASRs) that Tracked AAL 587

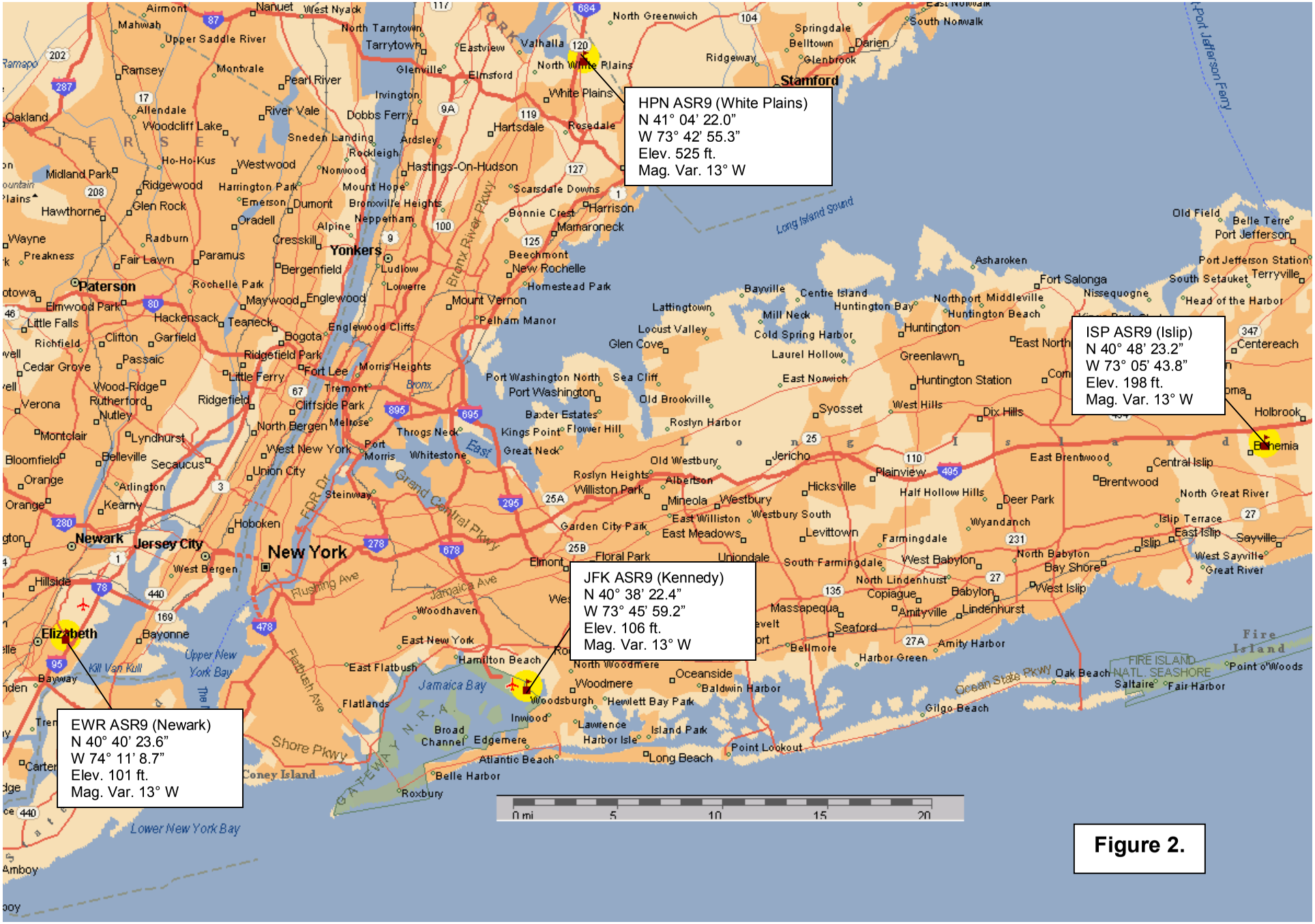

Figure 2.

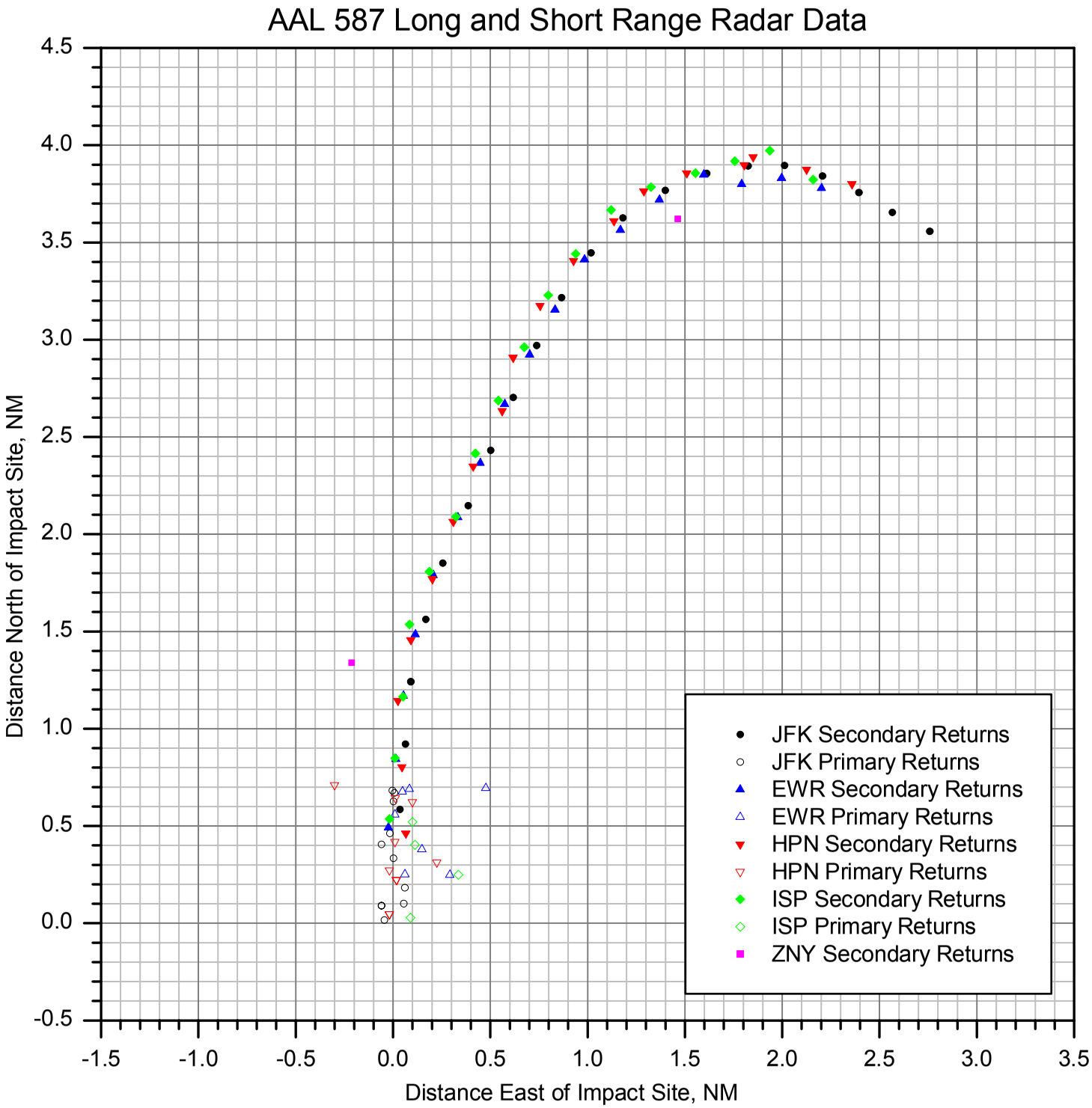
AAL 587 Long and Short Range Radar Data
Distance North of Impact Site, NM
Distance East of Impact Site, NM
4.5
4.0
3.5
3.0
2.5
2.0
1.5
1.0
0.5
0.0
-0.5
-1.5
-1.0
-0.5
0.0
0.5
1.0
1.5
2.0
2.5
3.0
3.5
JFK Secondary Returns
JFK Primary Returns
EWR Secondary Returns
EWR Primary Returns
HPN Secondary Returns
HPN Primary Returns
ISP Secondary Returns
ISP Primary Returns
ZNY Secondary Returns

Figure 3a.

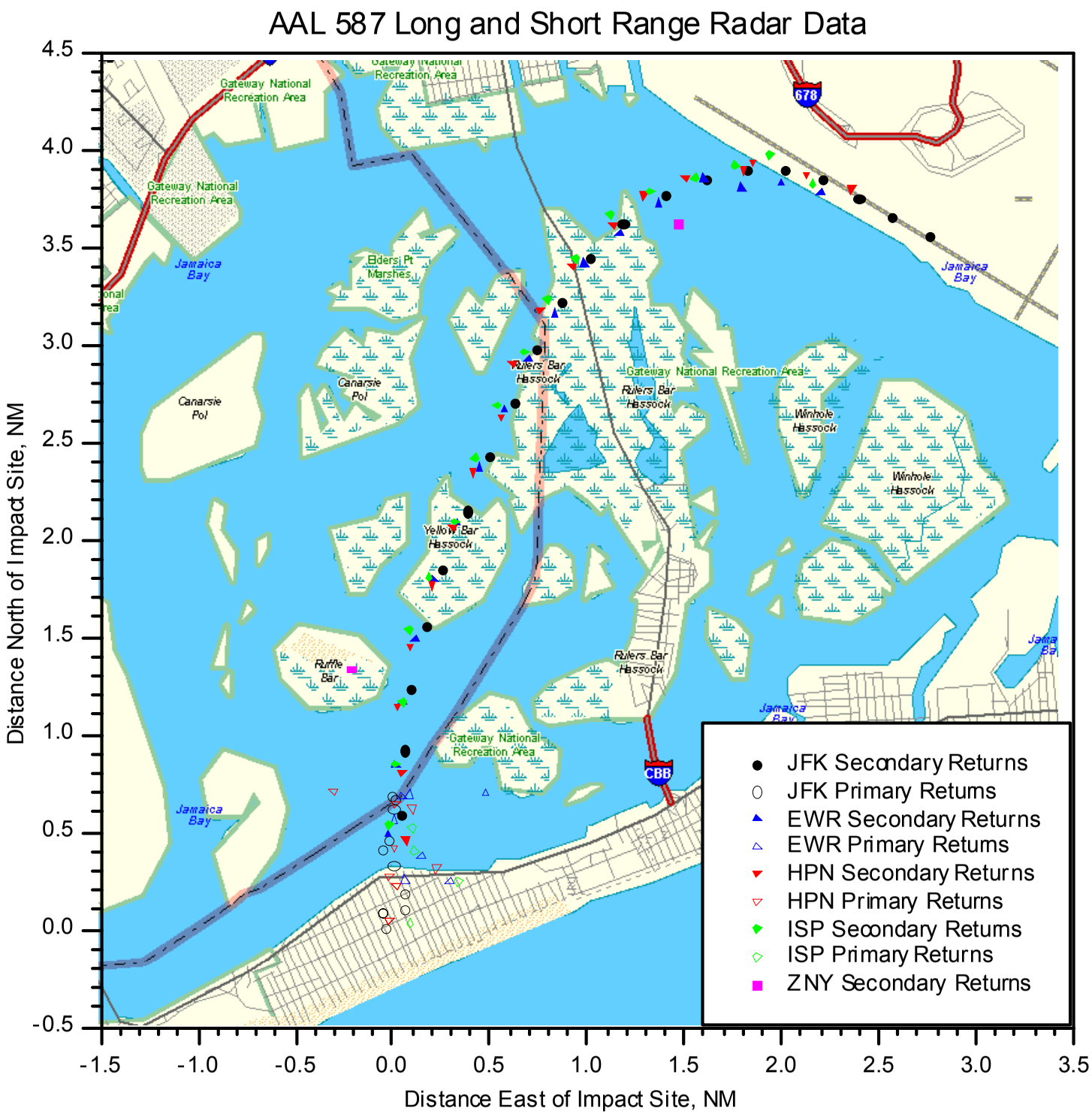
AAL 587 Long and Short Range Radar Data
Distance North of Impact Site, NM
Distance East of Impact Site, NM
4.5
4.0
3.5
3.0
2.5
2.0
1.5
1.0
0.5
0.0
-0.5
-1.5
-1.0
-0.5
0.0
0.5
1.0
1.5
2.0
2.5
3.0
3.5
Gateway National Recreation Area
Jamaica Bay
Elders Pt Marshes
Canarsie Pol
Rulers Bar Hassock
Yellow Bar Hassock
Ruffle Bar
Winhole Hassock
678
CBB
JFK Secondary Returns
JFK Primary Returns
EWR Secondary Returns
EWR Primary Returns
HPN Secondary Returns
HPN Primary Returns
ISP Secondary Returns
ISP Primary Returns
ZNY Secondary Returns

Figure 3b.

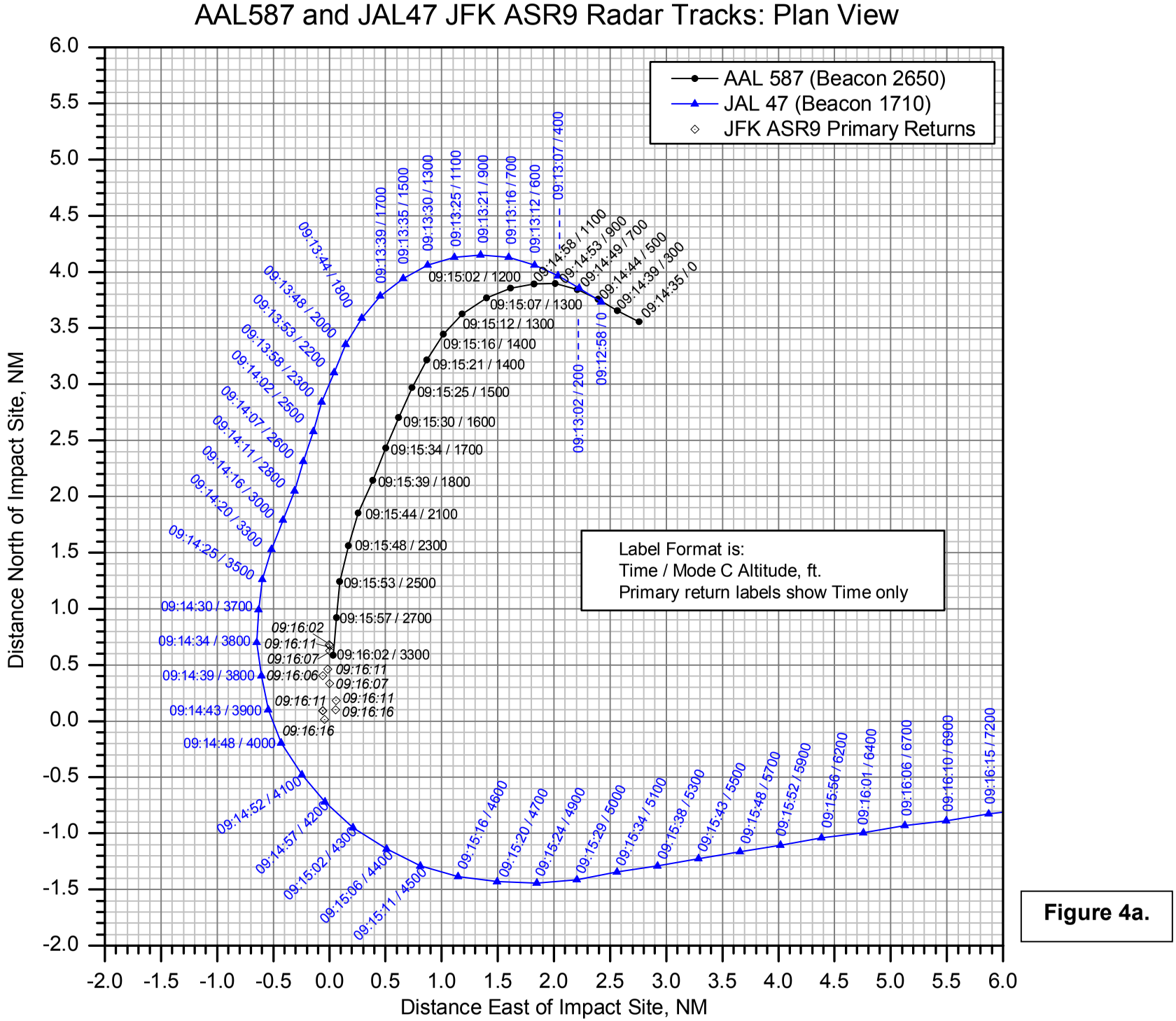
AAL587 and JAL47 JFK ASR9 Radar Tracks: Plan View
AAL 587 (Beacon 2650)
JAL 47 (Beacon 1710)
JFK ASR9 Primary Returns
Label Format is:
Time / Mode C Altitude, ft.
Primary return labels show Time only
Distance North of Impact Site, NM
Distance East of Impact Site, NM
09:13:07 / 400
09:13:12 / 600
09:13:16 / 700
09:13:21 / 900
09:13:25 / 1100
09:13:30 / 1300
09:13:35 / 1500
09:13:39 / 1700
09:13:44 / 1800
09:13:48 / 2000
09:13:53 / 2200
09:13:58 / 2300
09:14:02 / 2500
09:14:07 / 2600
09:14:11 / 2800
09:14:16 / 3000
09:14:20 / 3300
09:14:25 / 3500
09:14:30 / 3700
09:14:34 / 3800
09:14:39 / 3800
09:14:43 / 3900
09:14:48 / 4000
09:14:52 / 4100
09:14:57 / 4200
09:15:02 / 4300
09:15:06 / 4400
09:15:11 / 4500
09:15:16 / 4600
09:15:20 / 4700
09:15:24 / 4900
09:15:29 / 5000
09:15:34 / 5100
09:15:38 / 5300
09:15:43 / 5500
09:15:48 / 5700
09:15:52 / 5900
09:15:56 / 6200
09:16:01 / 6400
09:16:06 / 6700
09:16:10 / 6900
09:16:15 / 7200
09:14:58 / 1100
09:14:53 / 900
09:14:49 / 700
09:14:44 / 500
09:14:39 / 300
09:14:35 / 0
09:12:58 / 0
09:13:02 / 200
09:15:02 / 1200
09:15:07 / 1300
09:15:12 / 1300
09:15:16 / 1400
09:15:21 / 1400
09:15:25 / 1500
09:15:30 / 1600
09:15:34 / 1700
09:15:39 / 1800
09:15:44 / 2100
09:15:48 / 2300
09:15:53 / 2500
09:15:57 / 2700
09:16:02 / 3300
09:16:02
09:16:11
09:16:07
09:16:06
09:16:11
09:16:07
09:16:11
09:16:11
09:16:16
09:16:16

Figure 4a.

AAL587 and JAL47 JFK ASR9 Radar Tracks: Plan View

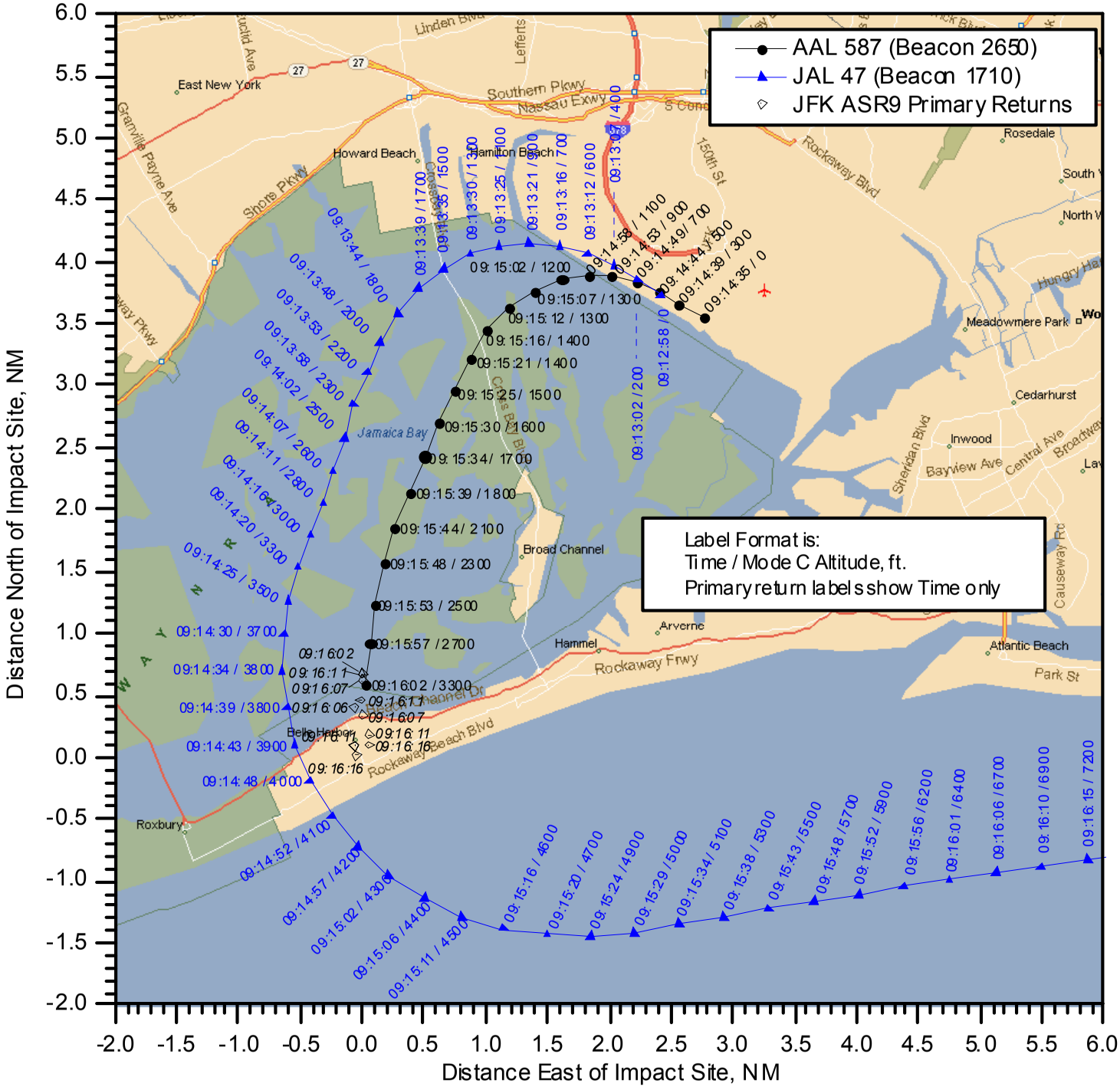

Figure 4b.

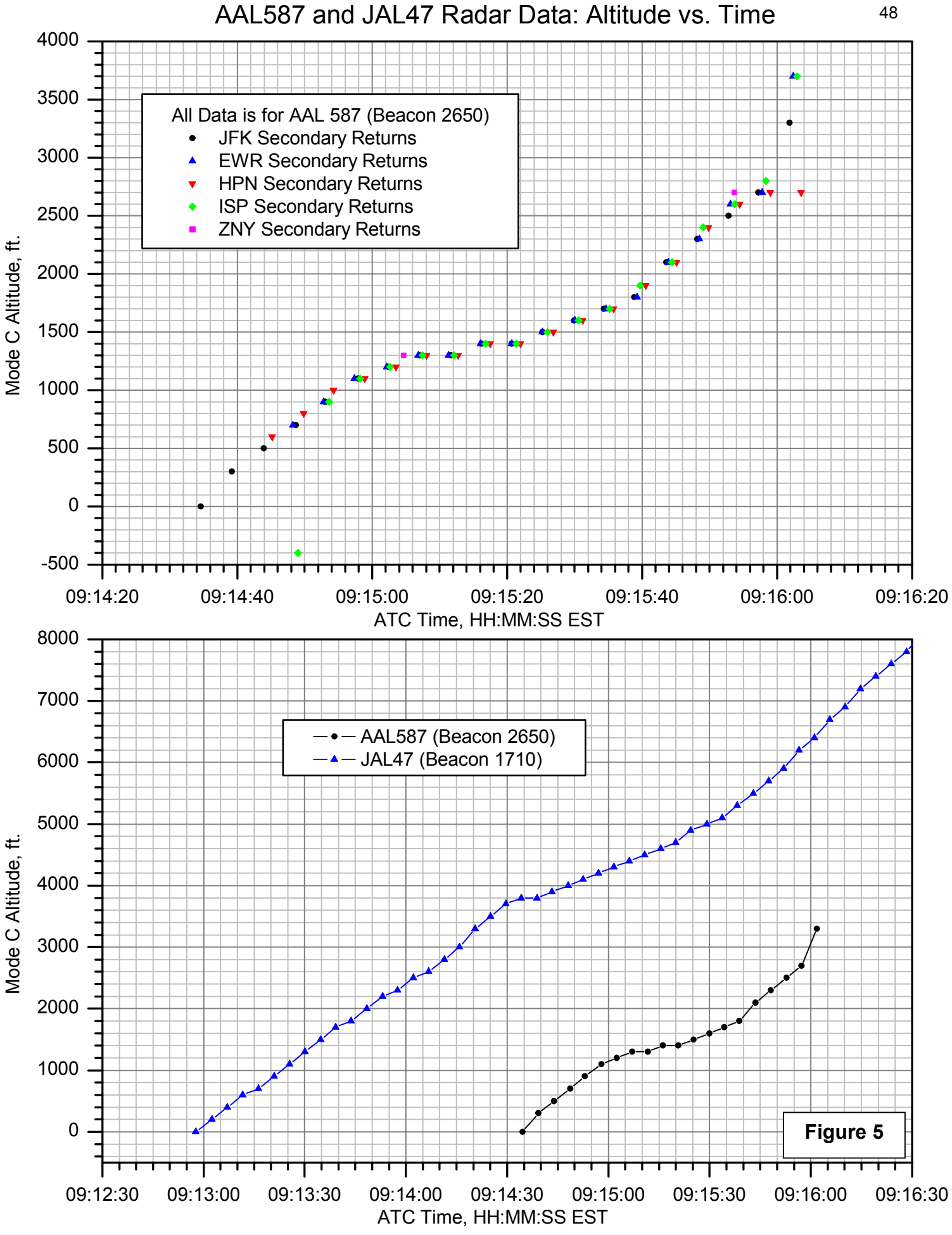
AAL587 and JAL47 Radar Data: Altitude vs. Time
All Data is for AAL 587 (Beacon 2650)
JFK Secondary Returns
EWR Secondary Returns
HPN Secondary Returns
ISP Secondary Returns
ZNY Secondary Returns
Mode C Altitude, ft.
4000
3500
3000
2500
2000
1500
1000
500
0
-500
09:14:20
09:14:40
09:15:00
09:15:20
09:15:40
09:16:00
09:16:20
ATC Time, HH:MM:SS EST
AAL587 (Beacon 2650)
JAL47 (Beacon 1710)
Mode C Altitude, ft.
8000
7000
6000
5000
4000
3000
2000
1000
0
09:12:30
09:13:00
09:13:30
09:14:00
09:14:30
09:15:00
09:15:30
09:16:00
09:16:30
ATC Time, HH:MM:SS EST

Figure 5

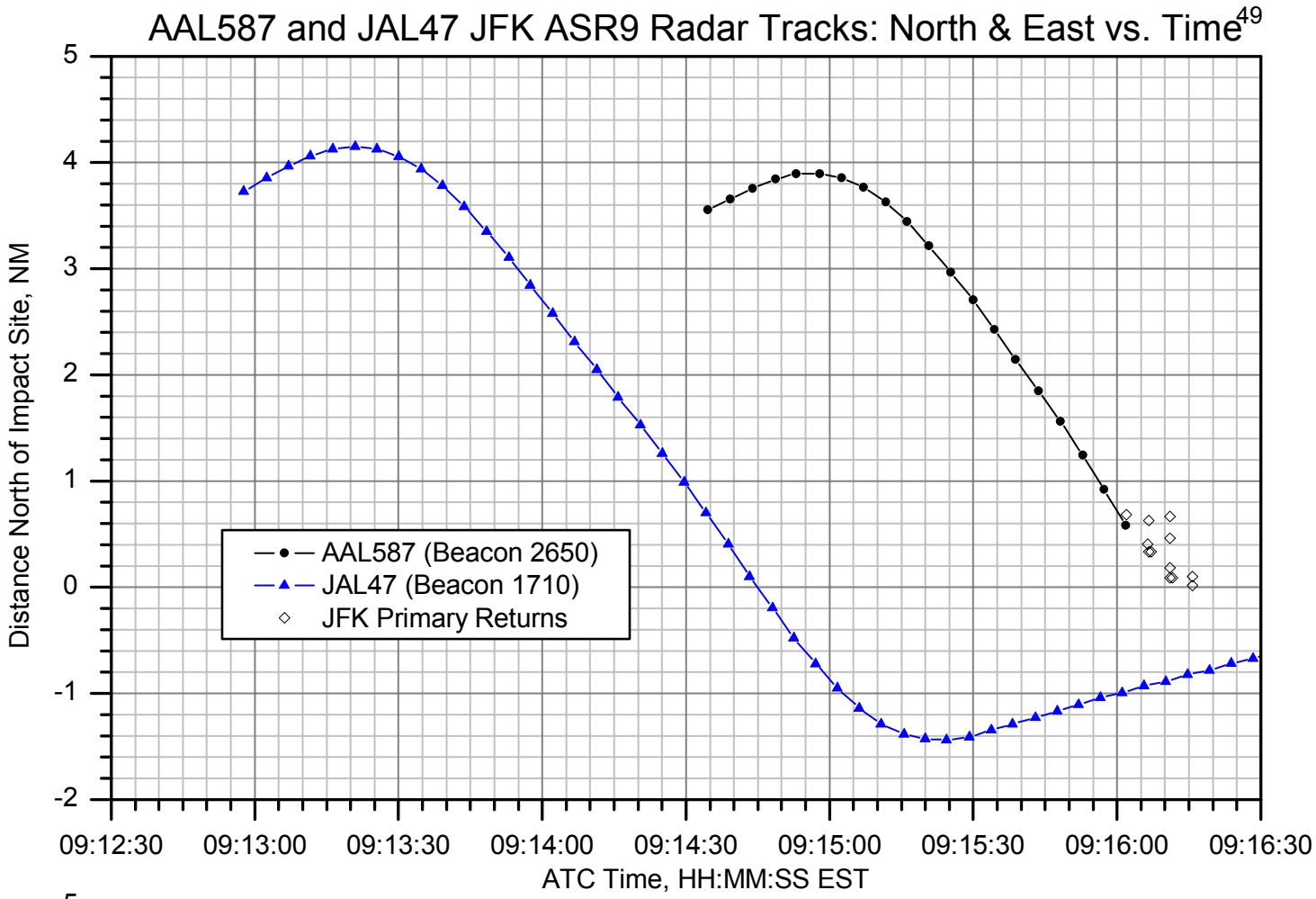
AAL587 and JAL47 JFK ASR9 Radar Tracks: North & East vs. Time
Distance North of Impact Site, NM
5
4
3
2
1
0
-1
-2
AAL587 (Beacon 2650)
JAL47 (Beacon 1710)
JFK Primary Returns
09:12:30
09:13:00
09:13:30
09:14:00
09:14:30
09:15:00
09:15:30
09:16:00
09:16:30
ATC Time, HH:MM:SS EST

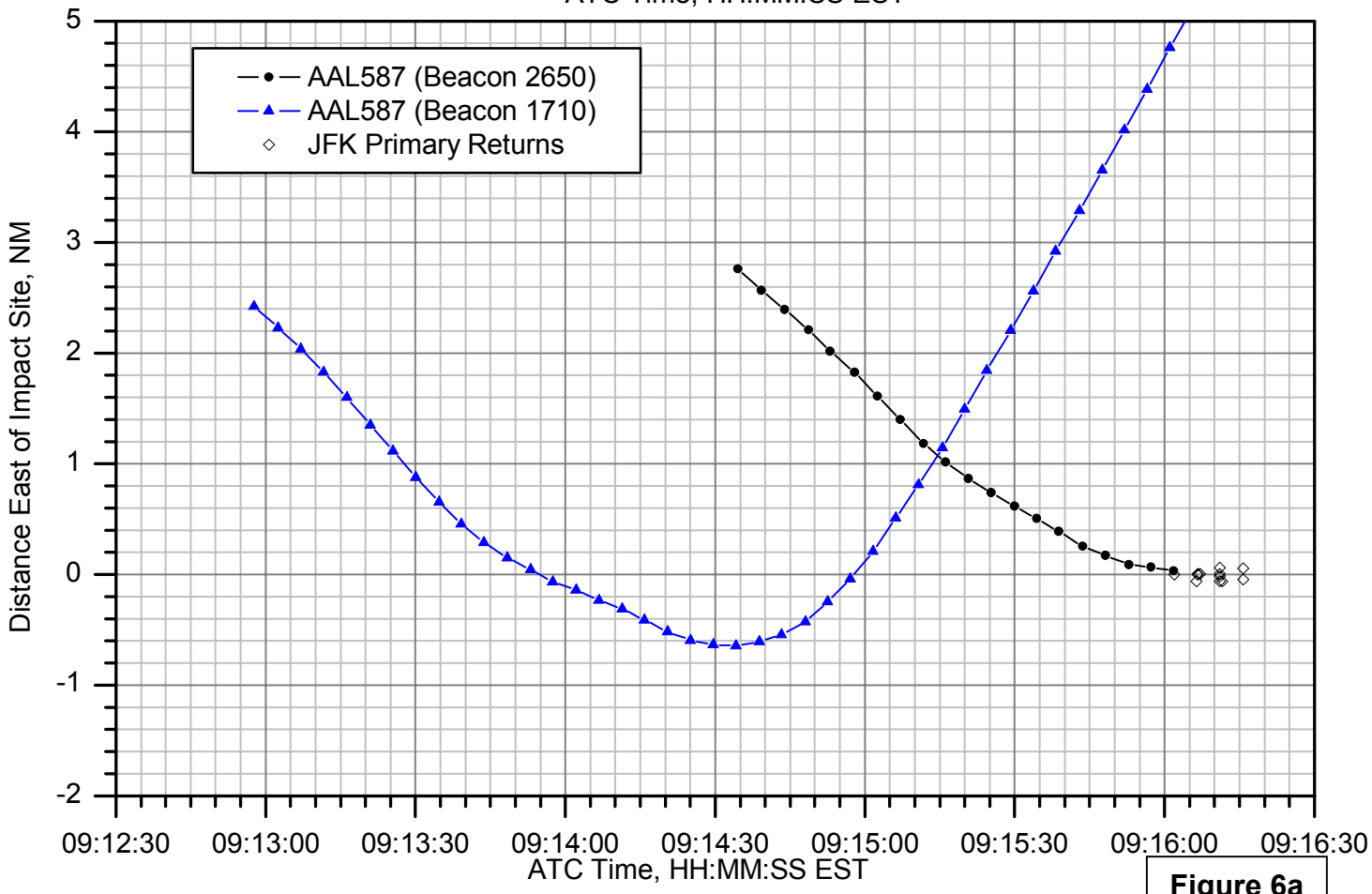
Distance East of Impact Site, NM
5
4
3
2
1
0
-1
-2
AAL587 (Beacon 2650)
AAL587 (Beacon 1710)
JFK Primary Returns
09:12:30
09:13:00
09:13:30
09:14:00
09:14:30
09:15:00
09:15:30
09:16:00
09:16:30
ATC Time, HH:MM:SS EST

Figure 6a

Separation Between JAL 47 and AAL 587

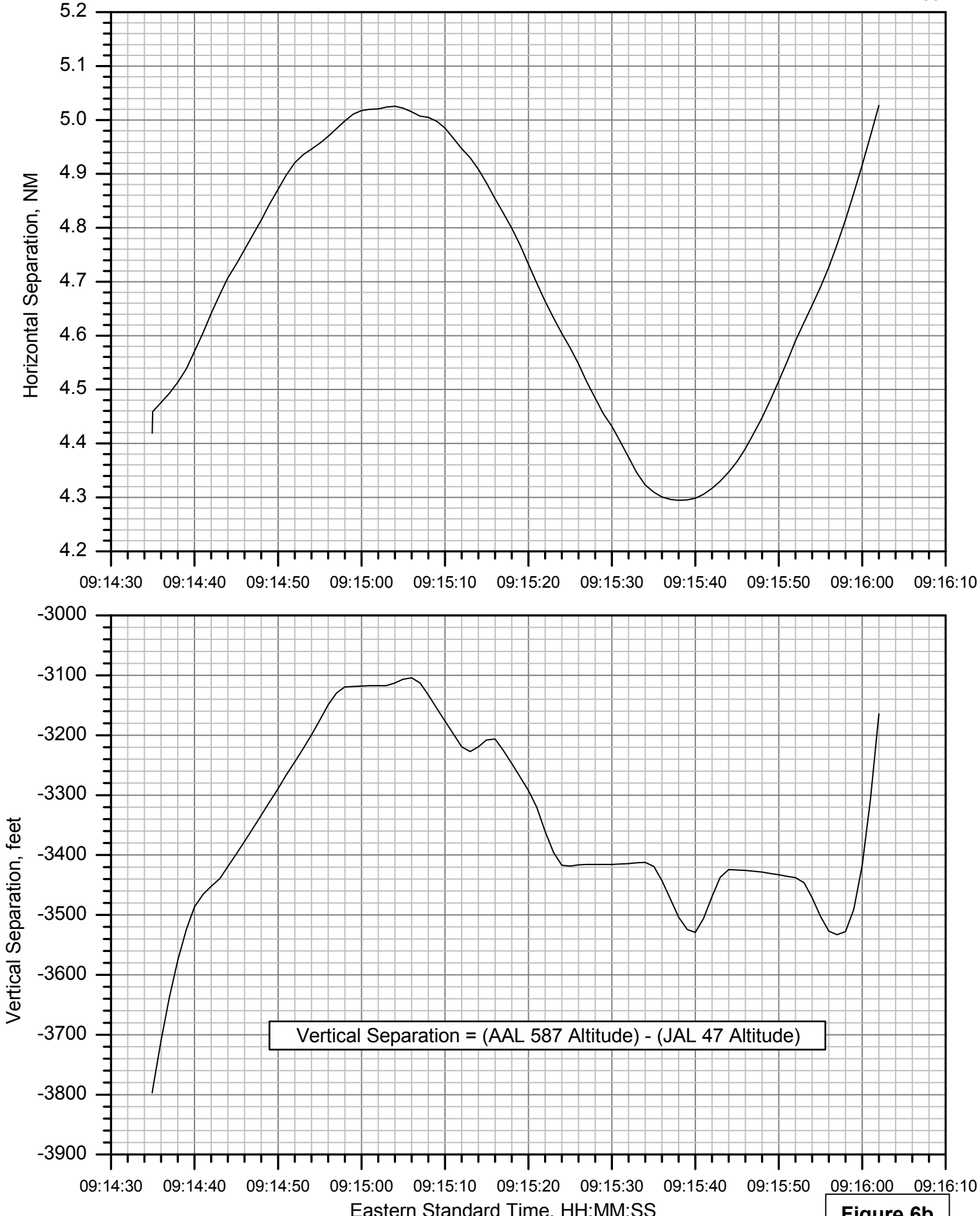

Figure 6b

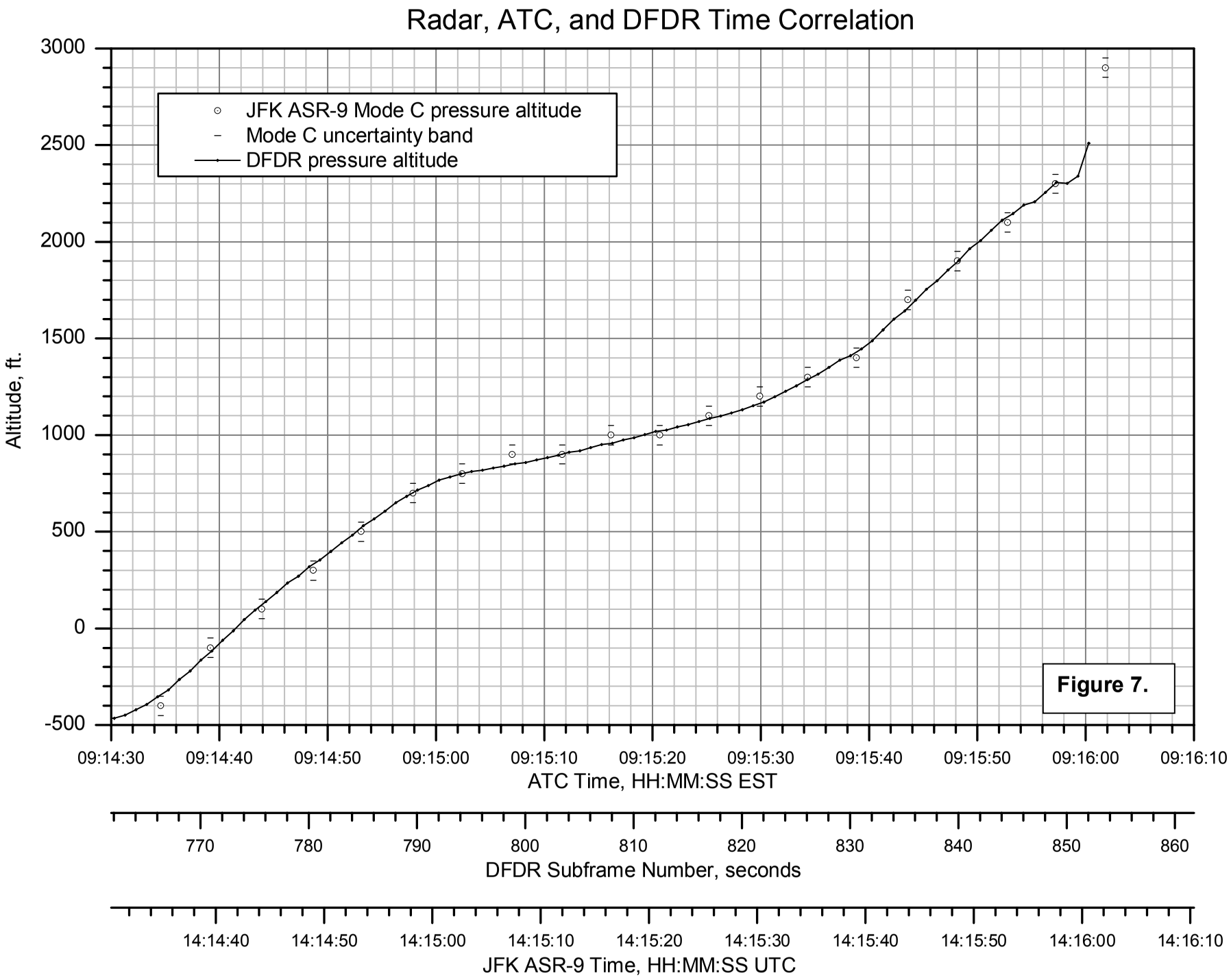
Radar, ATC, and DFDR Time Correlation
JFK ASR-9 Mode C pressure altitude
Mode C uncertainty band
DFDR pressure altitude
Altitude, ft.
3000
2500
2000
1500
1000
500
0
-500
09:14:30
09:14:40
09:14:50
09:15:00
09:15:10
09:15:20
09:15:30
09:15:40
09:15:50
09:16:00
09:16:10
ATC Time, HH:MM:SS EST
770
780
790
800
810
820
830
840
850
860
DFDR Subframe Number, seconds
14:14:40
14:14:50
14:15:00
14:15:10
14:15:20
14:15:30
14:15:40
14:15:50
14:16:00
14:16:10
JFK ASR-9 Time, HH:MM:SS UTC

Figure 7.

AAL 587 and JAL 47 Radar Tracks

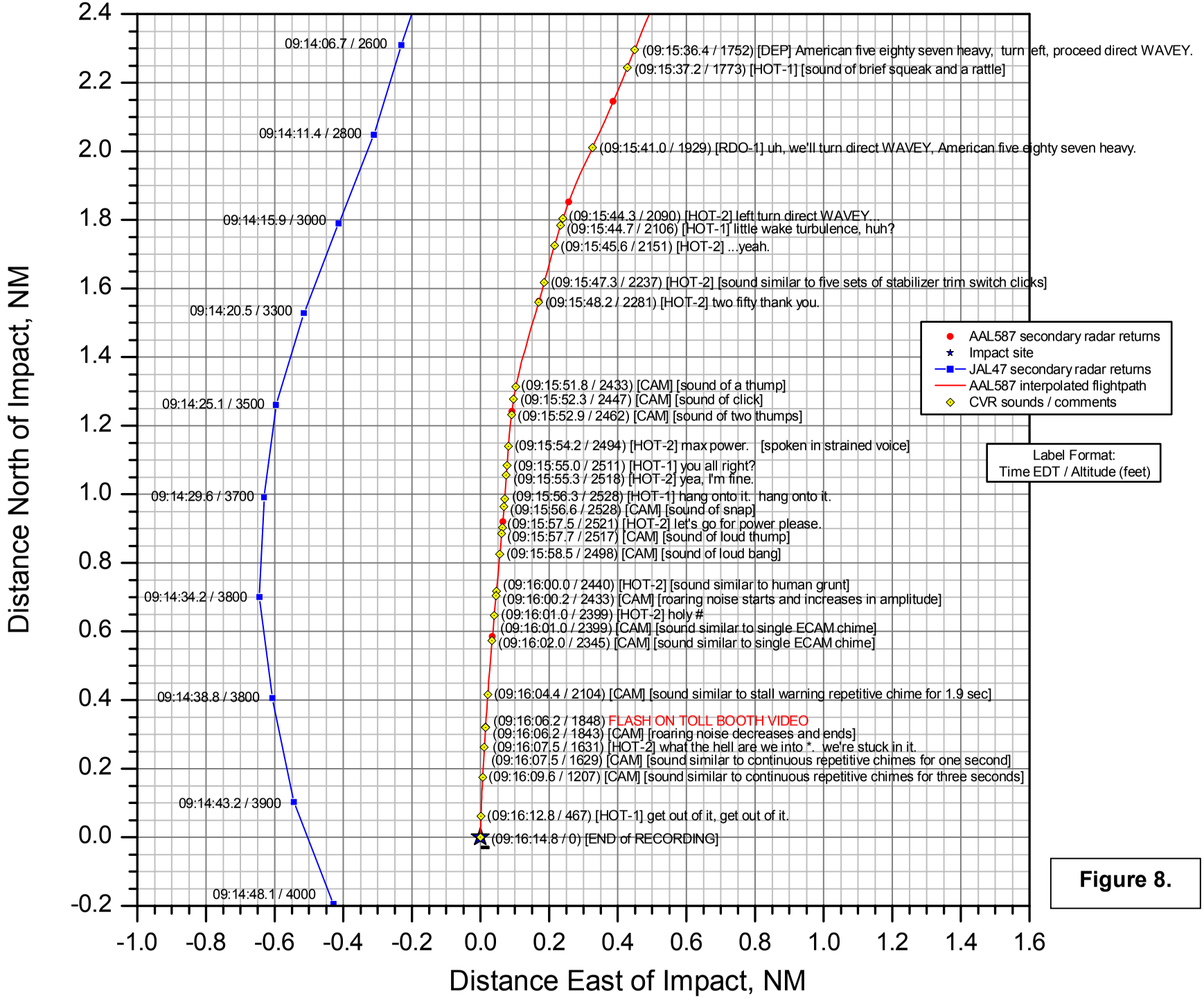

Figure 8.

American Airlines Flight 587 - Altitude

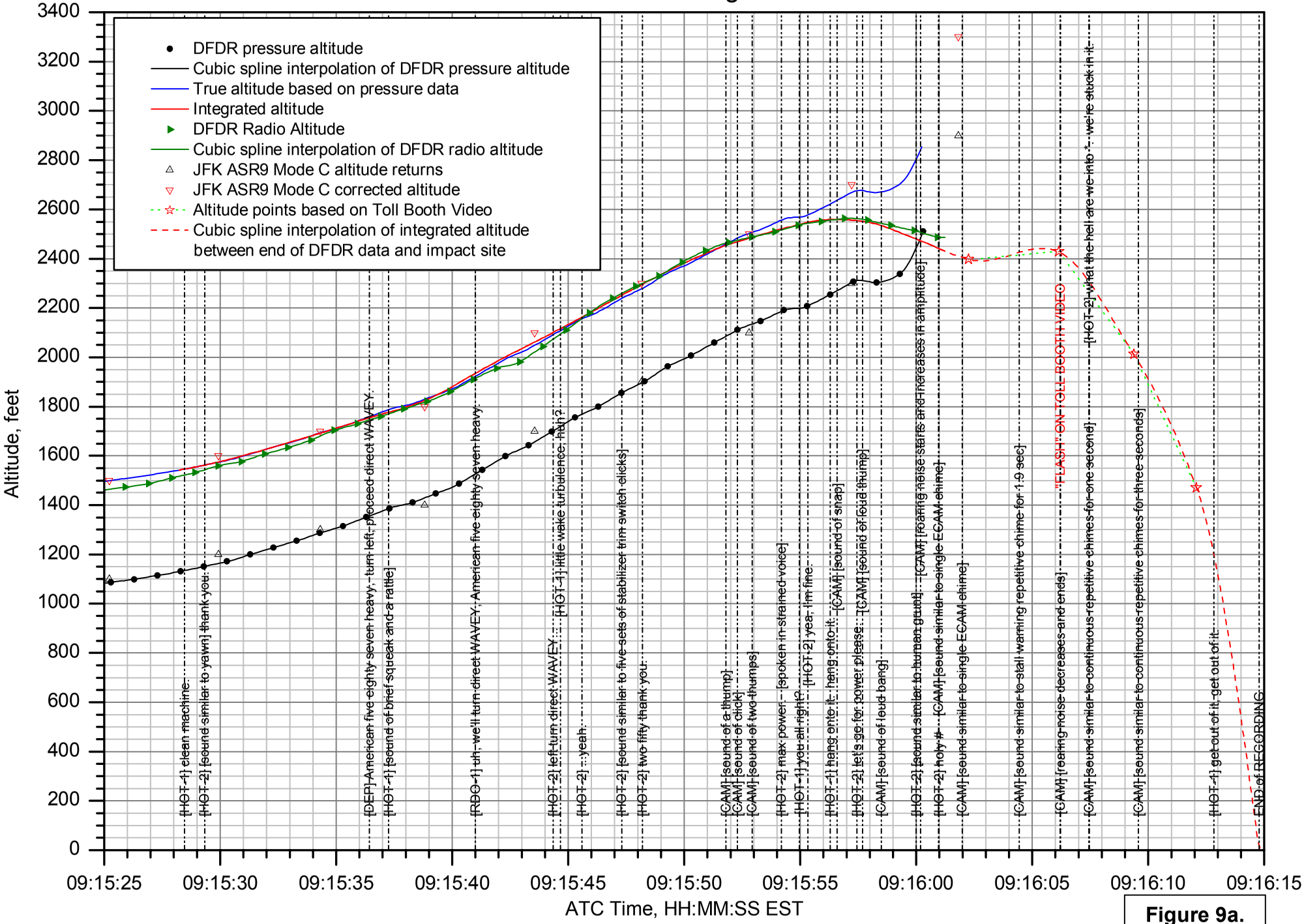

Figure 9a.

American Airlines Flight 587 - Altitude (detail)

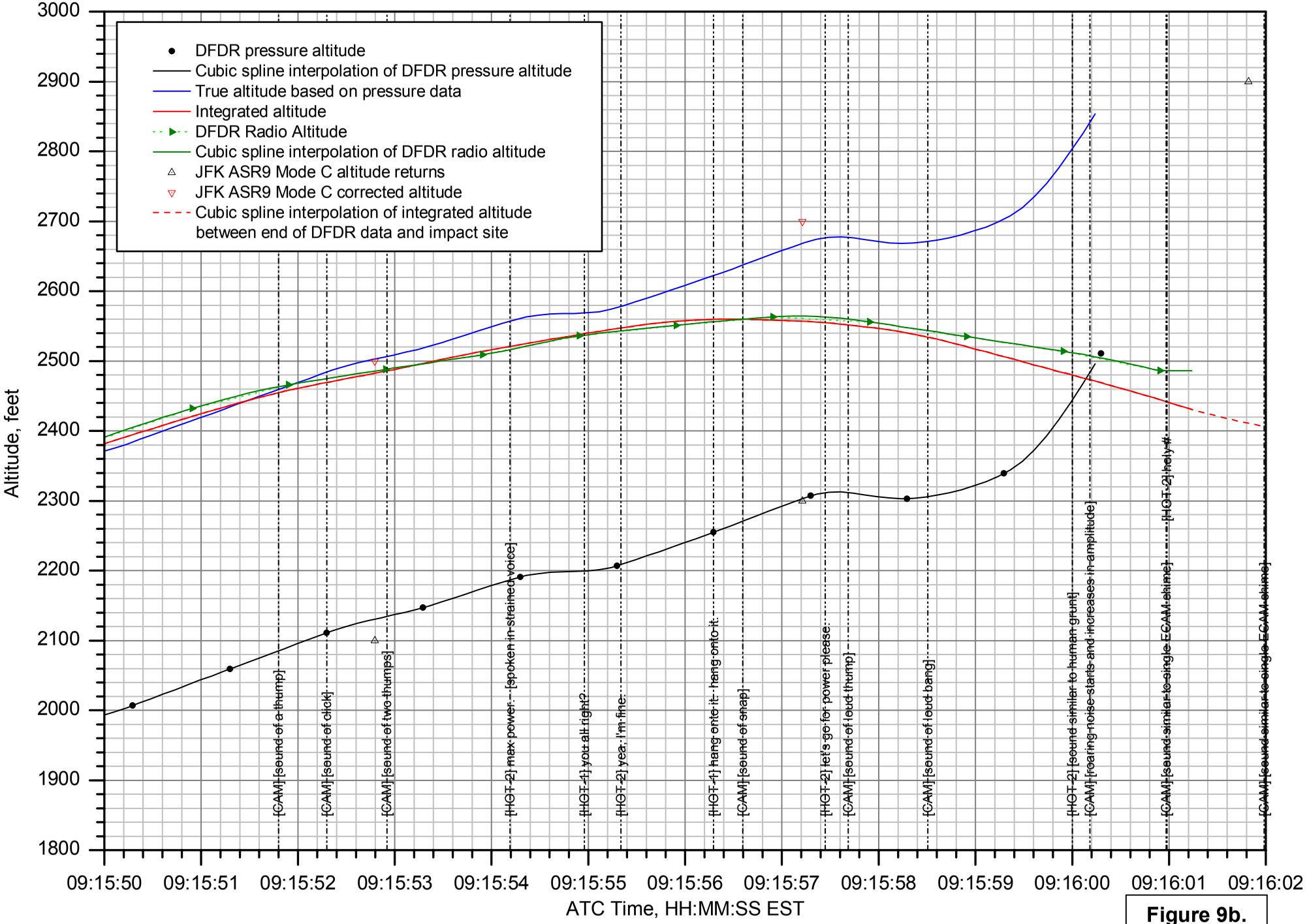

Figure 9b.

American Airlines Flight 587 - Speed

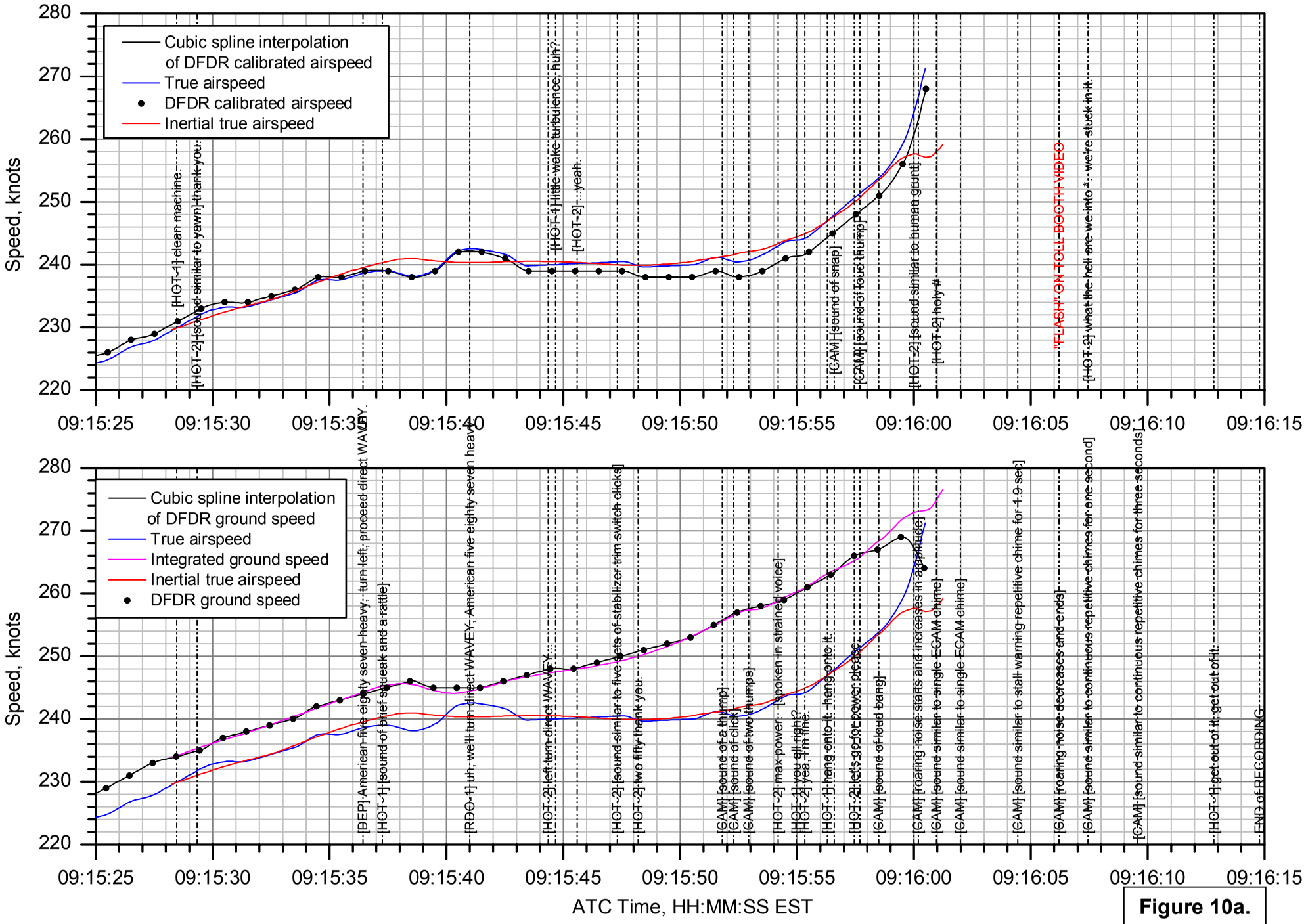

Figure 10a.

American Airlines Flight 587 - Speed (detail)

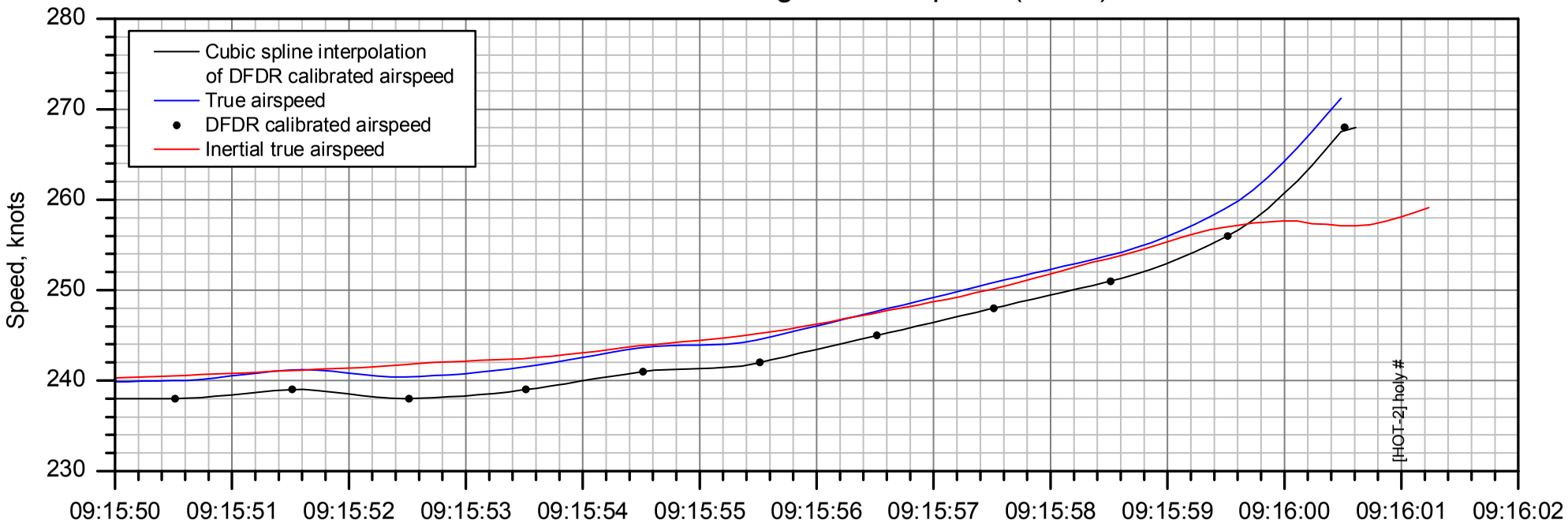

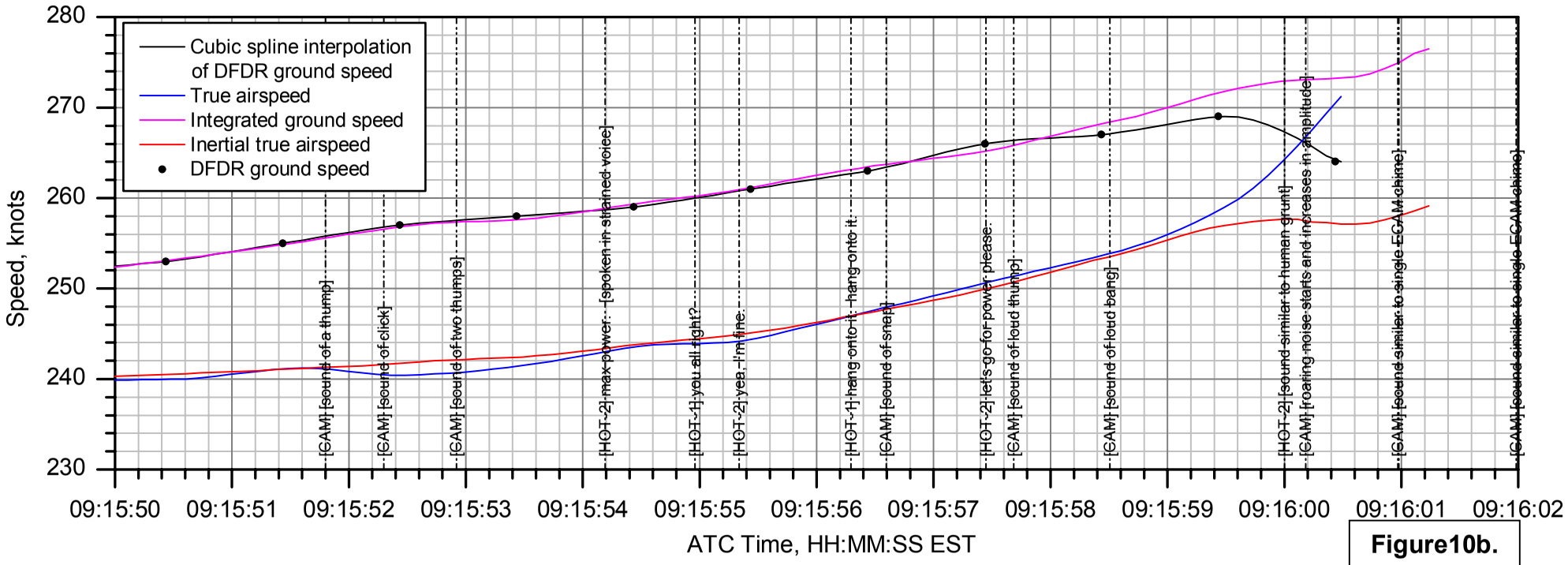

Figure10b.

American Airlines Flight 587 - Rate of Climb, Mach, & Dynamic Pressure

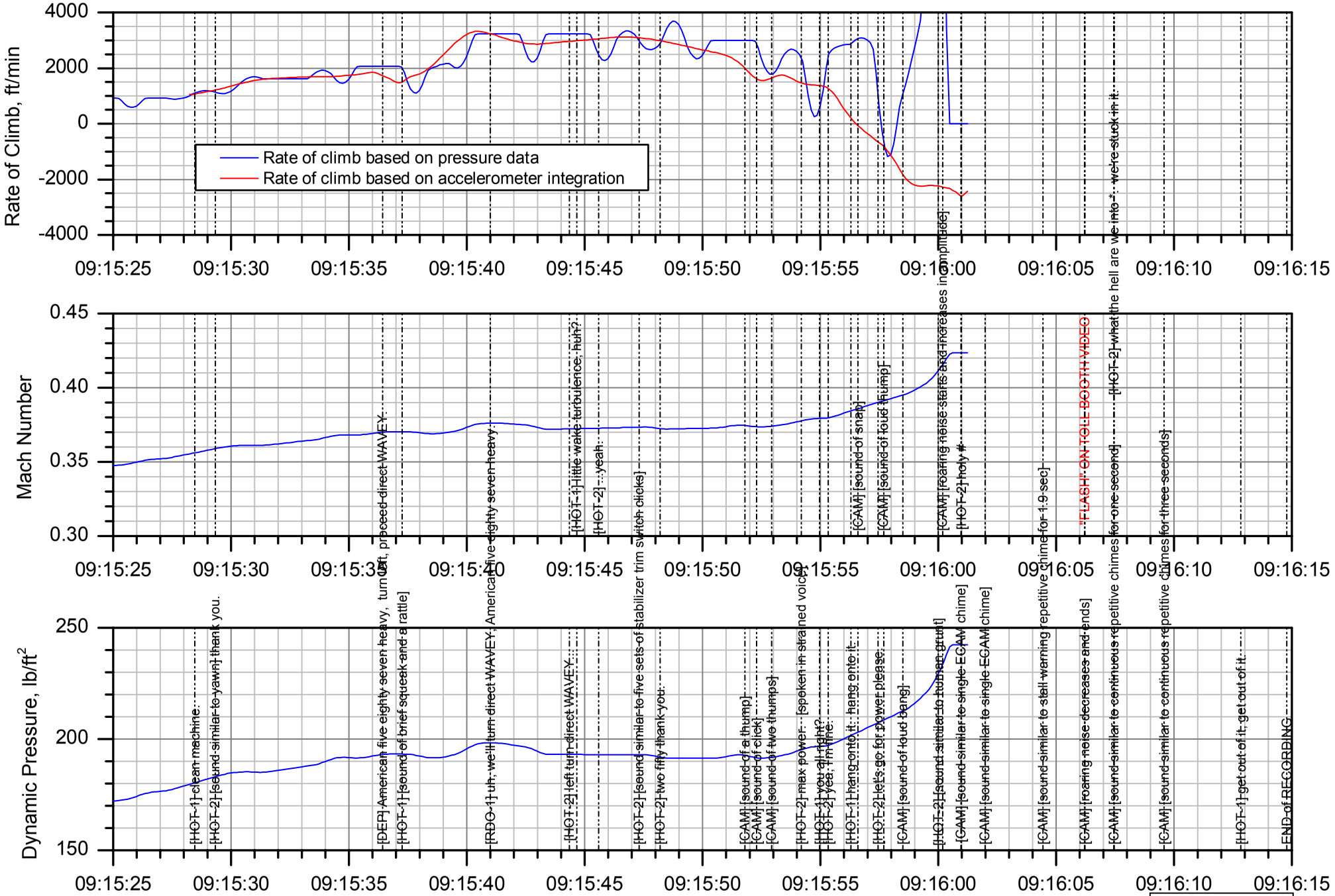

Figure11a.

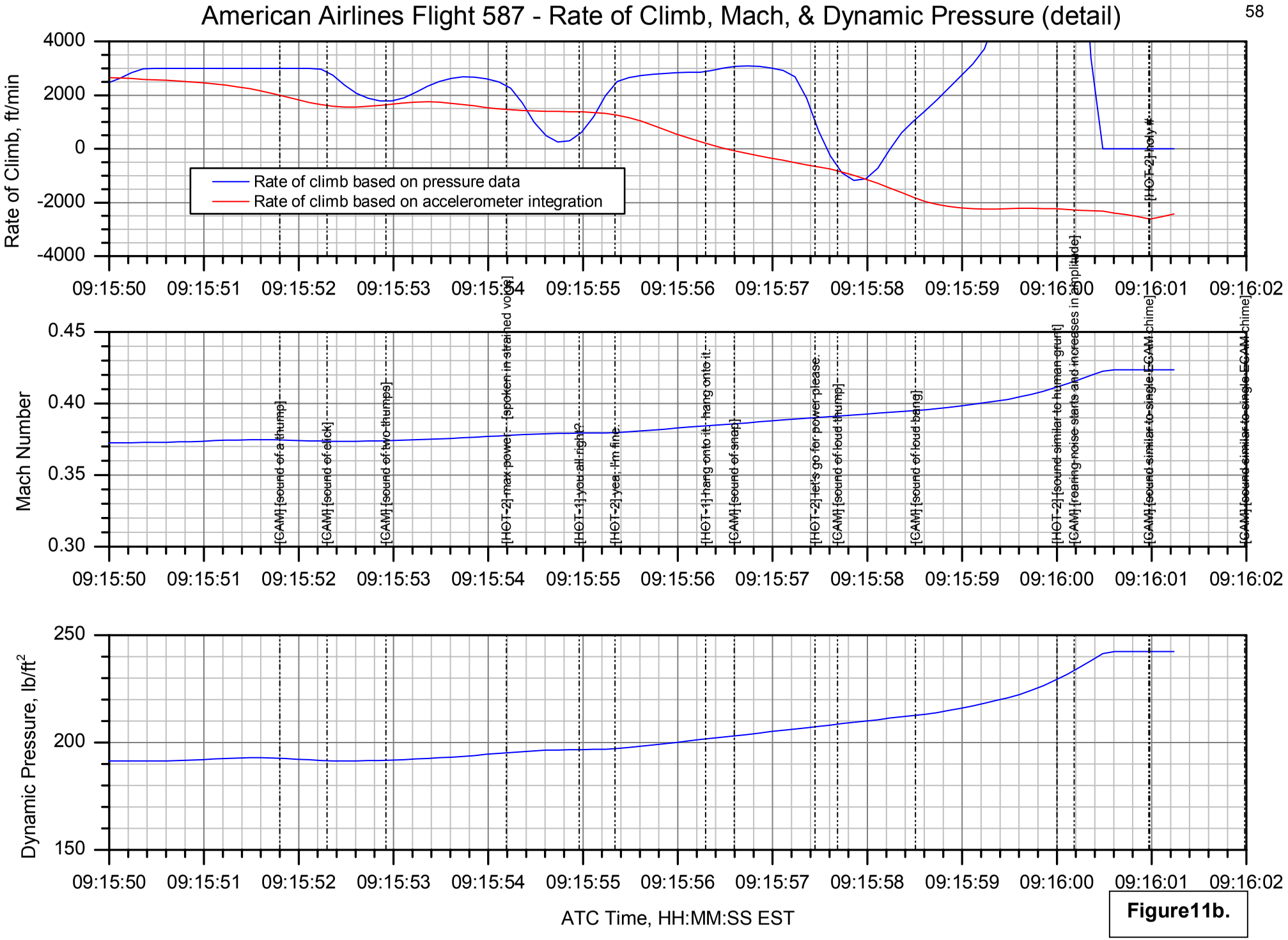
American Airlines Flight 587 - Rate of Climb, Mach, & Dynamic Pressure (detail)
Rate of Climb, ft/min
4000
2000
0
-2000
-4000
Rate of climb based on pressure data
Rate of climb based on accelerometer integration
09:15:50
09:15:51
09:15:52
09:15:53
09:15:54
09:15:55
09:15:56
09:15:57
09:15:58
09:15:59
09:16:00
09:16:01
09:16:02
[HOT-2] holy #...
Mach Number
0.45
0.40
0.35
0.30
[CAM] [sound of a thump]
[CAM] [sound of click]
[CAM] [sound of two thumps]
[HOT-2] max power... [spoken in strained voice]
[HOT-1] you all right?
[HOT-2] yea, I'm fine.
[HOT-1] hang onto it. hang onto it.
[CAM] [sound of snap]
[HOT-2] let's go for power please.
[CAM] [sound of loud thump]
[CAM] [sound of loud bang]
[HOT-2] [sound similar to human grunt]
[CAM] [roaring noise starts and increases in amplitude]
[CAM] [sound similar to single EGAM chime]
[CAM] [sound similar to single EGAM chime]
Dynamic Pressure, lb/ft2
250
200
150
ATC Time, HH:MM:SS EST

Figure11b.

American Airlines Flight 587 - Longitudinal Flight Angles

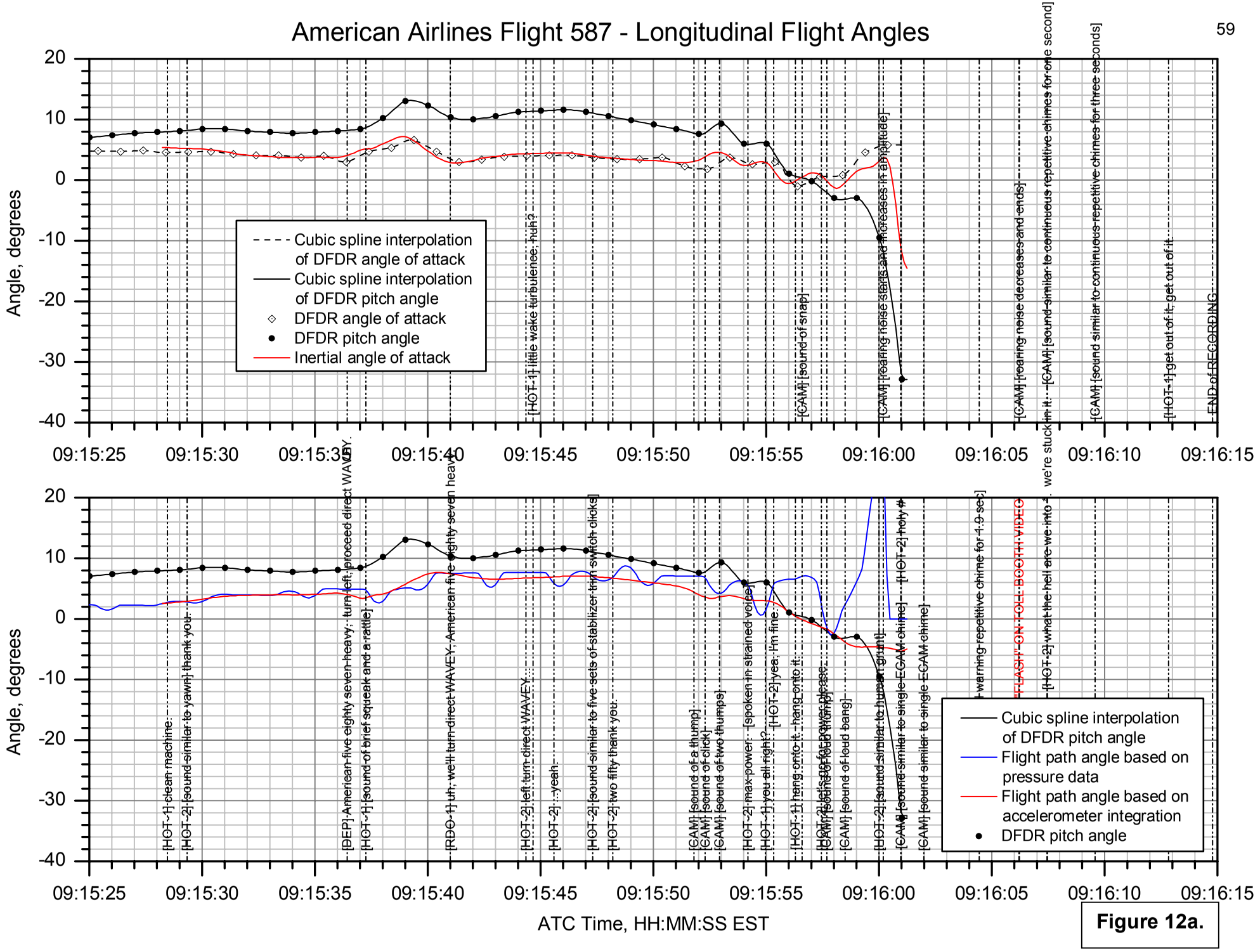

Figure 12a.

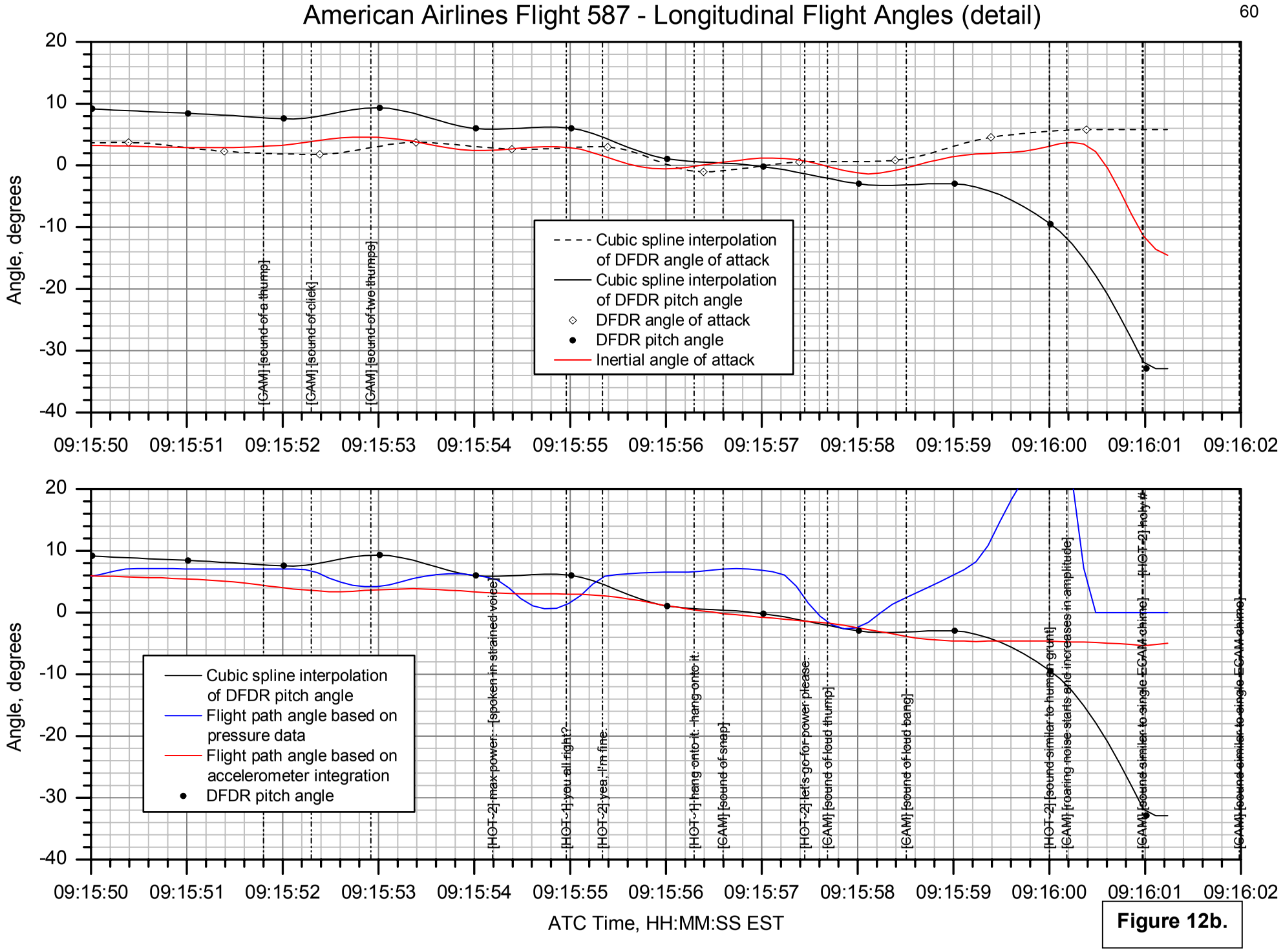
American Airlines Flight 587 - Longitudinal Flight Angles (detail)
Angle, degrees
20
10
0
-10
-20
-30
-40
09:15:50
09:15:51
09:15:52
09:15:53
09:15:54
09:15:55
09:15:56
09:15:57
09:15:58
09:15:59
09:16:00
09:16:01
09:16:02
Cubic spline interpolation of DFDR angle of attack
Cubic spline interpolation of DFDR pitch angle
DFDR angle of attack
DFDR pitch angle
Inertial angle of attack
[CAM] [sound of a thump]
[CAM] [sound of click]
[CAM] [sound of two thumps]
Cubic spline interpolation of DFDR pitch angle
Flight path angle based on pressure data
Flight path angle based on accelerometer integration
DFDR pitch angle
[HOT-2] max power. [spoken in strained voice]
[HOT-1] you all right?
[HOT-2] yea, I'm fine.
[HOT-1] hang onto it. hang onto it.
[CAM] [sound of snap]
[HOT-2] let's go for power please.
[CAM] [sound of loud thump]
[CAM] [sound of loud bang]
[HOT-2] [sound similar to human grunt]
[CAM] roaring noise starts and increases in amplitude
[CAM] [sound similar to single ECAM chime]
[HOT-2] holy #
[CAM] [sound similar to single ECAM chime]
ATC Time, HH:MM:SS EST

Figure 12b.

American Airlines Flight 587 - Lateral Flight Angles

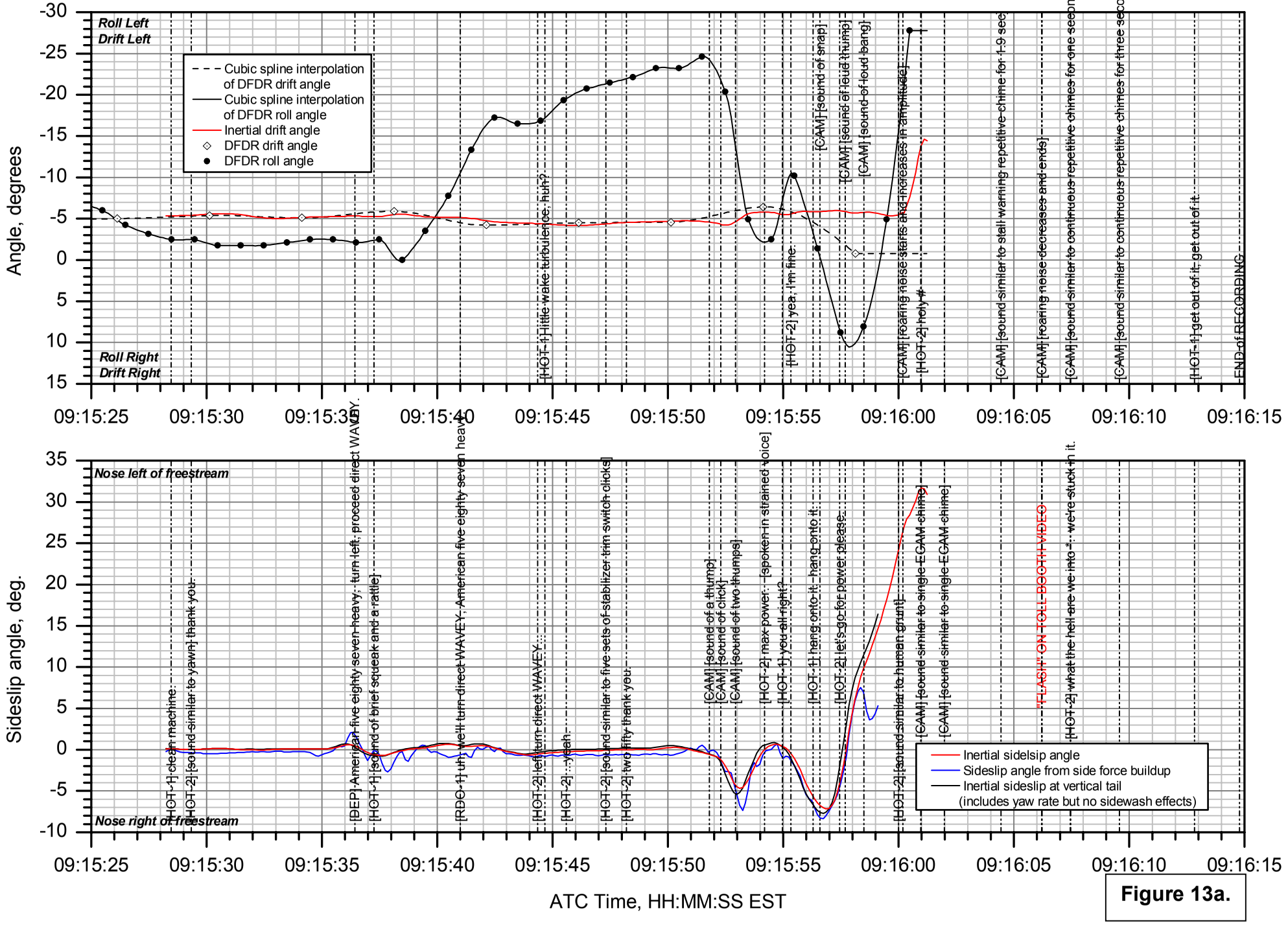

Figure 13a.

American Airlines Flight 587 - Lateral Flight Angles (detail)

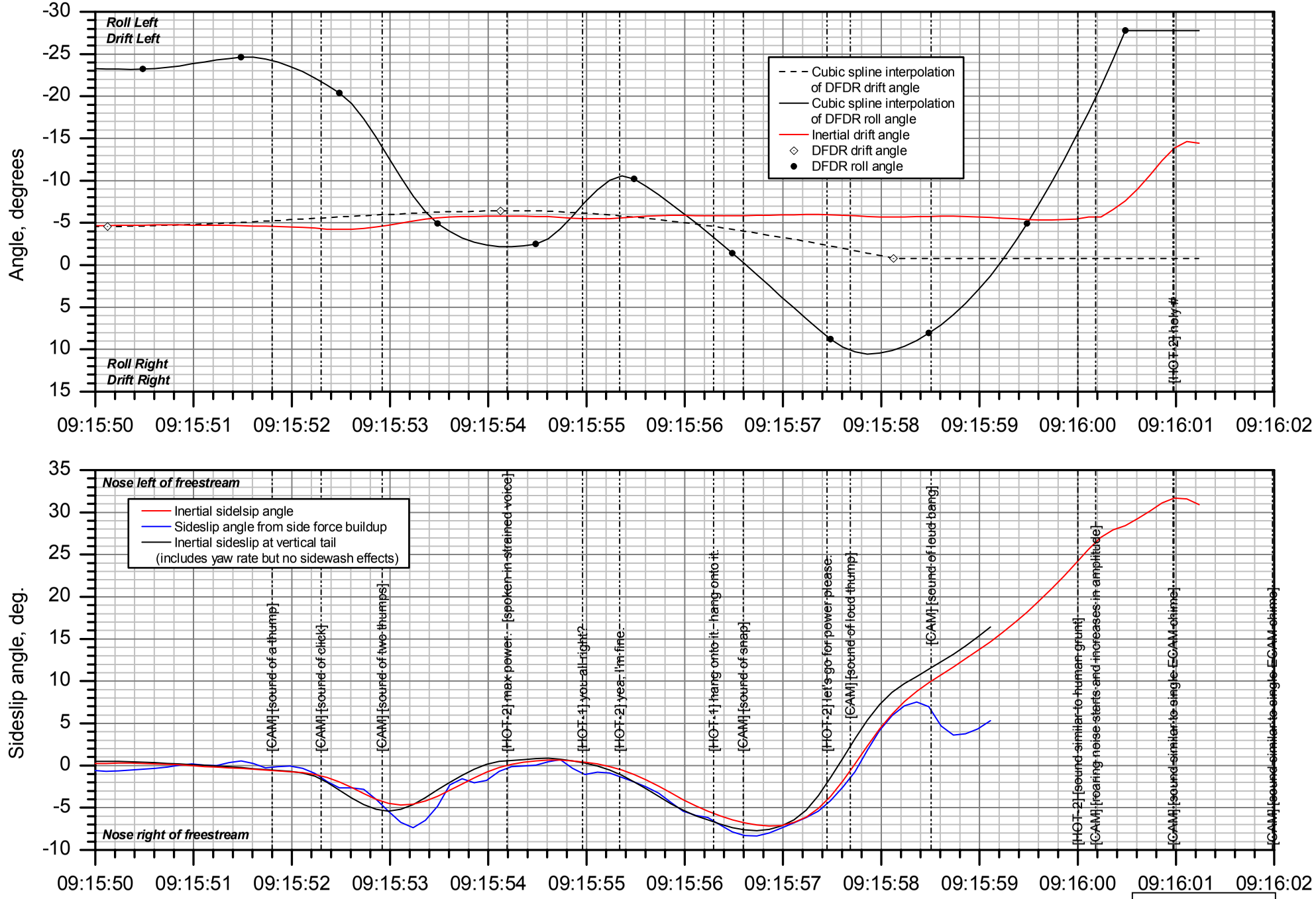

Figure 13b.

American Airlines Flight 587 - Directional Flight Angles

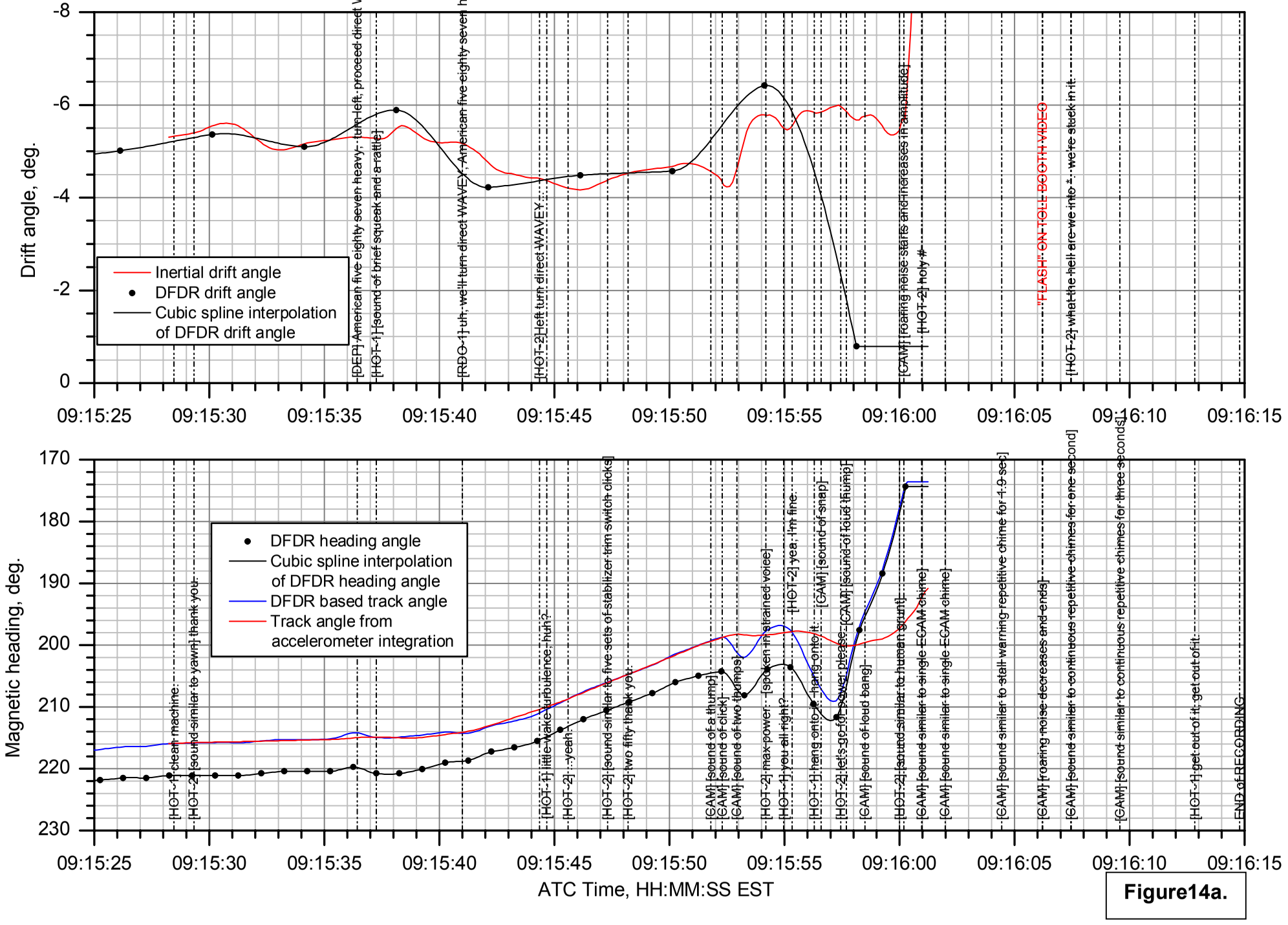

Figure14a.

American Airlines Flight 587 - Directional Flight Angles (detail)

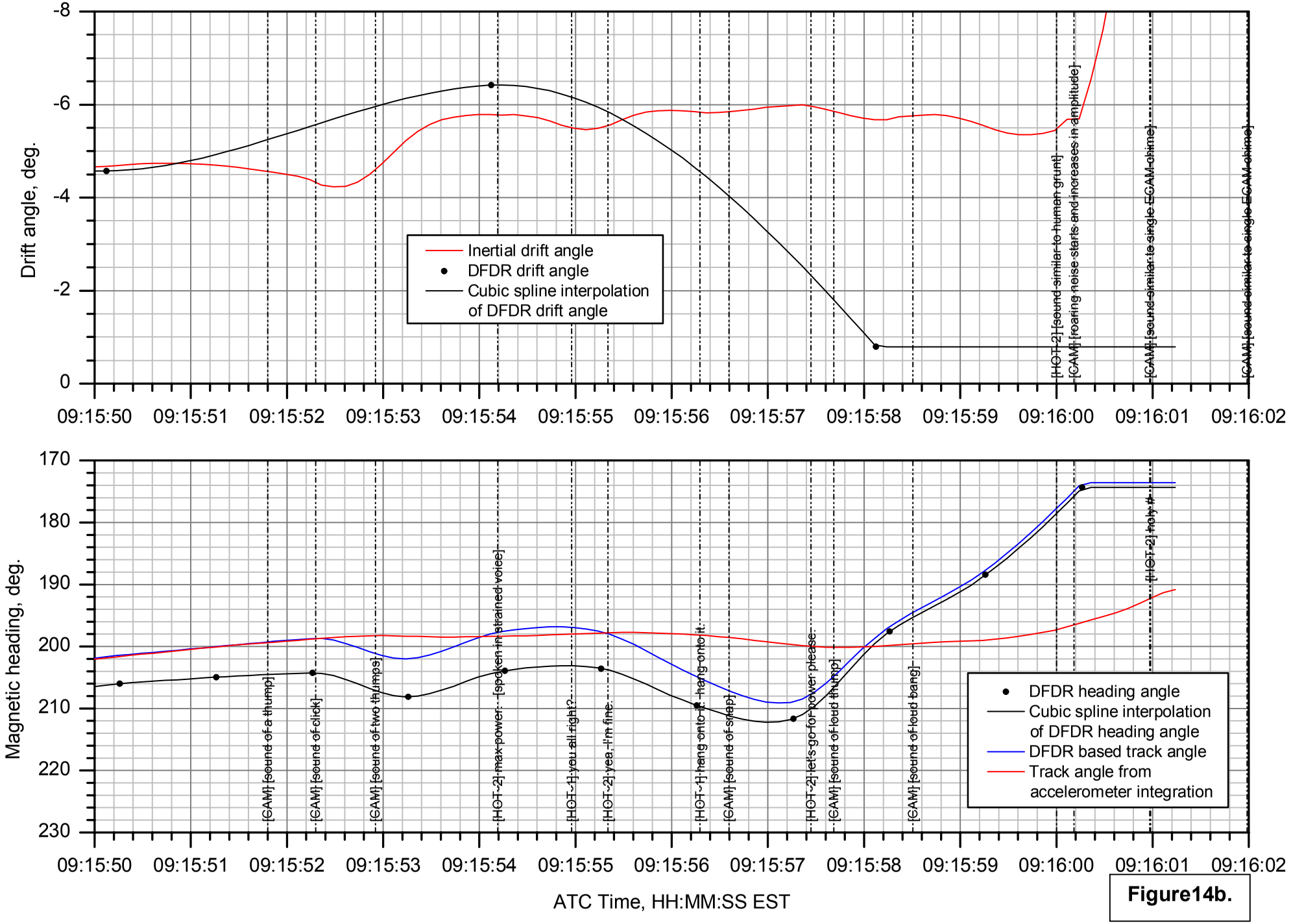

Figure14b.

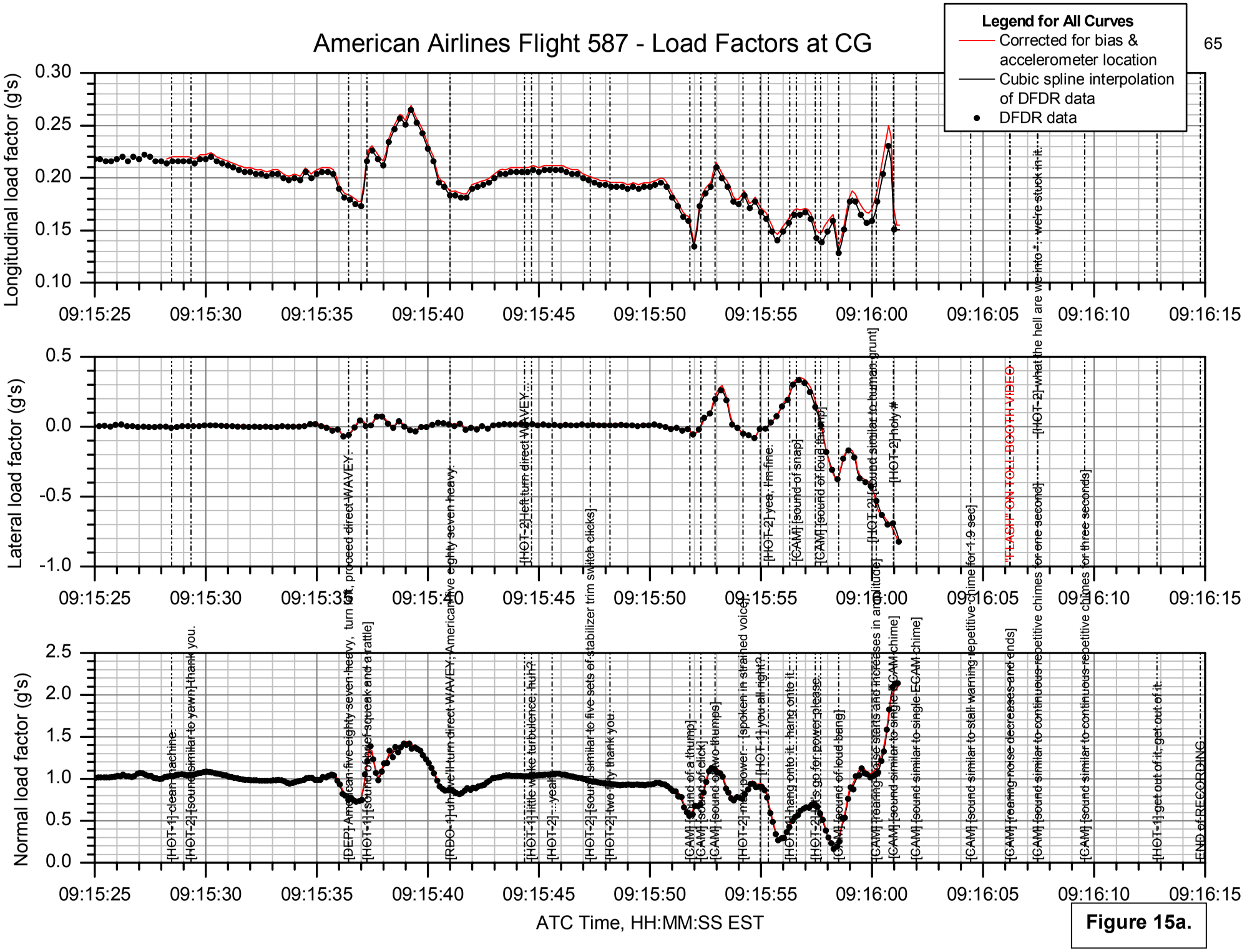
American Airlines Flight 587 - Load Factors at CG
Legend for All Curves
Corrected for bias & accelerometer location
Cubic spline interpolation of DFDR data
DFDR data
Longitudinal load factor (g's)
Lateral load factor (g's)
Normal load factor (g's)
ATC Time, HH:MM:SS EST
09:15:25
09:15:30
09:15:35
09:15:40
09:15:45
09:15:50
09:15:55
09:16:00
09:16:05
09:16:10
09:16:15
[HOT-1] clean machine.
[HOT-2] [sound similar to yawn] thank you.
[BEP] American five eighty seven heavy, turn left, proceed direct WAVEY.
[HOT-1] [sound of brief squeak and a rattle]
[RDO-1] uh, we'll turn direct WAVEY, American five eighty seven heavy.
[HOT-1] little white turbulence, huh?
[HOT-2] ...yeah.
[HOT-2] [sound similar to five sets of stabilizer trim switch clicks]
[HOT-2] two fifty thank you.
[CAM] [sound of a thump]
[CAM] [sound of click]
[CAM] [sound of two thumps]
[HOT-2] ma'am, [spoken in strained voice]
[HOT-1] you all right?
[HOT-1] hang onto it, hang onto it.
[HOT-2] let's go for power please.
[CAM] [sound of loud bang]
[CAM] [sound of a thump]
[CAM] [sound similar to single EGAM chime]
[CAM] [sound similar to single EGAM chime]
[CAM] [sound similar to single EGAM chime]
[CAM] [sound similar to stall warning repetitive chime for 1.9 sec]
[CAM] [warning noise decreases and ends]
"FLASH ON TOLL BOOTH VIDEO"
[CAM] [warning noise starts and increases in amplitude]
[HOT-2] [sound similar to human grunt]
[HOT-2] what the hell are we into*.. we're stuck in it.
[CAM] [sound similar to continuous repetitive chimes for one second]
[CAM] [sound similar to continuous repetitive chimes for three seconds]
[HOT-2] holy #
[HOT-2] yea, I'm fine.
[CAM] [sound of snap]
[CAM] [sound of loud thump]
[HOT-1] get out of it, get out of it.
END of RECORDING

Figure 15a.

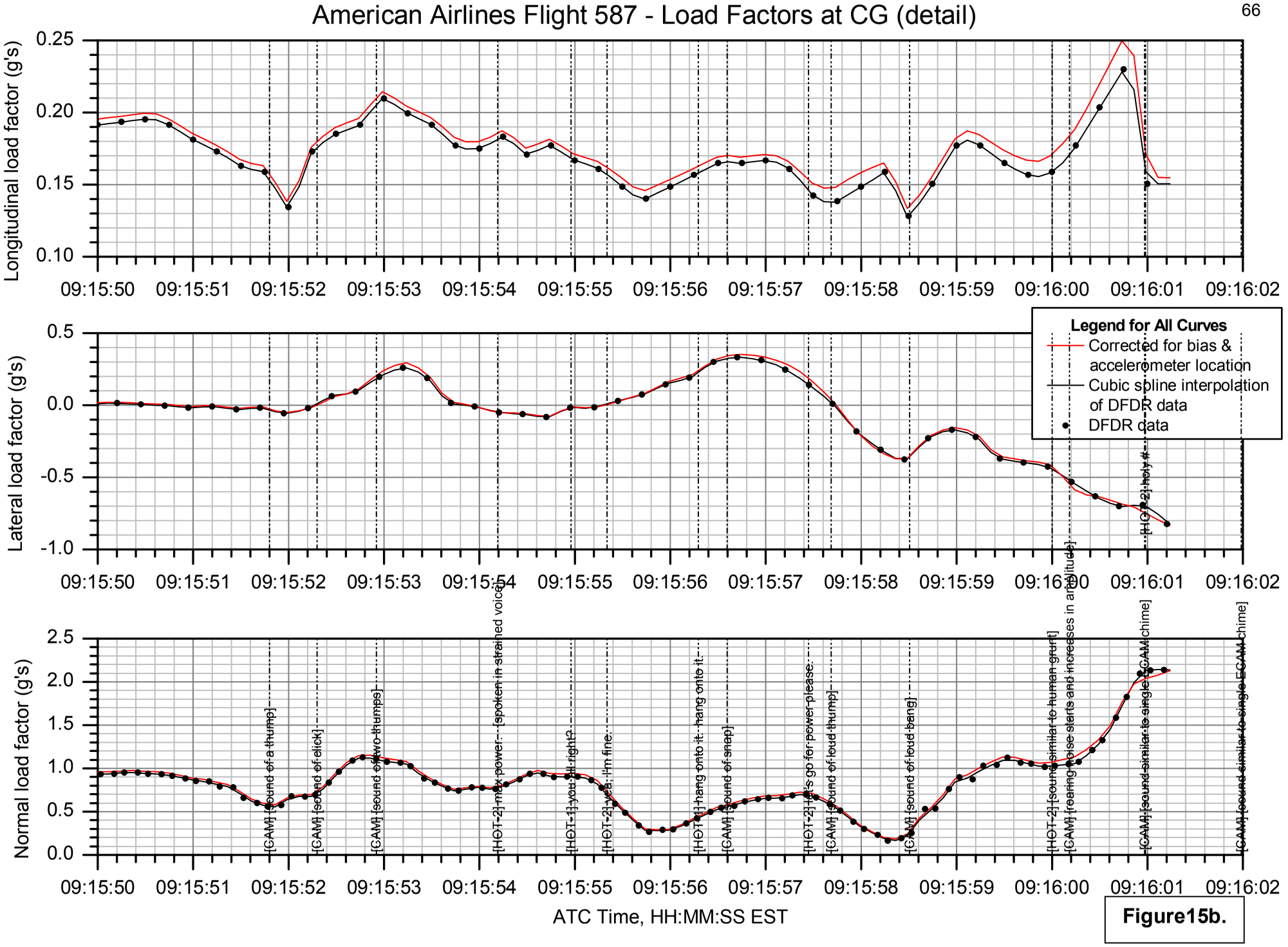
American Airlines Flight 587 - Load Factors at CG (detail)
Longitudinal load factor (g's)
0.25
0.20
0.15
0.10
09:15:50
09:15:51
09:15:52
09:15:53
09:15:54
09:15:55
09:15:56
09:15:57
09:15:58
09:15:59
09:16:00
09:16:01
09:16:02
Lateral load factor (g's)
0.5
0.0
-0.5
-1.0
Legend for All Curves
Corrected for bias & accelerometer location
Cubic spline interpolation of DFDR data
DFDR data
[HOT-2] holy #
Normal load factor (g's)
2.5
2.0
1.5
1.0
0.5
0.0
[CAM] [sound of a thump]
[CAM] [sound of click]
[CAM] [sound of two thumps]
[HOT-2] max power. [spoken in strained voice]
[HOT-1] you all right?
[HOT-2] yes, I'm fine.
[HOT-1] hang onto it. hang onto it.
[CAM] [sound of snap]
[HOT-2] let's go for power please.
[CAM] [sound of loud thump]
[CAM] [sound of loud bang]
[HOT-2] [sound similar to human grunt]
[CAM] [roaring noise starts and increases in amplitude]
[CAM] [sound similar to single EGAM chime]
[CAM] [sound similar to single EGAM chime]
ATC Time, HH:MM:SS EST

Figure15b.

Load Factors In Cockpit Using Various Calculation Methods

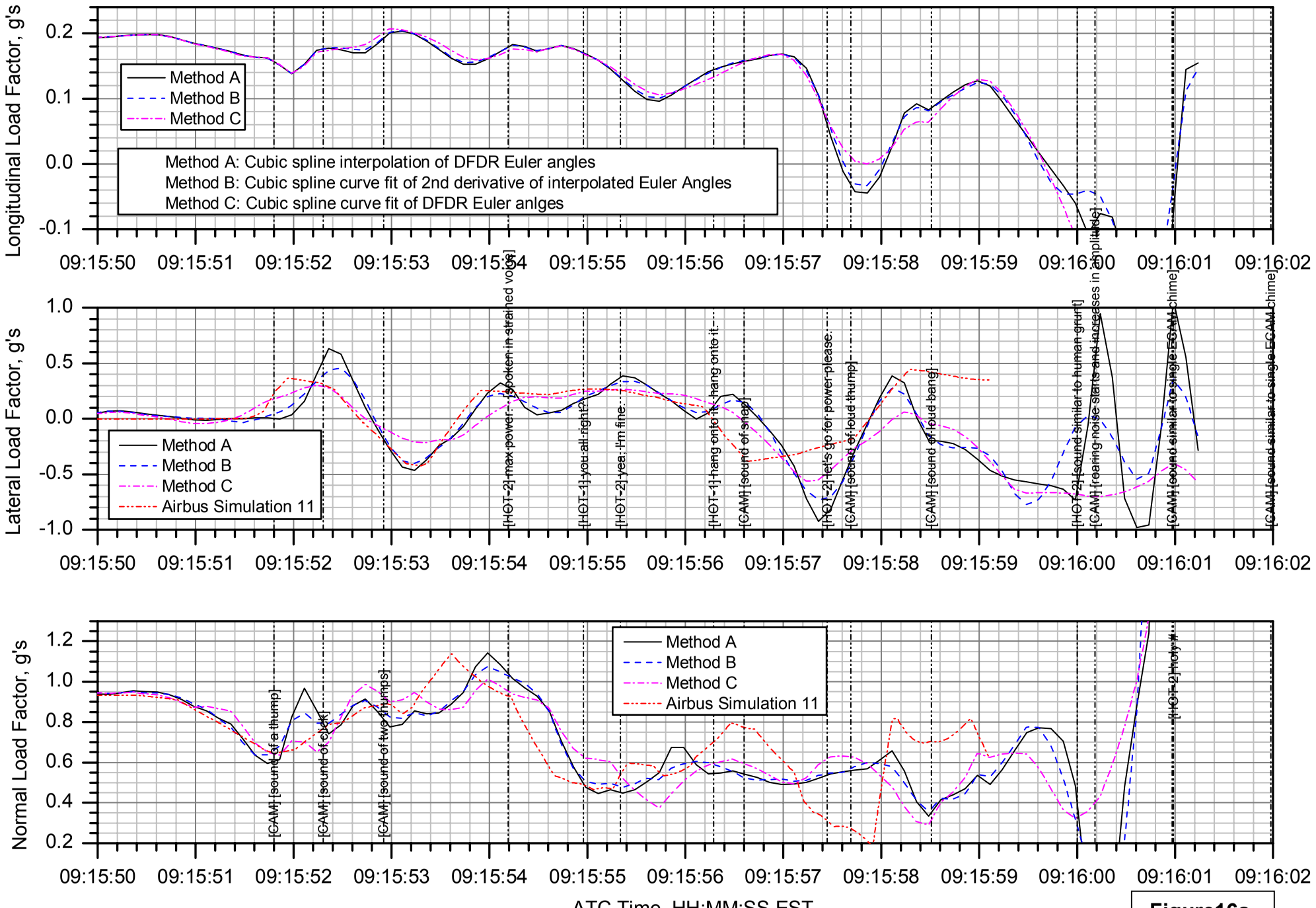

Figure16a.

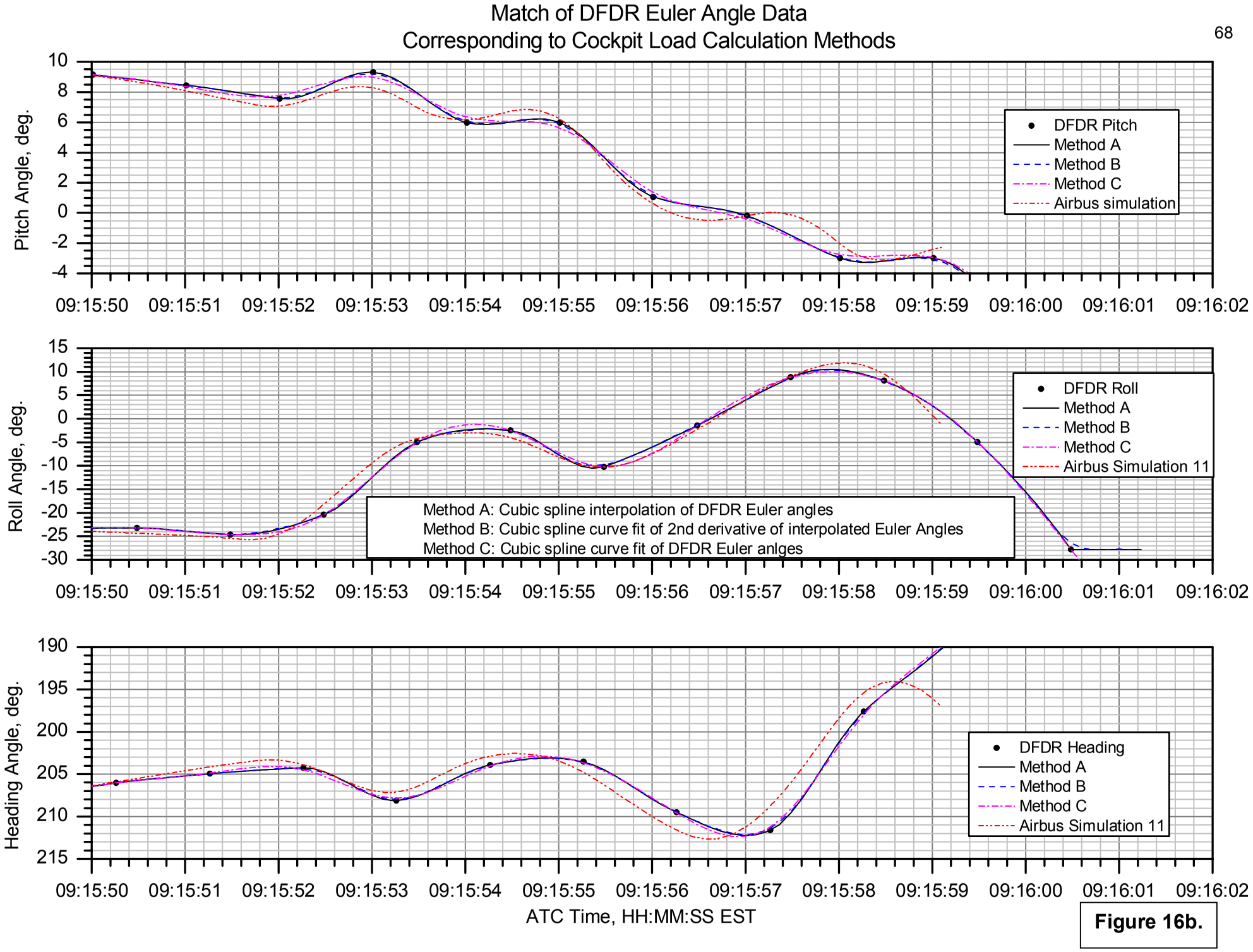
Match of DFDR Euler Angle Data
Corresponding to Cockpit Load Calculation Methods
Pitch Angle, deg.
DFDR Pitch
Method A
Method B
Method C
Airbus simulation
Roll Angle, deg.
DFDR Roll
Method A
Method B
Method C
Airbus Simulation 11
Method A: Cubic spline interpolation of DFDR Euler angles
Method B: Cubic spline curve fit of 2nd derivative of interpolated Euler Angles
Method C: Cubic spline curve fit of DFDR Euler anlges
Heading Angle, deg.
DFDR Heading
Method A
Method B
Method C
Airbus Simulation 11
09:15:50 09:15:51 09:15:52 09:15:53 09:15:54 09:15:55 09:15:56 09:15:57 09:15:58 09:15:59 09:16:00 09:16:01 09:16:02
ATC Time, HH:MM:SS EST

Figure 16b.

American Airlines Flight 587 - Body Axis Angular Rates

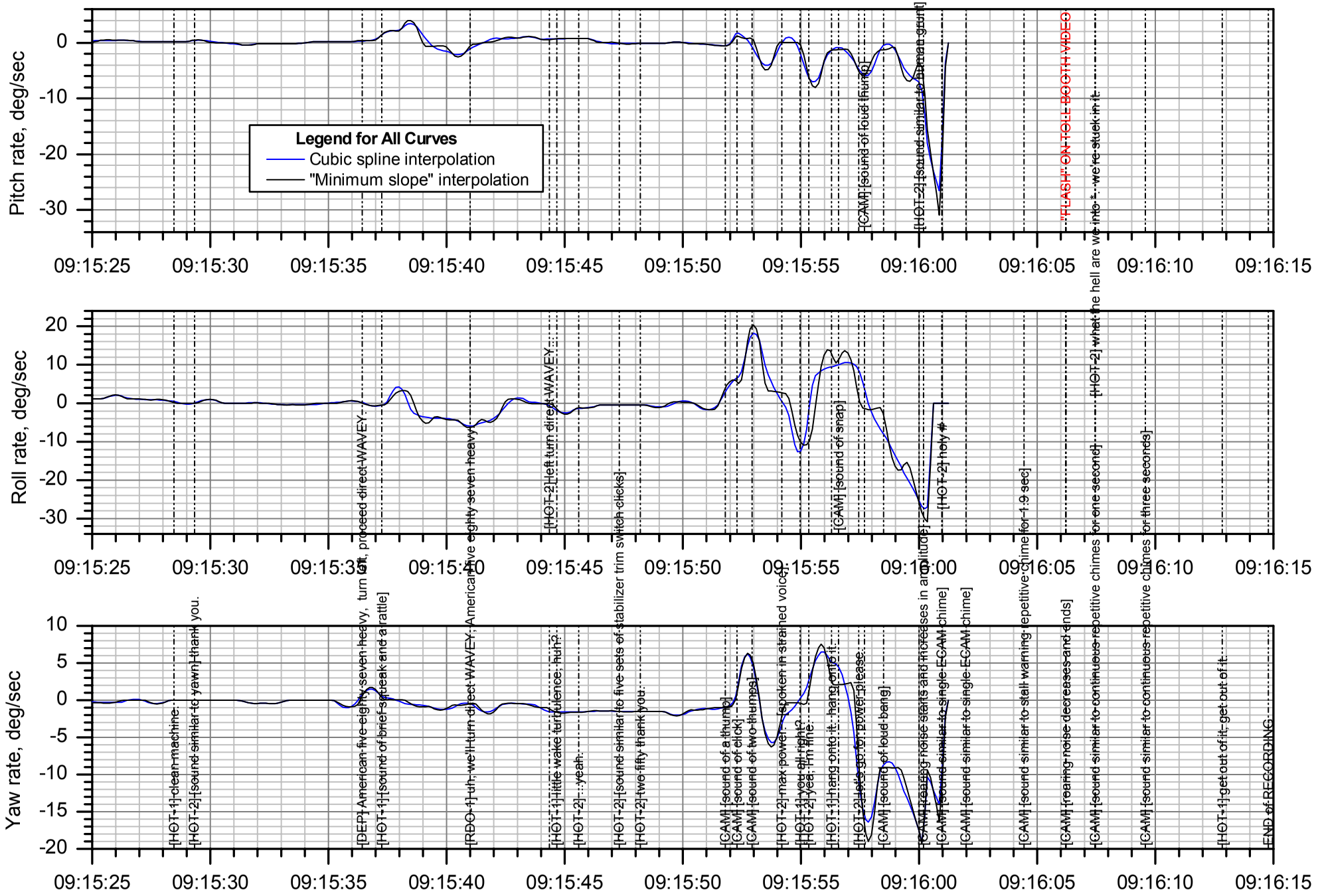

Figure 17a.

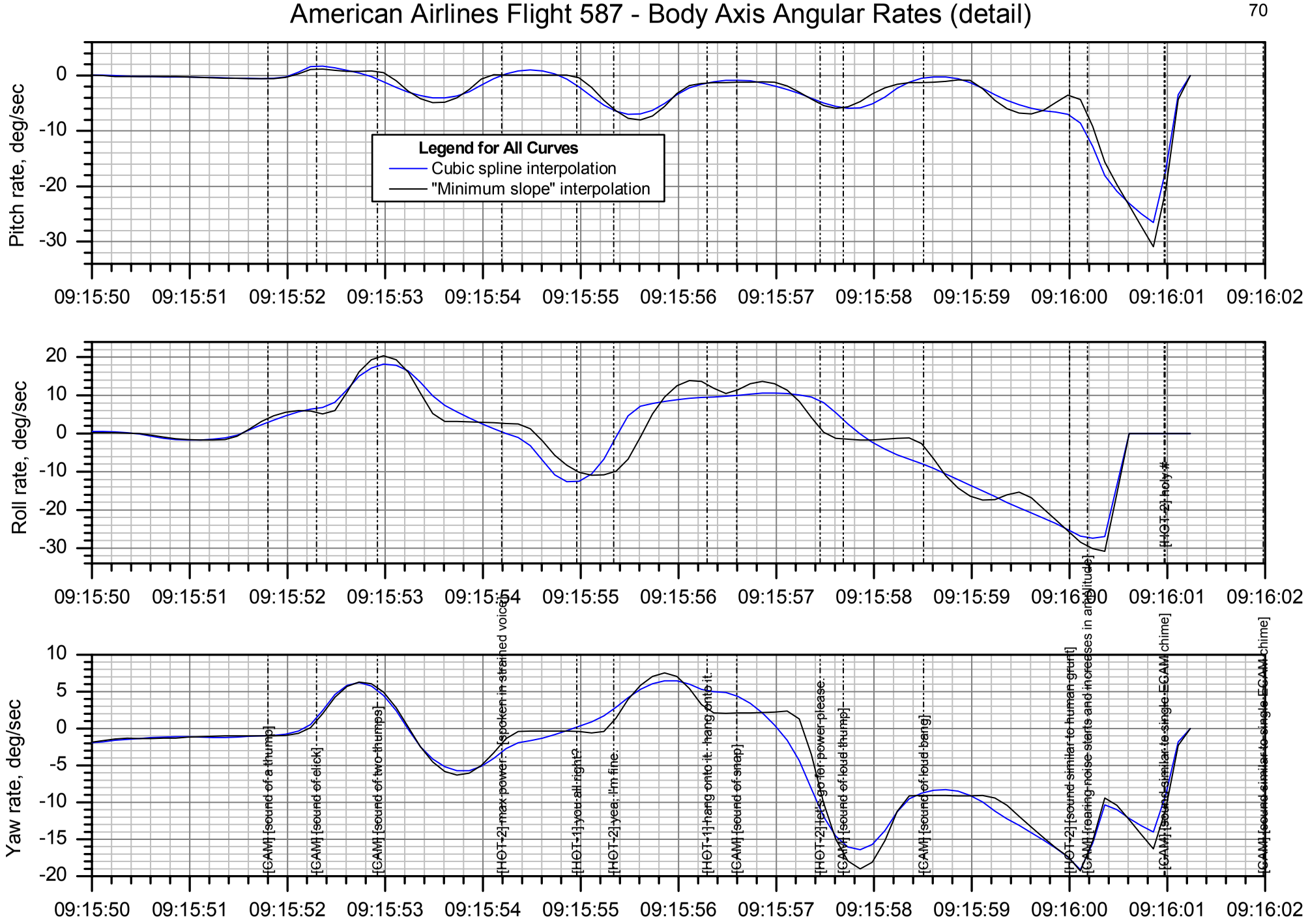
American Airlines Flight 587 - Body Axis Angular Rates (detail)
Pitch rate, deg/sec
Roll rate, deg/sec
Yaw rate, deg/sec
Legend for All Curves
Cubic spline interpolation
"Minimum slope" interpolation
09:15:50
09:15:51
09:15:52
09:15:53
09:15:54
09:15:55
09:15:56
09:15:57
09:15:58
09:15:59
09:16:00
09:16:01
09:16:02
[CAM] [sound of a thump]
[CAM] [sound of click]
[CAM] [sound of two thumps]
[HOT-2] max power. [spoken in strained voice]
[HOT-1] you all right?
[HOT-2] yea, I'm fine.
[HOT-1] hang onto it. hang onto it.
[CAM] [sound of snap]
[HOT-2] let's go for power please.
[CAM] [sound of loud thump]
[CAM] [sound of loud bang]
[HOT-2] [sound similar to human grunt]
[CAM] [roaring noise starts and increases in amplitude]
[HOT-2] holy #
[CAM] [sound similar to single EGAM chime]
[CAM] [sound similar to single EGAM chime]

Figure 17b.

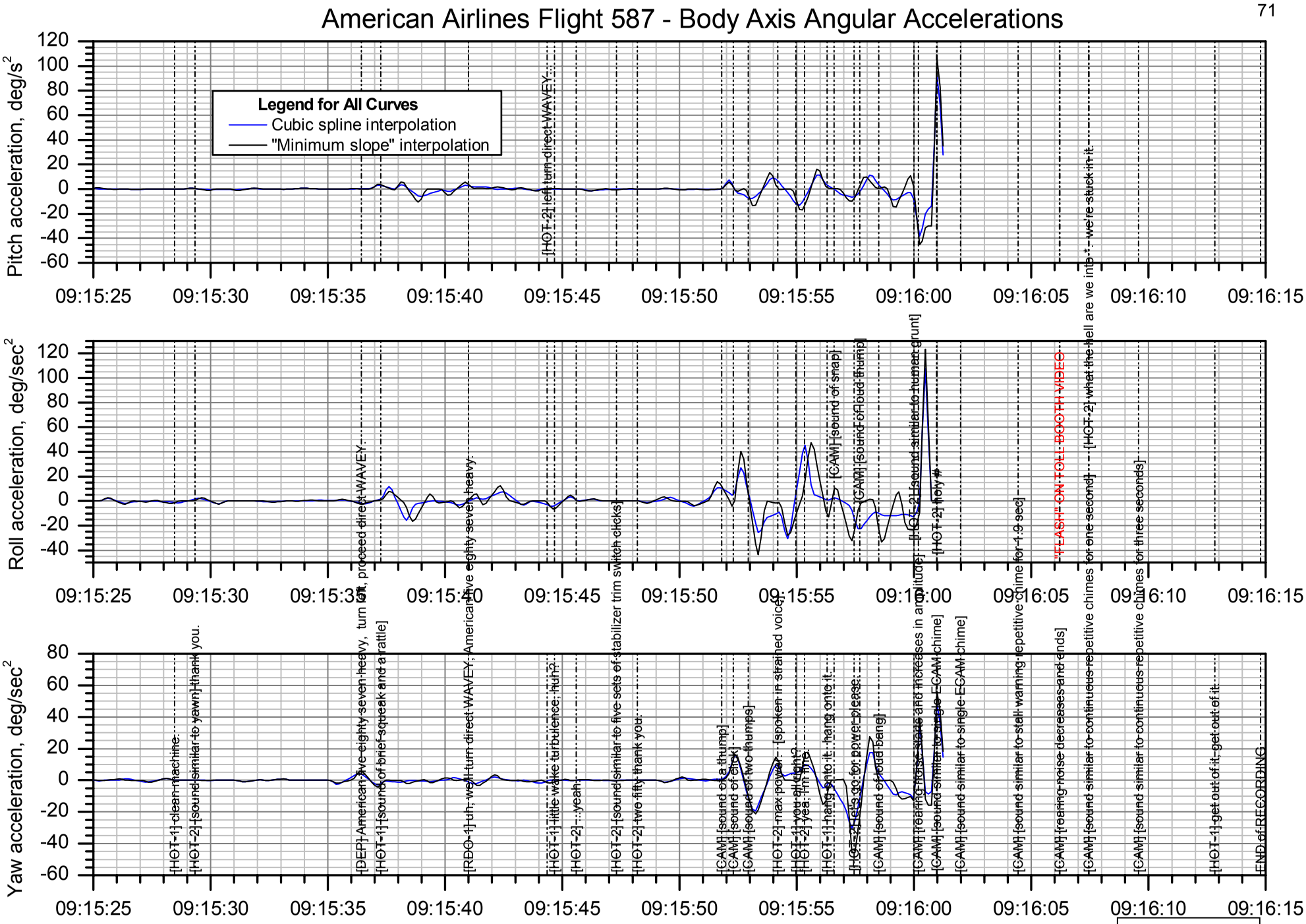
American Airlines Flight 587 - Body Axis Angular Accelerations
Legend for All Curves
Cubic spline interpolation
"Minimum slope" interpolation
Pitch acceleration, deg/s2
Roll acceleration, deg/sec2
Yaw acceleration, deg/sec2
09:15:25
09:15:30
09:15:35
09:15:40
09:15:45
09:15:50
09:15:55
09:16:00
09:16:05
09:16:10
09:16:15
[HOT-2] left turn direct WAVEY.
[HOT-1] what the hell are we into?: we're stuck in it.
[HOT-1] clean machine.
[HOT-2] sound similar to yawn] thank you.
[DEP] American five eighty seven heavy, turn left, proceed direct WAVEY.
[HOT-1] sound of brief squeak and a rattle]
[RDO-1] uh, well turn direct WAVEY, American five eighty seven heavy.
[HOT-1] little wake turbulence, huh?
[HOT-2] yeah.
[HOT-2] sound similar to five sets of stabilizer trim switch clicks]
[HOT-2] two fifty, thank you.
[CAM] sound of a thump]
[CAM] sound of click]
[CAM] sound of two thumps]
[HOT-2] max power. [spoken in strained voice]
[HOT-1] you alright?
[HOT-1] hang onto it. hang onto it.
[HOT-2] let's go for power please.
[CAM] sound of loud bang]
[CAM] sound of snap]
[CAM] sound of loud thump]
[HOT-2] sound similar to human grunt]
[HOT-2] holy #
[CAM] sound similar to single EGAM chime]
[CAM] sound similar to single EGAM chime]
[CAM] sound similar to stall warning repetitive chime for 1.9 sec]
[CAM] roaring noise decreases and ends]
[CAM] sound similar to continuous repetitive chimes for one second]
[CAM] sound similar to continuous repetitive chimes for three seconds]
[HOT-1] get out of it, get out of it.
END of RECORDING
FLASH ON TOLL BOOTH VIDEO

Figure 18a.

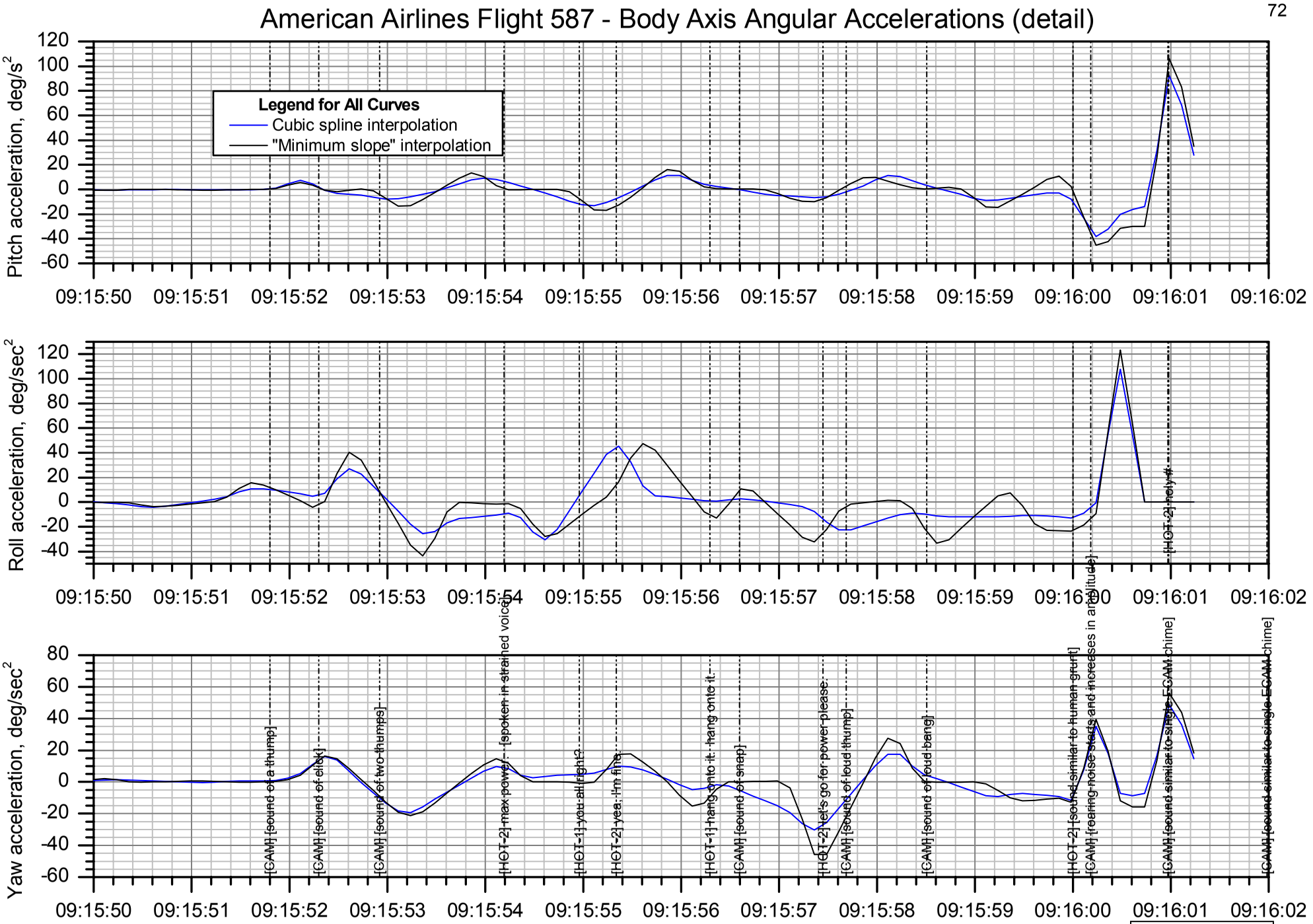
American Airlines Flight 587 - Body Axis Angular Accelerations (detail)
Legend for All Curves
Cubic spline interpolation
"Minimum slope" interpolation
Pitch acceleration, deg/s2
Roll acceleration, deg/sec2
Yaw acceleration, deg/sec2
09:15:50
09:15:51
09:15:52
09:15:53
09:15:54
09:15:55
09:15:56
09:15:57
09:15:58
09:15:59
09:16:00
09:16:01
09:16:02
[CAM] [sound of a thump]
[CAM] [sound of click]
[CAM] [sound of two thumps]
[HOT-2] max power! - [spoken in strained voice]
[HOT-1] you all right?
[HOT-2] yea, I'm fine.
[HOT-1] hang onto it. hang onto it.
[CAM] [sound of snap]
[HOT-2] let's go for power please.
[CAM] [sound of loud thump]
[CAM] [sound of loud bang]
[HOT-2] [sound similar to human grunt]
[CAM] [roaring noise steps and increases in amplitude]
[HOT-2] help!
[CAM] [sound similar to single EGAM chime]
[CAM] [sound similar to single EGAM chime]

Figure 18b.

American Airlines Flight 587 - Longitudinal and Lateral Flight Controls

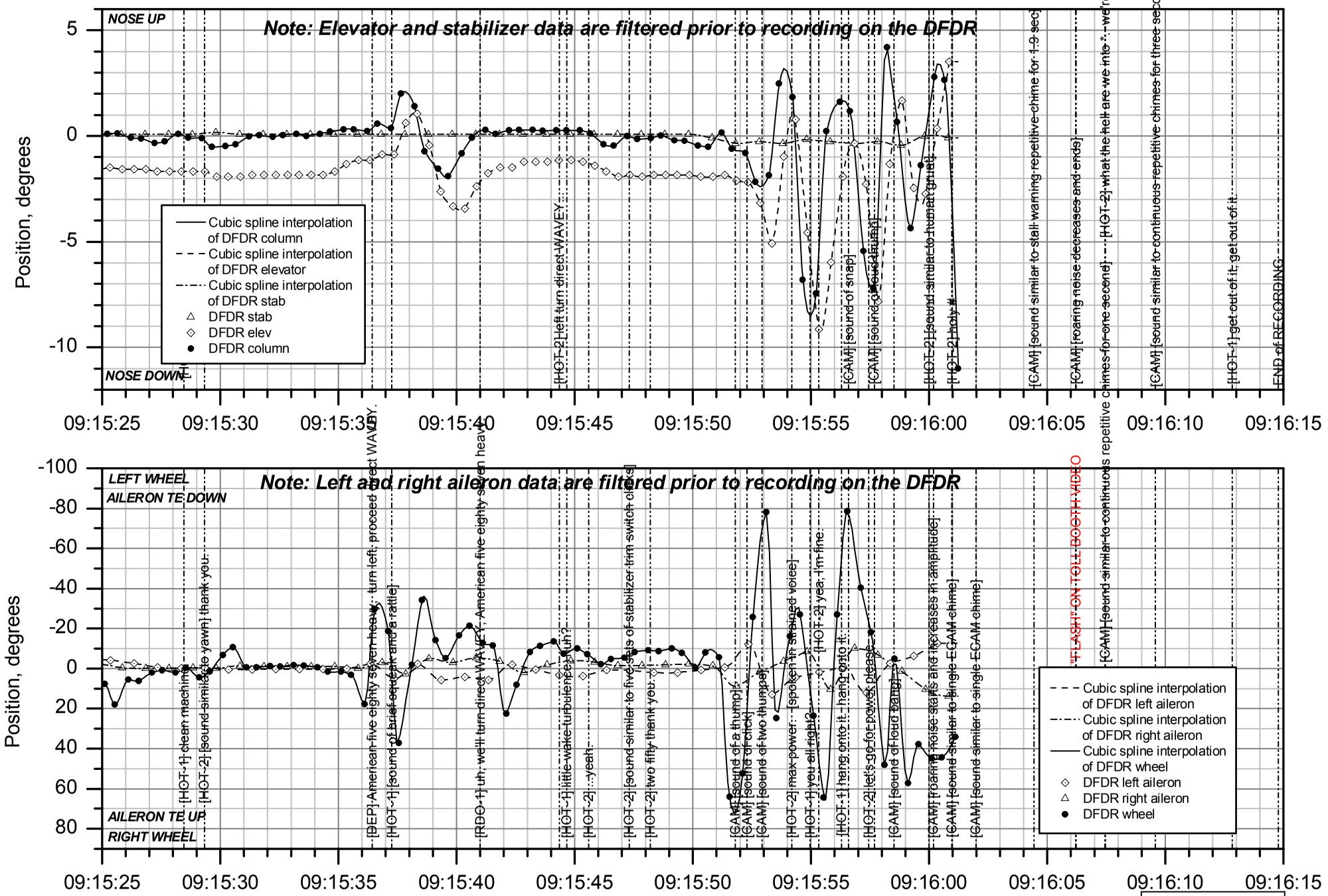

Figure 19a.

American Airlines Flight 587 - Longitudinal and Lateral Flight Controls (detail)

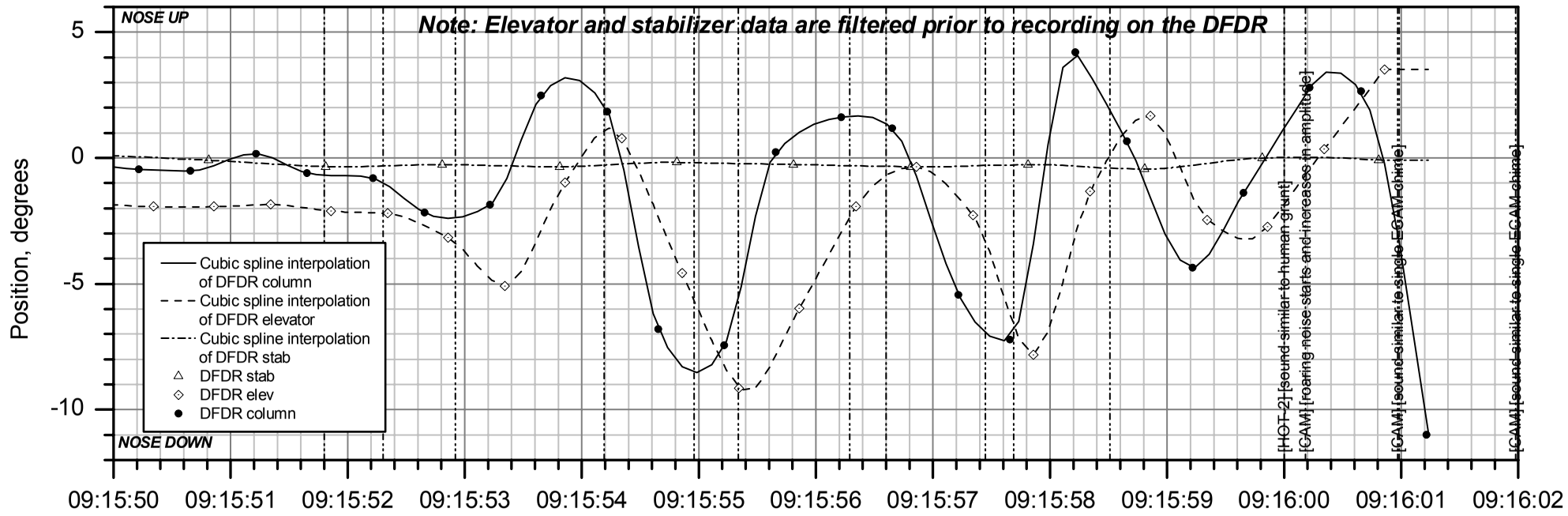

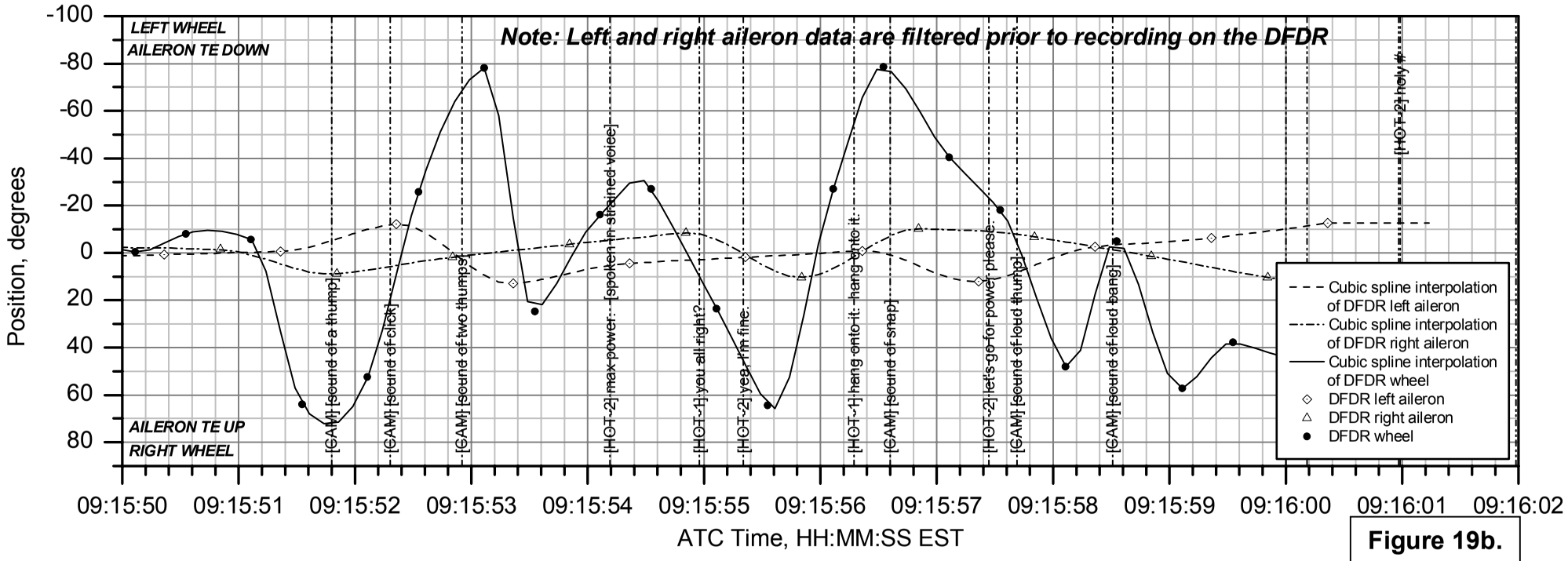

Figure 19b.

American Airlines Flight 587 - Pedal and Rudder

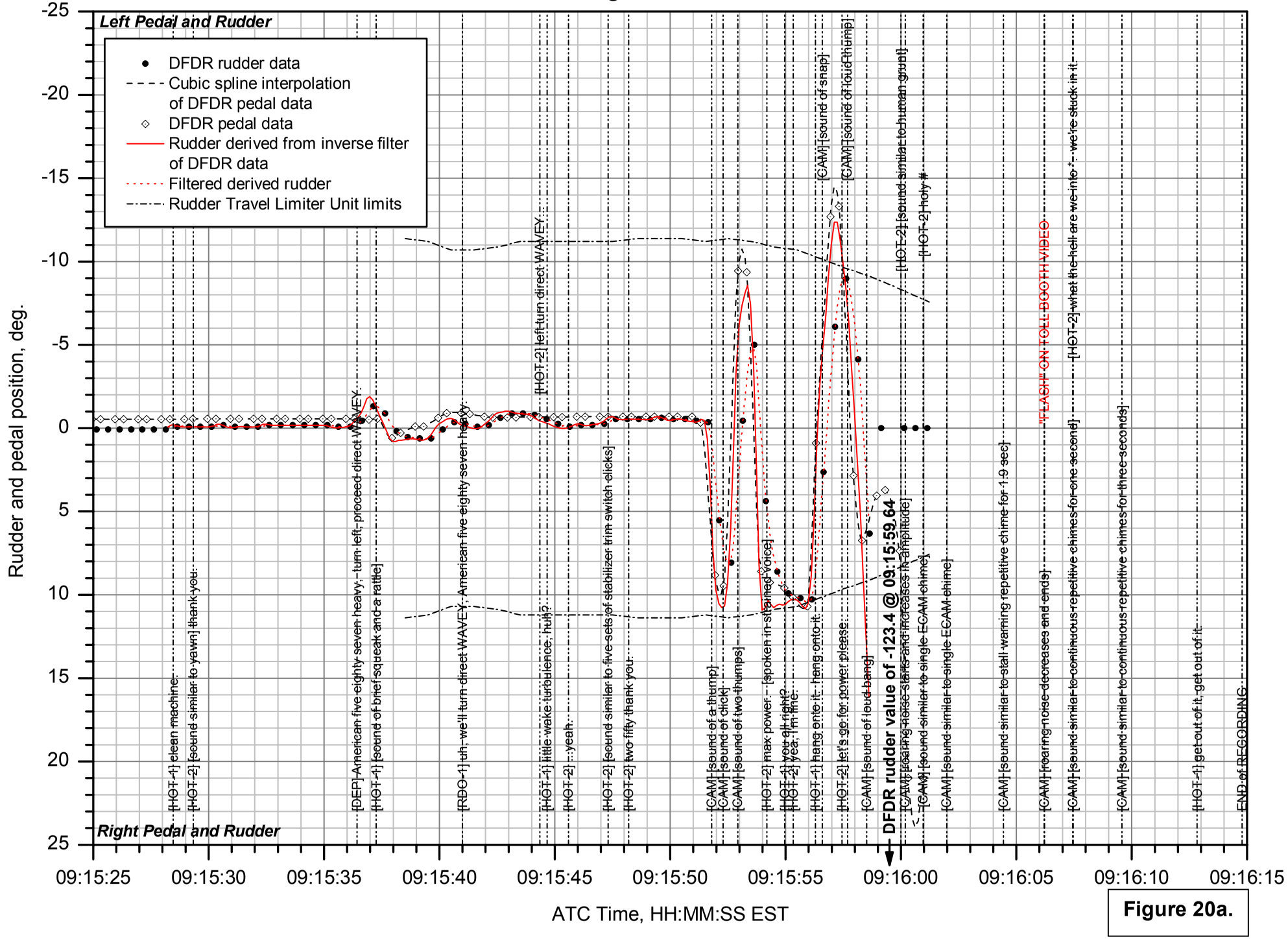

Figure 20a.

American Airlines Flight 587 - Pedal and Rudder (detail)

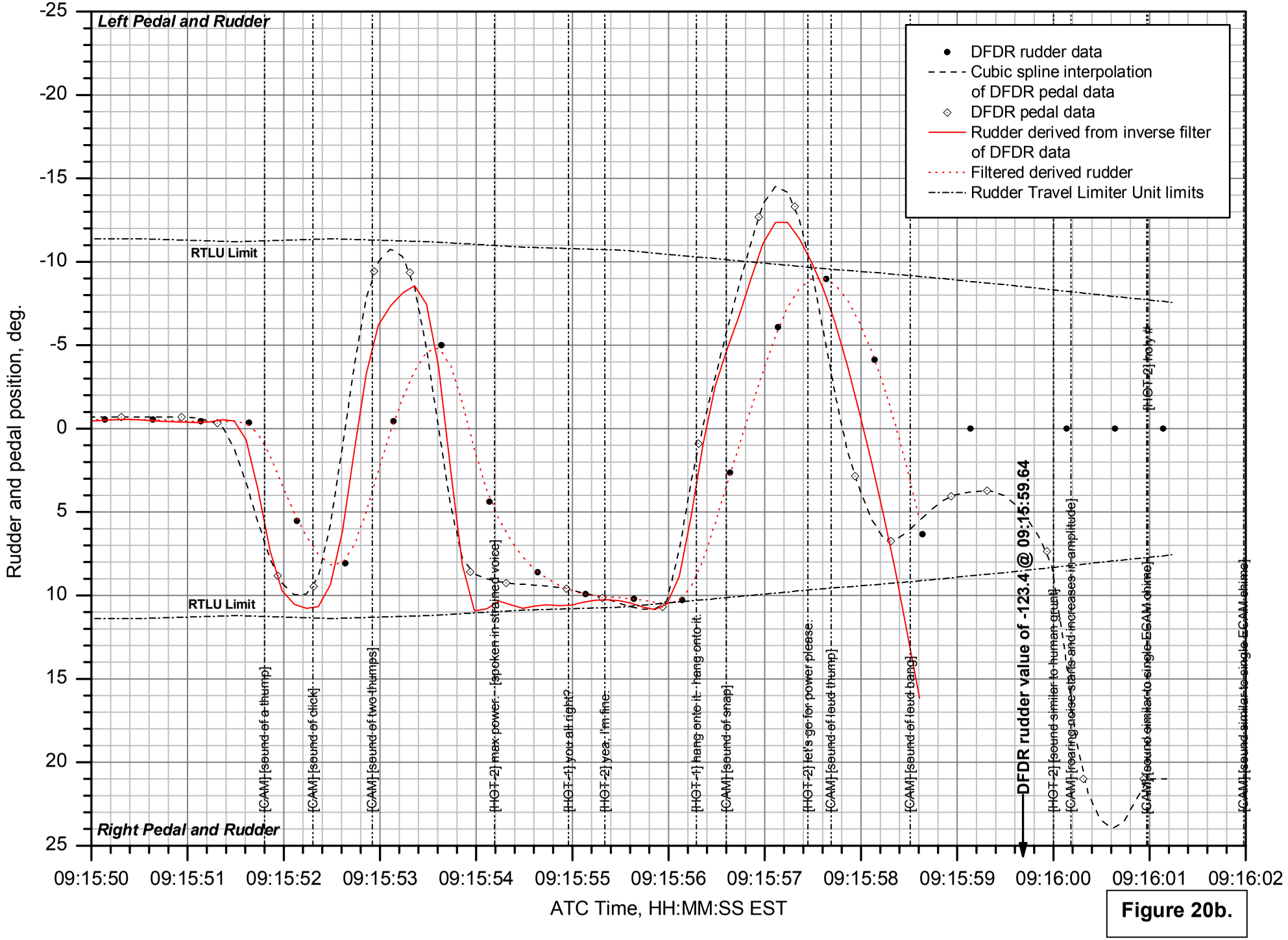

Figure 20b.

AAL587 Calculated Control Forces

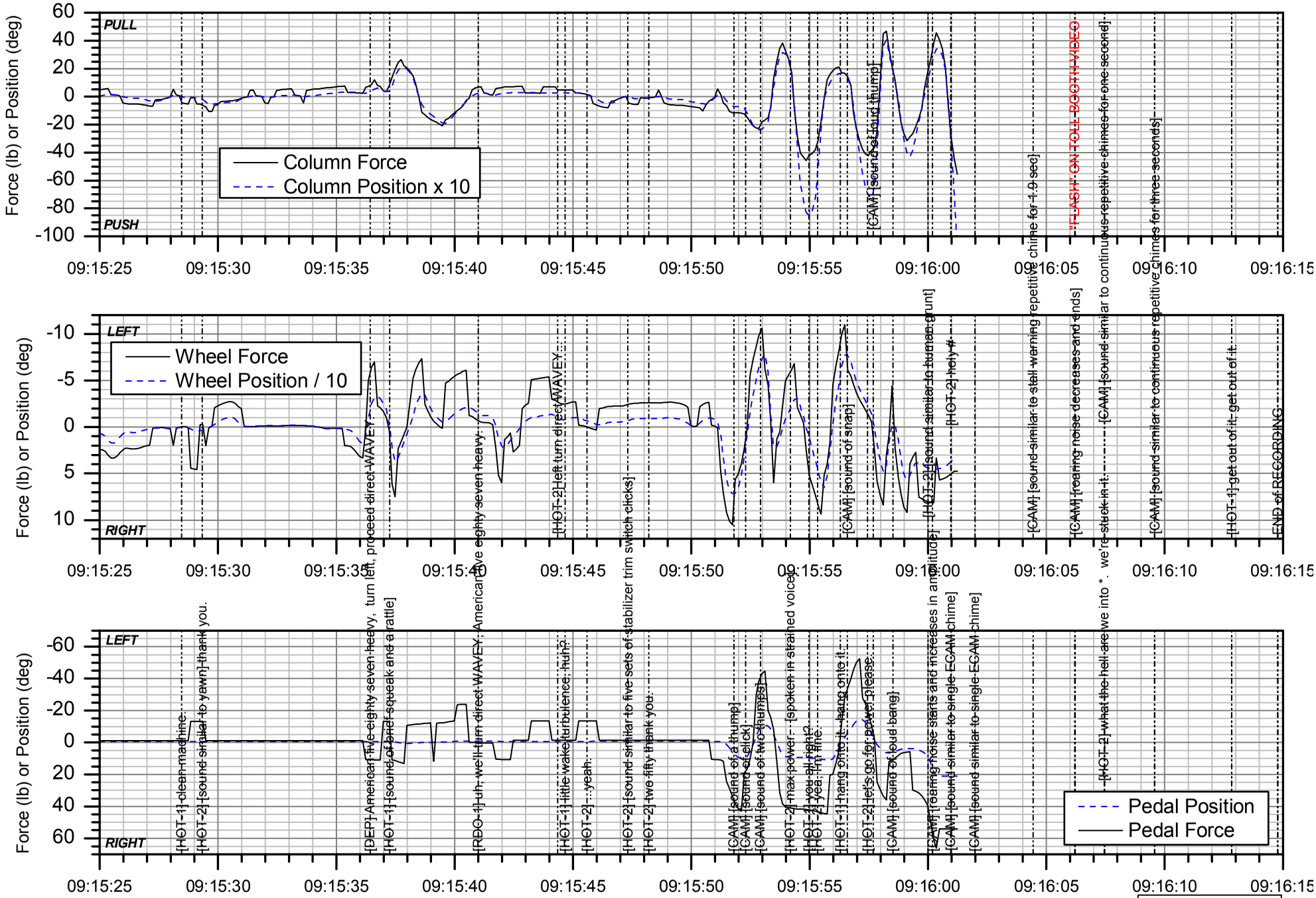

Figure 21a.

AAL587 Calculated Control Forces (detail)

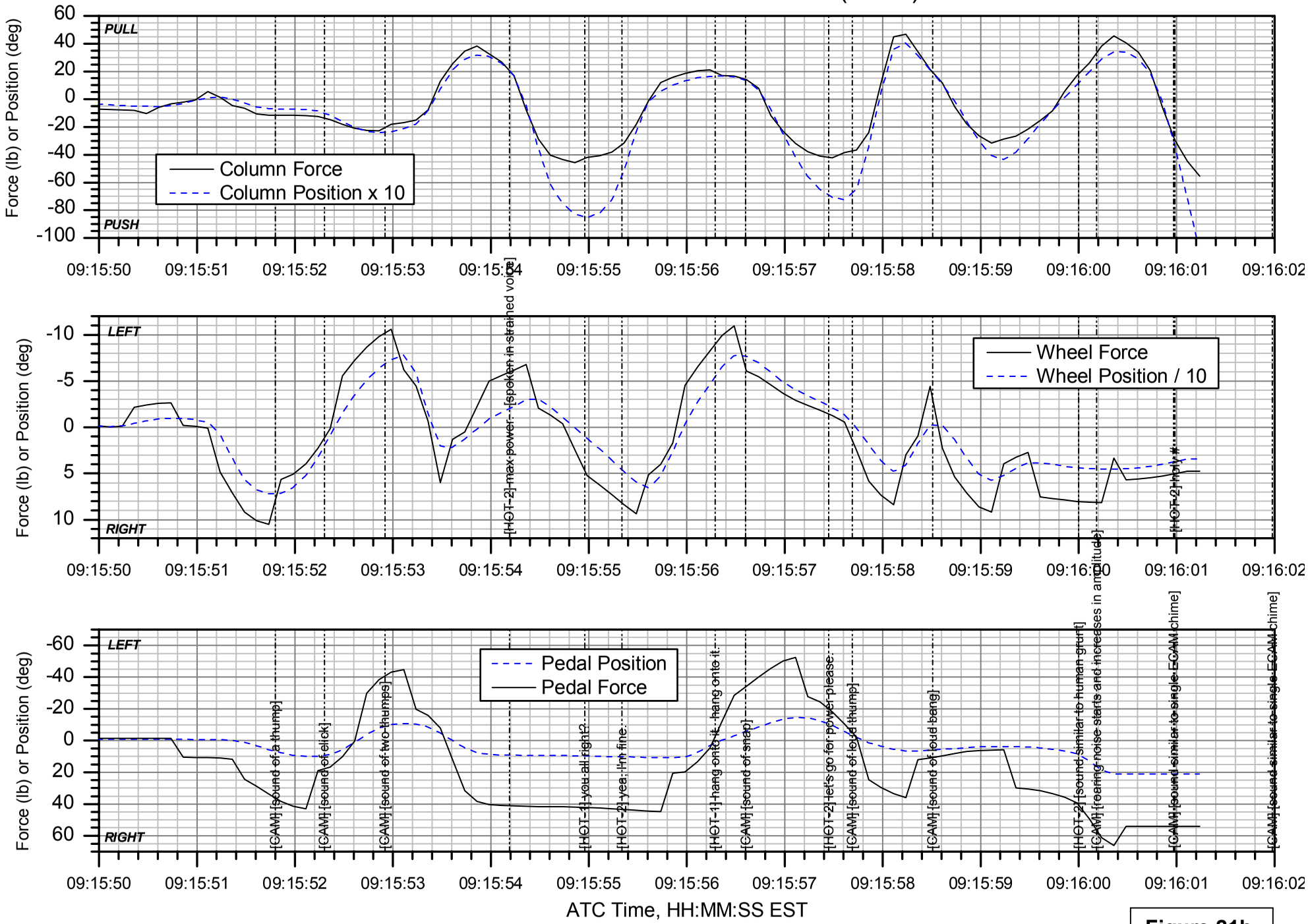

Figure 21b.

American Airlines Flight 587 - Engine Power

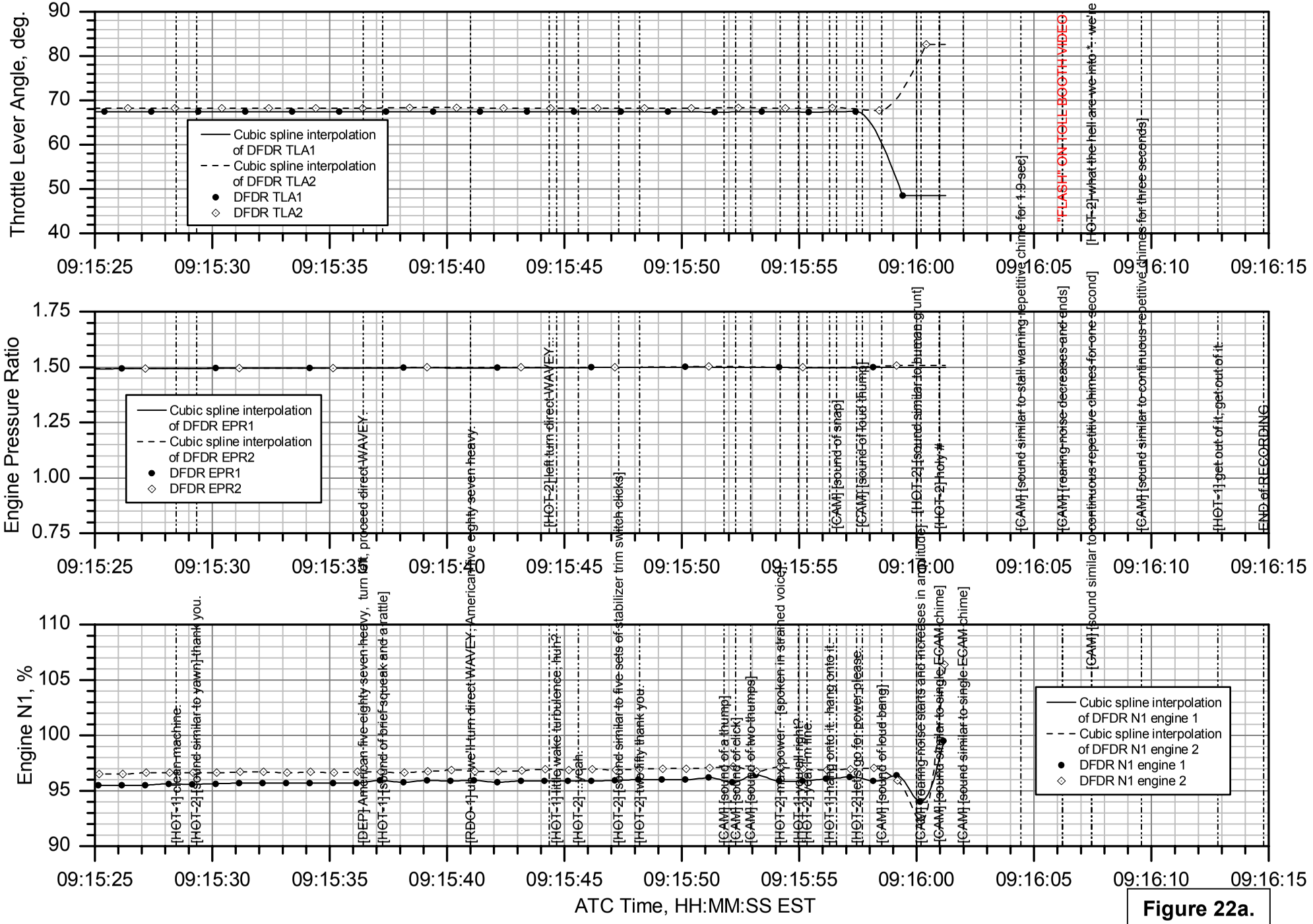

Figure 22a.

American Airlines Flight 587 - Engine Power (detail)

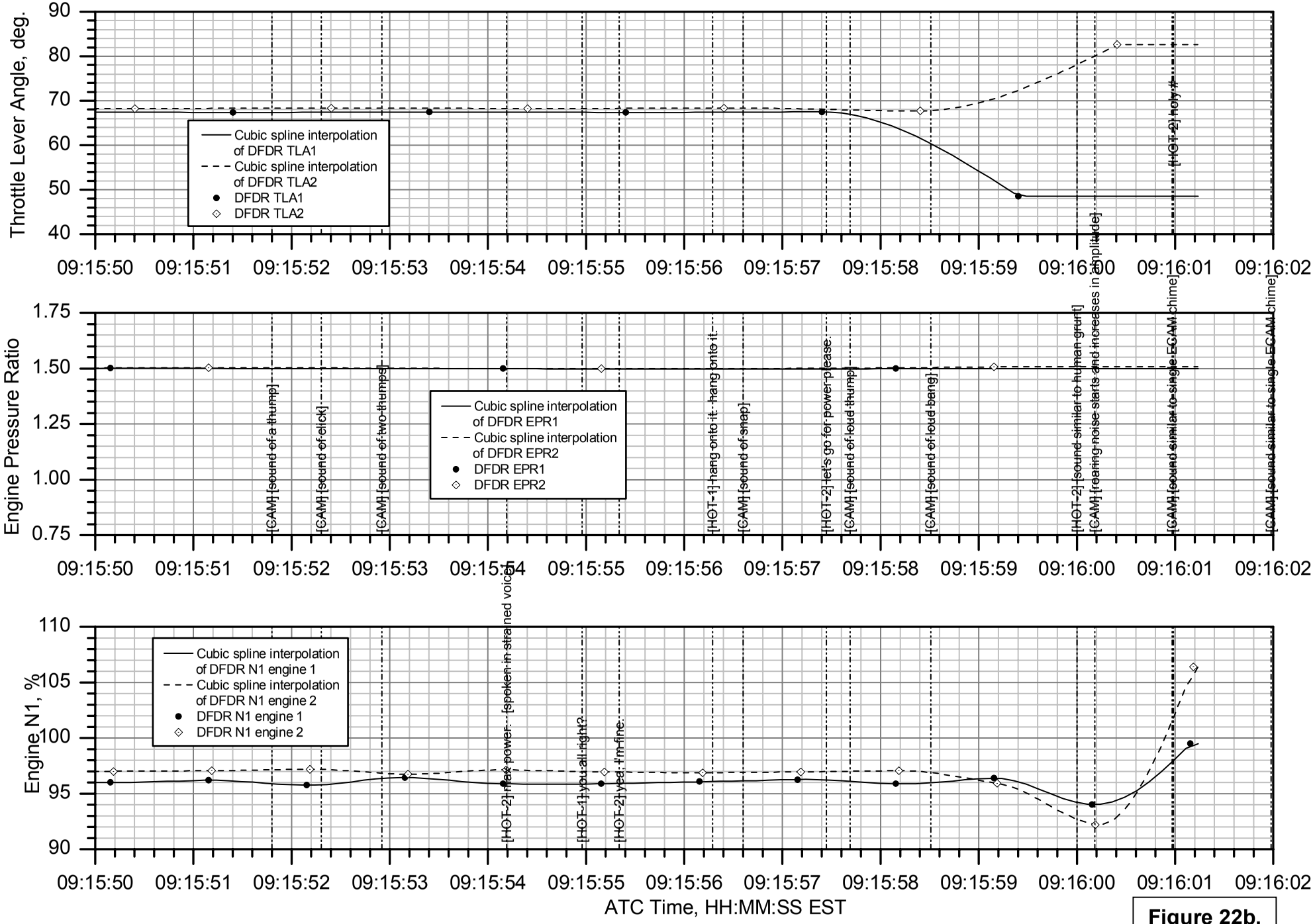

Figure 22b.

American Airlines Flight 587 - Atmosphere

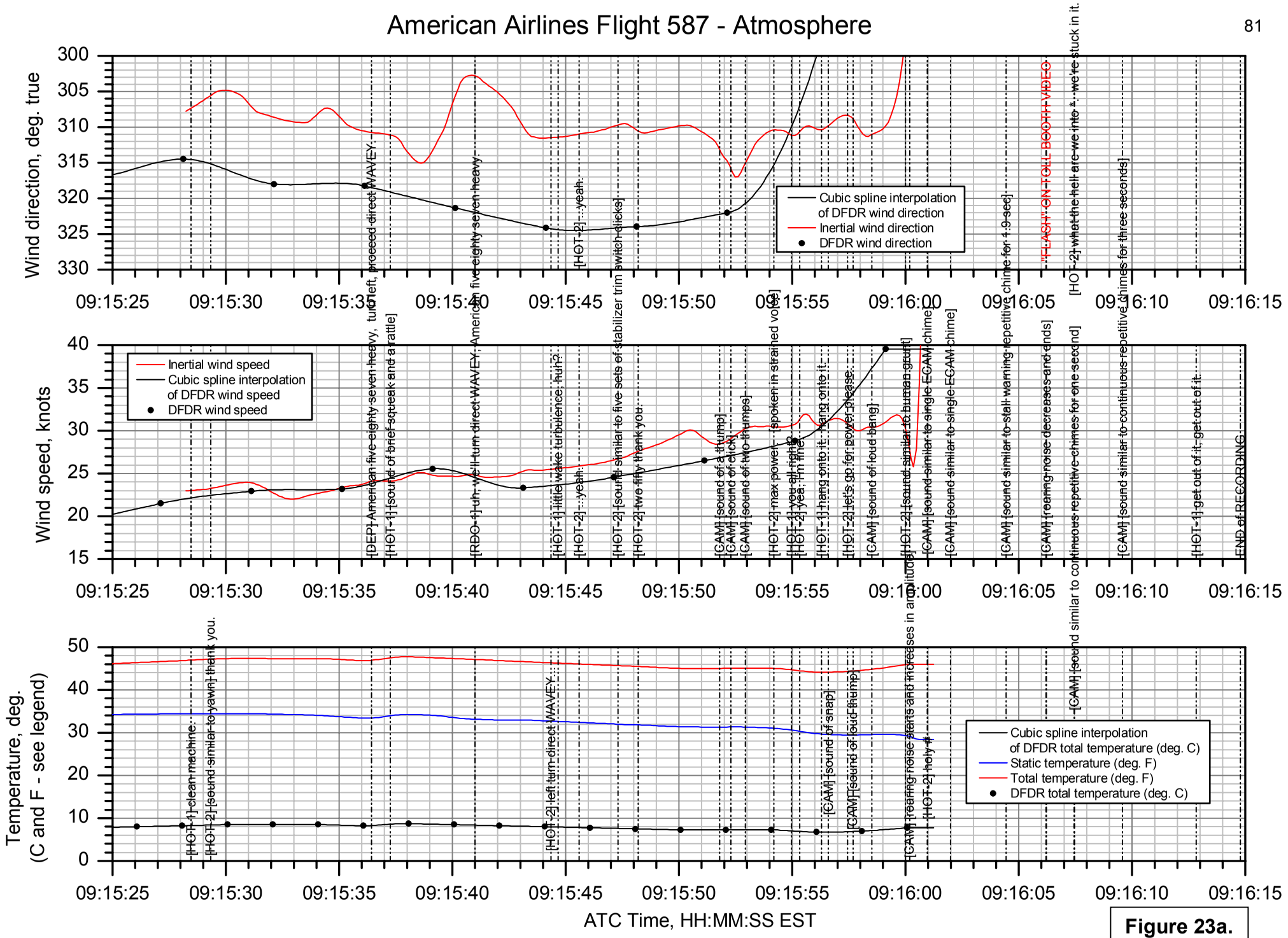

Figure 23a.

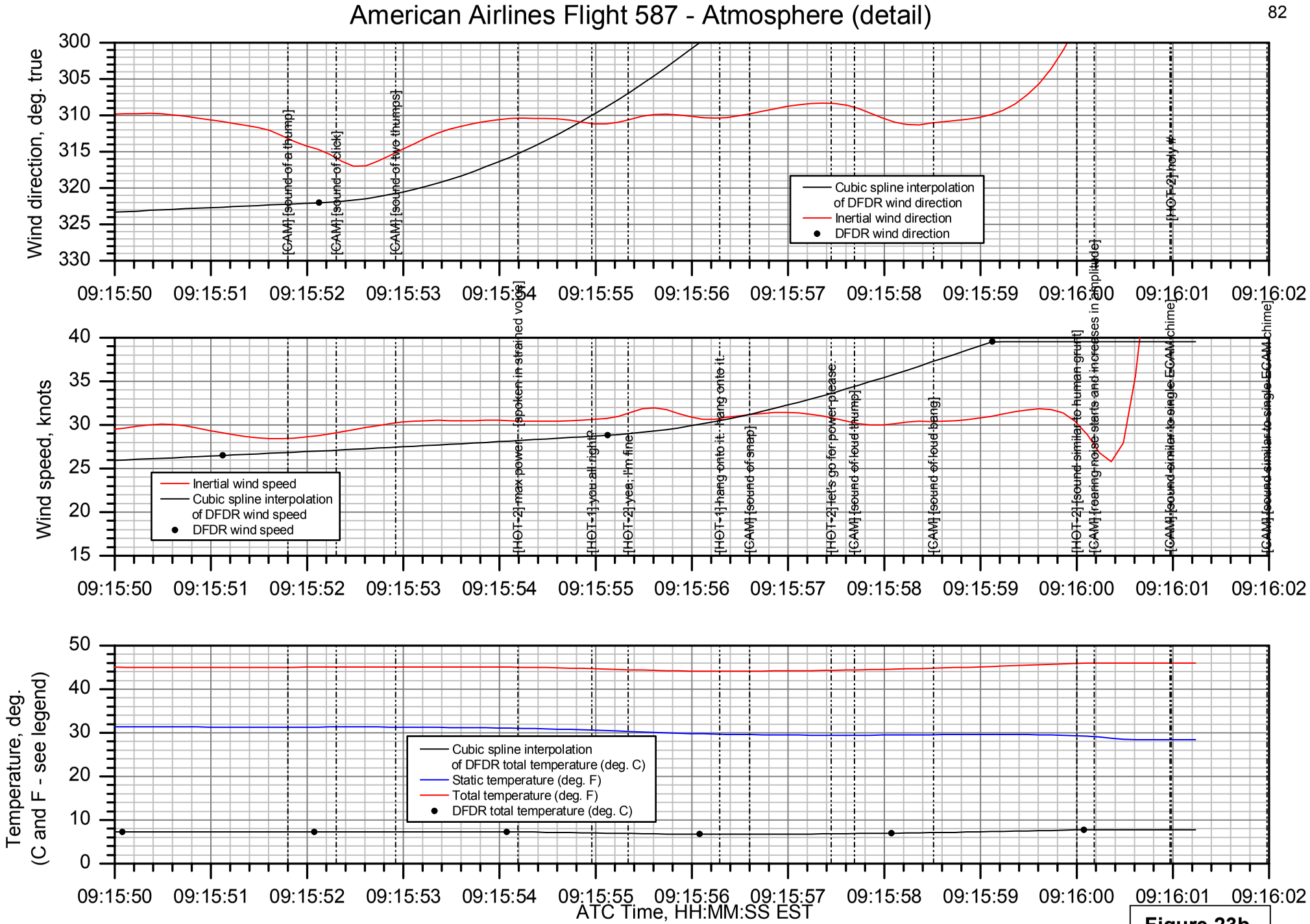
American Airlines Flight 587 - Atmosphere (detail)
Wind direction, deg. true
Cubic spline interpolation of DFDR wind direction
Inertial wind direction
DFDR wind direction
[CAM] [sound of a thump]
[CAM] [sound of click]
[CAM] [sound of five thumps]
[HOT-2] holy #
Wind speed, knots
Inertial wind speed
Cubic spline interpolation of DFDR wind speed
DFDR wind speed
[HOT-2] max power! [spoken in strained voice]
[HOT-1] you all right?
[HOT-2] yea, I'm fine
[HOT-1] hang onto it. hang onto it.
[CAM] [sound of snap]
[HOT-2] let's go for power please.
[CAM] [sound of loud thump]
[CAM] [sound of loud bang]
[HOT-2] [sound similar to human grunt]
[CAM] [roaring noise starts and increases in amplitude]
[CAM] [sound similar to single EGAM chime]
[CAM] [sound similar to single EGAM chime]
Temperature, deg. (C and F - see legend)
Cubic spline interpolation of DFDR total temperature (deg. C)
Static temperature (deg. F)
Total temperature (deg. F)
DFDR total temperature (deg. C)
09:15:50
09:15:51
09:15:52
09:15:53
09:15:54
09:15:55
09:15:56
09:15:57
09:15:58
09:15:59
09:16:00
09:16:01
09:16:02
ATC Time, HH:MM:SS EST

Figure 23b.

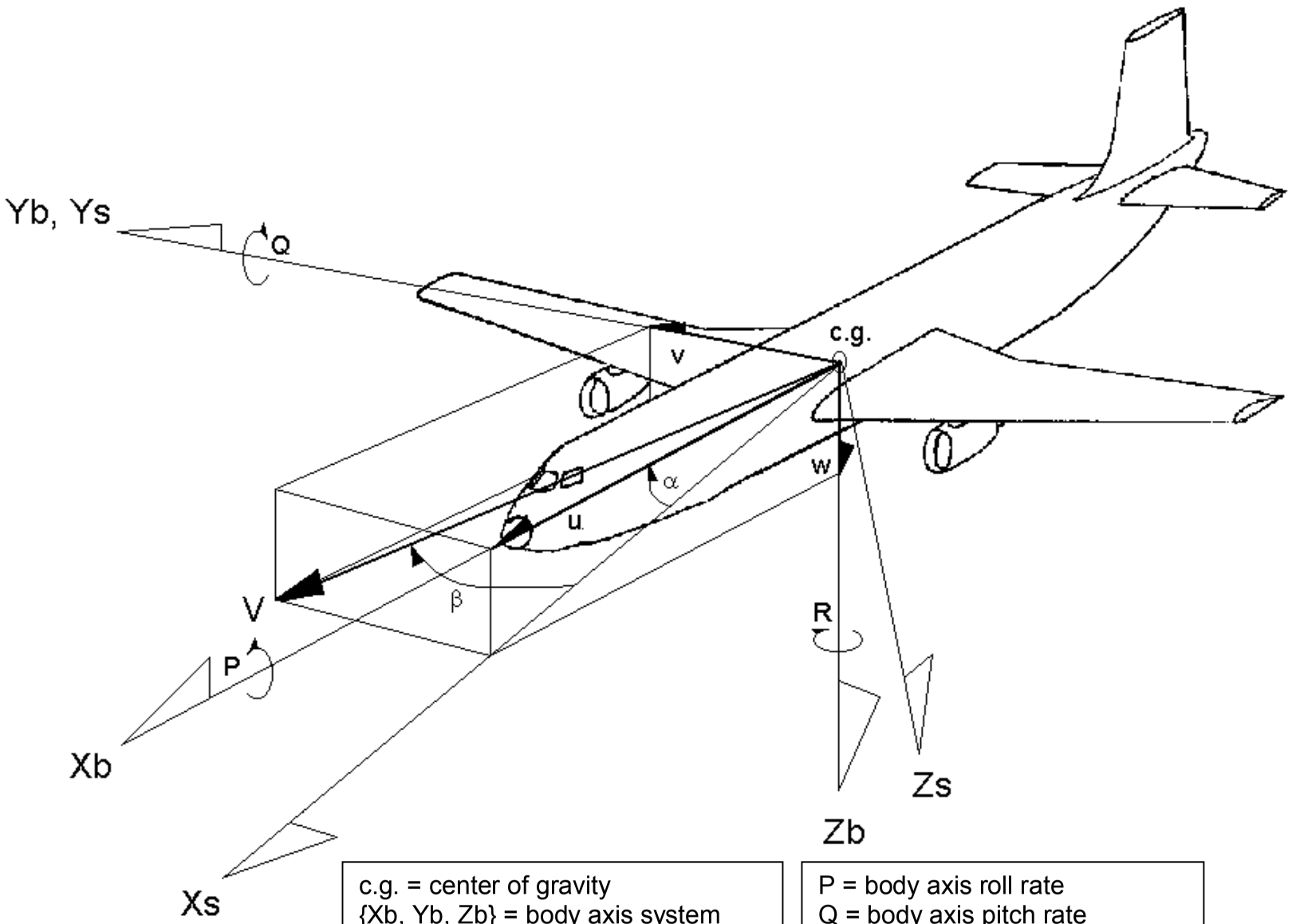

c.g. = center of gravity
{Xb, Yb, Zb} = body axis system
{Xs, Ys, Zs} = stability axis system
V = airplane velocity vector
α = angle of attack
β = sideslip angle

P = body axis roll rate
Q = body axis pitch rate
R = body axis yaw rate
u = component of V along Xb
v = component of V along Yb
w = component of V along Zb

Figure 24a.

Relationship Between Airspeed, Wind Speed, & Ground Speed

$$\vec{V}_{GROUND} = \vec{V}_{AIR} + \vec{V}_{WIND}$$

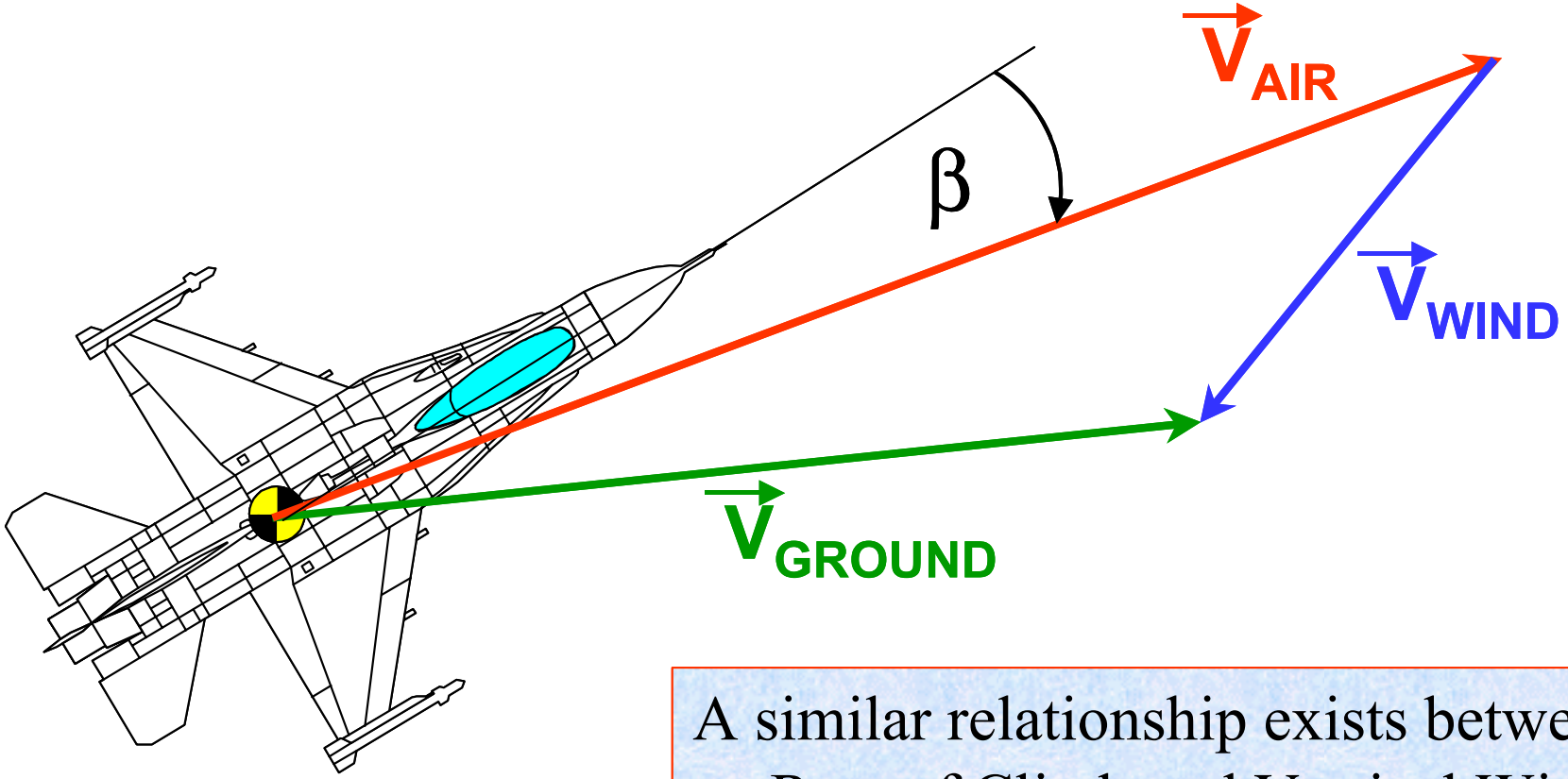

A similar relationship exists between γ, Rate of Climb and Vertical Wind

γ = Flight path angle relative to air

Figure 24b.

Effect of First Order Lag Filter on a Step Input

$$\text{Lag Transfer Function} = \frac{1}{1 + (Tc)s}$$

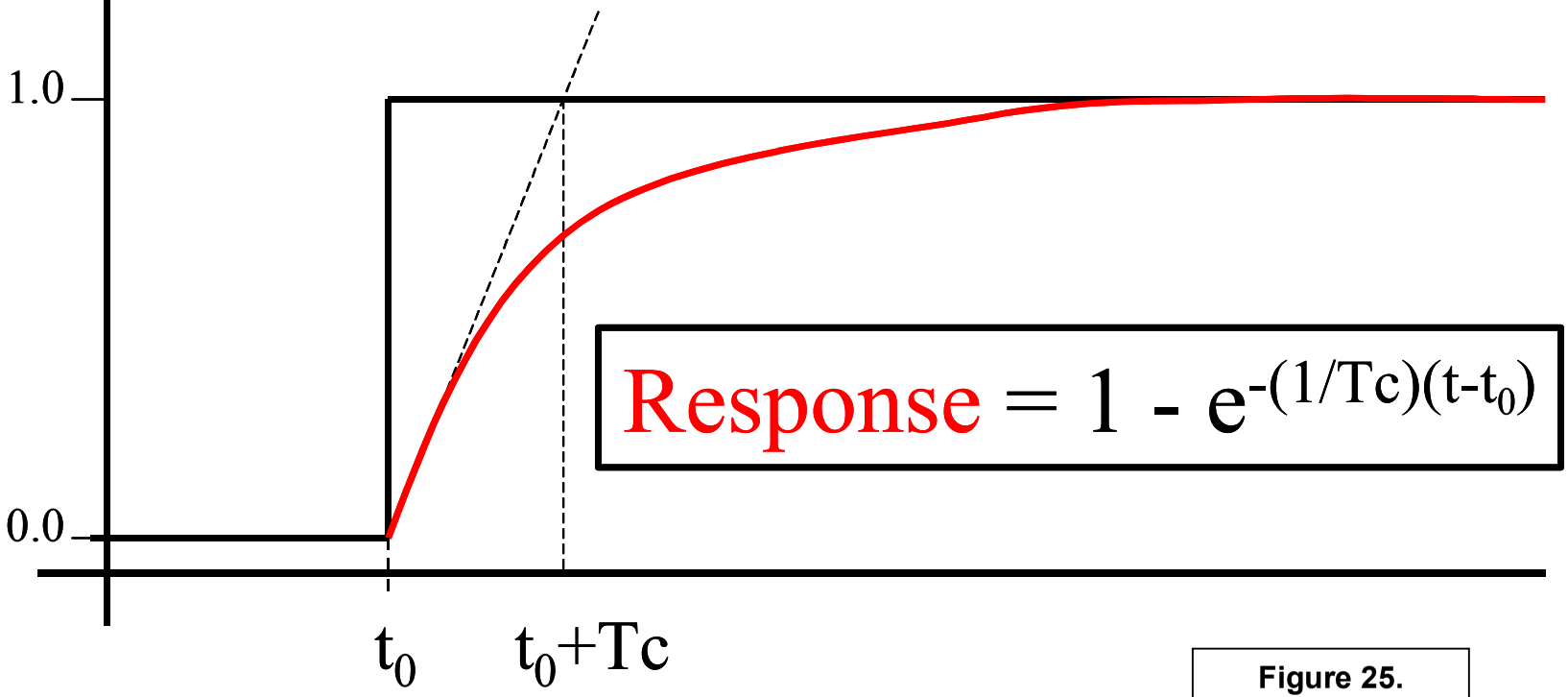

Figure 25.

Typical Baseline Simulation Logic/Data Flow.

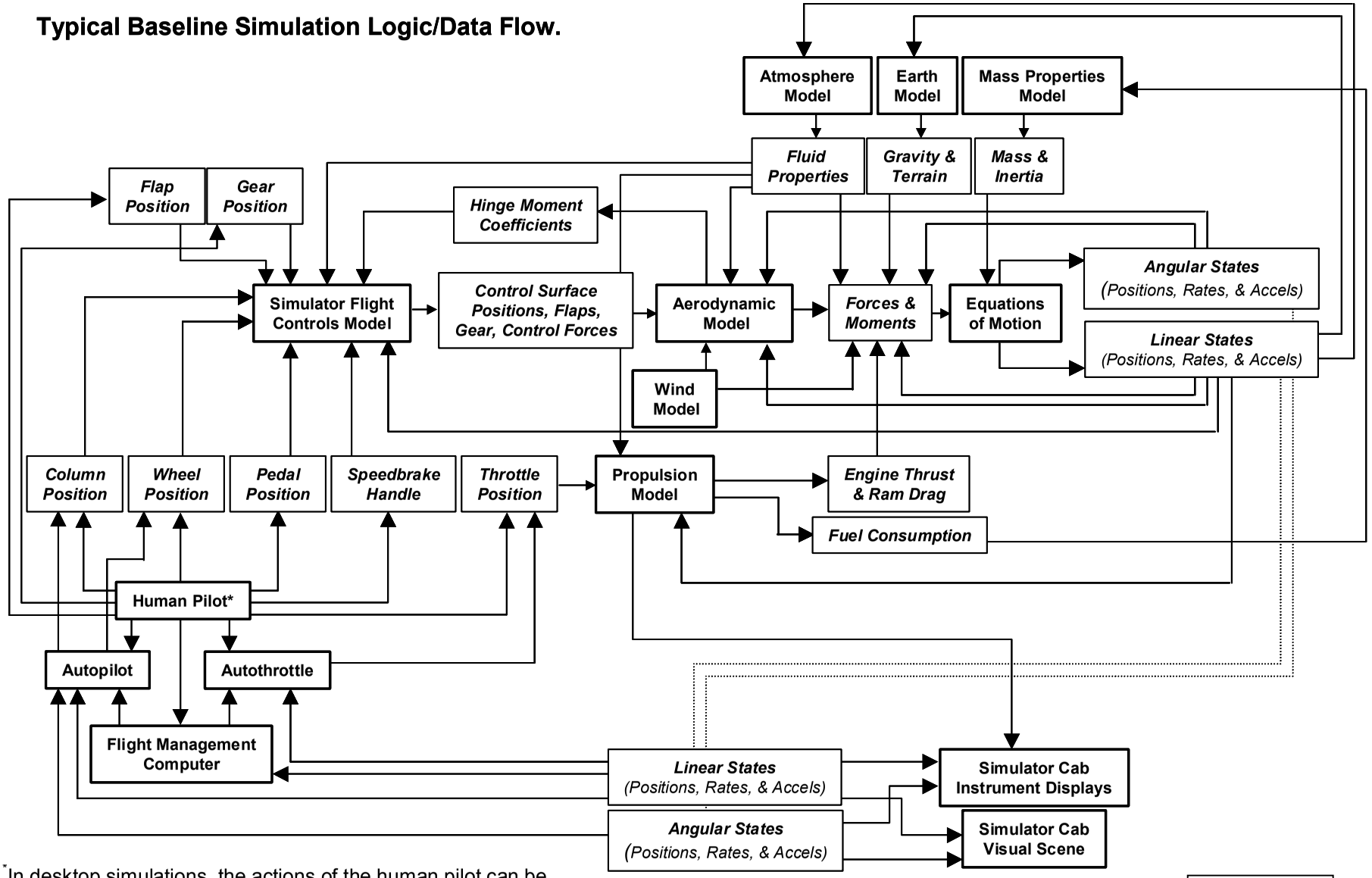

*In desktop simulations, the actions of the human pilot can be replaced by computer-based instructions.

Figure 26.

Airbus Simulation #11: Longitudinal Control Data

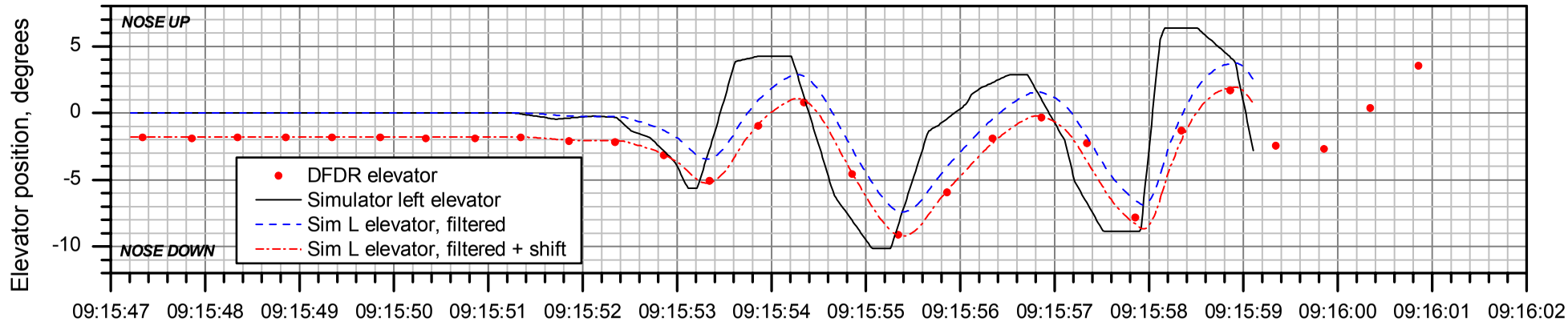

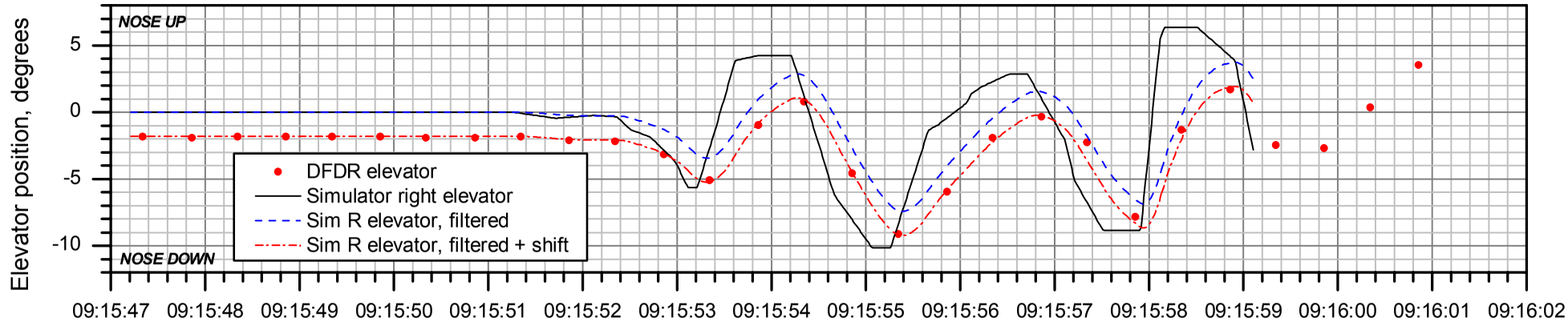

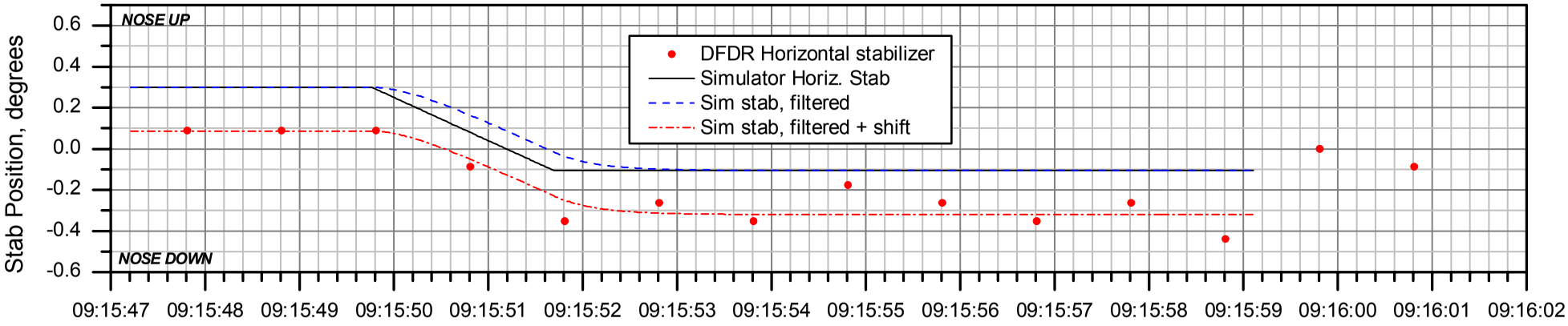

Figure 27.

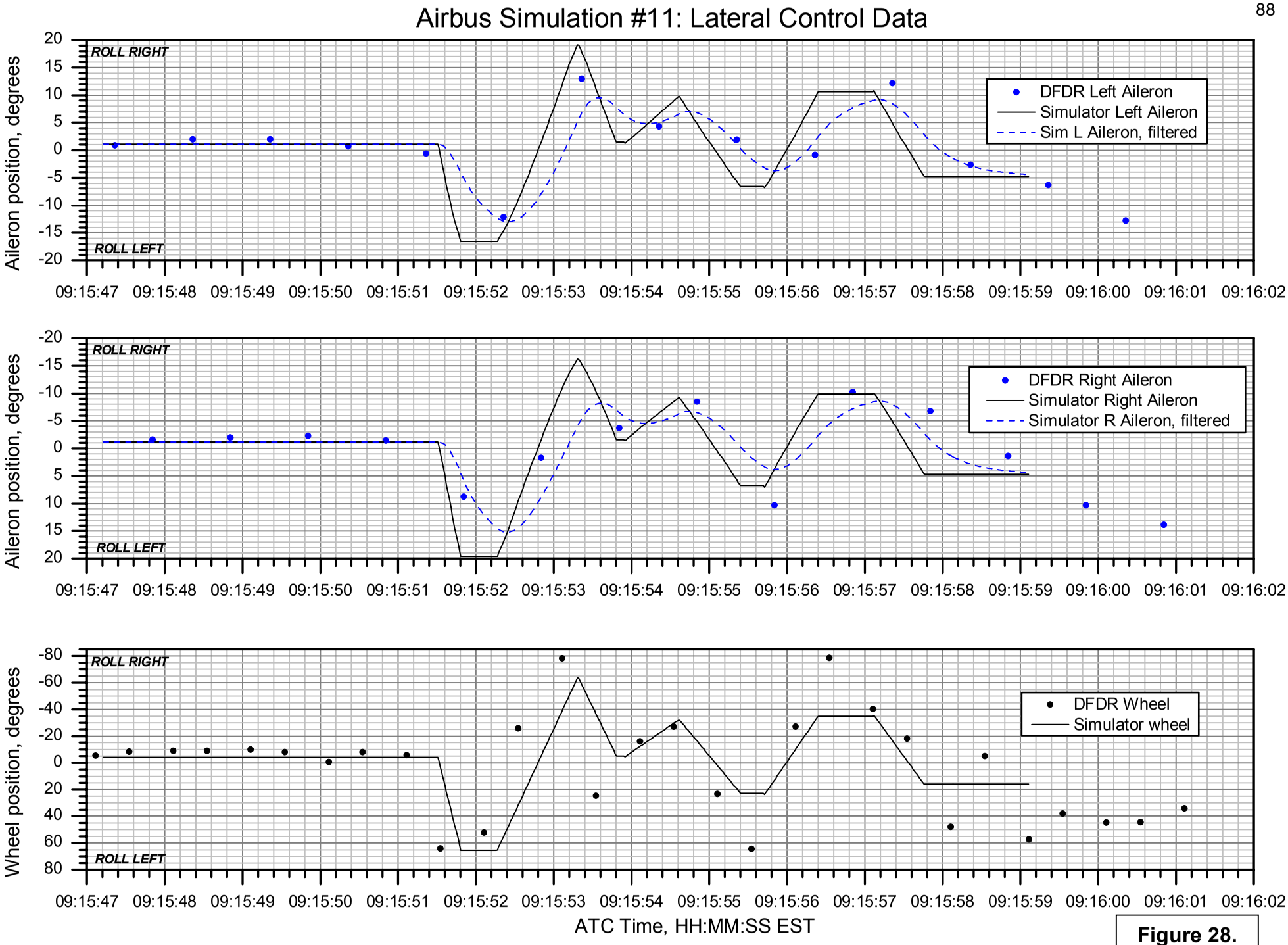
Airbus Simulation #11: Lateral Control Data
Aileron position, degrees
ROLL RIGHT
ROLL LEFT
DFDR Left Aileron
Simulator Left Aileron
Sim L Aileron, filtered
DFDR Right Aileron
Simulator Right Aileron
Simulator R Aileron, filtered
Wheel position, degrees
DFDR Wheel
Simulator wheel
09:15:47 09:15:48 09:15:49 09:15:50 09:15:51 09:15:52 09:15:53 09:15:54 09:15:55 09:15:56 09:15:57 09:15:58 09:15:59 09:16:00 09:16:01 09:16:02
ATC Time, HH:MM:SS EST

Figure 28.

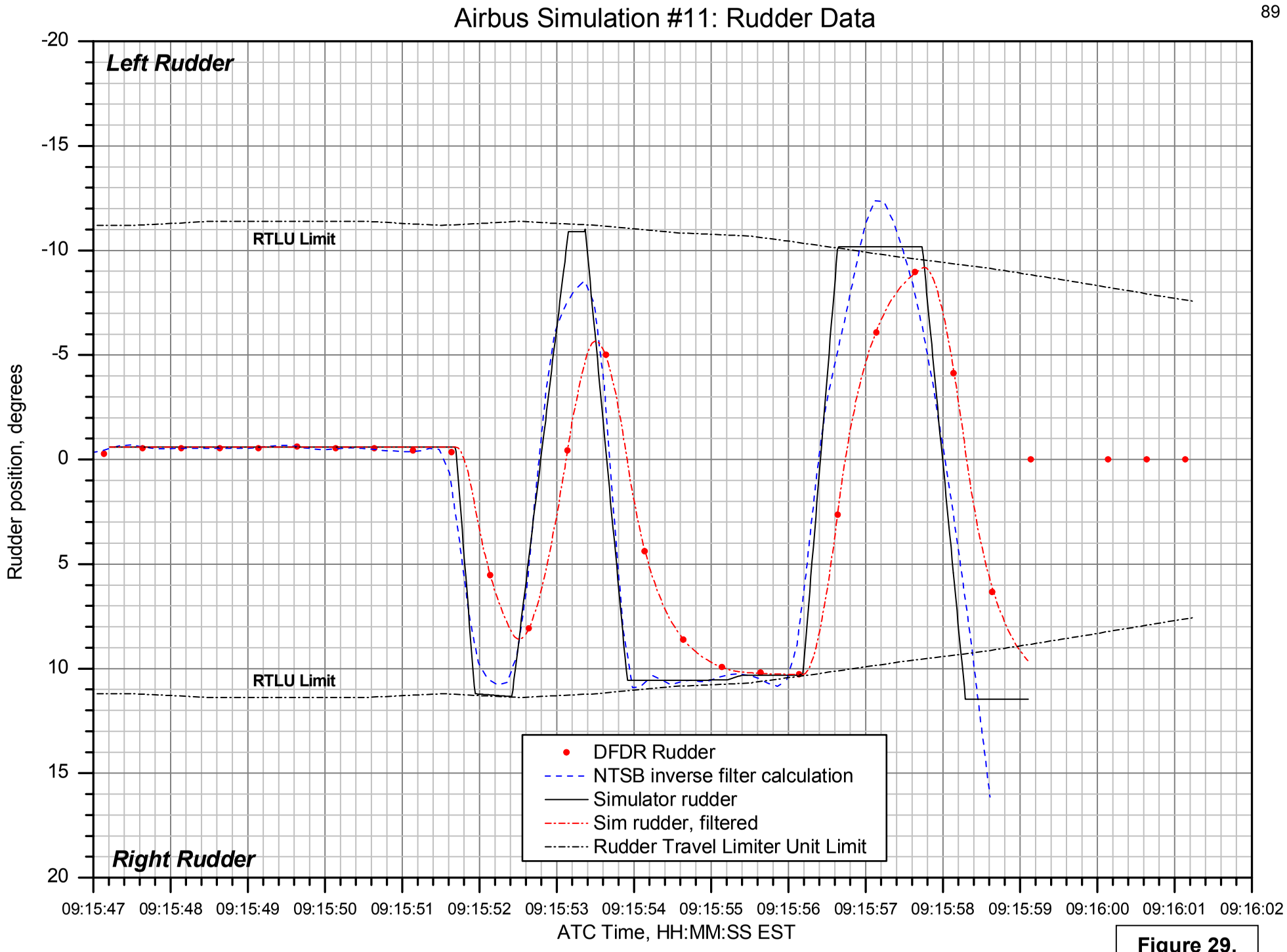
Airbus Simulation #11: Rudder Data
Left Rudder
Right Rudder
RTLU Limit
RTLU Limit
DFDR Rudder
NTSB inverse filter calculation
Simulator rudder
Sim rudder, filtered
Rudder Travel Limiter Unit Limit
Rudder position, degrees
-20
-15
-10
-5
0
5
10
15
20
09:15:47
09:15:48
09:15:49
09:15:50
09:15:51
09:15:52
09:15:53
09:15:54
09:15:55
09:15:56
09:15:57
09:15:58
09:15:59
09:16:00
09:16:01
09:16:02
ATC Time, HH:MM:SS EST

Figure 29.

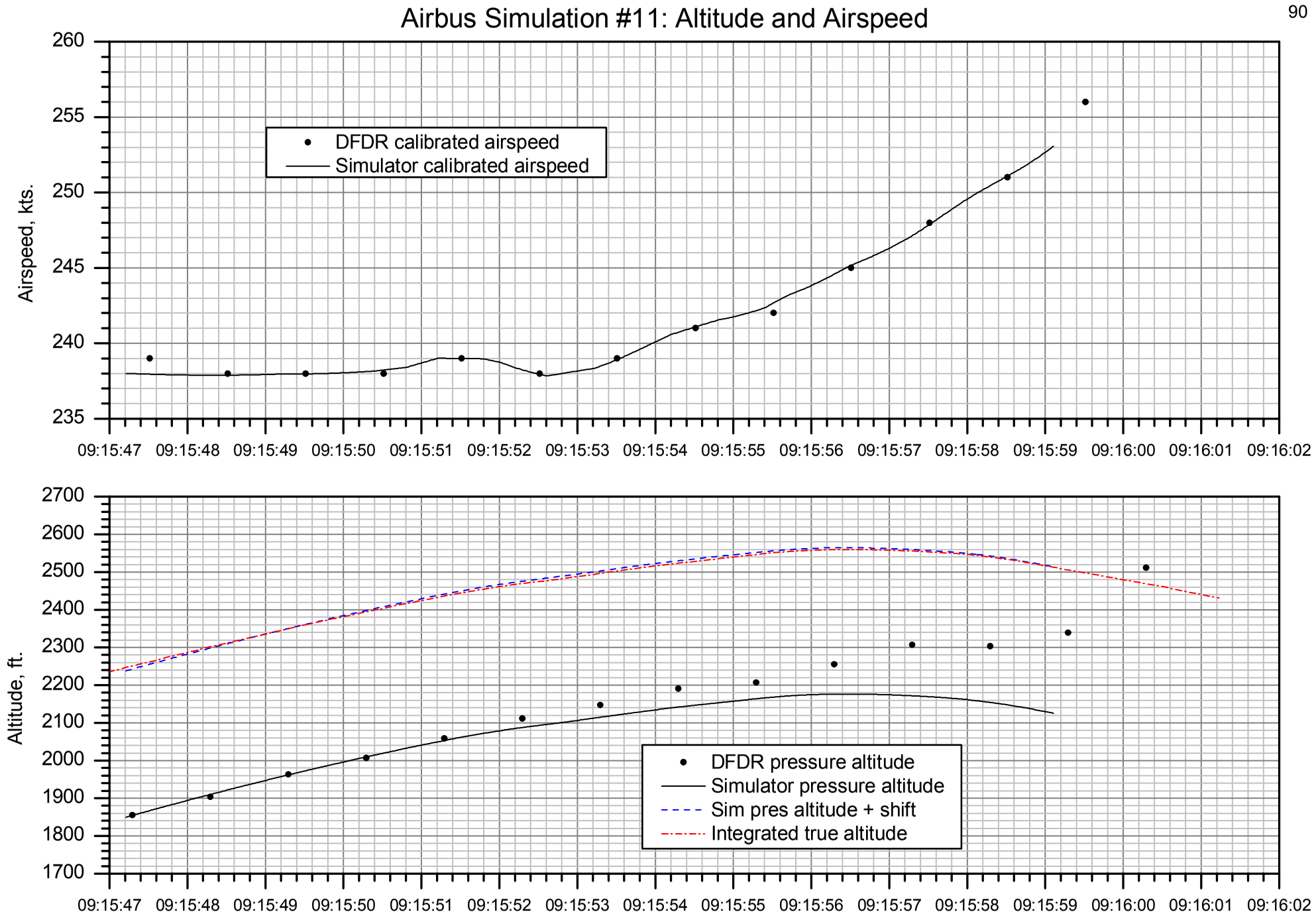
Airbus Simulation #11: Altitude and Airspeed
Airspeed, kts.
260
255
250
245
240
235
DFDR calibrated airspeed
Simulator calibrated airspeed
09:15:47
09:15:48
09:15:49
09:15:50
09:15:51
09:15:52
09:15:53
09:15:54
09:15:55
09:15:56
09:15:57
09:15:58
09:15:59
09:16:00
09:16:01
09:16:02
Altitude, ft.
2700
2600
2500
2400
2300
2200
2100
2000
1900
1800
1700
DFDR pressure altitude
Simulator pressure altitude
Sim pres altitude + shift
Integrated true altitude
ATC Time, HH:MM:SS EST

Figure 30.

Airbus Simulation #11: Euler Angles

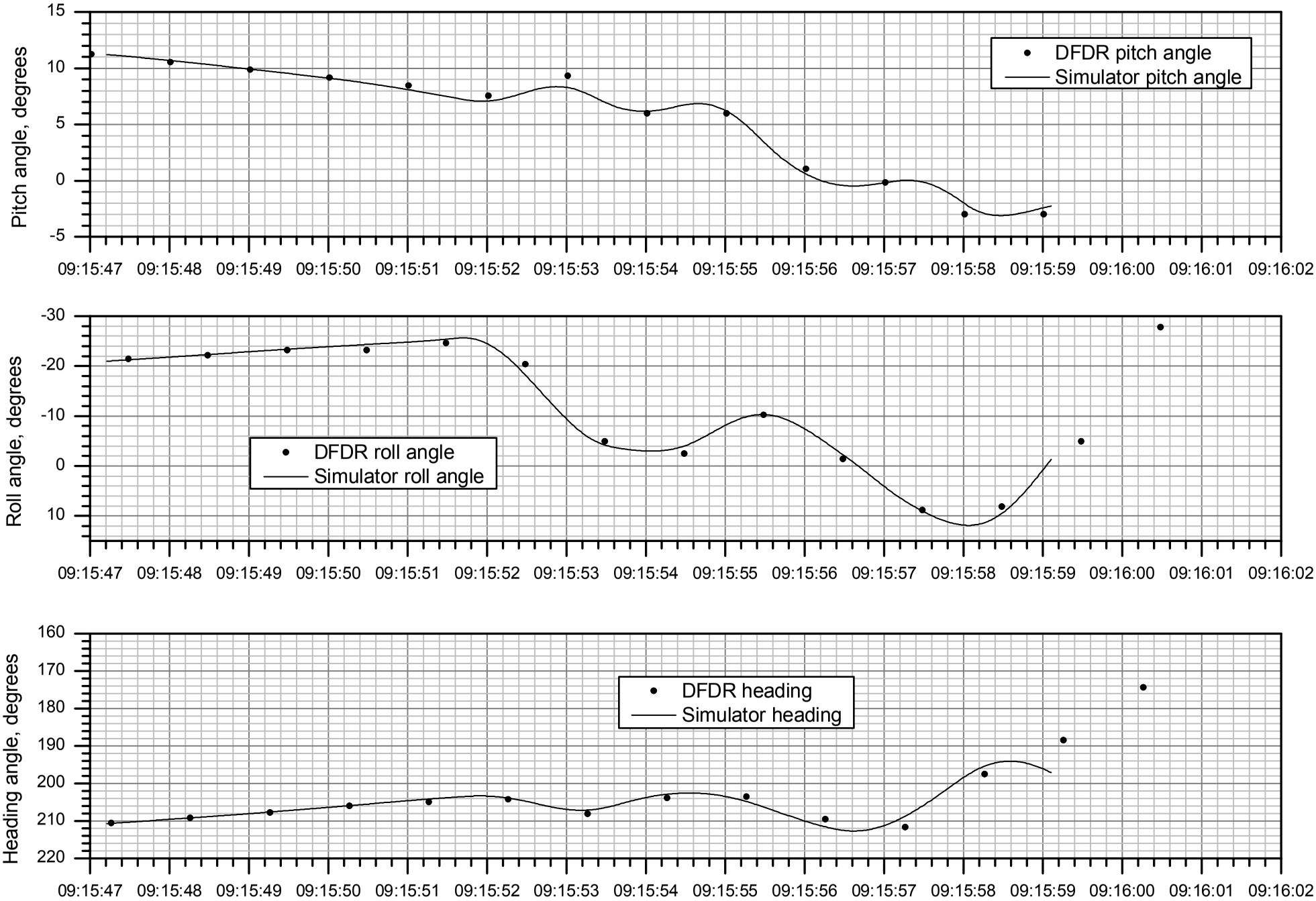

Figure 31.

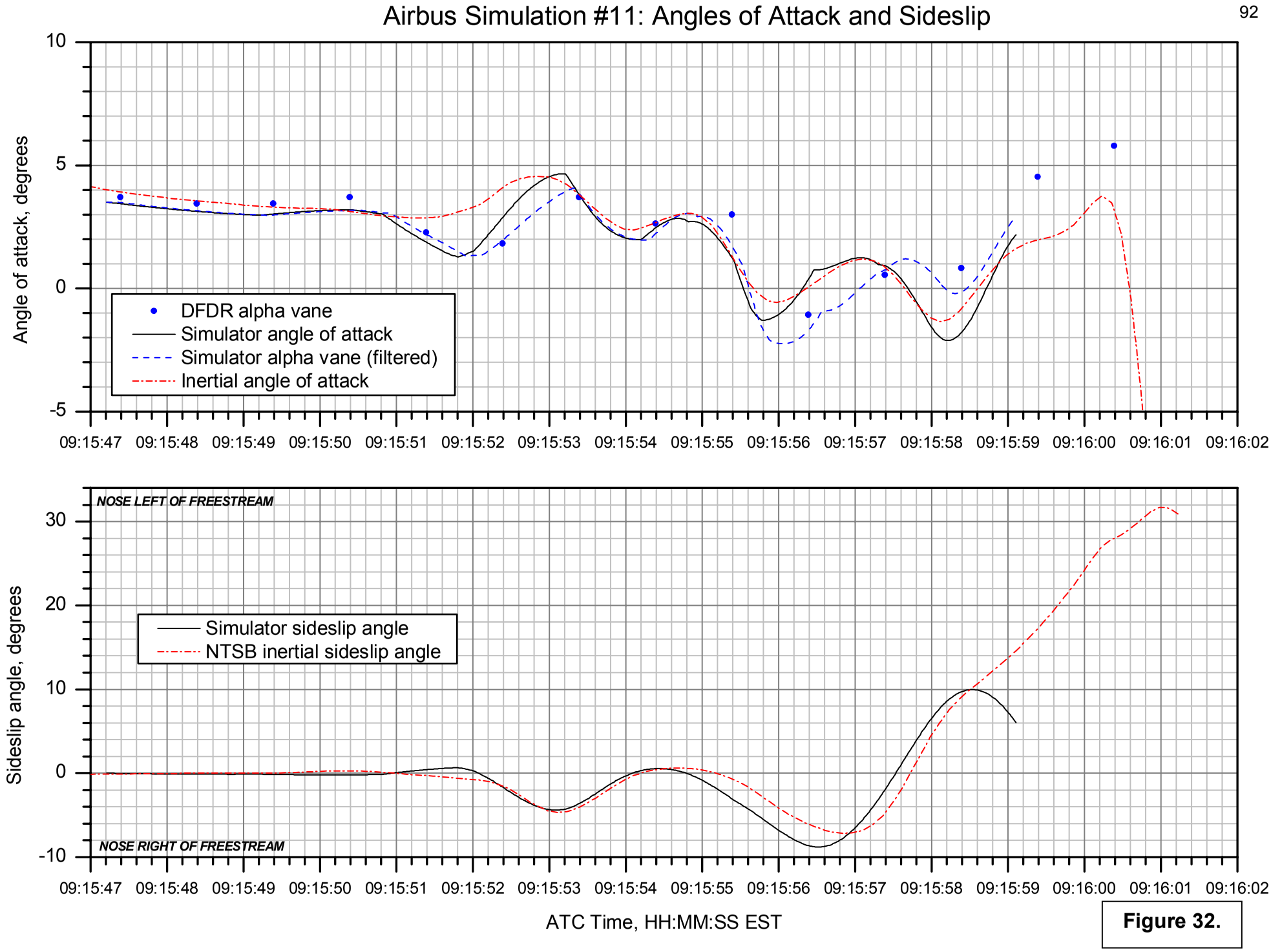
Airbus Simulation #11: Angles of Attack and Sideslip
Angle of attack, degrees
10
5
0
-5
DFDR alpha vane
Simulator angle of attack
Simulator alpha vane (filtered)
Inertial angle of attack
09:15:47
09:15:48
09:15:49
09:15:50
09:15:51
09:15:52
09:15:53
09:15:54
09:15:55
09:15:56
09:15:57
09:15:58
09:15:59
09:16:00
09:16:01
09:16:02
NOSE LEFT OF FREESTREAM
NOSE RIGHT OF FREESTREAM
Sideslip angle, degrees
30
20
10
0
-10
Simulator sideslip angle
NTSB inertial sideslip angle
ATC Time, HH:MM:SS EST

Figure 32.

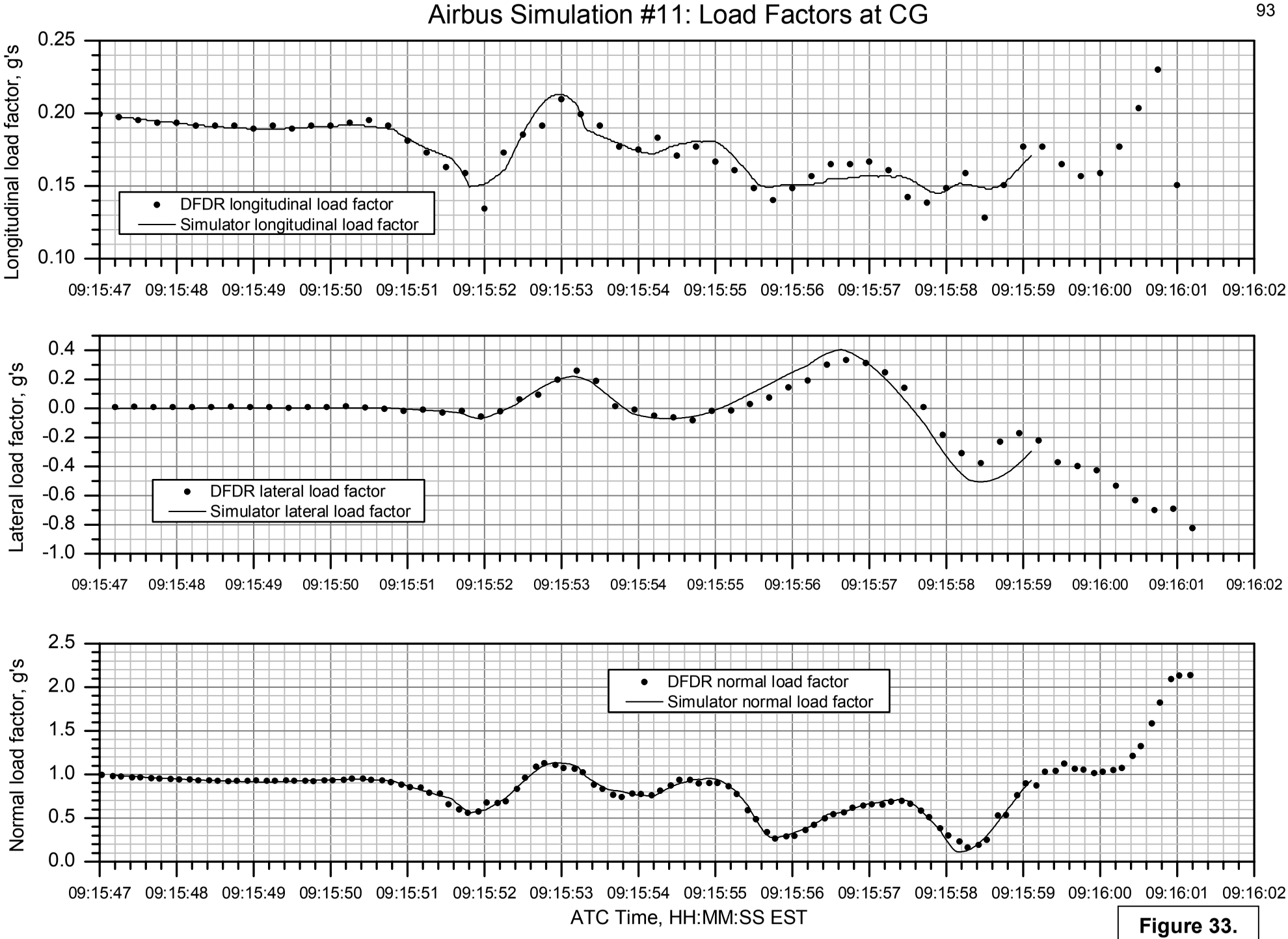
Airbus Simulation #11: Load Factors at CG
Longitudinal load factor, g's
0.25
0.20
0.15
0.10
DFDR longitudinal load factor
Simulator longitudinal load factor
Lateral load factor, g's
0.4
0.2
0.0
-0.2
-0.4
-0.6
-0.8
-1.0
DFDR lateral load factor
Simulator lateral load factor
Normal load factor, g's
2.5
2.0
1.5
1.0
0.5
0.0
DFDR normal load factor
Simulator normal load factor
09:15:47
09:15:48
09:15:49
09:15:50
09:15:51
09:15:52
09:15:53
09:15:54
09:15:55
09:15:56
09:15:57
09:15:58
09:15:59
09:16:00
09:16:01
09:16:02
ATC Time, HH:MM:SS EST

Figure 33.

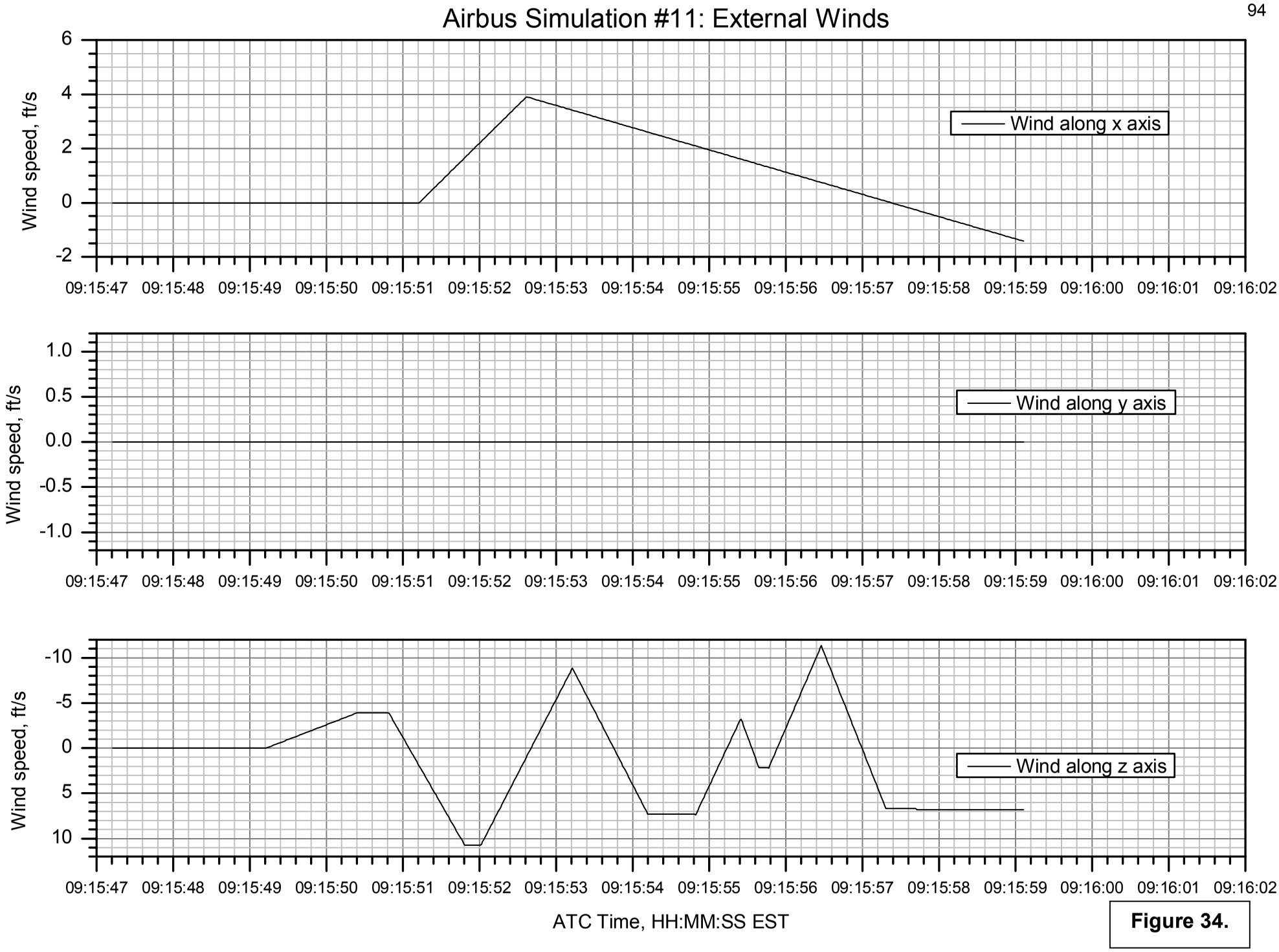
Airbus Simulation #11: External Winds
Wind speed, ft/s
6
4
2
0
-2
Wind along x axis
09:15:47 09:15:48 09:15:49 09:15:50 09:15:51 09:15:52 09:15:53 09:15:54 09:15:55 09:15:56 09:15:57 09:15:58 09:15:59 09:16:00 09:16:01 09:16:02
Wind speed, ft/s
1.0
0.5
0.0
-0.5
-1.0
Wind along y axis
09:15:47 09:15:48 09:15:49 09:15:50 09:15:51 09:15:52 09:15:53 09:15:54 09:15:55 09:15:56 09:15:57 09:15:58 09:15:59 09:16:00 09:16:01 09:16:02
Wind speed, ft/s
-10
-5
0
5
10
Wind along z axis
09:15:47 09:15:48 09:15:49 09:15:50 09:15:51 09:15:52 09:15:53 09:15:54 09:15:55 09:15:56 09:15:57 09:15:58 09:15:59 09:16:00 09:16:01 09:16:02
ATC Time, HH:MM:SS EST

Figure 34.

AAL587 Vertical Tail Load Calculations: Rudder and Sideslip

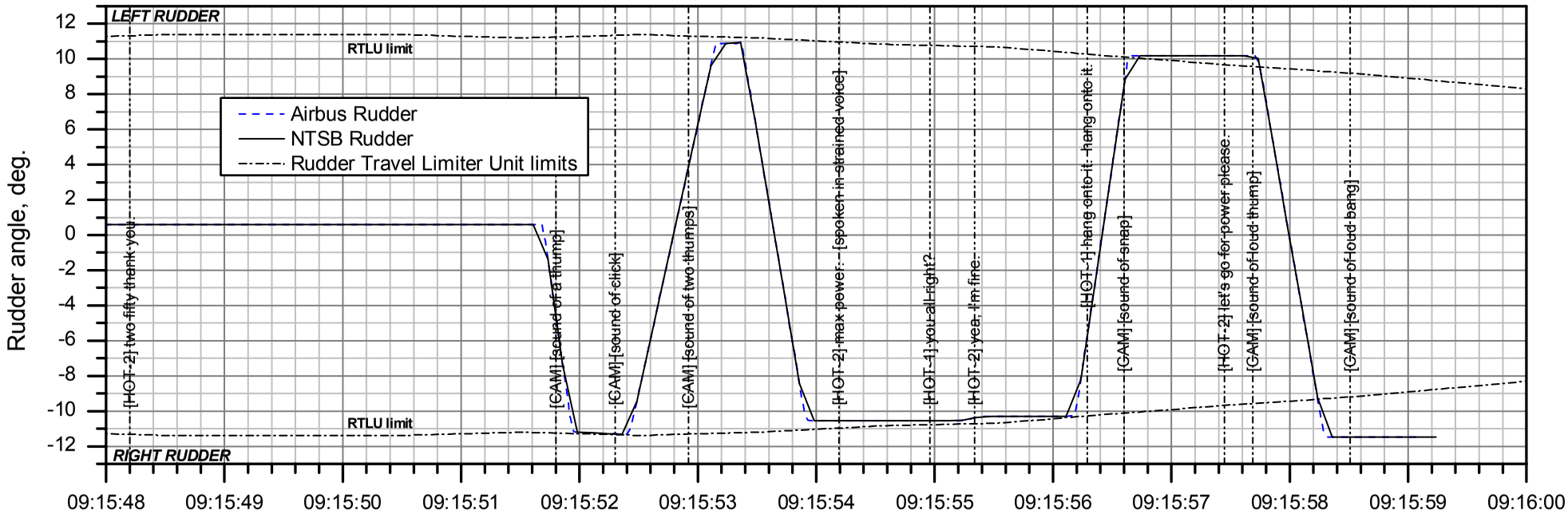

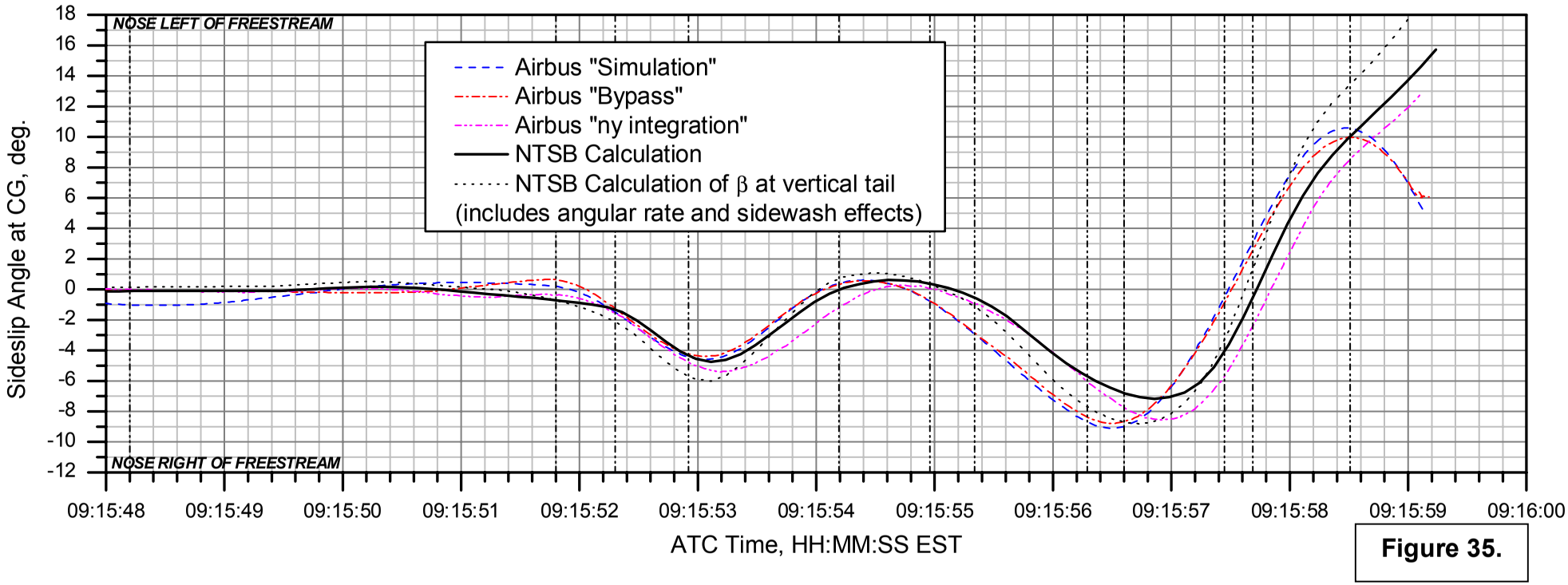

Figure 35.

AAL587 Vertical Tail Load Calculations: Shear Load and Torsion Moment, Fin Axis System

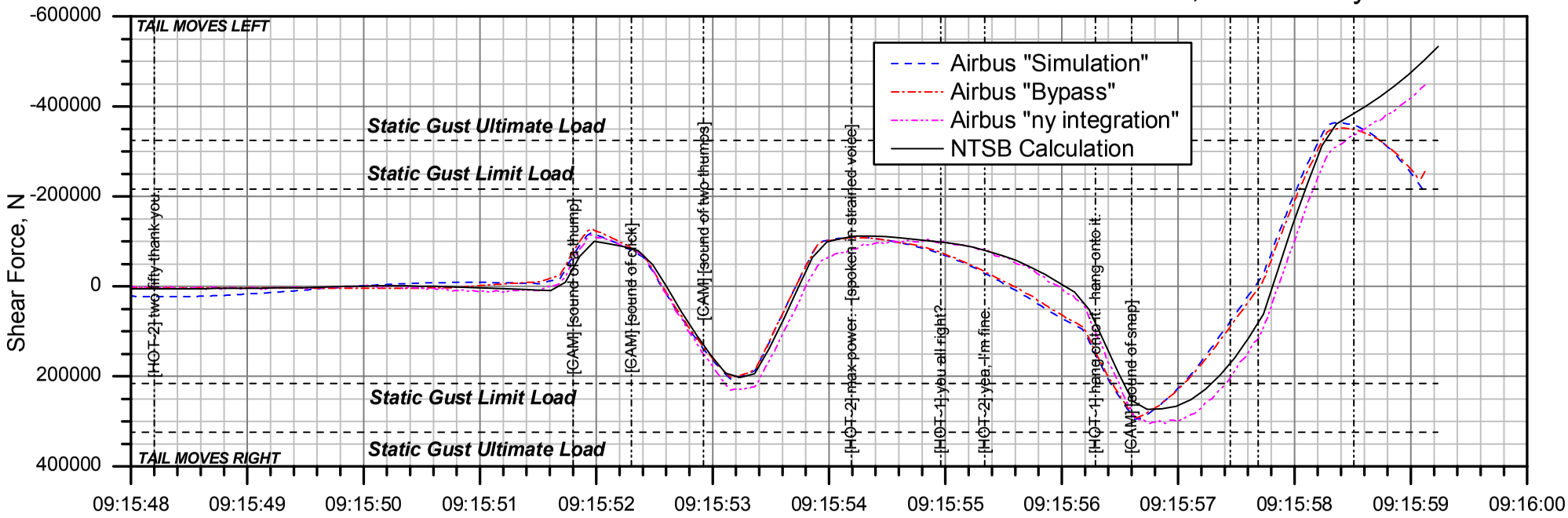

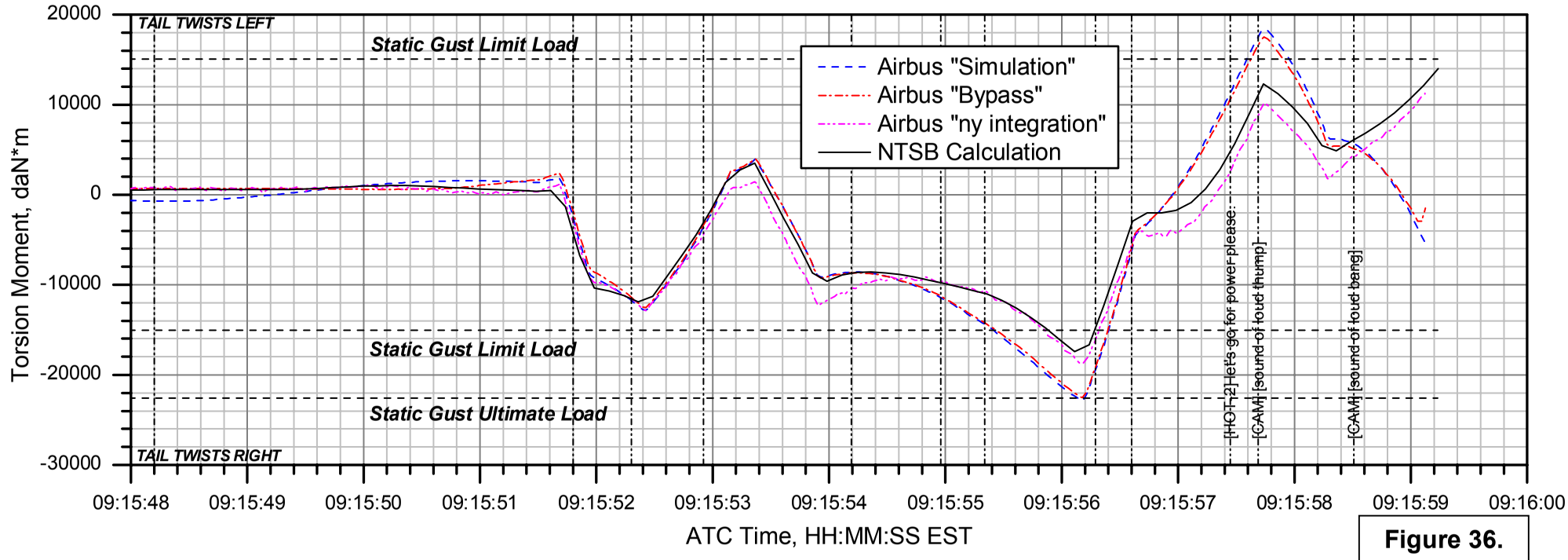

Figure 36.

AAL587 Vertical Tail Load Calculations: Bending Moment about Fin Root Chord, Fin Axis System

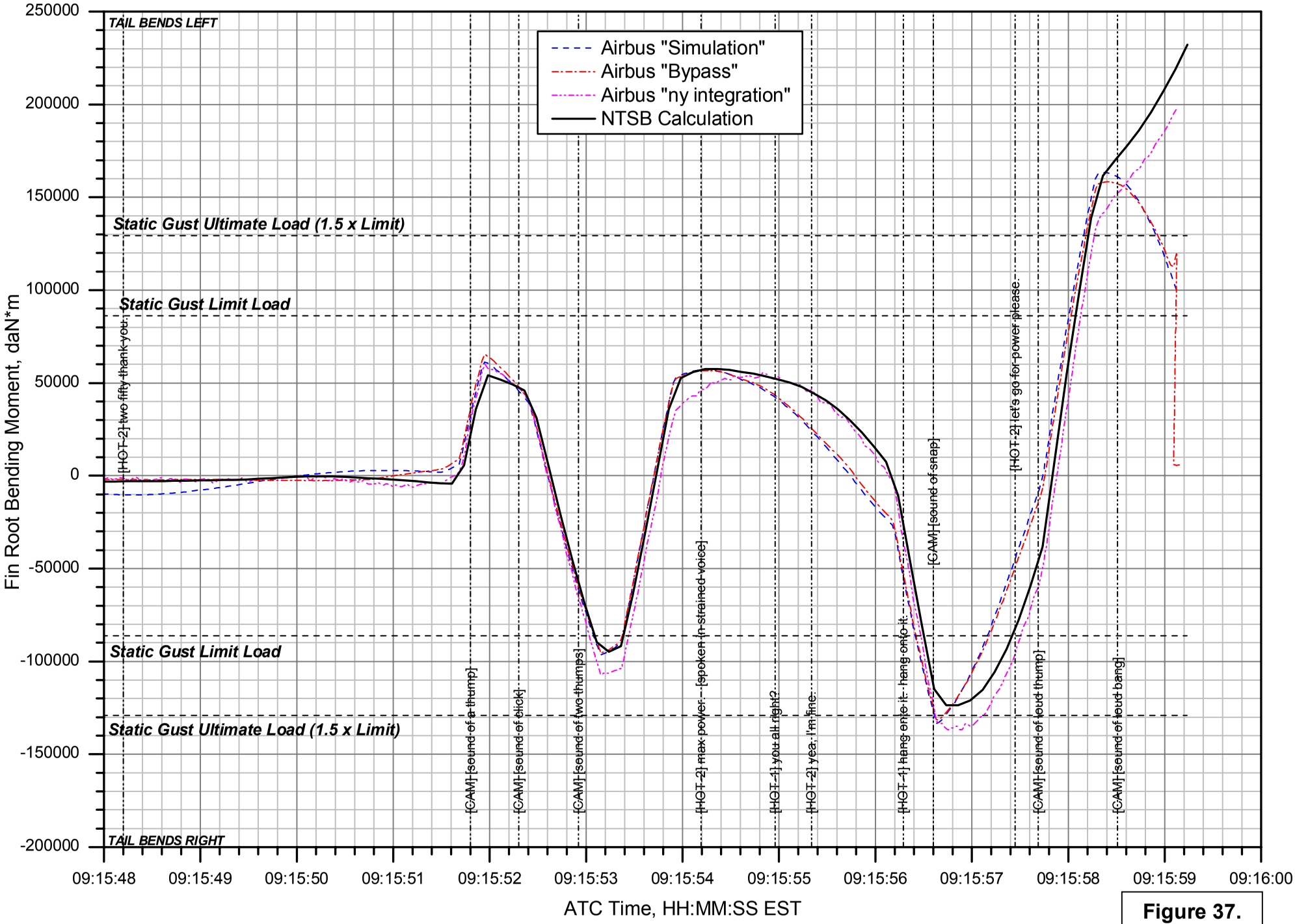

Figure 37.

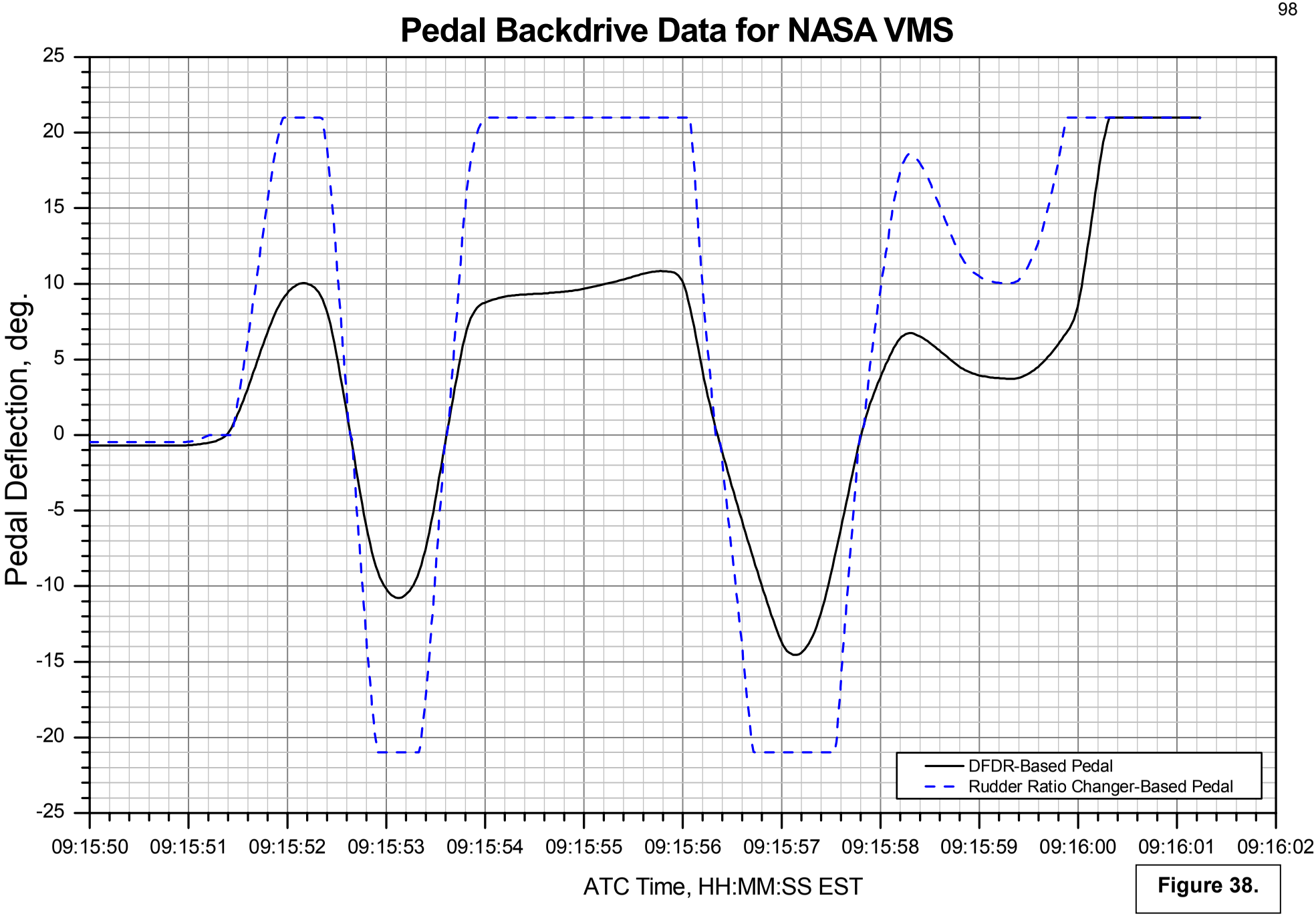
Pedal Backdrive Data for NASA VMS
Pedal Deflection, deg.
25
20
15
10
5
0
-5
-10
-15
-20
-25
09:15:50
09:15:51
09:15:52
09:15:53
09:15:54
09:15:55
09:15:56
09:15:57
09:15:58
09:15:59
09:16:00
09:16:01
09:16:02
ATC Time, HH:MM:SS EST
DFDR-Based Pedal
Rudder Ratio Changer-Based Pedal

Figure 38.

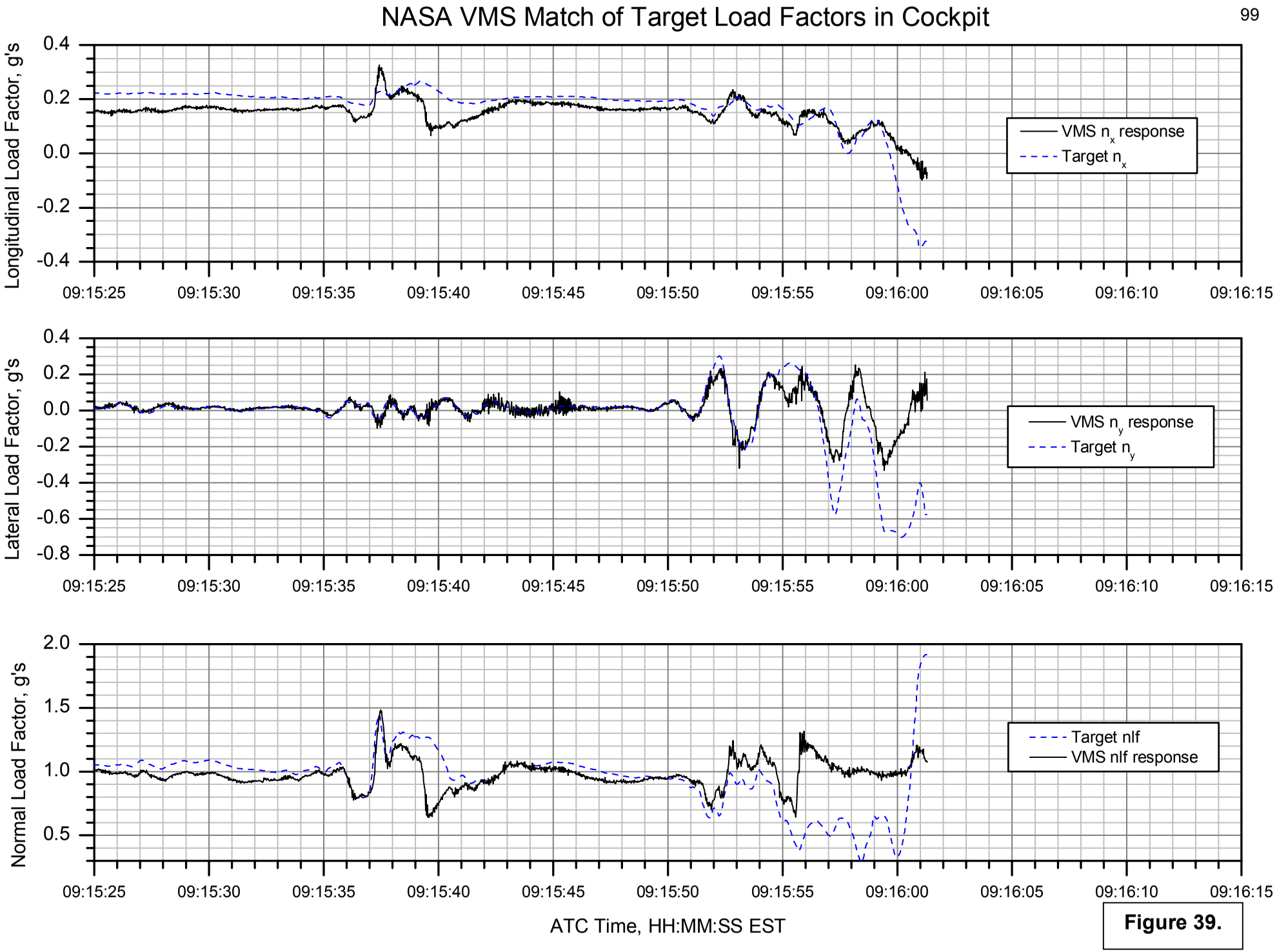
NASA VMS Match of Target Load Factors in Cockpit
Longitudinal Load Factor, g's
0.4
0.2
0.0
-0.2
-0.4
VMS n_x response
Target n_x
Lateral Load Factor, g's
0.4
0.2
0.0
-0.2
-0.4
-0.6
-0.8
VMS n_y response
Target n_y
Normal Load Factor, g's
2.0
1.5
1.0
0.5
Target nlf
VMS nlf response
09:15:25
09:15:30
09:15:35
09:15:40
09:15:45
09:15:50
09:15:55
09:16:00
09:16:05
09:16:10
09:16:15
ATC Time, HH:MM:SS EST

Figure 39.

This page intentionally left blank

Appendix A

Details of Selected Performance Calculations

Appendix A: Details of Selected Performance Calculations

Much of the data presented in this Performance Study is derived from or calculated using the information recorded on the DFDR. This Appendix provides additional details on the methods and equations used to compute some of the parameters described in the main body of the Study. The computations detailed in this Appendix are:

Flight condition calculations. These calculations provide additional parameters to describe the flight regime of the aircraft, including true altitude and airspeed, equivalent airspeed, Mach number, dynamic pressure, and flight path angle.

Accelerometer corrections. These calculations transfer the load factors measured at the accelerometer location to the actual CG position, and compute the accelerometer biases or offsets required to make the integrated accelerations match the position information recorded by the DFDR. The equations for calculating the load factors away from the CG are also presented.

A-I. Nomenclature

English

a	Speed of Sound
a	Measurement of Bias Error for n_y
$\vec{a}_P$	Acceleration of Point P
$\vec{a}_{CG}$	Acceleration of CG
b	Dimension Used in Measurement of Bias Error for n_y
c	Dimension Used in Measurement of Bias Error for n_y
c_1	Constant used in Altitude Equation
c_2	Constant used in Altitude Equation
CG	Center of Gravity
g	Gravitational Acceleration (= 32.17 ft/s^2)
$\vec{g}$	Gravity Vector
h	Altitude
h_T	True Altitude
m	Aircraft Mass
M	Mach Number
n	Ratio of Constant Pressure and Constant Volume Specific Heats in Standard Atmosphere (= 1.235)
$\vec{n}$	Load Factor Vector
n_x	Longitudinal Load Factor
n_y	Lateral Load Factor
n_z	Vertical Load Factor
nlf	Normal Load Factor (= -n_z)
P	Body Axis Roll Rate

P	Static Pressure
P_0	Sea Level Static Pressure (= 2116.22 lb/ft^2 for standard atmosphere)
P_T	Total Pressure
$\bar{q}$	Dynamic Pressure
Q	Body Axis Pitch Rate
$\vec{r}_P$	Vector from CG to Point P
R	Body Axis Yaw Rate
R	Gas Constant for Air (= 1716.56 (ft/s)^2/°R)
T	Static Temperature
T_0	Sea Level Static Temperature (=59.0 °F for standard atmosphere)
T_T	Total Temperature
$[T_{EB}]$	Earth to Body Axes Transformation Matrix
$[T_{BE}]$	Body to Earth Axes Transformation Matrix
u	Velocity along x axis
v	Velocity along y axis
V	Aircraft Velocity
V_A	Airspeed
V_C	Calibrated Airspeed
V_E	Equivalent Airspeed
V_G	Ground Speed
$\vec{V}_P$	Velocity Vector of Point P
V_T	True Airspeed
V_W	Wind Speed
V_x	x Velocity Component of Point P
V_y	y Velocity Component of Point P
V_z	z Velocity Component of Point P
V_∞	Freestream Velocity
w	Velocity along z axis
W	Aircraft Weight
x	Distance Along Body x Axis
y	Distance Along Body y Axis
z	Distance Along Body z Axis
X_{NEW}	New Earth-Fixed X Axis for Accelerometer Bias Calculations
Y	Side Force
Y_{NEW}	New Earth-Fixed Y Axis for Accelerometer Bias Calculations

Greek

α	Angle of Attack
β	Angle of Sideslip
δr	Rudder Deflection
$\Delta\vec{n}$	Vector of Accelerometer Biases
ε	Accelerometer Bias Increment
ϕ	Bank Angle
γ	Flight Path Angle

γ Ratio of Const. Press. and Const. Vol. Specific Heats in Air (=1.4)
θ Pitch Angle
ρ Air Density
ρ_0 Sea Level Air Density (= 0.002377 slug/ft^3 for standard atmosphere)
$\vec{\omega}$ Angular Velocity Vector
ξ Accelerometer Integration Error
ψ Heading Angle
ψ_{DRIFT} Drift Angle Between Heading and Ground Track (Earth Axes)
ψ_{TRACK} Ground Track Angle in Bias Correction Axis System $\{X_{NEW}, Y_{NEW}\}$
ψ_{NEW} Heading Angle in Bias Correction Axis System $\{X_{NEW}, Y_{NEW}\}$

A-II. Flight Condition Calculations

The DFDR records the following information that defines the flight condition:

- Indicated Airspeed
- Altitude (indicated or pressure, depending on the altimeter setting of the altimeter supplying data to the DFDR)
- Total Air Temperature

This information can be used to compute other important parameters such as true altitude and airspeed, dynamic pressure, and flight path angle.

Pressure Altitude

Pressure altitude is the altitude measured by an altimeter set to a sea level static pressure of 29.92” Hg. In standard atmospheric conditions, the pressure altitude equals the height of the airplane above sea level (true altitude). If 29.92” Hg is not set in the Kollsman window of the altimeter reporting to the DFDR, then the recorded altitude will have to be adjusted to obtain pressure altitude.

Altimeters approximate the effect of non-standard sea level pressure by adjusting the heights of pressure levels in the atmosphere up or down by an amount directly proportional to the difference between the actual sea level pressure and 29.92” Hg. This relationship can be used to determine what the altimeter would read if set to 29.92” Hg., i.e., the pressure altitude.

The change in altitude due to a change in altimeter setting follows from the following relationships governing the standard, adiabatic atmosphere. The pressure lapse with altitude is given by

$$P = P_0 \left\{ 1 - \frac{g}{RT_0} \left(\frac{n-1}{n} \right) h \right\}^{\frac{n}{n-1}} \qquad [A1]$$

Define constants c_1 and c_2 as

$$c_1 = \frac{RT_0}{g}\left(\frac{n}{n-1}\right) \qquad [A2]$$

$$c_2 = \frac{n-1}{n} \qquad [A3]$$

Using [A2] and [A3] when solving [A1] for h gives

$$h = c_1\left\{1-\left(\frac{P}{P_0}\right)^{c_2}\right\} \qquad [A4]$$

The change in altitude (h) with sea level pressure (P_0) is then

$$\frac{dh}{dP_0} = \frac{c_1 c_2}{P}\left(\frac{P_0}{P}\right)^{-c_2-1} = \frac{c_1 c_2}{P_0^{\,c_2+1}}P^{c_2} \qquad [A5]$$

[A5] indicates that the change in altitude with sea level pressure depends on the static pressure, and hence the altitude in question. However, altimeters do not account for this altitude dependency, but instead use the altitude increment that applies at sea level at all altitudes. With $P = P_0$, [A5] becomes

$$\frac{dh}{dP_0} = \frac{c_1 c_2}{P_0} = 924.82 \text{ ft/"Hg} \qquad [A6]$$

for standard sea level P_0 = 29.92” Hg. The pressure altitude can then be found from the indicated or recorded altitude:

$$h_P = h_I + \frac{dh}{dP_0}\left(P_{0(STD)} - P_{0(NSTD)}\right) = h_I + 924.82\left(29.92 - P_{0(NSTD)}\right) \qquad [A7]$$

where the subscript STD refers to standard day conditions, and NSTD to actual conditions. $P_{0(NTSD)}$ is the actual altimeter setting in inches of mercury.

The altimeter that reports to the DFDR is independent of the altimeters used by the flight crew, and is always set to 29.92 “ Hg. Therefore the altitude recorded by the DFDR is the pressure altitude. Once pressure altitude is known, [A1] can be used to find the freestream static pressure.

It is difficult to position static ports on the airplane so that they sense freestream static pressure correctly at all angles of attack and sideslip. Consequently, at

some angles the pressure measurement, and consequently the reported altitude, will be in error. The error is the *position error* is generally small (a few feet), and is assumed to be zero in this Study. That this assumption is not good at large sideslip is apparent in the disagreement between the pressure based altitude and the radio altimeter altitude near the end of the recorded DFDR data, during the period of large rudder movements.

Mach Number, Static Temperature, and True Airspeed

The indicated or recorded airspeed is the calibrated airspeed plus the error associated with the static port location (position error). However, the error is generally small (the equivalent of a few knots), and in this study is assumed to be zero everywhere, so that the calibrated airspeed equals the indicated airspeed. Note that this assumption breaks down at the end of the DFDR data when the sideslip angle is large; in this region, the indicated airspeed will suffer from the same static port pressure errors as the pressure altitude measurement.

The calibrated airspeed is given by

$$V_C = \sqrt{\frac{2\gamma R T_0}{\gamma - 1}\left\{\left(\frac{P_T - P}{P_0} + 1\right)^{\frac{\gamma-1}{\gamma}} - 1\right\}} \qquad [A8]$$

The Mach number is given by

$$M = \sqrt{\frac{2}{\gamma - 1}\left\{\left(\frac{P_T - P}{P} + 1\right)^{\frac{\gamma-1}{\gamma}} - 1\right\}} \qquad [A9]$$

Solving [A8] for P_T - P gives

$$P_T - P = P_0\left[\left\{V_C{}^2\left(\frac{\gamma - 1}{2\gamma R T_0}\right) + 1\right\}^{\frac{\gamma}{\gamma-1}} - 1\right] \qquad [A10]$$

P_0 and T_0 are the standard sea level static pressure and temperature, and P is known from [A7] and [A1]. Evaluating P_T - P with [A10] allows [A9] to be evaluated for M. M is of course the ratio of true airspeed to the speed of sound. The sound speed is given by

$$a = \sqrt{\gamma R T} \qquad [A11]$$

The static temperature T can be found from the Mach number as follows:

$$T = \frac{T_T}{1 + \frac{\gamma - 1}{2} M^2} \qquad [A12]$$

With T, *a* can be evaluated with [A11]. The true airspeed is then

$$V_T = aM \qquad [A13]$$

Equivalent Airspeed and Dynamic Pressure

The static density can be found from the equation of state:

$$\rho = \frac{P}{RT} \qquad [A14]$$

Equivalent airspeed and dynamic pressure are given by

$$V_E = \sqrt{\frac{\rho}{\rho_0}} V_T \qquad [A15]$$

$$\overline{q} = \frac{1}{2} \rho V_T^{\,2} \qquad [A16]$$

True Altitude

True altitude can be calculated by estimating the true altitude at the start of the calculation, and then keeping track of the actual change in altitude by accounting for the changes in air density at each point.

If the local altimeter setting for the airspace in which the airplane is flying is known, the initial true altitude can be estimated by solving Equation for h_I, with $P_{0(NSTD)}$ equal to the altimeter setting. Alternatively, the initial true altitude can be calculated using the radio altimeter, if the elevation of the terrain under the airplane is known (e.g., if the airplane is over open ocean).

The hydrostatic equation that describes the balance of forces on a cube of air is

$$dP = -\rho g dh \qquad [A17]$$

where dP is the increment in static pressure over the increment in altitude, dh. Solving [A17] for dh and integrating gives

$$h = -\frac{1}{g}\int \frac{dP}{\rho} + h_0 \qquad [A18]$$

Pressure is given by [A1] with $h=h_P$ as given in [A7] and T_0 equal to standard sea level temperature. Density is given by [A14]. h_0 is the true altitude at the start of the calculation described above. With these items, [A41] can be evaluated.

Flight Path Angle

The flight path angle γ is the angle the velocity vector of the aircraft makes with the horizontal plane, and is given by:

$$\gamma = \sin^{-1}\left(\frac{\dot{h}_T}{V_T}\right) \qquad [A19]$$

where $\dot{h}_T$ is the time derivative of true altitude.

A-III. Accelerometer Corrections

The load factors recorded by the DFDR are very useful parameters because when integrated properly they provide information about the inertial velocity and position of the aircraft. However, the accelerometers that measure the load factors suffer from inherent errors that must be corrected, or very misleading results will follow from the integrations.

The two errors that are accounted for in this Study are the 1) the error due to the accelerometer location not coinciding exactly with the CG, and 2) the error due to accelerometer offsets or biases. The accelerometers are located very near the CG, so error (1) is small. The bias error is very significant because even a small offset will generate large errors when integrated over time. The biases are usually constant over time frames such as the period of interest in this accident.

Accelerometer Location Error

The equations that provide the correction for the accelerometer location also provide the means for calculating the load factors at points other than the CG. The acceleration of a point P on the airplane is given by

$$\vec{a}_P = \dot{\vec{V}}_{CG}\Big|_{xyz} + \vec{\omega}\times\vec{V}_{CG} + \dot{\vec{\omega}}\Big|_{xyz}\times\vec{r}_P + \vec{\omega}\times\left(\vec{\omega}\times\vec{r}_P\right) \qquad [A20]$$

where $\vec{r}_P$ is the vector from the CG to the point P, and $\vec{\omega}$ is the vector of the angular velocity about the CG. The components of $\vec{r}_P$ and $\vec{\omega}$ in body axes are

$$\vec{r}_P = x\hat{i} + y\hat{j} + z\hat{k} = \begin{Bmatrix} x \\ y \\ z \end{Bmatrix} \qquad [A21]$$

$$\vec{\omega} = P\hat{i} + Q\hat{j} + R\hat{k} = \begin{Bmatrix} P \\ Q \\ R \end{Bmatrix} \qquad [A22]$$

where $\hat{i}, \hat{j}, \hat{k}$ are unit vectors along the Xb, Yb, Zb axes (throughout this Appendix, variables in matrix format represent the components of the vector in question in the body axis system). Using the shorthand convention $dx/dt = \dot{x}$ to denote time derivatives, the angular rates P, Q, R are:

$$\begin{Bmatrix} P \\ Q \\ R \end{Bmatrix} = \begin{bmatrix} -\sin\theta & 0 & 1 \\ \sin\phi\cos\theta & \cos\phi & 0 \\ \cos\phi\cos\theta & -\sin\phi & 0 \end{bmatrix} \begin{Bmatrix} \dot{\psi} \\ \dot{\theta} \\ \dot{\phi} \end{Bmatrix} \qquad [A23]$$

The yaw (ψ), pitch (θ), and roll (ϕ) angles are recorded by the DFDR.

The notation $\big|_{xyz}$ in Equation [A20] means that the derivative is relative to the body axis system (as opposed to the inertial or Earth-fixed axis system). Thus, with $\vec{V}_{CG}\big|_{xyz}$ = {u, v, w} (see A1), and

$$\dot{\vec{V}}_{CG}\Big|_{xyz} = \begin{Bmatrix} \dot{u} \\ \dot{v} \\ \dot{w} \end{Bmatrix} \qquad [A24]$$

From [A22] it follows that

$$\dot{\vec{\omega}}\Big|_{xyz} = \begin{Bmatrix} \dot{P} \\ \dot{Q} \\ \dot{R} \end{Bmatrix} \qquad [A25]$$

Substituting [A21], [A22], [A24] and [A25] into [A20] and performing the cross products gives

$$\vec{a}_P = \begin{Bmatrix} \dot{u} + wQ - vR \\ \dot{v} + uR - wP \\ \dot{w} + vP - uQ \end{Bmatrix} + \begin{Bmatrix} Q(yP - xQ) + R(zP - xR) + (z\dot{Q} - y\dot{R}) \\ R(zQ - yR) + P(xQ - yP) + (x\dot{R} - z\dot{P}) \\ P(xR - zP) + Q(yR - zQ) + (y\dot{P} - x\dot{Q}) \end{Bmatrix} = \vec{a}_{CG} + \Delta\vec{a} \qquad [A26]$$

Since by definition {x,y,z} at the CG = {0,0,0}, the first term in brackets in [A24] must be the acceleration of the CG, and the second term the increment in acceleration due to the point P being away from the CG.

A three axis accelerometer at point P will measure load factors as follows:

$$\vec{n}_P = \frac{\vec{a}_P - \vec{g}}{g} = \frac{\vec{a}_{CG} + \Delta\vec{a} - \vec{g}}{g} = \vec{n}_{CG} + \frac{\Delta\vec{a}}{g} \qquad [A27]$$

where [A24] has been used to substitute for $\vec{a}_P$. The components of $\vec{n}$ are $\{n_x,n_y,n_z\}$. The normal load factor (nlf) is

$$nlf = -n_z \qquad [A28]$$

The DFDR records n_x, n_y, and nlf as “Longitudinal Acceleration,” “Lateral Acceleration,” and “Vertical Acceleration.” The values of $\{n_x,n_y,n_z\}$ at the CG can be found using the DFDR data and [A28], [A27], and [A26], with {x,y,z} in [A26] being the distance of the accelerometer unit from the CG. In this study, the accelerometers are assumed to be at coordinates {2.3 ft.,0.,0.}. The errors associated with this location are very small.

Once the load factors at the CG have been calculated, [A27] and [A26] can be used to calculate the load factors at other points. In this study, the loads in the cockpit and at the center of mass of the vertical tail are calculated. The coordinates of these points are {68.9 ft., 0., 0.}, and {-78.38 ft., 0., -22.54 ft.}, respectively.

Accelerometer Bias Error

The load factors reported by the accelerometers are rarely the actual load factors at the accelerometer location because the sensor is not perfect. While load factor increments from a reference point are reported with very little error, the absolute value of the reference load factor is often offset from the true reference value by a constant bias. This error is readily seen in accelerometer data while the aircraft is at rest. The actual longitudinal, lateral, and vertical load factors in this case are given by [A27] with $\vec{a}_P$ = 0., i.e., by $-\vec{g}$, where

$$\vec{g} = g\begin{Bmatrix} -\sin\theta \\ \cos\theta\sin\phi \\ \cos\theta\cos\phi \end{Bmatrix} \qquad [A29]$$

The recorded data seldom reflects these exact values. For example, prior to the takeoff on the accident flight, while the aircraft is at rest (ground speed = 0), the following information is recorded on the DFDR:

θ	**ϕ**	**n_x**	**n_y**	**nlf**
-1.41	0.35	-0.0286	-0.0103	0.9763

The theoretical values for n_x, n_y, and nlf at this condition using [A27] and [A29] are -0.0246, 0.0061, and 1.000, respectively. Defining the biases as

$$\Delta\vec{n} = \vec{n}\Big|_{\text{ACTUAL}} - \vec{n}\Big|_{\text{RECORDED}} \qquad [A30]$$

shows that in this case the accelerometers are offset by 0.004, 0.0164, and -0.0237 g's in the x, y, and z directions, respectively. The biases that exist on the ground before takeoff are not necessarily those that exist at the time of the accident, because the bias errors can drift slightly. Thus the biases that apply to the accident event must be determined at a point prior to but as close to the event as possible. The biases must be accounted for because even small errors in load factor data will produce very large errors in speed and position calculations when integrated over time.

The accelerometer biases can be calculated for the aircraft in flight through an iterative process that compares the position resulting from integration of the accelerometer data with a position calculated using recorded navigation data. The groundspeed and drift angle recorded by the DFDR are calculated by the Flight Management Computer using accelerometer data updated and corrected with information from radio navigation aids (such as VOR/DME stations). The latitude and longitude of the aircraft are also recorded directly by the DFDR, but at a lower sample rate than groundspeed and drift angle. Thus the position can be defined more precisely by using the latter parameters.

Overview of Accelerometer Bias Calculation

This subsection presents an overview of the process for computing the accelerometer biases. The detailed steps and equations for the process are presented following this summary.

First, the "actual" position of the aircraft is defined using the groundspeed and drift angle navigation information recorded by the DFDR. Also, a better estimate of altitude is made by solving the hydrostatic equation with estimates of the actual air density at each point.

Next, an estimate of the accelerometer biases is made by computing the load factors that result from the position information just derived, and comparing these to the recorded load factors.

At this point the iteration begins. The load factors are updated with the bias estimates, and then integrated to obtain position information. These integrated positions are compared to the inertial positions calculated previously, and an error calculated.

The sensitivity of the position error to each of the accelerometer biases is calculated by changing the bias values slightly and recomputing the errors. Using these sensitivities, the biases are updated, and the positions, errors and biases recalculated. When changes in the biases no longer result in a reduction in the errors, then the best estimate of the biases has been found and the final load factors are computed. The final integrated velocities and positions are also calculated and represent the best available estimate of the inertial speeds. These speeds can be used along with airspeed information to calculate winds, as described in Section A-V.

Details of Accelerometer Bias Calculation

1. The "actual" position of the aircraft is computed from the groundspeed and drift angle. This position is measured in an Earth fixed axis system in which the origin is the position of the airplane at the start of the calculation, and where the X_{NEW} axis is aligned with the original ground track angle (see Figure A2). The track angle (i.e., the heading of the velocity vector) in this axis system is

$$\psi_{TRACK} = \psi + \psi_{DRIFT} - \left[\psi + \psi_{DRIFT}\right]_{TIME=0} \quad [A31]$$

The heading of the aircraft in this axis system is

$$\psi_{NEW} = \psi - \left[\psi + \psi_{DRIFT}\right]_{TIME=0} \quad [A32]$$

The components of inertial velocity in the x and y axes are

$$V_{XNEW} = V_{GROUND} \cos\left(\psi_{TRACK}\right) \quad [A33]$$

$$V_{YNEW} = V_{GROUND} \sin\left(\psi_{TRACK}\right) \quad [A34]$$

The position coordinates of the aircraft are

$$X_{NEW} = \int V_{XNEW} dt \quad [A35]$$

$$Y_{NEW} = \int V_{YNEW} dt \quad [A36]$$

2. The load factors resulting from the inertial positions are computed to provide an initial estimate of the accelerometer biases. Combining [A26], [A27] and [A29], the load factors at the CG are

$$\vec{n}_{CG} = \frac{1}{g}\begin{Bmatrix} \dot{u} + wQ - vR \\ \dot{v} + uR - wP \\ \dot{w} + vP - uQ \end{Bmatrix} + \begin{Bmatrix} \sin\theta \\ -\cos\theta\sin\phi \\ -\cos\theta\cos\phi \end{Bmatrix} \qquad [A37]$$

The Euler angles are recorded by the DFDR and the angular rates are given by [A23]. The velocity components in body axes can be calculated from the velocity components in Earth axes by transformation:

$$\begin{Bmatrix} u \\ v \\ w \end{Bmatrix} = \left[T_{EB}\right]\begin{Bmatrix} V_{XNEW} \\ V_{YNEW} \\ {}^{dh}\!/_{dt} \end{Bmatrix} \qquad [A38]$$

The transformation matrix is given by

$$\left[T_{EB}\right] = \begin{bmatrix} \cos\theta\cos\psi_{NEW} & \cos\theta\sin\psi_{NEW} & -\sin\theta \\ \sin\phi\sin\theta\cos\psi_{NEW} - \cos\phi\sin\psi_{NEW} & \sin\phi\sin\theta\sin\psi_{NEW} + \cos\phi\cos\psi_{NEW} & \sin\phi\cos\theta \\ \cos\phi\sin\theta\cos\psi_{NEW} + \sin\phi\sin\psi_{NEW} & \cos\phi\sin\theta\sin\psi_{NEW} - \sin\phi\cos\psi_{NEW} & \cos\phi\cos\theta \end{bmatrix}$$

[A39]

Note that since $\left[T_{EB}\right]$ is orthogonal, its inverse is simply its transpose:

$$\left[T_{BE}\right] = \left[T_{EB}\right]^{-1} = \left[T_{EB}\right]^{T} \qquad [A40]$$

Calling the $\vec{n}_{CG}$ calculated using [A37]-[A39] $\vec{n}_{INERT}$ and the recorded load factors corrected for position errors $\vec{n}_{DFDR}$, an initial estimate of the biases follows from [A30] as

$$\Delta\vec{n}_{EST} = \vec{n}_{NERT} - \vec{n}_{DFDR} \qquad [A41]$$

Since in reality the accelerometer biases (the $\Delta\vec{n}$) are approximately constant over the period of interest, the average $\Delta\vec{n}_{EST}$ from [A41] during the period is used as the initial bias estimate.

3. This is the start of the iteration loop. The $\vec{n}_{DFDR}$ are updated with the average $\Delta\vec{n}_{EST}$ from step 2 to obtain new load factor values:

$$\vec{n}_{NEW} = \vec{n}_{DFDR} + \Delta\vec{n}_{EST}\Big|_{AVG} \qquad [A42]$$

4. The $\vec{n}_{NEW}$ and [A37] provide three simultaneous non-linear differential equations for {u,v,w}. These equations are integrated numerically with a Runge-Kutta scheme, using the initial points of the {u,v,w} given in [A38] as initial values for the integration.

5. The $\{u_{INT},v_{INT},w_{INT}\}$ obtained in step 4 are transformed into Earth axis components using the inverse of [A38]:

$$\begin{Bmatrix} V_{XINT} \\ V_{YINT} \\ \dot{h}_{INT} \end{Bmatrix} = \left[T_{BE}\right] \begin{Bmatrix} u_{INT} \\ v_{INT} \\ w_{INT} \end{Bmatrix} \qquad [A43]$$

6. Integrated X_{INT} and Y_{INT} positions are calculated using [A35] & [A36] and the integrated velocities from step 5. dh_{INT}/dt is integrated to get h_{INT}.

7. The differences between the integrated positions $\{X_{INT},Y_{INT},h_{INT}\}$ and the inertial positions $\{X_{NEW},Y_{NEW},h\}$ are a measure of the error still inherent in the accelerometers. To calculate how the load factors should change to reduce the error, the effect of each bias on the errors needs to be understood. Ideally, each bias should be associated with a unique error measurement that is relatively independent of the other biases and which can be monitored to determine the effects of changing the bias. Such error measurements for the $\{\Delta n_x, \Delta n_y, \Delta n_z\}$ biases are illustrated in Figure A2.

For transport airplanes that remain at relatively shallow pitch and bank angles, an error in n_x will result in a difference between the integrated and actual horizontal distance traveled during the integration period, as illustrated by the l_{INT} and l_{ACT} curves in Figure A2. An error in n_y will result in track angle differences between the integrated and actual paths; at the end of the integration, this will appear as a difference in aircraft position that is not wholly accounted for by the difference in distance traveled (length *a* in Figure A2). An error in n_z will result in differences between the integrated and actual altitudes.

l_{ERROR}, the time-averaged difference between l_{INT} and l_{ACT}, is given by

$$l_{ERROR} = \frac{\int_0^t \sqrt{\left(l_{INT} - l_{ACT}\right)^2}\,dt}{\int_0^t dt} \qquad [A44]$$

where

$$l_i(t) = \int_0^t \left(\frac{dl_i}{dt}\right) dt = \int_0^t v_i(t)\,dt \qquad [A45]$$

$$v_i(t) = \sqrt{v_{xi}^2 + v_{yi}^2} \qquad [A46]$$

and the subscript i refers to the integrated data in one case, and the actual data in another.

An approximate equation for the distance *a* in Figure A2, which provides the measure of the ny error, is

$$a \cong \sqrt{c^2 - b^2} \qquad [A47]$$

where

$$b = l_{INT} - l_{ACT} \qquad [A48]$$

and c is the distance between the final integrated and actual positions:

$$c = \sqrt{\left(X_{INT} - X_{NEW}\right)^2 + \left(Y_{INT} - Y_{NEW}\right)^2} \qquad [A49]$$

For use in the error calculations, the value of *a* is time averaged:

$$a_{AVG} = \frac{\int_0^t a\,dt}{\int_0^t dt} \qquad [A50]$$

The time averaged altitude error is

$$h_{ERROR} = \frac{\int_0^t \sqrt{\left(h_{INT} - h\right)^2}\,dt}{\int_0^t dt} \qquad [A51]$$

8. To use these error measurements to determine how the bias should change, the sensitivity of each error to its associated bias must be calculated. This is done by incrementing each bias independently by a small amount and recalculating the integrated positions and errors. If ξ_i is the error associated with n_i, $\Delta\xi_i$ the change in error due to the bias increment, and ε the increment, then the new n_i is

$$n_i\Big|_{NEW} = n_i + \frac{\xi_i}{\Delta\xi_i}\varepsilon \qquad [A52]$$

In practice, the increment in n_i during each iteration should not be allowed to exceed a given amount or poor convergence may result. In this study, bias increments are limited to 0.002 g's each iteration.

If after several iterations the decrease in ξ_i is below a certain threshold, then the biases that result in the best fit of the integrated data to the inertial data have been found and the process is complete.

A-IV. Angle of Attack Corrections

The angle of attack is the angle between the longitudinal axis of the airplane and the projection of the velocity vector onto the plane defined by the longitudinal and vertical axes. In steady, level flight, the velocity vectors of all parts of the airplane are the same, and so α is the same everywhere. When the airplane is rotating about its center of gravity, however, the rotation imparts additional velocities to different parts of the airplane according to their positions relative to the CG, and so each part can have a different velocity and angle of attack.

The angle of attack is measured in flight with a vane that aligns itself with the direction of the local airflow. This vane is generally located near the nose of the airplane to minimize the effects of the upwash of the wing. However, this location is far from the CG and makes the α vane sensitive to pitch rate, which induces a vertical velocity component at the vane and makes its local α differ from the α at the CG. However, if the pitch rate is known, its effects can be calculated and removed from the vane measurements to provide an estimate of the CG α. Similarly, if the roll and yaw rates are also known, the α induced at any point on the airplane can be determined.

It follows from Figure A1 that

$$u = V\cos(\beta)\cos(\alpha) \qquad [A53]$$

$$v = V\sin(\beta) \qquad [A54]$$

$$w = V\cos(\beta)\sin(\alpha) \qquad [A55]$$

Consequently

$$\alpha = \tan^{-1}\left(\frac{w}{u}\right) \qquad [A56]$$

To determine the α at a point, then, the velocity components of that point along the Xb and Zb axes must be known. The velocity of a point P on the aircraft is given by

$$\vec{V}_P = \vec{V}_{CG} + \vec{\omega} \times \vec{r}_P \qquad [A57]$$

where $\vec{r}_P$ is the vector from the CG to the point P. Using [A21], [A22], and [A23], and letting u, v, and w denote the velocity components of the CG gives

$$\vec{V}_P = \begin{Bmatrix} V_x \\ V_y \\ V_z \end{Bmatrix} = \begin{Bmatrix} u + (Qz - Ry) \\ v + (Rx - Pz) \\ w + (Py - Qx) \end{Bmatrix} \qquad [A58]$$

The $\{V_x, V_y, V_z\}$ velocity components can be calculated using [A53]-[A55] and the known α at the vane. The β at the vane is assumed to be small, which for this calculation works well. Since {P, Q, R} and {x, y, z} are known, $\{V_x, V_y, V_z\}$ can be used with [A58] to get the {u, v, w} at the CG. α at the CG then follows from [A20]. [A58] can then be used to calculate α at any point on the airplane.

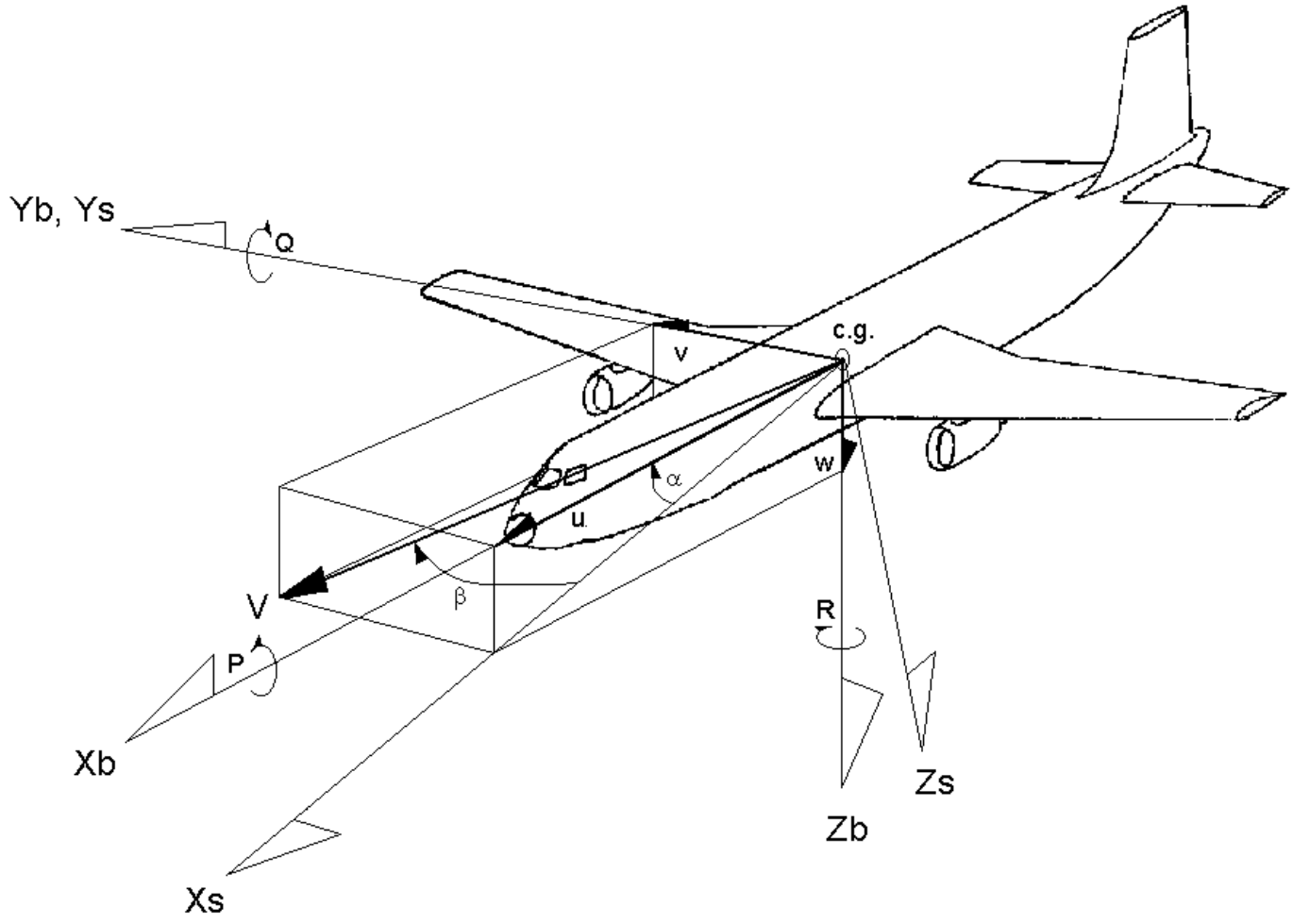

Figure A1. Airplane axis system showing definition of velocities, aerodynamic angles, and angular rates.

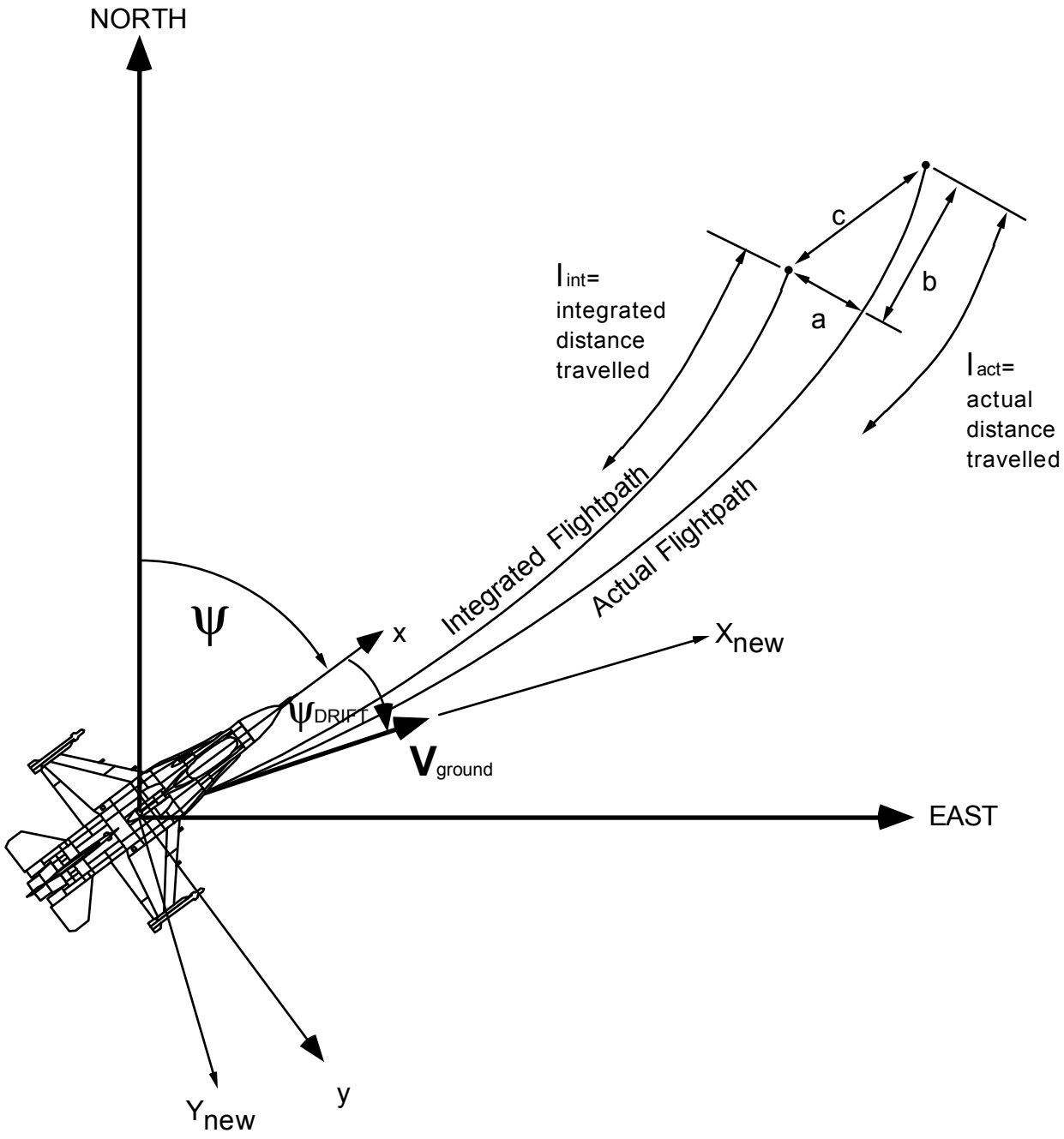

Figure A2. Conventions used in accelerometer bias calculations.

Appendix B

NASA Langley Research Center

Wake Vortex Modeling and Analysis

AA 587 Wake Vortex Investigation

Modeling and Analysis by NASA Langley Research Center

Fred H. Proctor [†], David Rutishauser, David Hamilton, George Switzer[+], Roland Bowles[‡], and Bill Buck[‡]

9 October 2002

[+]NASA Contractor, Research Triangle Institute

[‡]NASA Contractor, AeroTech Research, Inc.

[†]email: f.h.proctor@larc.nasa.gov

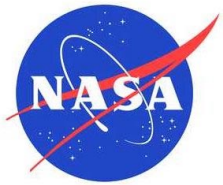

Outline

I. Accident Synopsis
II. Aircraft Wake Vortices: Background
III. Weather
IV. Models
    - APA
    - TASS 3-D
    - TASS 2-D
    - Proctor/Switzer
V. Summary and Conclusions
VI. Bibliography

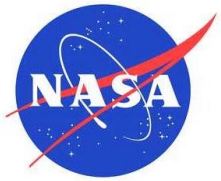

Plan view of Aircraft Trajectories

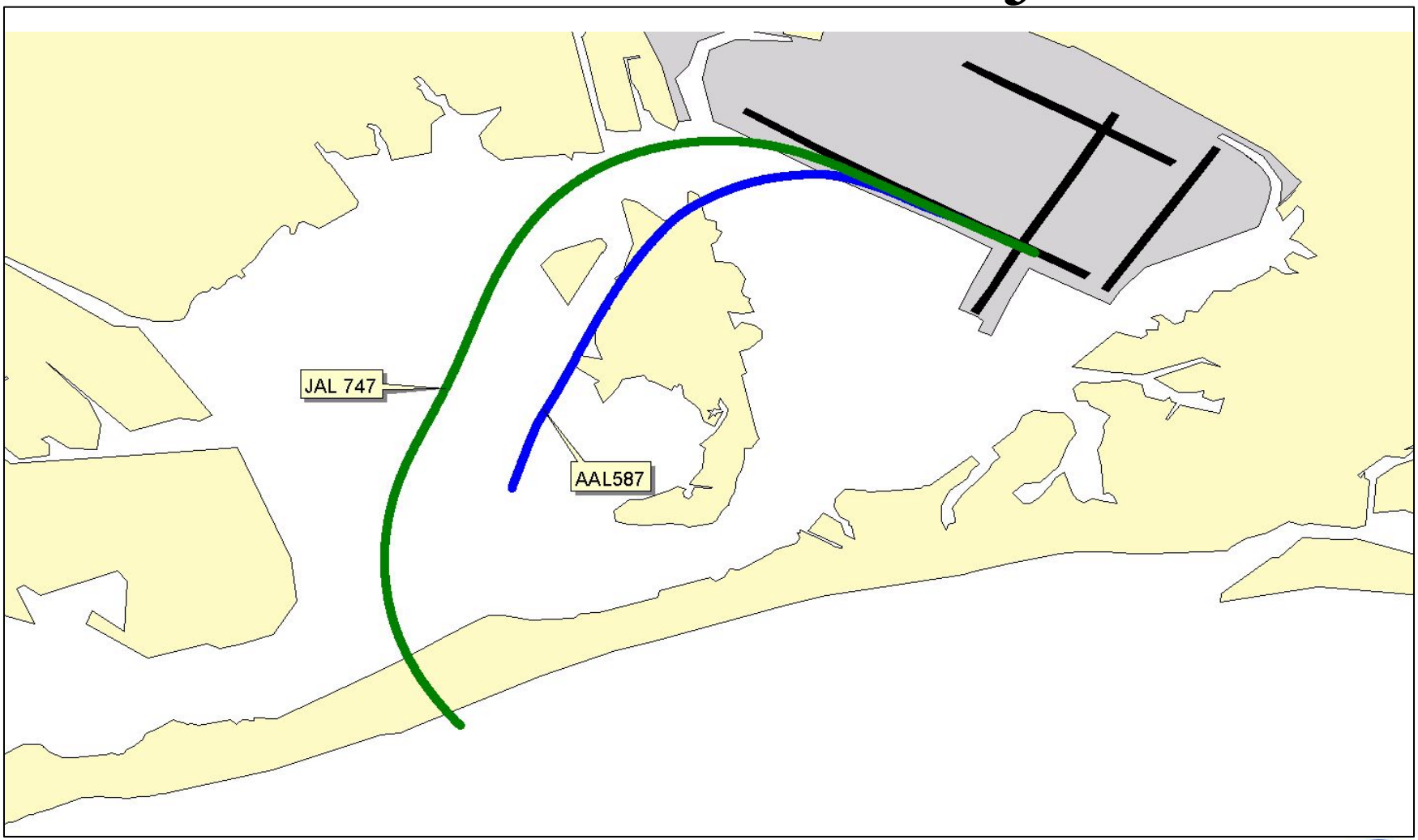

I. Accident Synopsis

- On 12 Nov 2001, 0917 EDT (1417 UTC), American Airline (AA) Flight 587 (Airbus A300-600) crashed ~103 seconds after liftoff from JFK Airport.
- NTSB reports two possible wake encounters (9:15:35 and 9:15:51), the last occurring 8 sec before the end of FDR and 18 sec before ground impact.
- Altitude of first and second encounters about 535 *m* (1750 *ft)* and 740 *m* (2430 *ft*) AGL, respectively.
- Japan Airlines (JAL) Flight 47 (B-747) took off 105 seconds ahead of AA 587.
- Flight path of JAL 47 was higher and upwind from AA 587.

II. Background
Aircraft Trailing Vortices (Wake Vortices)

- Vorticity --produced by aircraft lift-- wraps into a pair of counter-rotating vortices oriented horizontally along the flight path.
- Initial size and intensity depends on parameters of generating aircraft such as wing span, weight, and airspeed.
- The vortex hazard can be quantified in terms of the 5-15*m* average circulation (Hinton and Tatnall 1997).

The scale of a B-747 trailing vortex is made visible by industrial smoke in this sequence of photographs.

Wake Vortex Behavior

- Above the influence of the ground, wake vortices are transported laterally with the wind, while sinking due to mutual induction of the vortex pair.
- Their sink rate is a function of the vortex circulation.
- Crosswind shear may effect the sink rate of wake vortices.
- Ambient turbulence and vortex instabilities may distort its path.
- Ambient turbulence influences the time of vortex pair linking; i.e. the time of occurrence of crude vortex rings that are elongated along the flight path.

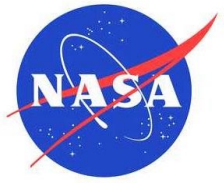

Wake Vortex Decay

- Lifetime of wake vortices are from 15 *sec* to several minutes depending on atmospheric conditions.
- Wake vortices have longest lifetime within environments having weak turbulence and near-neutral thermal stratification.
- Aircraft wake vortices decay primarily due to influences of:
  - Intensity of ambient turbulence (eddy dissipation rate - ε)
  - Magnitude of thermal stratification (Brunt Vaisala frequency - N)
  - Ground interaction
  - Three-dimensional instabilities.
- Three-dimensional instabilities result in rapid vortex decay.
  - Onset time is a function of: aircraft parameters, ε, and N.

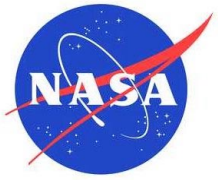

Vortex Normalization

- Vortex parameters
  - Initial vortex separation: b_0
  - Initial vortex circulation: Γ_0
  - Normalized Height: $Z = z/b_0$
  - Normalized Time: $T = t\,\Gamma_0/2\pi b_0^2$
  - Initial Descent velocity: $V_0 = \Gamma_0/2\pi b_0$
  - Normalized Circulation: $\Gamma = \Gamma\,/\,\Gamma_0$

Environmental Normalization

- Stratification parameters
  - Brunt-Vaisala frequency $N^2 = \frac{g}{\theta}\frac{\partial\theta}{\partial z}$
  - $N^* = \frac{2\pi N b_0}{\Gamma_0}$

  where θ is potential temperature.
- Turbulence intensity levels
  - Eddy Dissipation Rate ε
  - $\varepsilon^* = \frac{\left(\varepsilon b_0\right)^{1/3}}{V_0}$

Wake Vortex Time to Link vs Turbulence Intensity (Proctor and Switzer 2000)

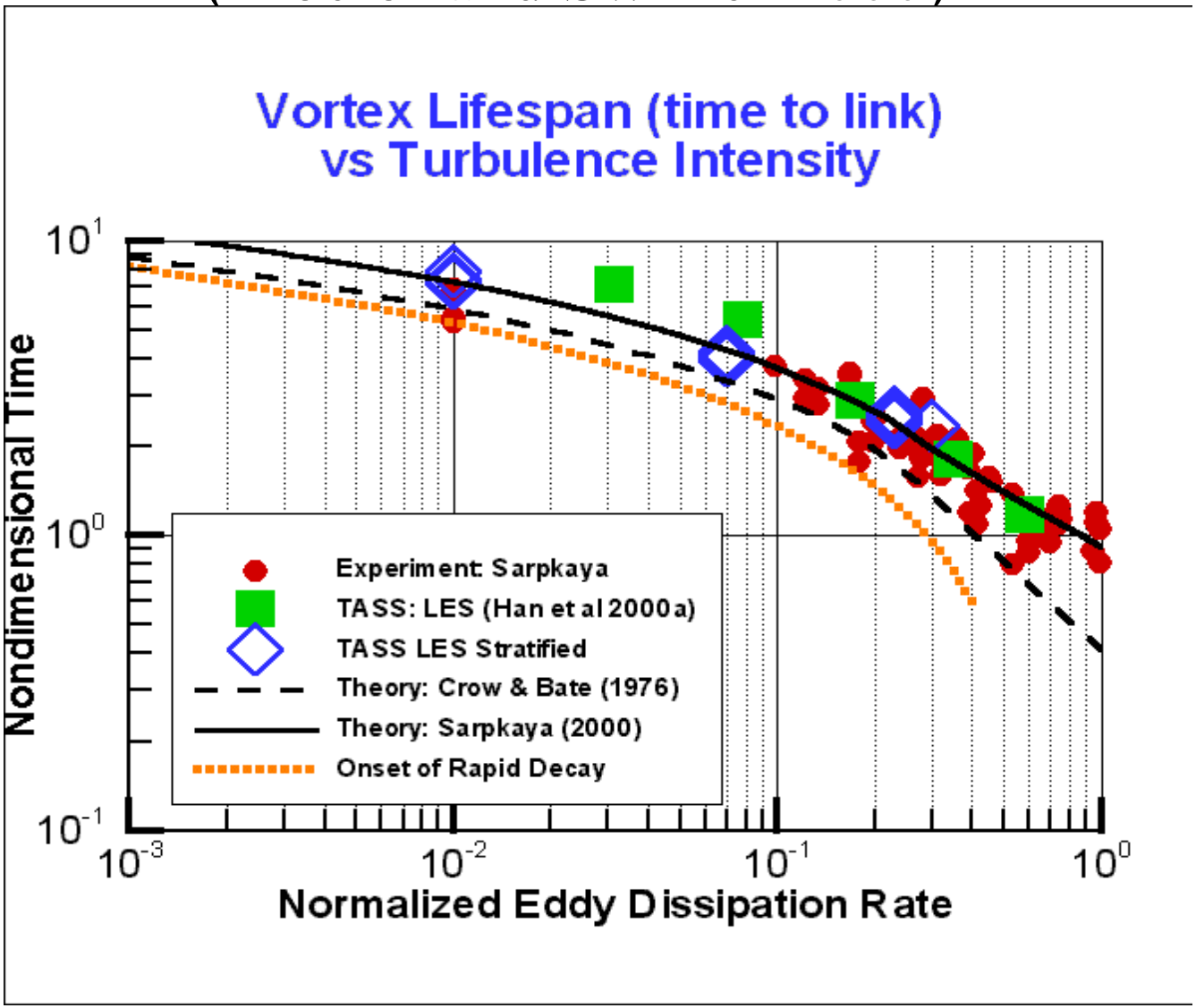

III. Weather Associated with Accident

- VMC (Visual Meteorological Conditions)
  - Clear Skies
  - Good Visibility
  - No Unusual Weather Conditions

Ambient Winds

- Wind profiles provided by NTSB.
- Derived from FDR of JAL 47 and AA 587.
- Comparison shows significant differences at elevation of first vortex encounter (~1750 ft).

Ambient Wind Direction Comparison

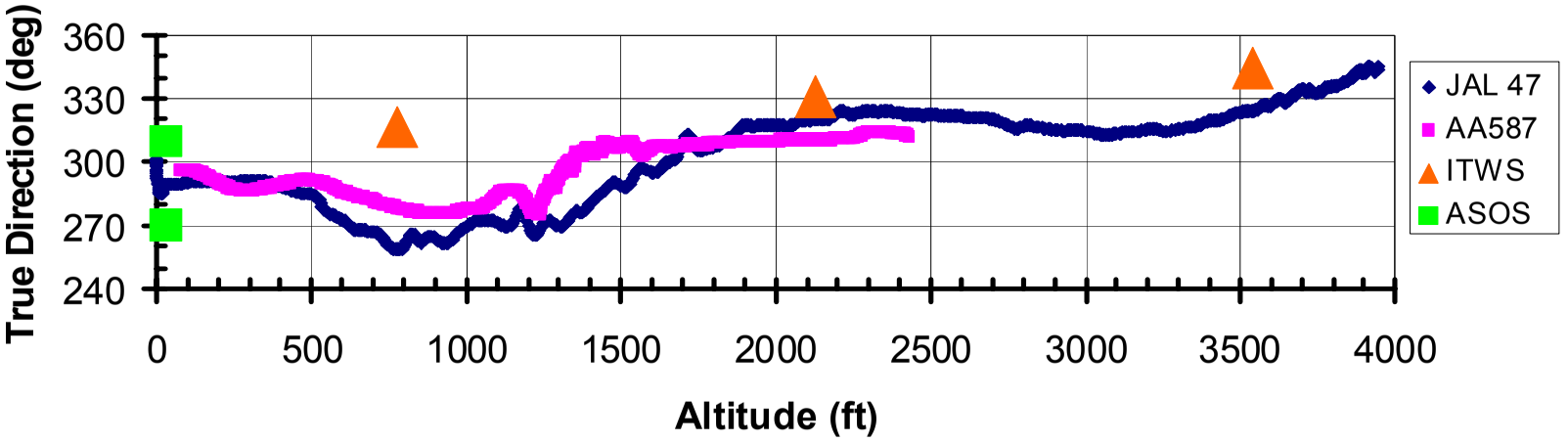

Ambient Wind Speed Comparison

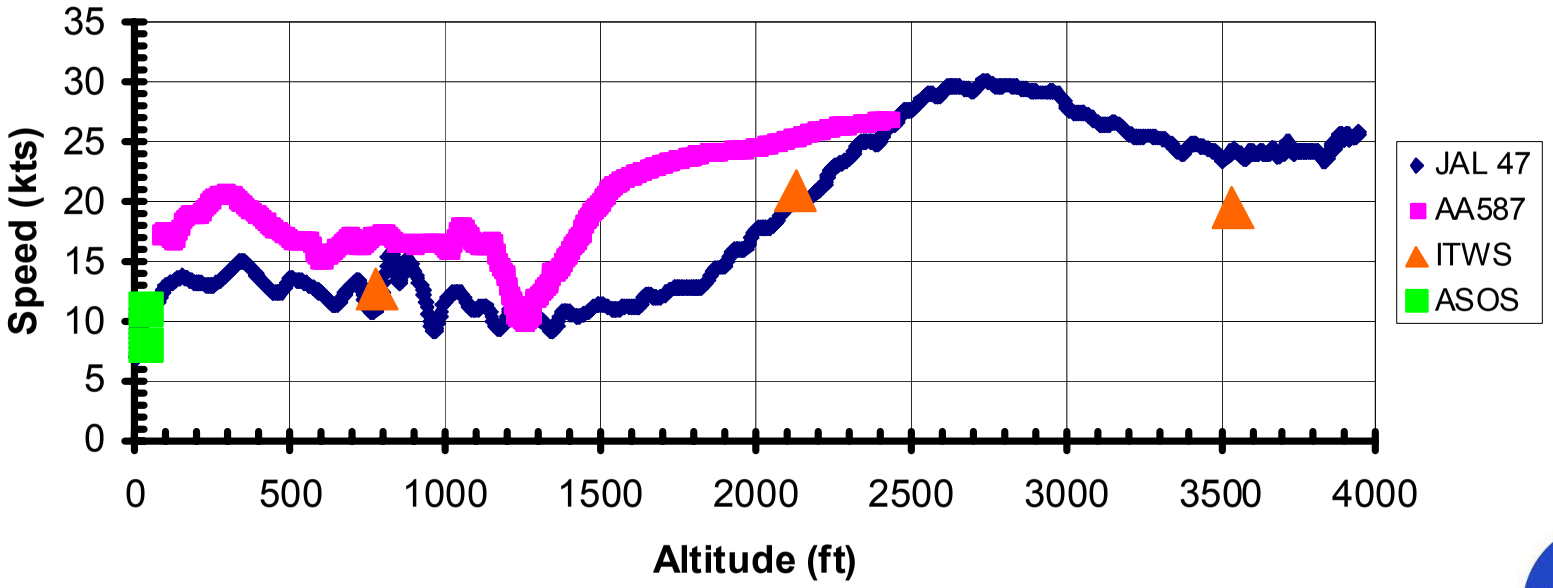

Ambient Horizontal Winds

- As derived from JAL 47
  - crosswind
  - along track wind
  - vertical shear
  - ambient turbulence intensity.

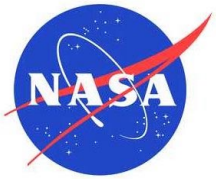

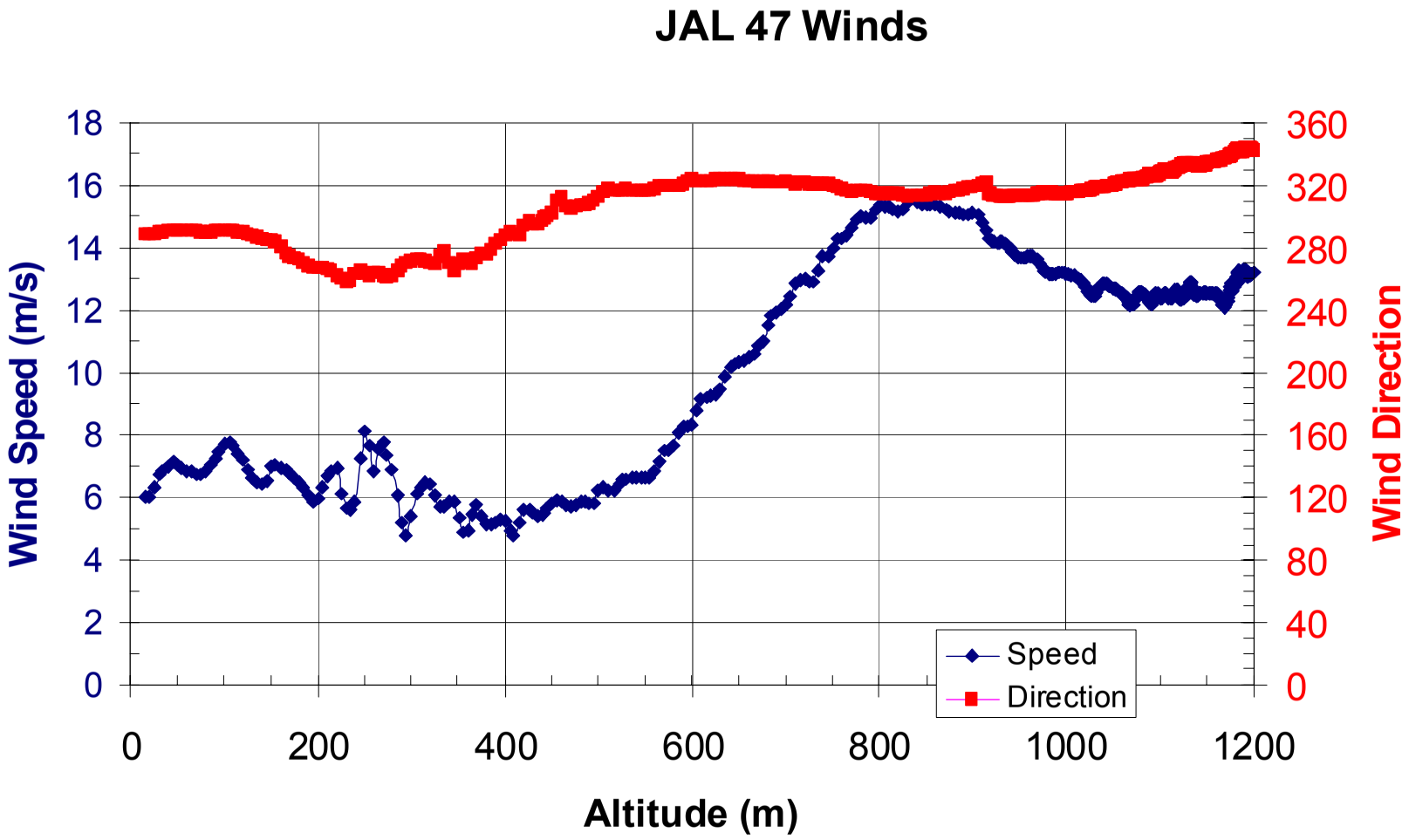
JAL 47 Winds
Wind Speed (m/s)
Wind Direction
Altitude (m)
Speed
Direction
0
2
4
6
8
10
12
14
16
18
0
40
80
120
160
200
240
280
320
360
0
200
400
600
800
1000
1200

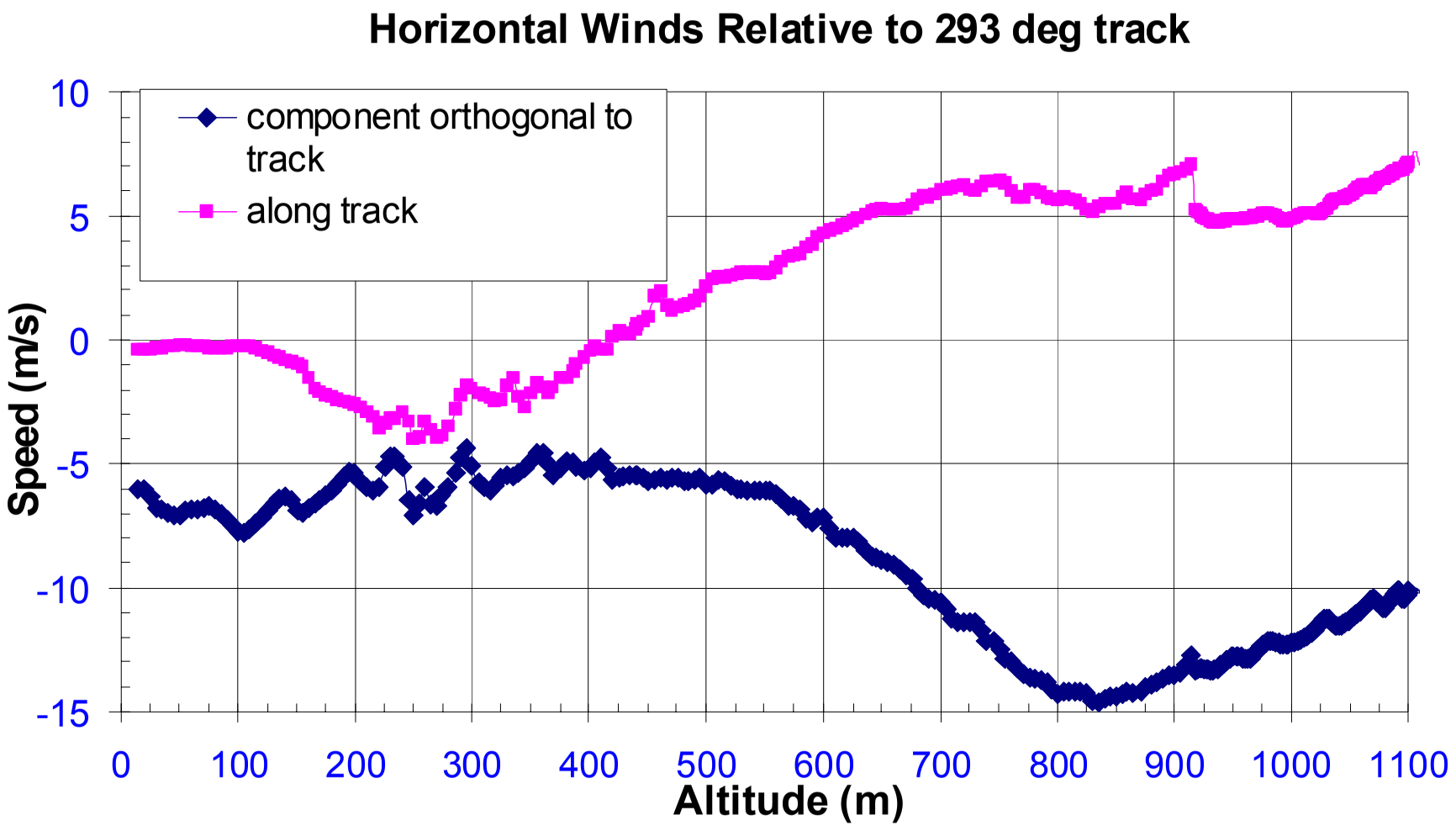
Horizontal Winds Relative to 293 deg track
component orthogonal to track
along track
Speed (m/s)
10
5
0
-5
-10
-15
0
100
200
300
400
500
600
700
800
900
1000
1100
Altitude (m)

Crosstrack Component of Ambient Wind Shear

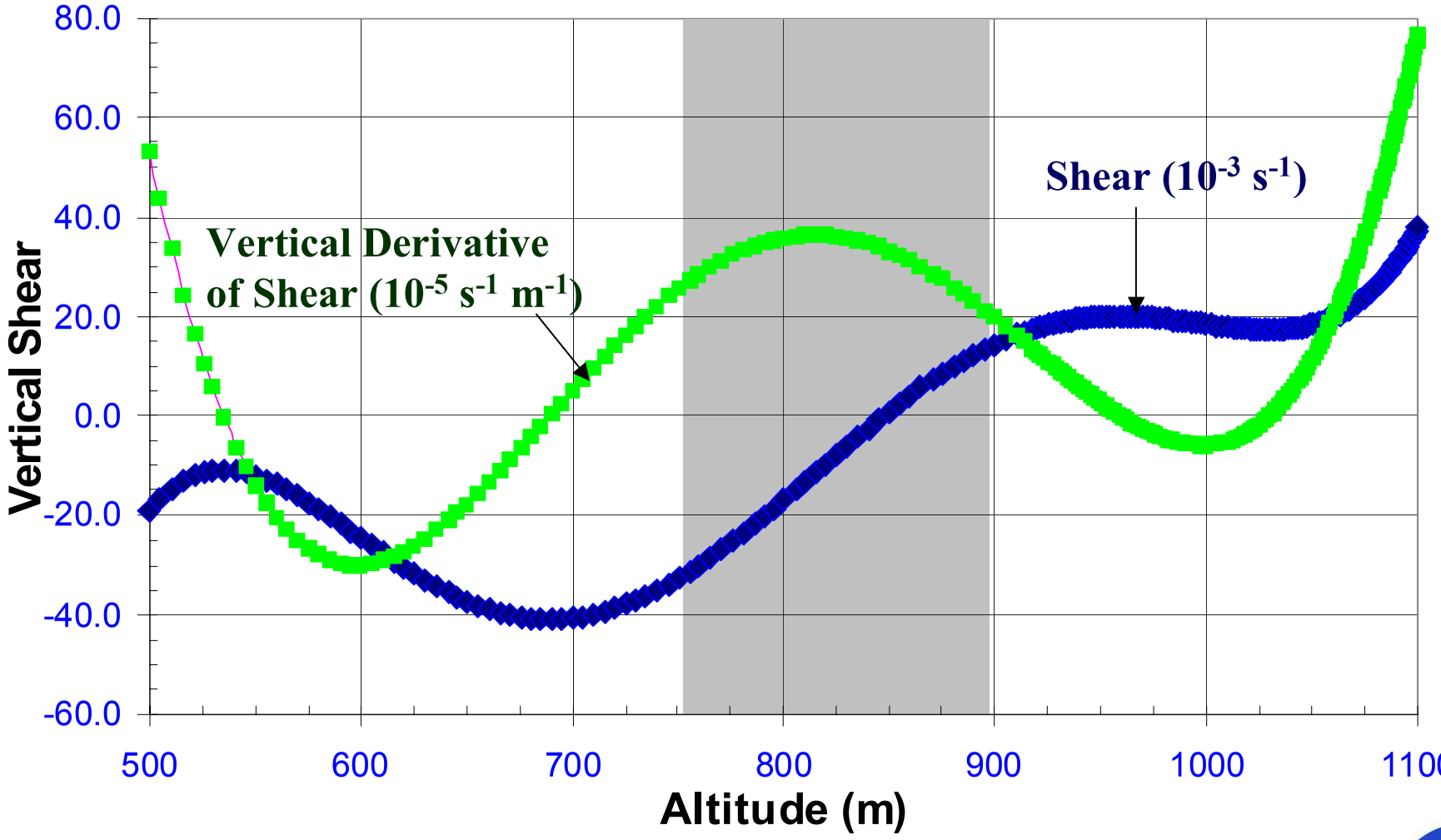

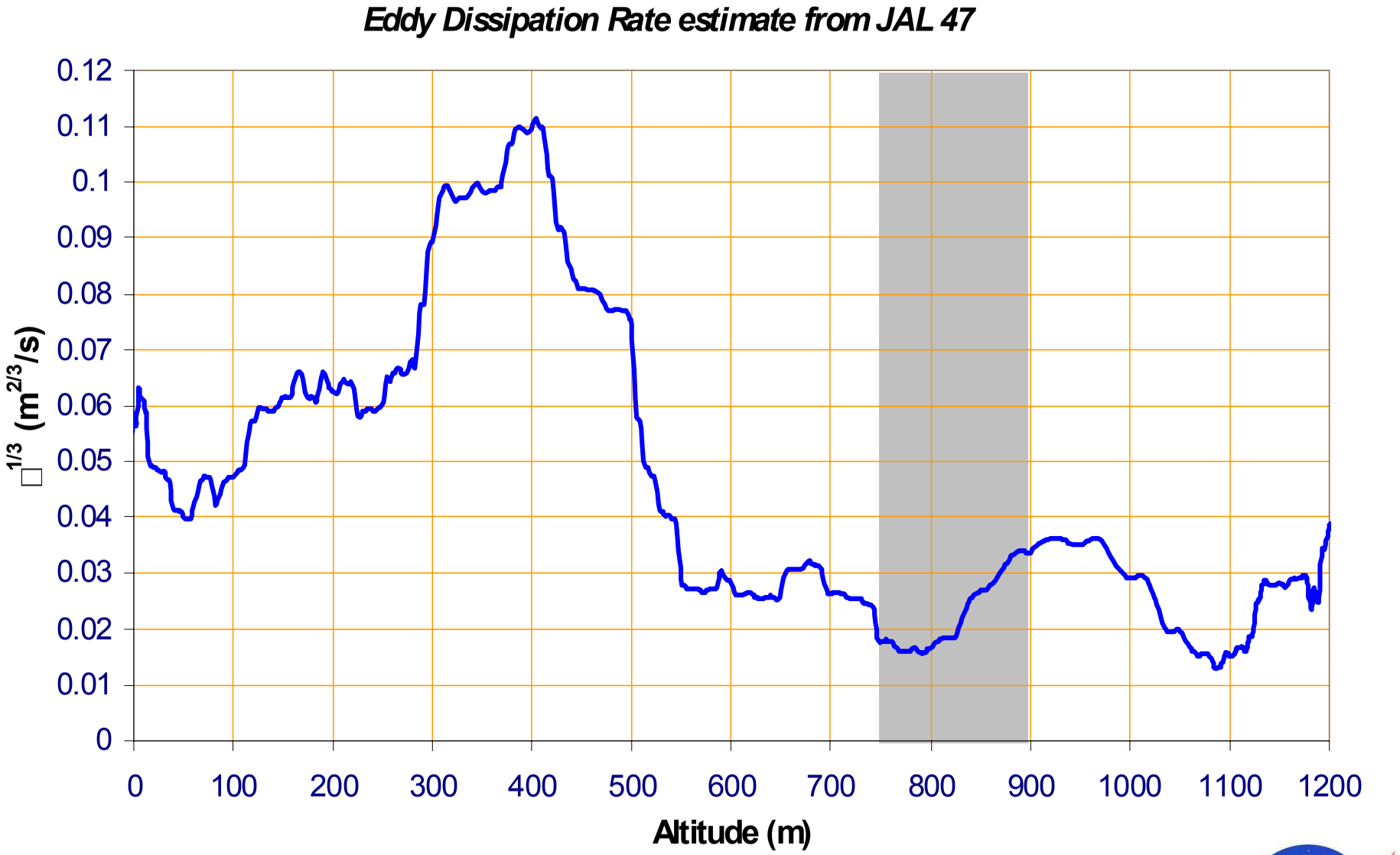
Eddy Dissipation Rate estimate from JAL 47
0.12
0.11
0.1
0.09
0.08
0.07
0.06
0.05
0.04
0.03
0.02
0.01
0
□1/3 (m2/3/s)
0
100
200
300
400
500
600
700
800
900
1000
1100
1200
Altitude (m)

Elevation of Suspected Wake Vortex Encounters

- The two suspected wake vortex encounters occur at altitudes of 535 *m* and 740 *m*, respectively.
- Both occurrences are above the top of atmospheric boundary (has top near 500 *m* AGL).

Characteristics of Ambient Atmosphere at altitudes between 535-900 *m*

- Weak turbulence intensity ($\varepsilon = 2.5 \times 10^{-5}\ m^2 s^{-3}$).
- Weak thermal stratification ($N = 8.77 \times 10^{-3}\ s^{-1}$).
- Moderate crosswind in region of interest
  - Wind speed and direction: 6-15 *m/s* from ~315^0
  - Wind speed maximum at 850 *m* AGL
  - Weak vertical wind shear
  - Significant vertical derivative of wind shear.

IV. Wake Prediction Models Assumed in Study

- APA
- TASS 3-D
- TASS 2-D
- Proctor/Switzer

AVOSS Prediction Algorithm (APA)

Prediction Subsystem

- Semi-empirical, real-time engineering model of wake vortex transport and decay
- Accepts vertical profiles of winds, temperature, atmospheric turbulence, and generating aircraft physical parameters as input
- Outputs time history of wake vortex trajectory and circulation
- Wake wind field distribution not predicted

Contributors:

- *NASA*
- *North West Research Associates*
- *Naval Post-Graduate School*

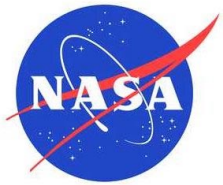

APA Basic Assumptions

- Simple semi-empirical framework.
- Fine-tuned and tested with real wake vortex measurements.
- Does not account for effects from ambient windshear.
- References: Robins and Delisi (2002), Sarpkaya *et al* (2001), Sarpkaya (2000).

APA Initialization

- Initialized with appropriate aircraft parameters representing JAL 47 (generating aircraft).
- For first “wake vortex encounter,” separate studies are conducted for each of the two wind profiles.
- Second “wake vortex encounter” assumes JAL 47 wind profile only.

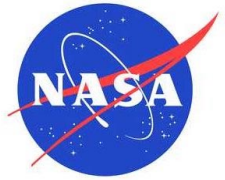

APA Results

- At time of suspected first wake encounter (9:15:35 EST):
  - APA predicts JAL 47 wake to be in close proximity to AA 587 when initialized with wind profile from AA 587.
  - APA does not predict encounter when initialized with wind profile from JAL 47.
- At time of second wake encounter (9:15:51 EST):
  - APA predicts encounter with JAL 47's wake (assumes wind profile from JAL 47).
- Age of the vortex is approximately 97 seconds at time of either encounter.
- Circulation of the wake vortex is 344 $m^2 s^{-1}$ (63% of initial strength) at either encounter.

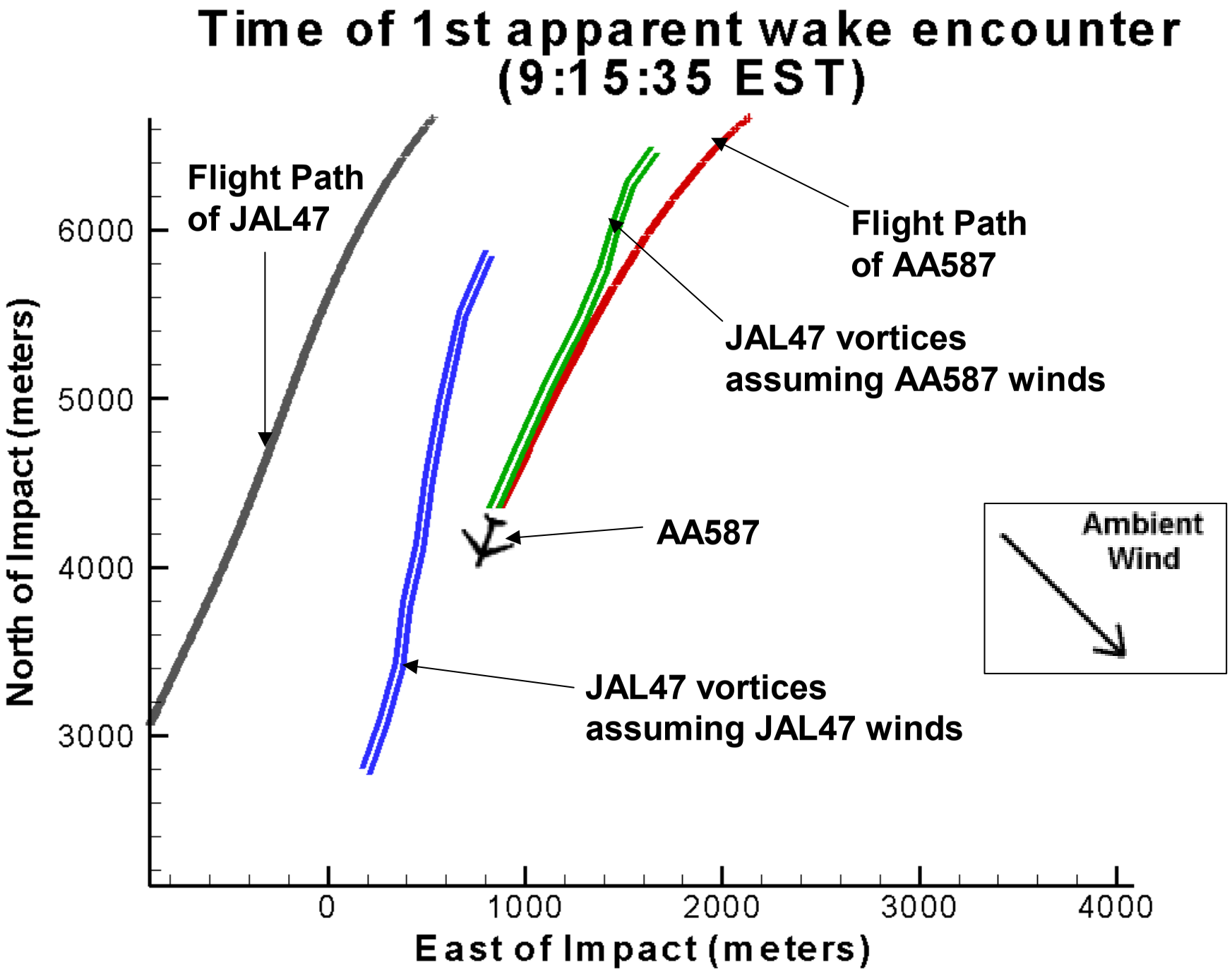
Time of 1st apparent wake encounter
(9:15:35 EST)
Flight Path
of JAL47
Flight Path
of AA587
JAL47 vortices
assuming AA587 winds
AA587
Ambient
Wind
JAL47 vortices
assuming JAL47 winds
North of Impact (meters)
6000
5000
4000
3000
0
1000
2000
3000
4000
East of Impact (meters)

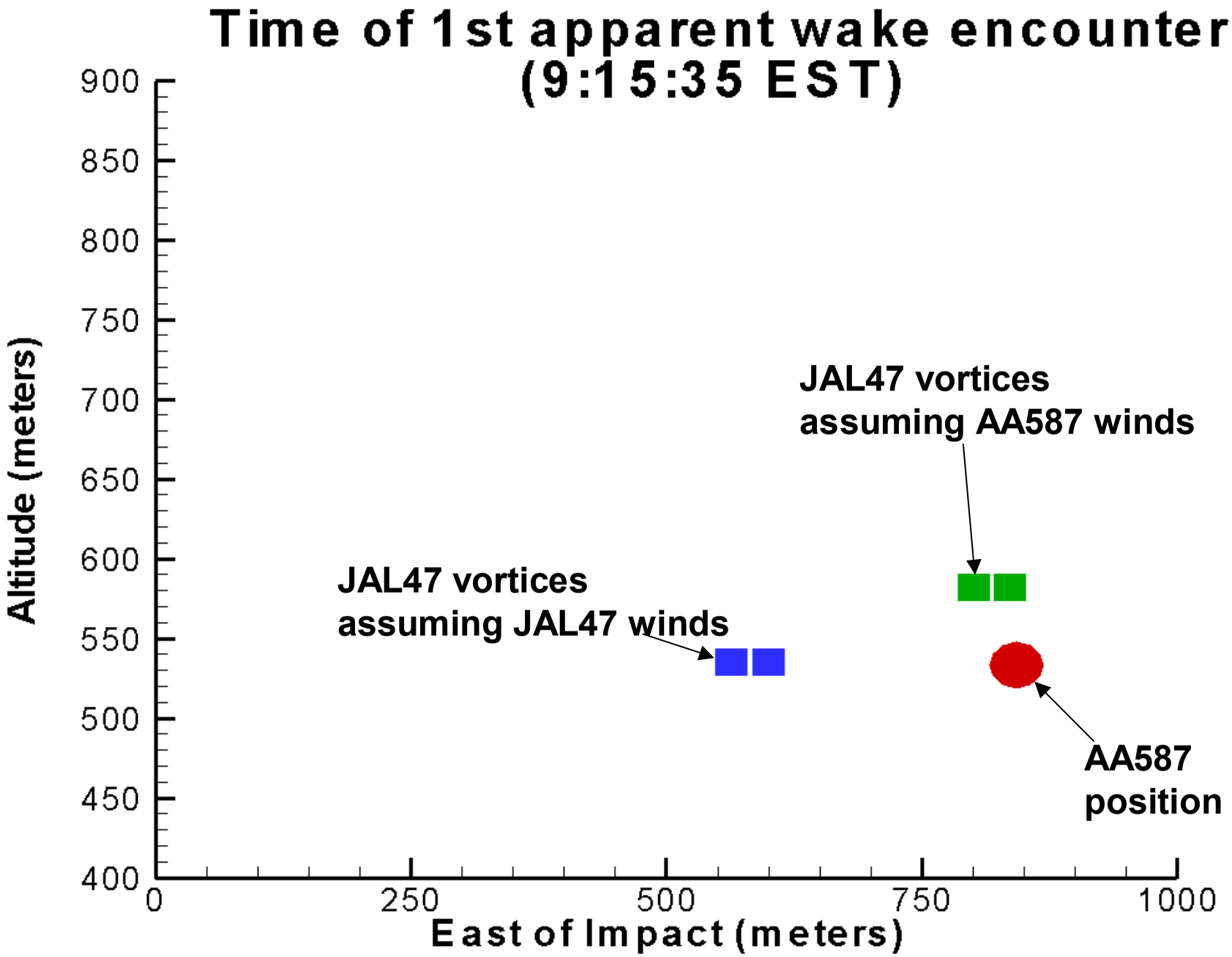
Time of 1st apparent wake encounter
(9:15:35 EST)
Altitude (meters)
900
850
800
750
700
650
600
550
500
450
400
0
250
500
750
1000
East of Impact (meters)
JAL47 vortices
assuming AA587 winds
JAL47 vortices
assuming JAL47 winds
AA587
position

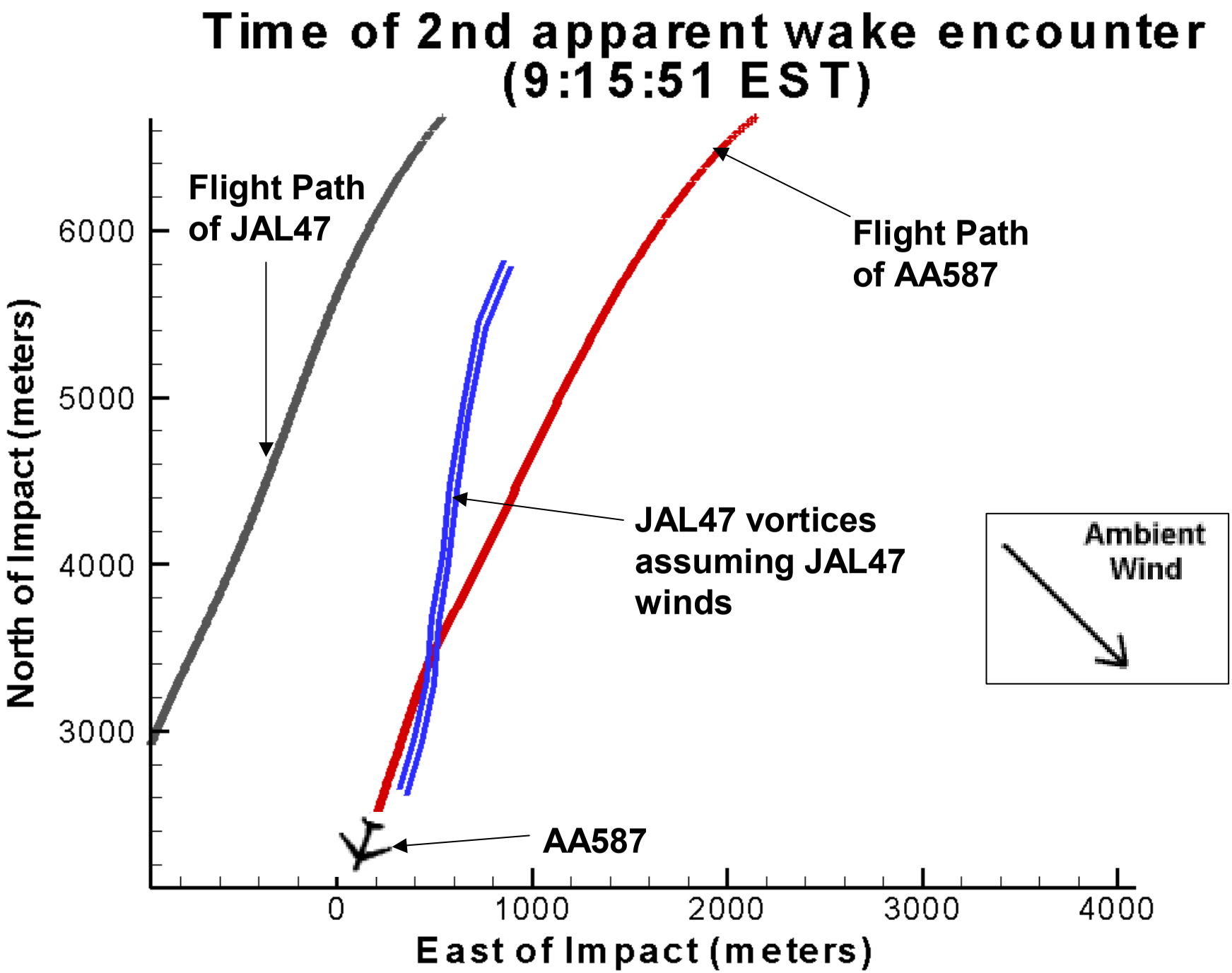
Time of 2nd apparent wake encounter
(9:15:51 EST)
Flight Path
of JAL47
Flight Path
of AA587
JAL47 vortices
assuming JAL47
winds
Ambient
Wind
AA587
North of Impact (meters)
6000
5000
4000
3000
0
1000
2000
3000
4000
East of Impact (meters)

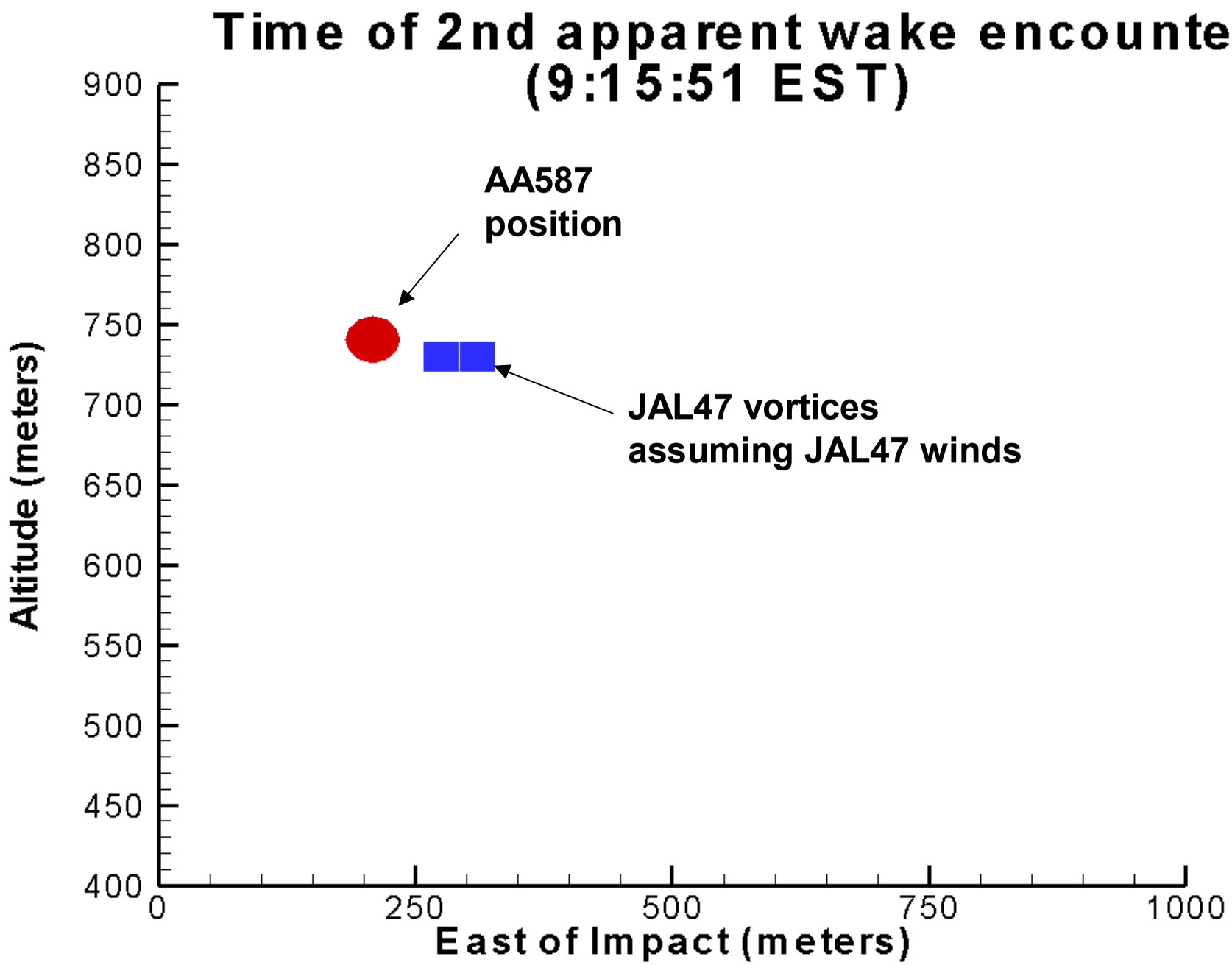
Time of 2nd apparent wake encounter
(9:15:51 EST)
AA587
position
JAL47 vortices
assuming JAL47 winds
Altitude (meters)
900
850
800
750
700
650
600
550
500
450
400
0
250
500
750
1000
East of Impact (meters)

TERMINAL AREA SIMULATION SYSTEM (TASS)

- 3-D Large Eddy Simulation (LES) Model
- Meteorological Framework
- Prognostic Equations for:
  - 3-Components of Velocity - Pressure
  - Potential Temperature - Rain
  - Water Vapor - Snow
  - Liquid Cloud Droplets - Hail/graupel
  - Cloud Ice Crystals

- 1st-order subgrid turbulence closure with Richardson-number dependency.
- Accepts vertical profiles of winds, temperature, and moisture as input.
- Wake vortex simulations can be initialized with atmospheric turbulence, and generating aircraft physical parameters.

TASS -- History

- Development began in 1983 for NASA/FAA Windshear Program.
- Recently applied in NASA's Wake Vortex Program for improving airport capacity (i.e. AVOSS).
- Currently being used in NASA/FAA program to study Convectively Induced Turbulence and improve Aviation Safety.
- Generation of data sets for Windshear Sensor Certification.
- Generation of data sets for potential certification of onboard turbulence radars.
- Supported NTSB Investigation of 1994 Charlotte and 1999 Little Rock Aircraft Accidents.

3-D TASS Simulation

- Simulates wake vortex structure assuming JAL 47 (B-747) as generating aircraft.
- Initialized with ambient turbulence and thermal stratification representing ambient environment of AA 587 and JAL 47.
- Assumes periodic boundaries, and no wind shear.
- Outputs time-dependent 3-dimensional velocity fields.

3-D TASS Model: Initialization

- Domain (*x*-along track, *y*-cross track, and *z*-vertical directions):
  - 960 x 648 x 360 meters
  - Grid resolution of 2 x 1.5 x 1.5 meters
- Atmospheric Conditions
  - No ambient wind shear
  - Slightly stable stratification ($N^* = 0.257$)
  - Light ambient turbulence ($\varepsilon^* = 0.065$)
- Initial Wake Vortex Conditions for JAL 47
  - Average *5-15m* Circulation: 490.5 $m^2 s^{-1}$ ($\Gamma_{◎} = 547\ m^2 s^{-1}$)
  - Separation of vortex pair: 50.5 *m*
  - Vortex core radius: 3 *m*

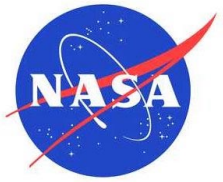

3-D TASS Model Results

Output Time: 100 seconds

- age of JAL wake at estimated encounter time
- 100 *s* = 3.41 nondimensional time units
- Average *5-15 m* circulation at output time: 393 $m^2 s^{-1}$ (80% of initial strength).
- Vertical separation:

	Aircraft Flight Paths	Vortex Descent Values
Min	124 *m*	151 *m*
Max	158 *m*	176 *m*

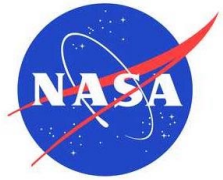

TASS Simulated Wake Vortex
3-D Perspective at T= 100 sec

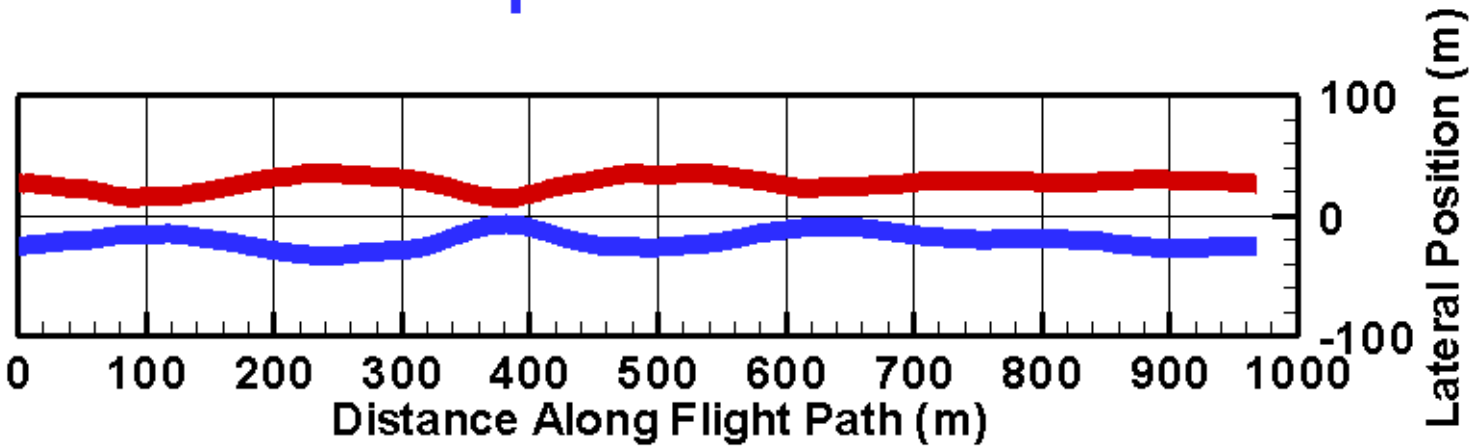

Top View

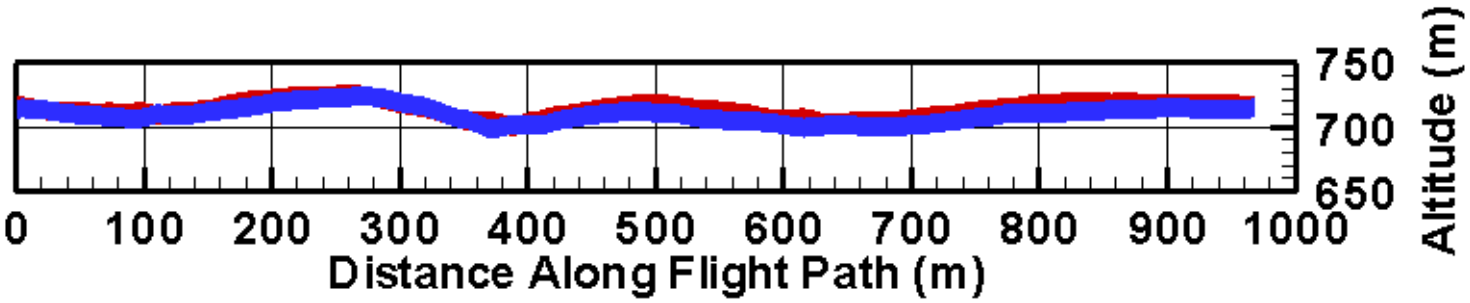

Side View

GFS/FHP
8/2002

NASA

Vertical Cross Section of Velocity

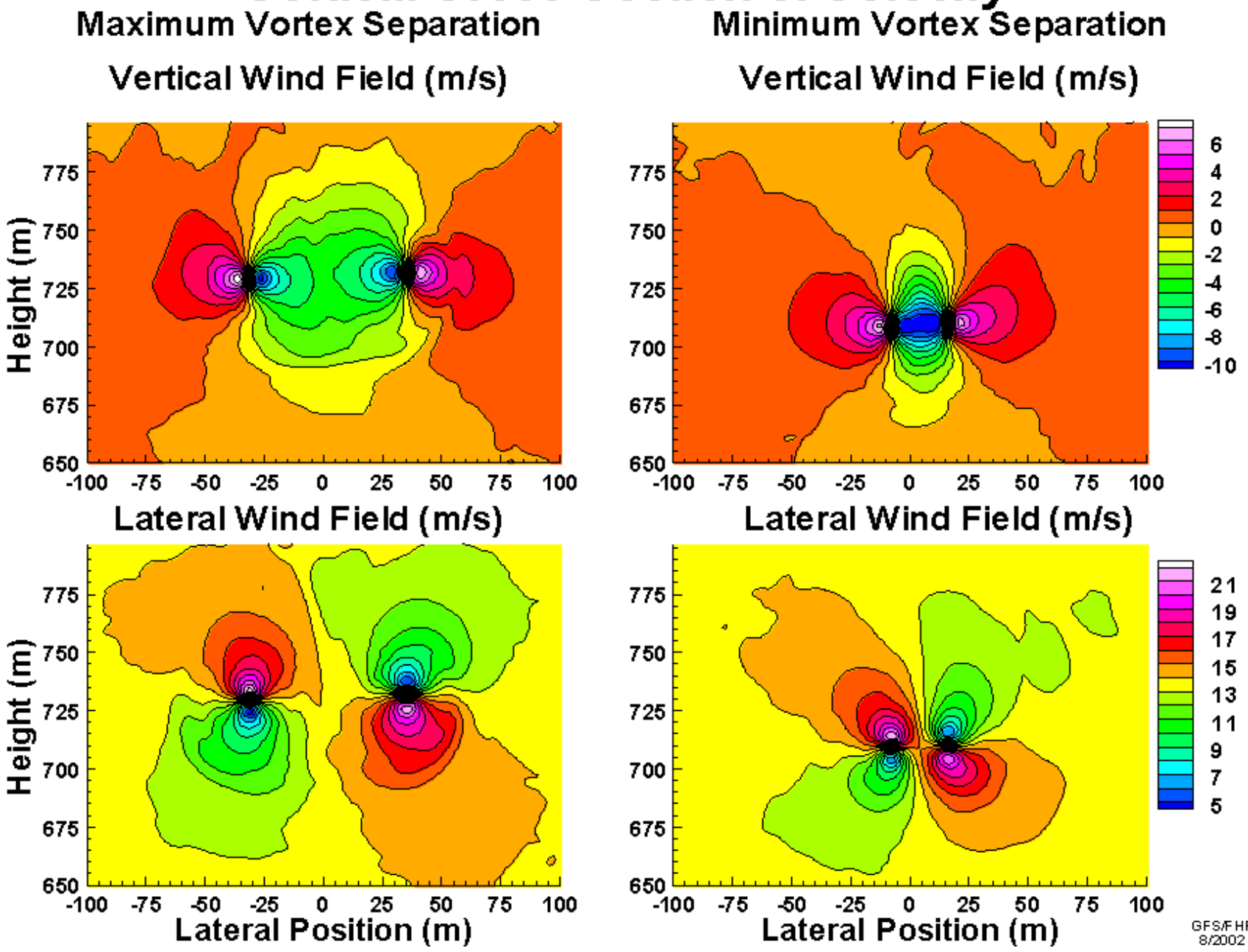

Vertical Cross Section of Velocity Vectors

(Ambient Wind Removed)

Wind Vectors at Maximum Separation

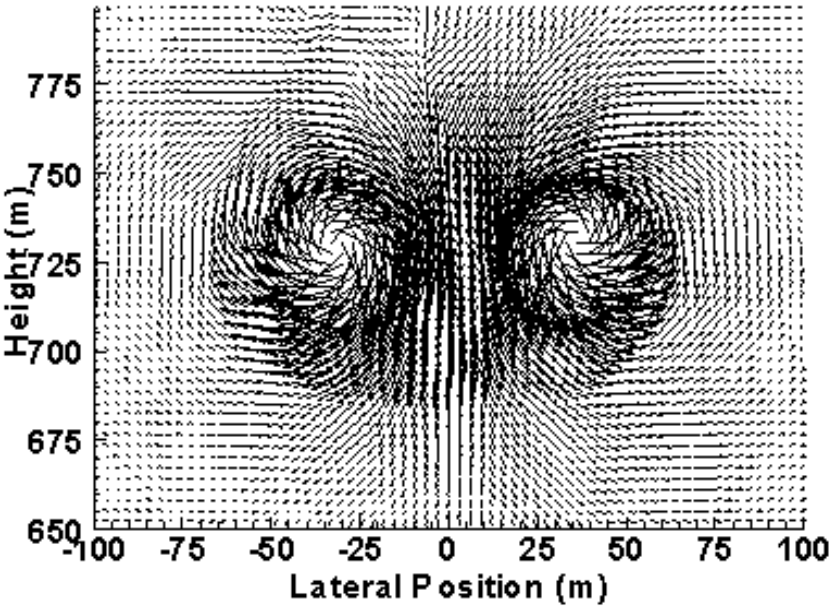

Wind Vectors at Minimum Separation

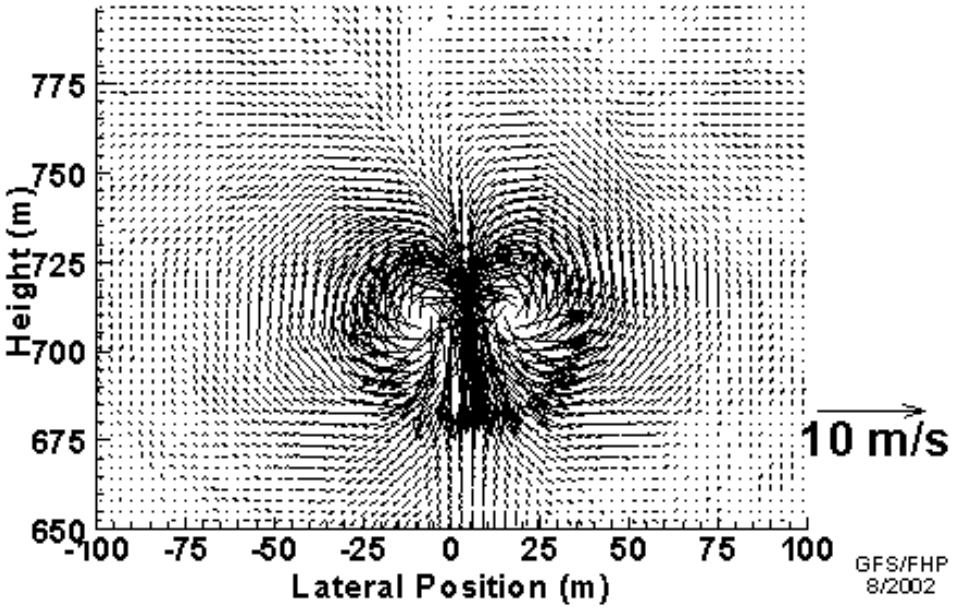

Data sets from 3-D simulation - Options:

- Can provide full 3-D data set at t=100 seconds.
  - Very large: 481 *x* 432 *x* 241 data points for each of 3 velocity components.
- Can provide one or more *y-z* cross sections.
  - 432 *x* 241 data points per cross section for each velocity component.
- Can provide simple algebraic model fit of a representative *y-z* cross section.
  - Simple model described next.

Simple 2-D Algebraic Model

- Describes velocity field in *y*-*z* cross-section.
- Two superimposed velocity fields representing wake vortex pair.
- Circulation based on TASS 3-D simulation at t=100 seconds.
- Rolling moments and other aircraft dynamics can be easily obtained (e.g. Tatnall 1995).

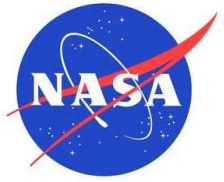

Wake Vortex Tangential Velocity
at Suspected Time of Vortex Encounter

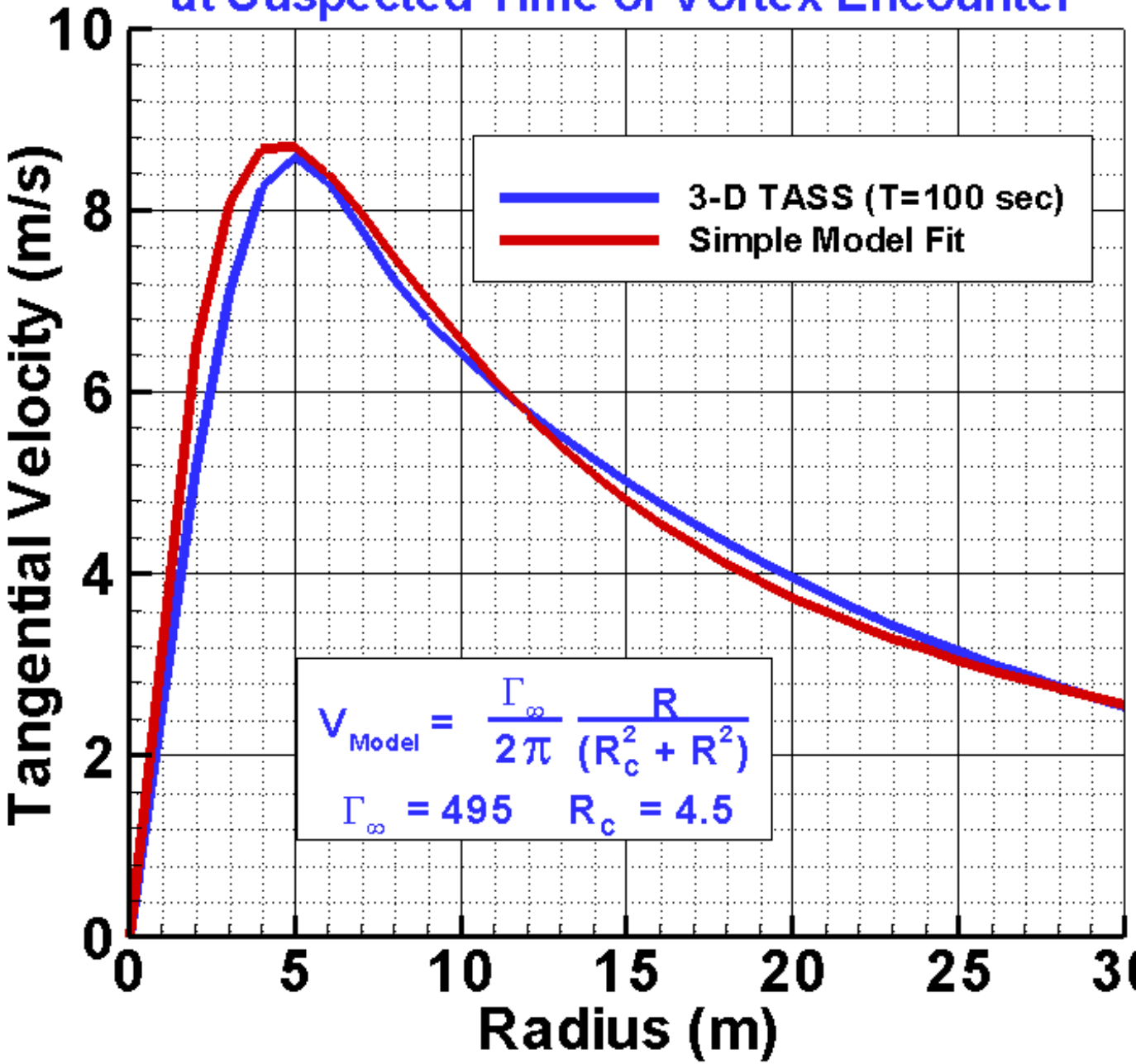

GFS/FHP

NASA

Coordinates for Vortex System

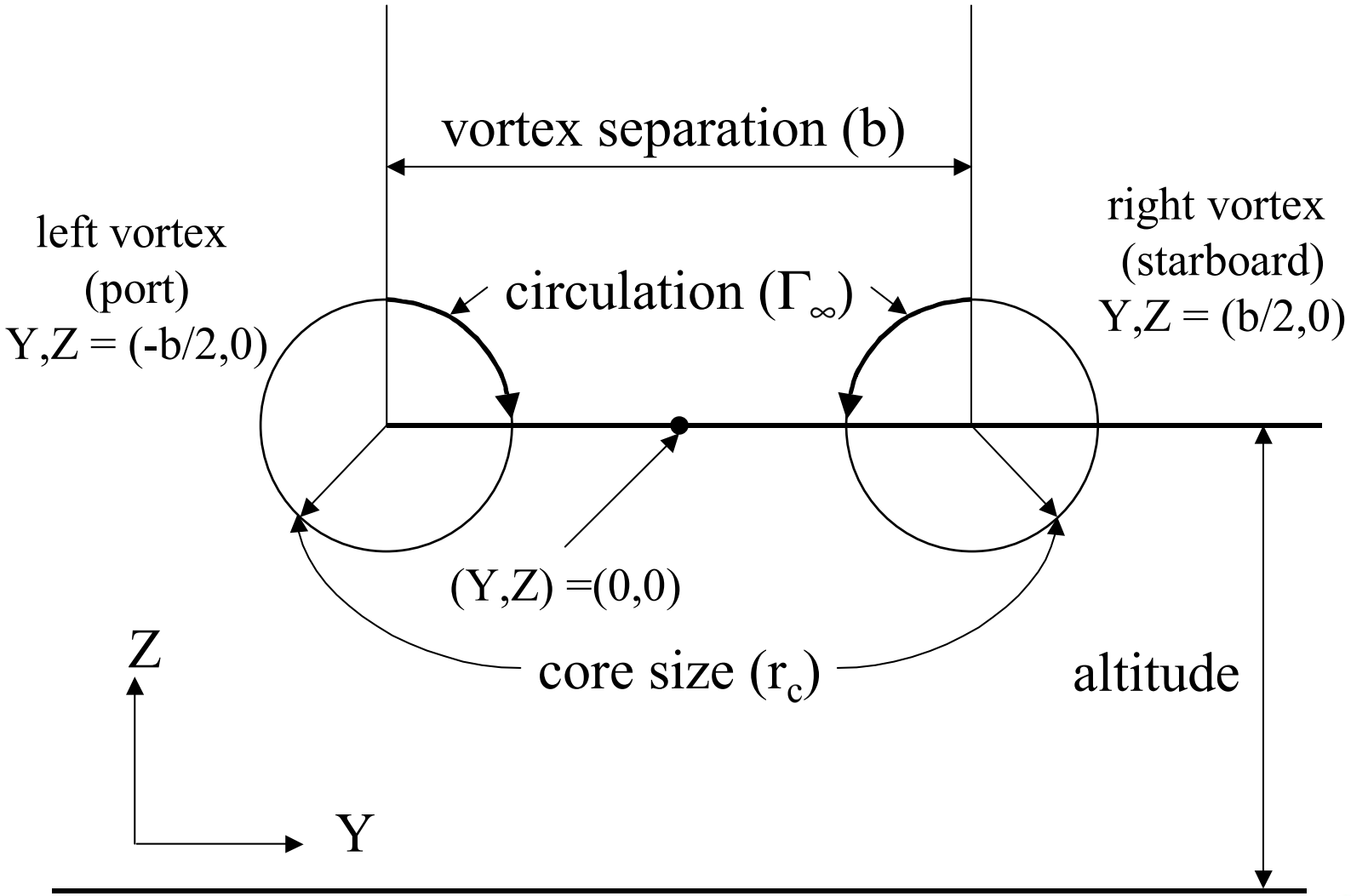

Equations for Vortex System Velocity

(adapted from Tatnall 1995)

$$\vec{V} = V\hat{j} + W\hat{k}$$

$$\vec{V} = \left\{ \frac{\Gamma_\infty (Z - Z_0)}{2\pi[(Y + b/2)^2 + (Z - Z_0)^2 + r_c^2]} + \frac{\Gamma_\infty (Z - Z_0)}{2\pi[(Y - b/2)^2 + (Z - Z_0)^2 + r_c^2]} + V_{ambient} \right\} \hat{j} \quad +$$

$$\left\{ \frac{\Gamma_\infty \left(Y + b/2\right)}{2\pi[(Y + b/2)^2 + (Z - Z_0)^2 + r_c^2]} - \frac{\Gamma_\infty \left(Y - b/2\right)}{2\pi[(Y - b/2)^2 + (Z - Z_0)^2 + r_c^2]} \right\} \hat{k}$$

Where: $\Gamma_\infty = 495\ m^2/s$, $r_c = 4.5\ m$, $Z_0 = 0$, and $b = 50.5\ m$

$Y,Z = (0,0)$ at midpoint between vortex pair and the
Vortex centers are located at $Y,Z = (\pm b/2, 0)$

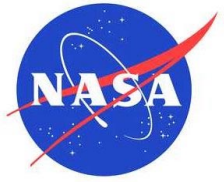

Equations for Vortex System Velocity
(continued)

Parameters for cross-sections at Maximum and Minimum Vortex Separation:

At Maximum Separation:

$\Gamma_\infty = 495\ m^2/s$, $r_c = 4.5\ m$, $Z_0 = 11$ m, and $b = 67.6\ m$

At Minimum Separation:

$\Gamma_\infty = 495\ m^2/s$, $r_c = 4.5\ m$, $Z_0 = -10$ m, and $b = 22.6\ m$

Downstream distance between Maximum and Minimum separation ~ 130 m

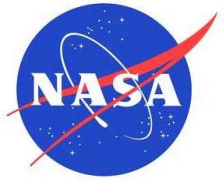

Summary from 3-D TASS

- An encounter time of 100 *s* would be prior to the onset of vortex linking and subsequent rapid decay.
- Weak sinusoidal oscillations would be present in the wake at the time of vortex encounter.
- Wake vortex position and strength is similar to that predicted by APA (although slightly stronger).
- Lateral dimension of the wake vortex oval is about 130 *m*.
- Simple model of the wake vortex wind field is proposed based on the results of TASS.

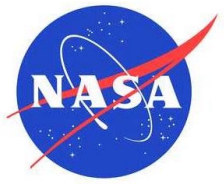

2-D TASS

- Useful for examining effect of vertical variation in ambient crosswind on vortex trajectory (e.g., Proctor 1998).
- Initialized similar to 3-D TASS, but includes ambient wind profile.
- Predicts time-dependent two-dimensional wind field in *y*-*z* cross plane.
- Cannot reliably predict vortex decay due to 2-D limitation.

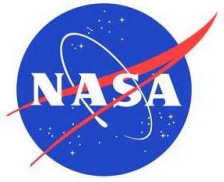

2-D TASS Results

- Sink rate of port vortex reduced by vertical change in crosswind shear.
- Descent of port vortex stalls about 75-110 *m* below generation height.
- Starboard vortex descends to lower altitudes.
- Angle between port and starboard vortex about 45 degrees after 100 *s*.

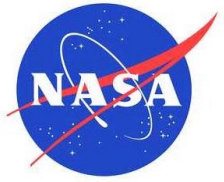

Proctor/Switzer Model

- Similar to Sarpkaya's (2000) decay model that is used in APA.
- Semi-empirical model with separate equations for vortex transport and decay.
- Based on results from parametric studies with 3-D TASS.
- Described in Switzer and Proctor (2002).

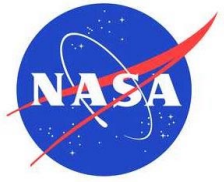

Comparison of Model Data for second encounter time*

*Assuming wind profile from JAL 747 and vortex age of 100 seconds
†For port vortex

Vortex Parameters	Estimated from Aircraft Data	APA	PROC/SWIT Model	3-D TASS	2-D TASS
Vertical Descent (*m*)	125-160	140	162	151-176	Port: 77-106 Starboard: 131-152
Lateral Drift from Aircraft Track† (*m*)	1400-1600*	1450	1450	1430-1465	Port: 1321-1418 Starboard: 1221-1372
5-15 *m* Average Circulation (m^2/s)	N/A	344	397	391	N/A

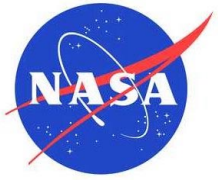

V. Summary & Conclusions

- Analysis shows that the flight path of AA 587 was downwind and below the path of JAL 47.
- Models indicate that the wake vortex from JAL 47 was likely transported into the path AA 587.
- Atmospheric conditions aloft were favorable for a slow rate of vortex decay.
- AA 587 would have encountered a B-747 wake vortex with an age of about 100 seconds – at a time *prior* to vortex linking and rapid vortex decay.
- The predicted circulations at the time of the apparent encounter were 63-80% of the initial strength.

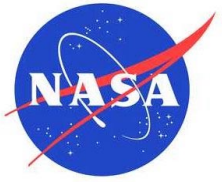

Bibliography

- Crow, S.C., and E.R. Bate, 1976: Lifespan of trailing vortices in a turbulent atmosphere. *J. Aircraft,* **13**, 476-482.
- Donohue, G. L.; and D.K. Rutishauser, 2001: The effect of aircraft wake vortex separation on air transportation capacity. 4th USA/Europe Air Traffic Management R&D Seminar, December 3-7, Santa Fe, New Mexico. Paper No. 22.
- Hamilton, D.W. and F.H. Proctor, 2000: Wake vortex transport in proximity to the ground. 19th Digital Avionics Systems Conference, 7-13 October, Philadelphia, PA, AIAA and IEEE, 8 pp.
- Han, J., Y-L. Lin, D.G. Schowalter, S.P. Arya, and F.H. Proctor, 2000: Large eddy simulation of aircraft wake vortices within homogeneous turbulence: Crow Instability. *AIAA Journal*, **38**, 292-300.
- Han, J., Y-L. Lin, S.P. Arya, and F.H. Proctor, 2000: Numerical study of wake vortex decay and descent in a homogeneous atmospheric turbulence, *AIAA Journal*, **38**., pp. 643-656.
- Hinton, D.A., 1995: Aircraft Vortex Spacing System (AVOSS) Conceptual Design. NASA TM - 110184.
- Hinton, D.A., and C.R. Tatnall, 1997: A candidate wake vortex strength definition for application to the NASA aircraft vortex spacing system (AVOSS). NASA TM. - 110343, 35 pp.
- O'Connor, C. J.; and D.K. Rutishauser, 2001: Enhanced airport capacity through safe, dynamic reductions in aircraft separation NASA's Aircraft VOrtex Spacing System. *Journal of Air Traffic Control*, **43**, 4-10.
- Perry, R.B., D.A. Hinton, and R.A. Stuever, 1997: NASA wake vortex research for aircraft spacing. 35th Aerospace Sciences Meeting & Exhibit, AIAA 97-0057, 9 pp.
- Proctor, F. H., 1996: Numerical simulation of wake vortices measured during the Idaho Falls and Memphis field programs. 14th AIAA Applied Aerodynamics Conference, Proceedings, Part-II, 17-20 June, New Orleans, LA, AIAA Paper No. 96-2496, 943-960.

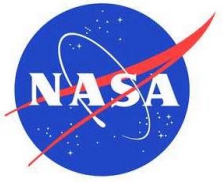

Bibliography (continued)

- Proctor, F. H., D. A. Hinton, J. Han, D. G. Schowalter, and Y.-L. Lin, 1997: Two dimensional wake vortex simulations in the atmosphere: Preliminary sensitivity studies. 35th Aerospace Sciences Meeting & Exhibit, 6-10 January, Reno, NV, AIAA Paper No. 97-0056, 13 pp.
- Proctor, F.H., 1998: The NASA-Langley wake vortex modelling effort in support of an operational aircraft spacing system. Invited paper, 36th Aerospace Sciences Meeting & Exhibit, 12-15 January, Reno, NV, AIAA Paper No. 98-0589, 19 pp.
- Proctor, F.H., and J. Han, 1999: Numerical study of wake vortex interaction with the ground using the Terminal Area Simulation System. 37th Aerospace Sciences Meeting & Exhibit, 11-14 January, Reno, NV, AIAA Paper No. 99-0754, 12 pp.
- Proctor, F.H., D.W. Hamilton, and J. Han, 2000: Wake vortex transport and decay in ground effect: vortex linking with the ground. 38th Aerospace Sciences Meeting & Exhibit, 10-13 January, Reno, NV, AIAA Paper No. 2000-0757, 14 pp.
- Proctor, F.H., D.A. Hinton, and R.L. Bowles, 2000: A windshear hazard index. 9th Conference on Aviation, Range and Aerospace Meteorology, 11-15 September, Orlando, FL, Amer. Meteor. Soc., 482-487.
- Proctor, F.H., and G.F. Switzer, 2000: Numerical simulation of aircraft trailing vortices. 9th Conference on Aviation, Range and Aerospace Meteorology, 11-15 September, Orlando, FL, Amer. Meteor. Soc., 511-516.
- Robins, R.E., and D.P. Delisi: 2002: NWRA AVOSS wake vortex prediction algorithm version 3.3.1. NASA CR-2002-21746, 64 pp.
- Robins, R.E., and D.P. Delisi, 2002: Wake vortex algorithm scoring results. NASA CR-2002-21745, 44 pp.
- Rutishauser, D. K.; and C.J. O'Connor, 2001: Aircraft Wake Vortex Spacing System (AVOSS) Performance Update and Validation Study. NASA TM-2001-211240, 25 pp.
- Sarpkaya, T., 1998: Decay of wake vortices of large aircraft. AIA*A Journal,* **36**, 1671-1679.

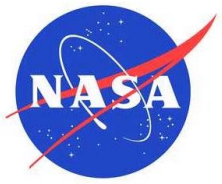

Bibliography (continued)

- Sarpkaya, T., 2000: A new model for vortex decay in the atmosphere. *J. Aircraft,* **37**, 53-61.
- Sarpkaya, T., Robins, R. E., and D.P. Delisi, 2001: Wake-vortex eddy-dissipation model predictions compared with observations. *Journal of Aircraft*, **38**, 687-692.
- Shen, S., F. Ding, J. Han, Y-L, Lin, S.P. Arya, and F.H. Proctor, 1999: Numerical modeling studies of wake vortices: real case simulations. 37th Aerospace Sciences Meeting & Exhibit, 11-14 January, Reno, NV, AIAA Paper No. 99-0755, 16 pp.
- Stewart, E.C., 1998: A piloted simulation study of wake turbulence on final approach. AIAA Atmospheric Flight Mechanics Conference, Boston, Massachusetts, AIAA Paper No. 98-4339, 16 pp.
- Switzer, G.F., and F.H. Proctor, 2000: Numerical study of wake vortex behavior in turbulent domains with ambient stratification. 38th Aerospace Sciences Meeting & Exhibit, 10-13 January, Reno, NV, AIAA Paper No. 2000-0755, 14 pp.
- Switzer, G.F., and F.H. Proctor, 2002: Wake vortex prediction models for decay and transport within stratified environments. 40th Aerospace Sciences Meeting & Exhibit, 14-17 January, Reno, NV, AIAA Paper No. 2002-0945, 6 pp.
- Tatnall, C.R., 1995: A Proposed Methodology for Determining Wake-Vortex Imposed Aircraft Separation Constraints. Masters Thesis, George Washington University, 119 pp.